Exploring Excitonic properties of vertically coupled semiconductor nanostructures using Path Integral Quantum Monte Carlo

Jarosław R. Jarzynka

Submitted for the degree of Doctor of Philosophy

Heriot-Watt University
School of Engineering and Physical Sciences
Edinburgh, February 2016

Abstract

In this thesis electron and exciton systems in atomistic model semiconductor nanostructures are theoretically studied using the Path Integral Quantum Monte Carlo (PI-QMC) technique. The application of this method gave us the opportunity to fully investigate Coulomb interacting systems at finite temperature, with an exact treatment of the impact of inter-particle correlations on the properties of a system without relying on complex trial functions or basis sets.

Using confining potentials calculated from a strained atomistic model of semiconductor vertically stacked dot and ring nano-structures gave us insight into the ground state properties of vertically stacked quantum dot and ring systems, including the interplay between vertical electric and piezoelectric fields. Interactions between external electric fields, strain and piezoelectric potential revealed novel and unique for the stacked structures properties.

The recombination rate of exciton (X) and bi-excitons (XX) as a function of structure vertical separation is investigated and compared against recombination in a multiple quantum dot, both with and without the application of an external electric field.

The novel piezoelectric properties of stacked dots and rings in the presence of a vertical electric field, inducing in-plane charge probability distribution switching of an exciton, are explored. Results obtained from calculations of the lateral polarisability of X and XX indicates the possibility of experimental verification of this unique phenomenon.

Acknowledgements

I would like to thank my advisor, Professor Ian Galbraith, for his thoughtful and patient guidance as I explored uncharted territory. He has inspired me by his enthusiasm for exploring new ideas and for developing helpful intuitive models. Working with Professor John Shumway has been an incredible pleasure. He has been generous in taking the time to discuss his theories to me, and he continues to challenge me and inspires me to be curious about nature. I am grateful to all the group members of the Semiconductor Theory Group. They have helped me enormously to find empowerment and confidence in my work, and have been an incredible team. Peter McDonald introduced me to the topic and helped me to develop my own system for successful research. Peter also guided me through the early stages of this project and encouraged me to push forward even when I experienced uncertainties in the research. I would like to say big thanks to Ian Jones who also greatly helped my complete the writing up stage of my thesis. I would like to give big, big thank you Richard McCracken for your selfless help and time you spent proof-reading and constructively commenting on my thesis. A number of people have been generous and helpful to me while here at Heriot-Watt University and I am really grateful. I thank my friends, who have been supportive and curious about my work and have offered insight and perspective on this long path. I would lastly like to thank my incredible friend and life partner Patrycja for being my best friend and a joyful blessing my life.

Contents

Dla mojej Patrycji

Chapter 1

Introduction

The last two decades have been characterised by the fast development of new methods of designing and manufacturing physical structures, with dimensions that vary between a few and one hundred nanometers. These so called nanostructures demonstrate many novel and interesting physical properties, as their small size limits the movement of charge carriers in at least one spatial dimension, resulting in discrete energy levels [1, 2]. The impact of the system size on the charge distribution is known as the quantum confinement effect [3, 4].

One of the most important groups of nanostructures, from an applications point of view, are semiconductors. Their importance results from their physical properties which can be well described using quantum mechanics, and have broad applicability in modern optoelectronic devices.

Nanostructures can be classified into: quantum wells, rods, dots and rings. Quantum wells result from the heterojuction that is formed between two semiconductors characterised by different energy bandgaps. As a consequence of this bandgap difference the Fermi levels in both semiconductors align to each other, shifting the relative positions of the conduction and valence bands. Sandwiching a narrow band semiconductor between two wider band materials creates a quasi-two-dimensional potential well in the middle, which allows for the movement of charge carriers only in two spatial directions Fig. 1.1. This technique also allows for the fabrication of systems of coupled quantum wells, known as a super-lattices, in which the wells are separated by a potential barrier. Using this method, heterostructures are usually formed from group II and VI or III and V compounds, as the chemical composition affects the energy band gap and therefore gives control over the quantum confinement strength.

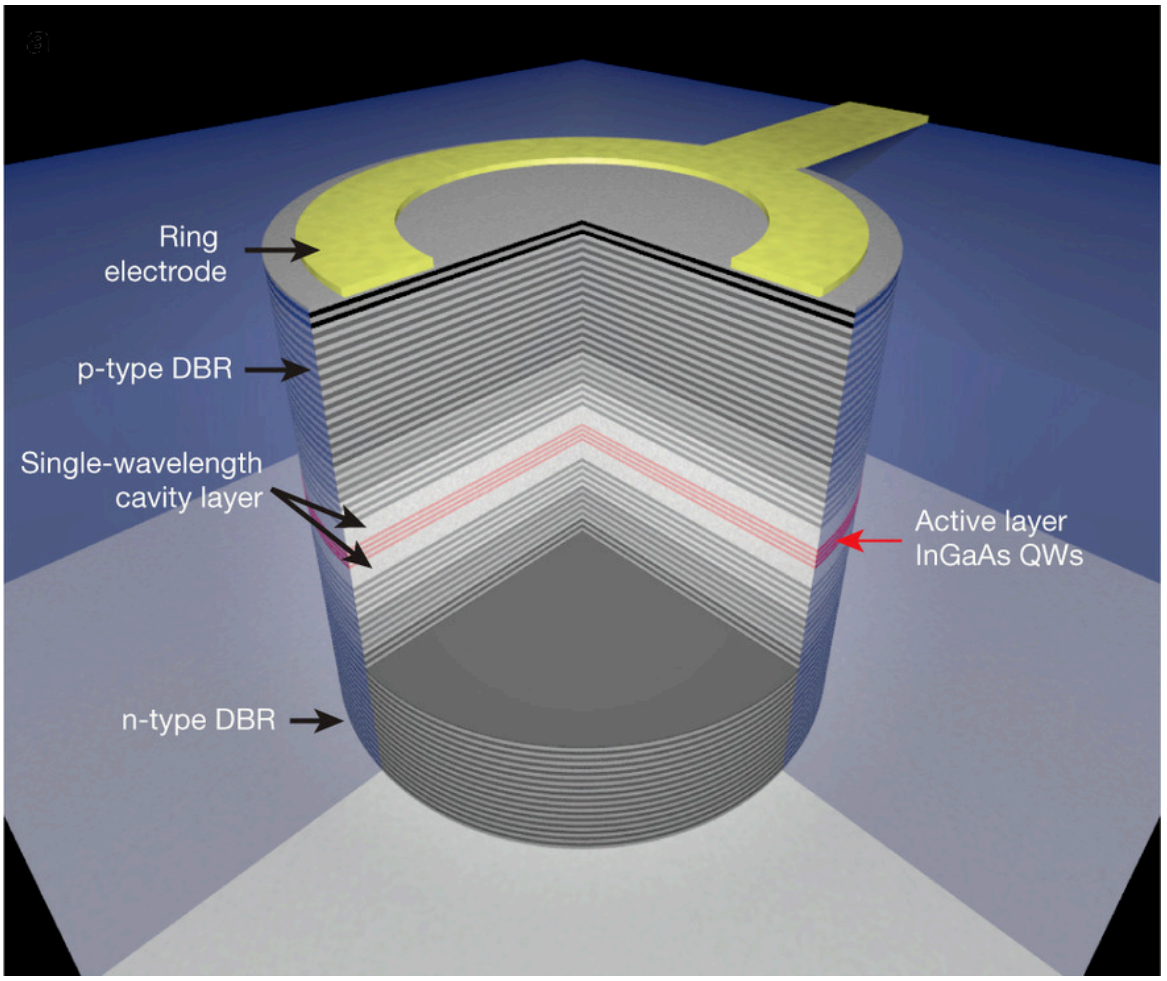

Figure 1.1: Visualization of an electrically contacted micro-pillar containing four quantum wells. The structure diameter is 20 μm. This quantum post is placed between slowly doped distributed Bragg reflectors. Taken from Ref.[5].

Depending on the Fermi level distribution and difference of energy band gaps of the semiconductors used, the electrons and holes can be trapped in the same region of space (which is known as Type I) or in different regions (Type II) where the quantum well for the electron is seen as the barrier for the hole and *vice versa* [6].

1.1 Quantum wells

1.1.1 Single square quantum well

A type I quantum well is formed by two thick identical semiconductor layers such as $Ga_{1-x}Al_xAs$ separated by a layer of GaAs, Fig. 1.2. If the electron mass m^* is set

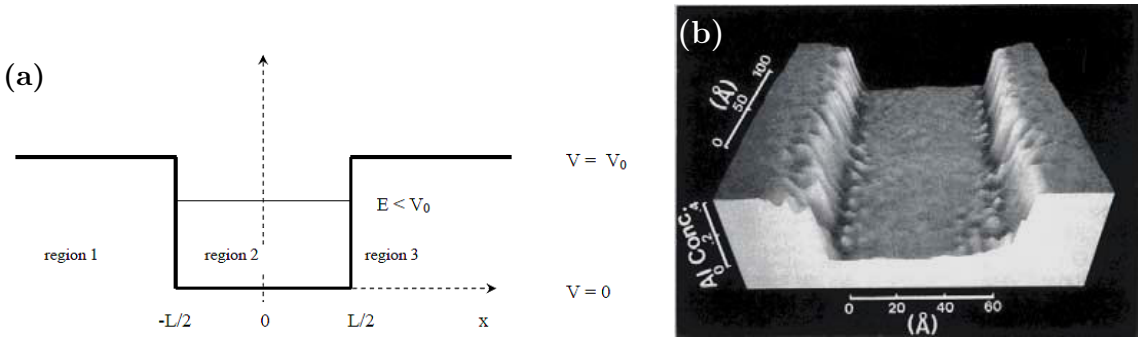

Figure 1.2: Finite square well potential under effective mass and envelope function approximation. In the above figure the potential energy V_0 represents the discontinuity in the conduction band edge due to different compounds. (a) Diagram of square quantum well, Ref.[7], (b) STM image of GaAs quantum well, Ref.[8].

constant in both $Ga_{1-x}Al_xAs$ and GaAs layers then the Schrödinger equation in the three layers depicted in Fig. 1.3a yields

$$-\frac{\hbar^2}{2m^*}\frac{d^2\psi_1(x)}{dx^2} + V_0\psi_1(x) = E\psi_1(x), \quad x \leqslant -L/2 \tag{1.1}$$

$$-\frac{\hbar^2}{2m^*}\frac{d^2\psi_2(x)}{dx^2} = E\psi_2(x), \quad -L/2 \leqslant x \leqslant +L/2 \tag{1.2}$$

$$-\frac{\hbar^2}{2m^*}\frac{d^2\psi_3(x)}{dx^2} + V_0\psi_3(x) = E\psi_c(x), \quad +L/2 \leqslant x. \tag{1.3}$$

The general solution of the Schrödinger equation (SE) in the central region (2) will be a sum of sine and cosine terms. One can see that we deal here with a symmetric potential, therefore the eigenstates of the system will also demonstrate a definite symmetry being either symmetric or anti-symmetric. If the centre of the coordinate system is located at the middle of the quantum well (QW) then the symmetric (even parity) eigenstates will be cosine terms and the anti-symmetric (odd parity) sine waves.

In the QW (region 2) the energy E of the quantum states must be smaller than the potential barrier height V_0. This leads to the following form of SE for the right-hand side region

$$-\frac{\hbar^2}{2m^*}\frac{d^2\psi(x)}{dx^2} = (E - V_0)\psi(x). \tag{1.4}$$

At this point we require the continuous function f for which a second derivative exists and is $+f$. This condition is fulfilled by an exponential function and the sum of the growing $f(x) = e^{+\kappa x}$ and decaying $g(x) = e^{-\kappa x}$ exponents can be exploited. In the

region (3), x is positive, and hence as x increases the growing exponential will increase too and without limit [9]. The probability density of the wave function must sum up to 1,

$$\int_{allspace} \psi^*(x)\psi(x)dx^2 = 1, \tag{1.5}$$

which further demands that, $\psi(x) \to 0$ and $\frac{\partial\psi(x)}{\partial x} \to 0$ as $x \to \pm\infty$. These are known as the standard boundary conditions for states confined to the QW. Taking all the above into consideration, the growing exponents must be discarded, which leads to the solutions for the even parity states [9]:

$$\psi(x) = B\exp(\kappa x), \quad x \leqslant -L/2 \tag{1.6}$$

$$\psi(x) = A\exp(kx), \quad |x| \leqslant L/2 \tag{1.7}$$

$$\psi(x) = B\exp(-\kappa x), \quad L/2 \leqslant x. \tag{1.8}$$

It is important to note that the above functions are real, additionally the eigenfunctions of such confined system are known as stationery states, as there is no current carried. Substitution of these trial functions in the SE yields k and κ,

$$k = \frac{\sqrt{2m^*E}}{\hbar}, \quad and \quad \kappa = \frac{\sqrt{2m^*(V_0 - E)}}{\hbar}. \tag{1.9}$$

At this point the boundary conditions need to be imposed with the requirement that $\psi(x)$ and its derivative are continuous, in order to avoid infinite kinetic energies. At the interface $x = +L/2$ the wave function in the barrier and the well must be equal, the same condition must be met by its derivatives, therefore

$$A\cos\left(\frac{kL}{2}\right) = B\exp\left(-\frac{\kappa L}{2}\right), \tag{1.10}$$

$$-kA\sin\left(\frac{kL}{2}\right) = -\kappa B\exp\left(-\frac{\kappa L}{2}\right). \tag{1.11}$$

Division of Eq.(1.10) by Eq.(1.11) and rearranging yields

$$k\tan\left(\frac{kL}{2}\right) - \kappa = 0. \tag{1.12}$$

The odd parity states in the well region are described by a sine wave, therefore similar to the above analysis results in the following equation

$$k \cot\left(\frac{kL}{2}\right) + \kappa = 0, \tag{1.13}$$

which solutions yields odd parity eigenenergies. Eqs.(1.12) and (1.13) are called transcendent as they depend on only one unknown, E; and do not have any analytical solution. For this reason we resort to a numerical solution. This is achieved by introducing two dimensionless parameters $\eta = \frac{kL}{2} = \frac{L}{2}\sqrt{\frac{2m^*}{\hbar^2}E}$, which depends on energy and $\zeta_0 = \frac{L}{2}\sqrt{\frac{2m^*}{\hbar^2}V_0}$, known as potential-strength parameter which depends on barrier height. Using these parameters the relationship between k and κ can be defined [7],

$$\frac{\kappa}{k} = \sqrt{\frac{\zeta_0^2}{\eta^2} - 1}. \tag{1.14}$$

Using Eq.(1.14) one can rewrite Eqs.(1.12) and (1.13) as follow,

$$\tan\eta = \sqrt{\left(\frac{\zeta_0}{\eta}\right)^2 - 1} \quad even \quad parity \tag{1.15}$$

$$\cot\eta = -\sqrt{\left(\frac{\zeta_0}{\eta}\right)^2 - 1} \quad odd \quad parity. \tag{1.16}$$

Solving Eqs.(1.15) and (1.16) yields energy eigenvalues E_n for a finite well. In Fig. 1.3 a plot of the solution as a function of η is presented. In order to obtain energy eigenvalues a plot of $\sqrt{\left(\frac{\zeta_0}{\eta}\right)^2 - 1}$ can be superimposed on plots of $\tan(\eta)$ and $-\cot(\eta)$ and solved graphically for different values of L, V_0 and ζ_0. In Fig. 1.4 the energy levels of the three bound states are plotted for ζ_0=3.83. In Fig. 1.5 eigenfunctions and first three energy eigenvalues of a finite square well are plotted and compared to the bound states in infinite square well. The eigenenergies of the finite well are much lower compared to an infinite well of the same width. This difference results from the fact that the wave functions in the finite square well extend into the classically forbidden region, therefore the corresponding wavelengths are longer as energies are lowered compared to those in the infinite potential.

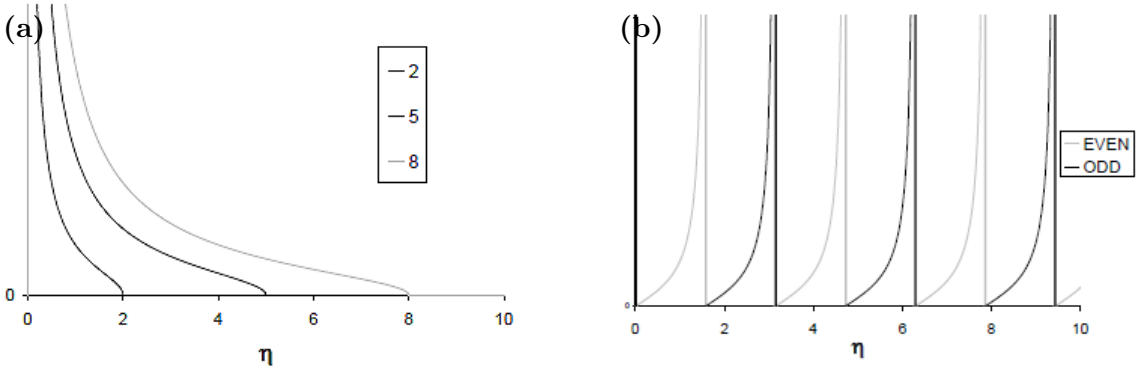

Figure 1.3: Finite square well potential under effective mass and envelope function approximation. In the above figure the potential energy V_0 represents the discontinuity in the conduction band edge due to different compounds. (a) A plot of $\sqrt{\left(\frac{\zeta_0}{\eta}\right)^2 - 1}$ vs. η, (b) Plots of $\tan(\eta)$ for even and odd parity solutions vs. η.

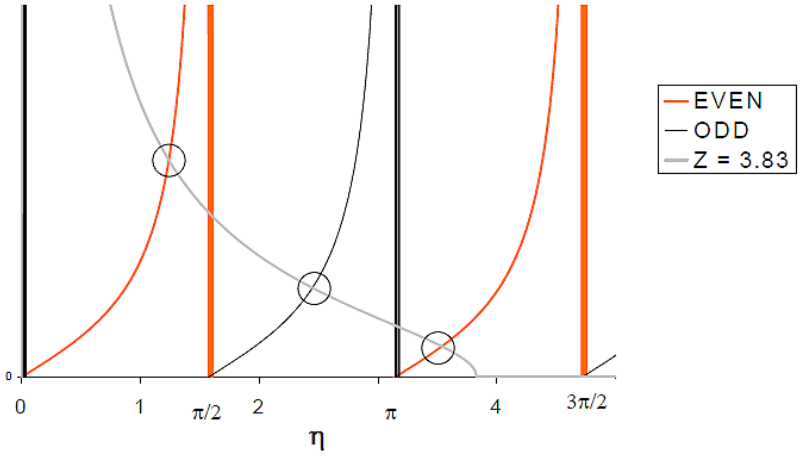

Figure 1.4: Graphical solution for the energy eigenvalues of three bound states in finite potential well. The width of the well is 14 A and V_0=14 eV. Taken from Ref.[7].

1.1.2 Impact of electric field on energy levels in a single quantum well

The application of an external electric field in the growth direction introduces an additional linear potential, Fig. 1.6 which can be written in the following form $\pm eFz$, depending on the charge of the particle. If the applied electrostatic field is small then its impact on the energy levels in a quantum well can be estimated using first-order perturbation theory. For the perturbing potential, namely the electric field in the

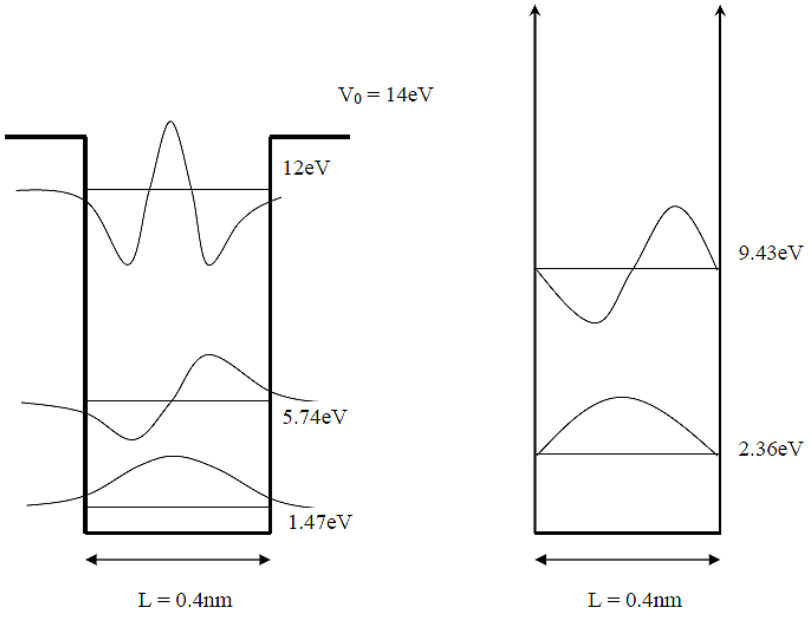

Figure 1.5: Eigenfunctions for the first three bound states of the finite GaAs well of depth 14 eV and with 0.4 nm compared to the infinite square well. Taken from Ref.[7].

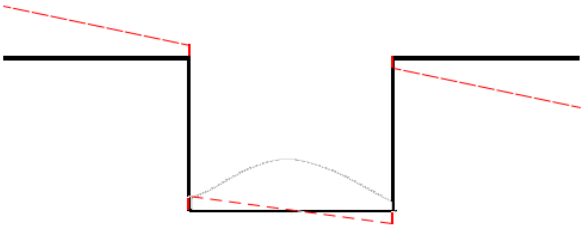

Figure 1.6: Comparison of the ground state wave function in absence (solid black line) and presence (red dashed line) of external electric field in a finite square well.

growth direction V', the shift of the ground state energy can be found using

$$\Delta E^{(1)} =< \psi_1|V'|\psi_1 > . \tag{1.17}$$

If the electric field is small it doesn't have any impact on the ground state energy in the symmetric quantum well. This results from the fact that the ground state wave function is of even parity, therefore the integrand of Eq.(1.17) is odd and its evaluation yields zero to the first-order the same applies to the excited state. The application of stronger electric fields require much more accurate treatment and the second-order correction is required

$$\Delta E^{(2)} = \frac{| < \psi_n|V'|\psi_1 > |^2}{E_n - E_1}, \tag{1.18}$$

in which one sums over all excited states, including those where $E_n > VL$. The external electric field is independent of z, therefore the second-order correction to the energy $\Delta E^{(2)}$ is directly proportional to the value of field F^2. Charged particles preferentially localise in the lowest potential regions. In the case of the symmetric QW this area is to the right of the well Fig. 1.6. This lowers the overall energy of the system even further $\Delta E^{(2)} \propto -F^2$ and is known as the quantum confined Stark effect, which will be discussed in detail in the following chapters.

1.1.3 Non-interacting double square well system

More complex electronic devices are based on the heterostructures made of multiple quantum wells. The method of solving the Schrödinger equation in each layer separately and then estimating the unknown coefficient by superimposing boundary condition discussed in Section 1.1.1 is still valid in multiple quantum wells. In this section the symmetric system of equal depth quantum wells will be briefly outlined Fig. 1.7. A simplified model can be imagined as two non-interacting particles are

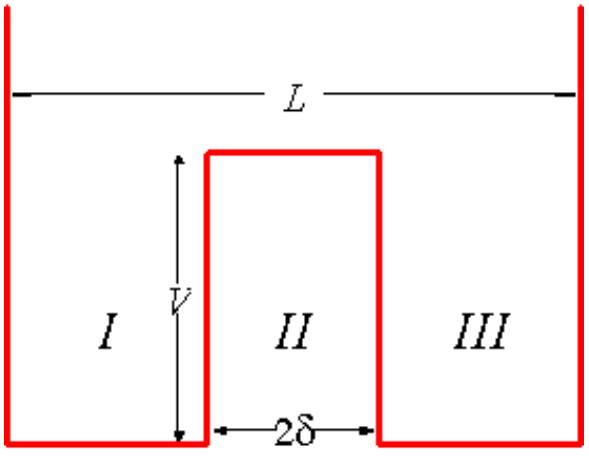

Figure 1.7: Solutions to the Schrödinger equation in a double square well. Taken from Ref.[10].

allowed to move only in one spatial dimension. Fig. 1.7 depicts system an infinite square well with a potential barrier of the finite height in the middle. The particles can be placed the regions I and III with energies lower than the barrier height. Now we try to find the energy eigenstates and corresponding eigenfunctions for the single particle states. Assuming that the central potential region II is very large leads to the observation that energy eigenstates of the trapped particles should be approximately equal to those of a single particle in an infinite well [10]. As before the solutions to

the SE in all three region yields

$$\psi_I(x) = \sin(k(E_i)x) + A(E_i)\cos(k(E_i)x), \tag{1.19}$$

$$\psi_{II}(x) = B_i(E_i)(e^{\kappa(E_i)x} + n_i e^{-\kappa(E_i)x}), \tag{1.20}$$

$$\psi_{III}(x) = n_i \psi_I(-x), \tag{1.21}$$

where index i indicates even/odd parity states and $n_{even} = 1$ and $n_{odd} = -1$. The usual boundary conditions require the wave function to vanish in the potential walls, in our case for $x < -L/2$ and $x > L/2$, and also that the function and its derivative is continuous at $x = \pm\delta$. Application of these conditions allows us to set A and B_i, [10]

$$A(E) = \tan(k(E)), \tag{1.22}$$

$$B_i(E) = \frac{A(E)\cos(k(E)\delta) - \sin(k(E)\delta)}{e^{-\kappa(E)\delta} + n_i e^{\kappa(E)\delta}} \tag{1.23}$$

and the boundary conditions also yield the following transcendental equation

$$\frac{\kappa(E)[-\sin(k(E)\delta) + A(E)\cos(k(E)\delta)]}{k(E)[\cos(k(E)\delta) + A(E)\sin(k(E)\delta)]} + \frac{e^{\kappa(E)\delta} + n_i e^{-\kappa(E)\delta}}{e^{\kappa(E)\delta} - n_i e^{-\kappa(E)\delta}} = 0. \tag{1.24}$$

Fixing δ and V one can solve the equation numerically which leads to two energy eigenvalues E_{even} and E_{odd} with corresponding eigenfunctions plotted in Fig. 1.8. It is worth to note that there are two almost degenerate energy eigenstates for every one energy eigenstate in the corresponding infinite square well [10].

1.1.4 Quantum mechanical tunnelling

Charge carriers placed into multiple well systems localise in the regions which minimise their energy and there is no quantum-confined energy states [9]. However, the situation changes when an external electric field is introduced perpendicular to the layers in a multiple quantum well system. An additional potential accelerates and impinge the electrons (holes) upon the barrier leading to the situation that some of them pass through the barrier even with an energy lower than the potential V. This phenomenon is known as quantum tunnelling.

In order to calculate the tunnelling probability that a single electron impinging upon the potential barrier will tunnel and contribute to the current flow through the

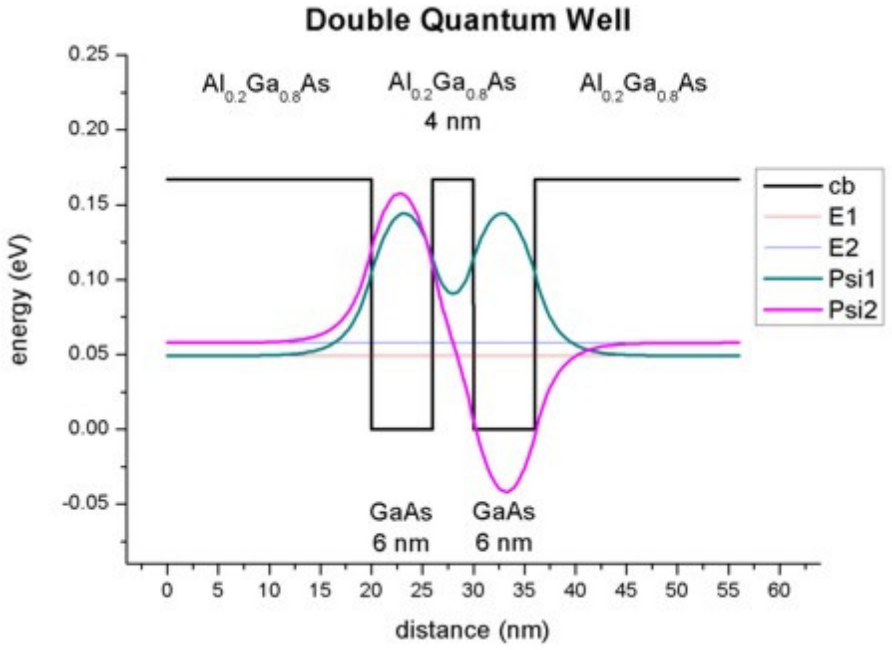

Figure 1.8: Eigenfunctions in a double square well. Taken from Ref.[11].

barrier the transmission coefficient needs to be defined. If a constant effective mass across the structure is assumed then the transmission coefficient at any energy E for a barrier of width L and height V is defined as [9]

$$T(E) = \frac{1}{1 + \left(\frac{k^2+\kappa^2}{2k\kappa}\right)^2 \sinh^2(\kappa L)} \quad for \quad E < V. \tag{1.25}$$

If the charge carriers have energy greater than barrier potential, then $\kappa \to ik'$ which yields

$$T(E) = \frac{1}{1 + \left(\frac{k^2-k'^2}{2kk'}\right)^2 \sin^2(k' L)} \quad for \quad E > V, \tag{1.26}$$

where $k' = \sqrt{\frac{2m^*(E-V)}{\hbar}}$. In the last case, for $E > V$ the transmission coefficient will oscillate with a resonance for sin component equal zero. This will be observed at $k'L = n\pi$ which is implied when [9]

$$E = \frac{(n\hbar\pi)^2}{2m^*L^2} + V. \tag{1.27}$$

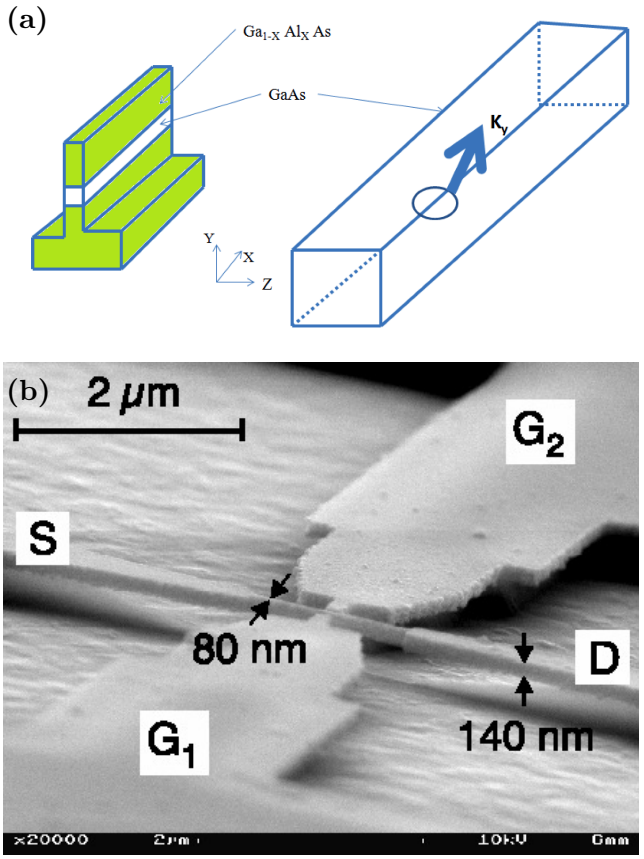

Figure 1.9: Quantum wire. (a) Diagram of a quantum wire. Taken from Ref.[9]. (b) SEM micrograph of a suspended silicon quantum wire in a highly n-doped SOI film. Taken from Ref.[12].

1.2 Quantum wires

Photolithography or electron-beam lithography can be used to pattern a quantum well layer, which after an etching process leaves a free standing strip of quantum well material. This structure can then be filled in with an overgrowth of the barrier material, for instance $Ga_{1-x}Al_x$. In Fig. 1.9 the expanded view of a single quantum wire is presented, from which one can see the electron (or hole) confinement to two dimensions and ability to move in only one direction, similar to a classical wire. If the effective-mass approximation is used the dispersion relation corresponding to the motion along the axis of wire can still be described by a parabolic function

$$E = \frac{\hbar^2 k^2}{2m^*}. \tag{1.28}$$

1.3 Self-assembled quantum dots

A quantum dot is basically a three-dimensional potential well in which the charge carriers can be trapped. Quite often this kind of confinement can be realised by restricting the movement of charge carriers in the plane of a two-dimensional quantum well. This can be done via reduction of the physical size of the structure or with an external electric potential. This can be achieved for example by the alternate distribution of two layers of semiconductor which suppress the charge movement in the growth direction of the dot and vertical external electric field, which prevents carriers from moving in the plane of the structure. As it will be explained in this thesis a vertical external electric field can be successfully used for electrode-less switching of the charge density distribution and for efficient exciton flux control. Quantum dots

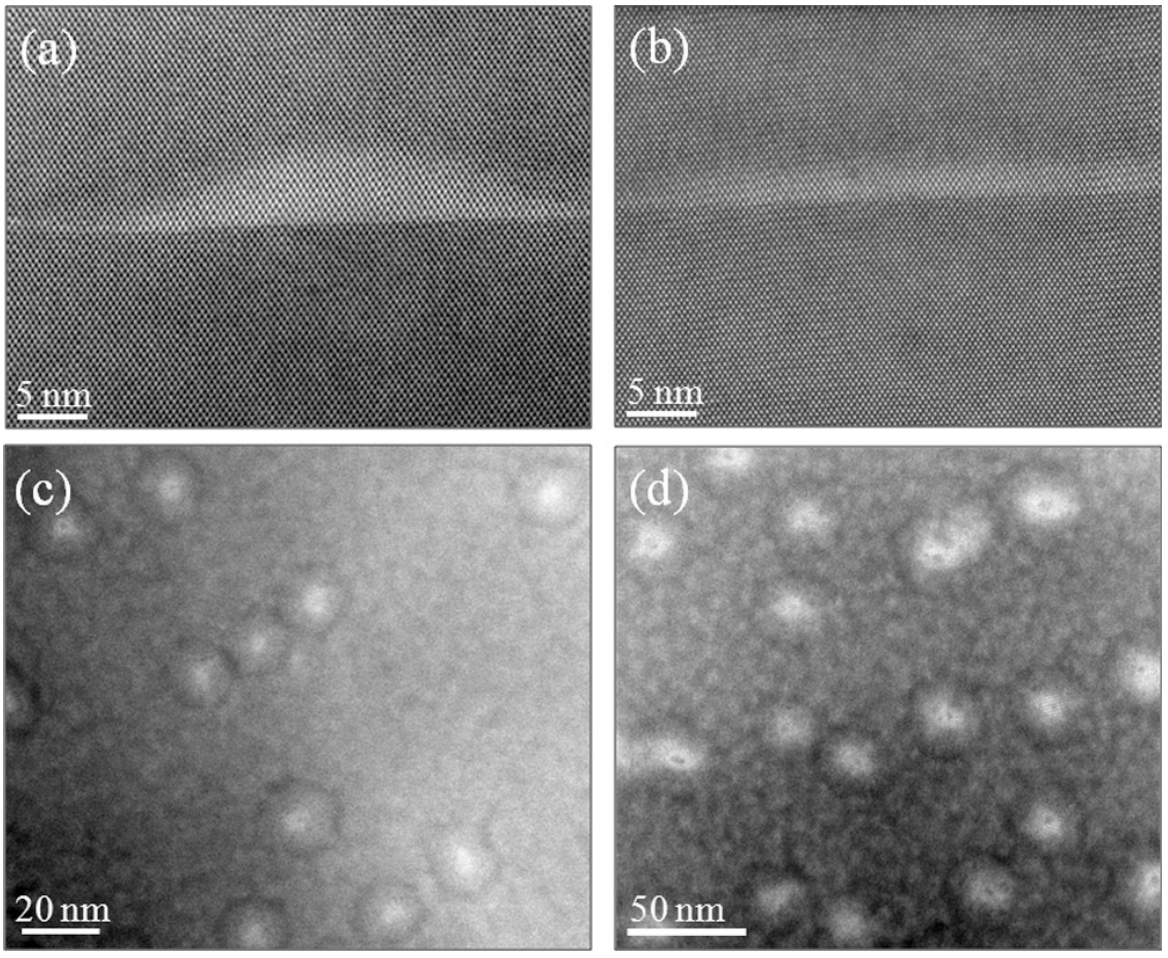

Figure 1.10: Cross-sectional HAADF STEM images of quantum dots (QDs) formed from depositing of InAs in a InGaAsP matrix and capped with with different compounds: (a) InGaAsP and (b) GaAs followed by InGaAsP. (c) and (d) Plan-view HAADF STEM images of the QDs in samples (a) and (b), respectively. Taken from Ref.[13].

possess many similarities to natural atoms. The central potential well has properties similar to the hydrogen atom reflecting the heavy proton in the atom core. Additionally the spectrum of the confined charge carriers is quantised and the electronic distribution demonstrates the shell structure in the symmetric dots [14]. Because of these similarities the single quantum dots are often called "artificial atoms", and multiple dot systems "artificial molecules". One of the most important and useful feature stems from the fact that the quantum dots allow for the formation of electron-hole bound systems, namely excitons [15], whom behaviour in quantum structures is the main topic of this thesis. At the present, due to their specific electronic and optoelectronic properties, the quantum dots are broadly applicable in novel devices. Self-assembled single quantum dots can be used as single photon sources or single electron transistors [16, 17] as well as in lasers [18] and for quantum computing [19]. In the following section we discuss the growth methods and the most important physical properties of these particular quantum structures.

1.3.1 Stranski-Krastanow growth mode

Stranski-Krastanow (SK) growth mode is the technique in which strain-induced self-assembly of dots takes place in heteroepitaxial lattice mismatched system [20]. The dot formation process results from a thermodynamic instability during the two-dimension growth and can be used to grow for example $In_xGa_{1-x}As$ structures on a GaAs substrate [21–23]. In Fig. 1.11 the self-assembly process of quantum dot grown in the SK mode is illustrated. In the first stage of the SK growth mode the InGaAs is deposited on a GaAs substrate. As the result of biaxial compression a thin layer, known as the wetting layer (WL) is formed, Fig. 1.11(b). The consequent layers of the InGaAs are then deposited until the critical thickness is reached. At this point heavily strained InGaAs WL starts to relax by releasing strain energy through the formation of three-dimensional dots [21, 24]. Formation of QDs lead to a reduction of the total free energy stored in the system. This results from the overcompensation of the increase of surface energy by the reduction of strain energy in the layer Fig. 1.11(c) [25]. As a result, free structures are spontaneously formed [22, 26], which makes them highly applicable in optical systems. Basic structural properties of QD structures e.g. islands density [27], composition gradient and shape [28, 29] can be controlled to some extent by adjusting the process parameters such as chemicals flux, time and temperature. Unfortunately due to the stochastic character of the self-assembly process one

can't avoid some fluctuations. If the substrate isn't initially pre-processed the nucleation sites can't be controlled and as a consequence the QDs form randomly on the WL. In order to obtain confined charge carriers in all spatial dimensions the newly formed quantum dot structures are buried in wider gap GaAs Fig. 1.11(d). The additional barrier formed in the last step separates the QD's electronic states from surface one. This also inhibits non-radiative recombinations resulting from the surface charge separation and prevents a degradation of the optical properties [30]. Ideal crystal structures created during self-assembly conjugated with the capping GaAs results in high optical quality quantum dot structures.

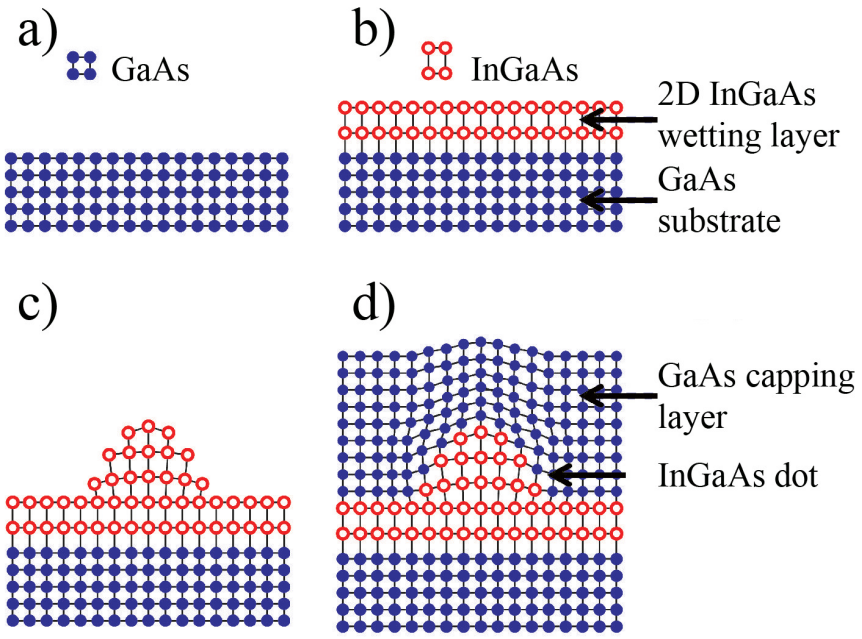

Figure 1.11: The Stranski-Krastanow growth mode of self-assembled quantum dots. (a) GaAs substrate, (b) deposition of InGaAs onto an atomically flat GaAs substrate leads to the growth of a biaxially strained InGaAs layer. (c) When a critical layer thickness is reached, partial strain relaxation minimises the free energy of the system resulting in the formation of dots on top of a wetting layer. (d) The self-assembled quantum structure is capped with intrinsic GaAs to form fully encapsulated InGaAs islands with three-dimensional confinement. Taken from Ref.[30].

There are two methods of obtaining self-assembled QD structures, the first one is metal-organic vapor phase deposition (MOVPD) [31] and the second one is molecular beam epitaxy (MBE) [24]. Semiconductor heterostructures obtained using MBE are characterised by high material purity and exceptional crystal quality. This technique allows for precise, up to atomic monolayer scale control of the material deposition [32]. Additionally, this method leads to the defect free growth which increases even more the optical quality of the QD structures.

1.4 Basic properties of self-assembled single quantum dots

A discrete, atom like energy spectrum in the QD confinement is similar to the particle in the box problem [33]. The energy level structure depends directly on the particular properties of the confining potentials of the structure which are the consequence of the size, shape, composition gradient and strain fields present in semiconductor used in the fabrication of the dot [33–37]. In the following section a simple model of the potential in three-dimensional QDs will be introduced. Using the InGaAs quantum dot as a model, the electronic properties of such a structure will be outlined and their impact on optoelectronic features of the quantum dot explained. We also discuss the impact of the external, static electric field on the energy spectrum and the charge carrier's behaviour in the QD [38, 39] including inter-particle interactions [40, 41].

1.4.1 Model of quantum dot

In this thesis the atomistic model of the QD, based on experimental results, is constructed and used to study the interacting particle systems. However in order to explain basic properties of the confinement potential in such a structure a simpler model can be used. Such a model will assist us in the qualitative explanation of fundamental electronic properties of the QD structure and better understand processes in the more complex systems.

A typical InGaAs hererostructure is characterised by the Type-I band alignment in which the bulk GaAs band gap has an energy of E_g=1500 meV [42] and the energy of $In_{0.5}Ga_{0.5}As$ is E_g=800 meV [43] at 2 K. However, it is important to note that these values are usually slightly different due to the significant strain energy resulting from the already mentioned lattice mismatch of the compounds. As we have already pointed out, the charge carriers are confined in all three spatial directions. This results from the fact that the InGaAs band structure forms a minimum energy region, which manifests itself as the dot, in GaAs surroundings [44].

Cross-sectional transmission electron microscopy (X-TEM) enables examination of the dots after they have been buried [34, 45, 46]. According to the structural investigations using the above technique, the QD's height is typically a factor of 5-7 times smaller compared to its base [22, 47]. As a result we observe much stronger

confinement in the growth direction compared to the lateral direction. Based on this observation a model QD confinement can be described by the square potential well in the z-direction Fig. 1.12(a), (b) and a two-dimensional rotationally-symmetric harmonic oscillator potential in the $x - y$ plain Fig. 1.12(c). We use the effective

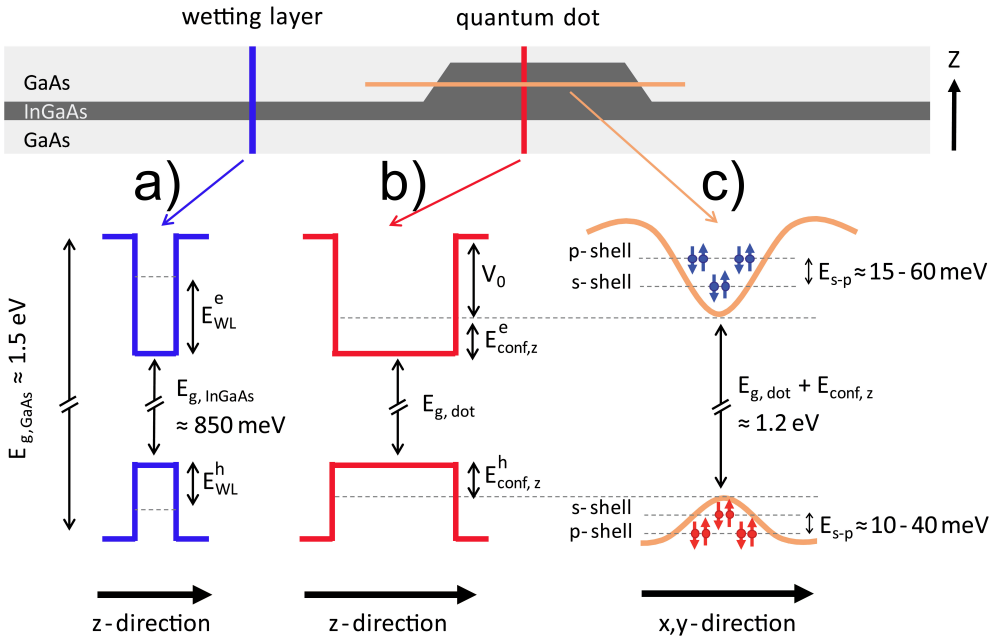

Figure 1.12: Confinement potentials for electrons and holes in quantum dots and the wetting layer arising from the type I band alignment in GaAs-InGaAs heterostructures. In the z-direction, it can be modeled by a square potential well. Typically, only the first level of the resulting discrete energy spectrum is observed to form a bound state in self-assembled InGaAs QDs. Since the QD base is significantly larger than its height, the lateral confinement is much weaker and more appropriately described by a 2D harmonic potential. Taken from Ref.[30].

mass approximation in both the above model and our simulations. This is a valid approach as we are interested in the ground state energies of the system which are close to the band minima (maxima) [48, 49]. Such a system can be described using the time-dependent Schrödinger equation

$$\left[-\frac{\hbar^2}{2m^*} + V(\mathbf{r})\right] = \Psi_k(\mathbf{r}) = E_k \Psi_k(\mathbf{r}) \tag{1.29}$$

in which the confining potential $V(\mathbf{r})$ is defined as

$$V(\mathbf{r}) = \begin{cases} \frac{1}{2} m^* \omega_0^2 (x^2 + y^2) & \text{for } |z| < \frac{h}{2} \\ V_0 & \text{for } |z| > \frac{h}{2} \end{cases}, \tag{1.30}$$

where m^* is the effective mass, ω_0 harmonic potential oscillation frequency and h is the height of the structure. Solution to Eq.(1.29) is obtained using the usual wave function substitution

$$\Psi_k(\mathbf{r}) = \Phi_{k_x k_y}(x, y)\chi_{k_z}(z), \tag{1.31}$$

in which $\Phi_{k_x k_y}(x, y)$ is the wave function in the (xy)-direction and $\chi_{k_z}(z)$ is in z-direction. This methods allows us to separate the equation and solve the problem in two perpendicular directions separately. Solutions to the harmonic potential problem are given by Hermite polynomials H_k [50], which multiplied by the solution for the square well confinement yield a complete set of the eigenstates of the quantum dot system

$$\Psi_k \propto H_{k_x}(x)H_{k_y}(y)\exp\left[-\frac{\omega_0 m^*}{2\hbar}(x^2+y^2)\right]\cos\left(\frac{\pi z k_z}{h}\right) \text{ for } k_i = 0, 1, \cdots, \tag{1.32}$$

with the eigenvalue energies given by

$$E_k = \hbar\omega_0(1 + k_x + k_y) + \frac{\pi^2\hbar^2}{2m^*h^2}(k_z + 1)^2 \text{ for } k_i = 0, 1, \cdots. \tag{1.33}$$

Most of the self-assembled InGaAs QDs measure less than 10 nm in the growth direction. This results in the vertical confinement energies $E_z^e + E_z^h$ of order of several hundred meV as observed experimentally [51–53]. Usually only one bound state in the growth direction is expected, which is located at the top of the band (k_z=0). As one can see in Fig. 1.12(a) the InGaAs wetting layer is much thicker than the QD structure in the z-direction. This leads to an increase in confinement energy $E_{WL}^e + E_{WL}^h$, typically by $\approx$ 100 - 200 meV, experienced by the charge carriers which would try to move from the QD structure towards wetting layer [54]. For this reason it is strongly suppressed. However, the opposite situation in which a charge carrier is created in the WL results in the propagation of it towards the QD structure and the quick relaxation at the energy minimum.

At the centre of the Brillouin zone, the valence band Bloch functions have the p-like character. This results in the reduction of the rotational symmetry leading to the formation of an effective mass m^* dependent valence sub-bands. The p-type orbitals are described by the internal angular momentum J_p=1 with corresponding $J_{p,z} = -1, 0, 1$ which couples to the spin of the electron $J_e = 1/2$ with $J_{e,z} = \pm 1/2$ and fill the valence band state. As a consequence the following hole sub-bands are created with a total angular momentum $\mathbf{J}_h = \mathbf{J}_p + \mathbf{J}_e$: heavy hole (hh) $J_{hh} = 3/2$,

$J_{hh,z} = \pm 3/2$; light hole (lh) $J_{lh} = 3/2$, $J_{lh,z} = \pm 1/2$ and spin-orbit split-off (so) $J_{so} = 1/2$, $J_{so,z} = \pm 1/2$.

The energy splitting of the split-off sub-band due to spin-orbit coupling is effectively increased by several hundred meV, [55, 56]. However, due to the characteristics of our model, it is of no relevance for our analysis and, therefore, will be omitted in the following discussion. The effective mass m^* in $In_{0.5}Ga_{0.5}As$ for a heavy hole (m^*=0.46 m_0) [57] is one order of magnitude greater compared to the light hole effective mass (m^*=0.054 m_0) [57]. This results in the lifting of the degeneracy between this two valence sub-bands in the vertical direction and a much stronger confinement of the light hole compare to the heavy hole. This leads to the situation in which the highest energy valence band state demonstrates predominantly heavy hole character [58–61]. Strong strain fields present in the self-assembled quantum structures amplify this effect even more.

In Fig. 1.12(c) the lateral confining potential (in the plane perpendicular to the growth direction) is visualised. The much stronger confinement in the vertical (growth) direction significantly modifies the energy band-gap lifting the lowest energy level above the band-gap energy by the value $\hbar\omega_0$ (energy of the 2D harmonic oscillator potential) which yields an effective energy band-gap value: $E_{g,eff}$=$E_{g,dot}$+$E_{conf,z}$. Typically, few bound excited states are present [51, 62] which can be seen analogically to atomic electronic shells. For this reason the *s*-, *p*-, *d*-, ... labels are commonly used to distinguish between them. The typical value of energy they are split by varies between $E_{s-p} = \hbar\omega \approx 15$ to 60 μeV for the conduction band and ≈10 to 40 μeV for the valence band in the InGaAs structure [30, 41, 51, 62, 63]. Inclusion of the spin of the charge carriers (blue and red arrows in Fig. 1.12(c)) introduces an additional degree of freedom which results in a 2 (k_x+k_y+1)-fold degeneracy of each energy level. As can be seen in Fig. 1.12(c) the band-gap energy seems to increase towards the QD edge as the result of the strain fields distribution in the system. This behaviour was predicted theoretically using numerical simulations on realistic model of the QD [64].

1.4.2 Optical selection rules

If the temperature is low, $k_BT \ll E_g$, the system is in its ground state, this mean that the valence band is fully populated and conduction band is empty. Introduction to the system of a photon with energy $\hbar\omega > E_g$ optically excites the system promoting

an electron from the valence band to the conduction band in the semiconductor. The excited electron creates an empty state in the valence band known as a quasi-particle hole state [30]. In this picture the incident photon generates an electron-hole pair known as an exciton, however in this scenario the binding is dominated by the confinement potential of the QD instead the Coulomb attraction. As already explained, the highest energy valence band state which plays a crucial role in the optical transitions has heavy hole character [58–61]. This results in the optical selection rules which, for two electron with $J_{e,z} = \pm 1/2$ and two heavy holes with $J_{hh,z} = \pm 3/2$ states can be summarised in the following diagram Fig. 1.13. As indicated on the diagram four excitonic states can be created. The helicity of circularly polarised light determines the angular momentum $M = \pm 1$ of photon. This results in the fact that only transitions with a difference in the z-component of the angular momentum of $\Delta J_z = \pm 1$ between the initial and final state can be optically excited *via* a single photon process due to spin conservation (green diagonal arrows in Fig. 1.13). The optically active excitons with $\Delta J_{ex,z} = \pm 1$ are commonly called bright in contrast to dark, optically inactive excitons with $\Delta J_{ex,z} = \pm 2$. In the dark exciton case the coupling to the light takes place in the process involving two photons [65] which is much weaker compared to single photon absorption (red arrows Fig. 1.13). The above properties can be really useful in the experiment as they expand the set of degrees of freedom of exciton by spin, if appropriately polarised light is used. A $\sigma^{\pm}$ polarised photon induces an exciton (with spin projection $\Delta J_{ex,z} = \pm 1$) formed from the electron and hole $|\downarrow\Uparrow\rangle$ ($|\uparrow\Downarrow\rangle$) relative to the direction of the light propagation. This leads to the capability of detecting the polarisation of the light emitted in photoluminescence measurements and determining the spin properties of recombining charge carriers.

1.4.3 Fine structure

Several properties of quantum dot structures can be qualitatively understand using the energy spectrum that was derived in Section 1.4.1 from a simplified QD model. However, there are other properties emerging from experimental data which this model is not able to reproduce. The limitations results from the fact that at this moment we do not consider inter-particle interactions, impact of the external conditions, such as coupling to static electric fields or confining potential directional asymmetry which manifests themselves in a prominent fine structure present in the energy spectrum [30, 33, 66–71]. In this section the interactions which predominantly influence the

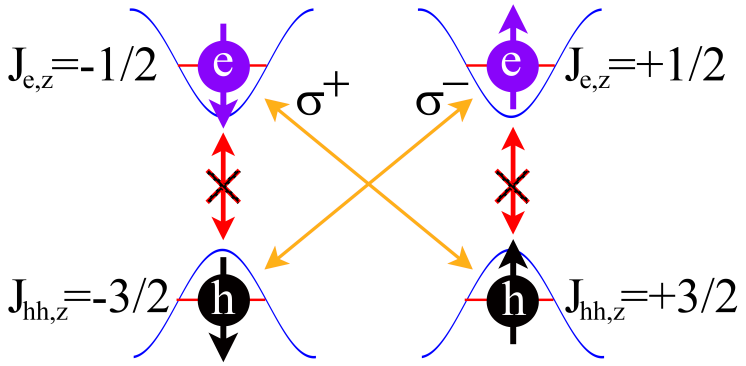

Figure 1.13: The optical selection rules. $\sigma^{\pm}$ indicates polarisation of the light to which transitions with $\Delta J_z = \pm 1$ are coupled. On the other hand the transitions with $\Delta J_z = \pm 2$ can not be optically excited by a single photon. Four possible configurations with respect to the electron $\uparrow \downarrow$ and hole $\Uparrow \Downarrow$ spin orientation can be distinguished. The angular momentum projection of $J_{ex,z} = +1$ ($|\downarrow\Uparrow\rangle$) and $J_{ex,z} = -1$ ($|\uparrow\Downarrow\rangle$) corresponds to a bright exciton while $J_{ex,z} = +2$ ($|\uparrow\Uparrow\rangle$) and $J_{ex,z} = -2$ ($|\downarrow\Downarrow\rangle$) to the dark one. Taken from Ref.[30].

QD's energy spectrum will be outlined. Here, we briefly discuss the consequences of the reduced symmetry in the QD confinement and Coulomb interactions while the impact of the electric field will be covered in the next section.

In Fig. 1.14 the excitonic energy spectrum characteristic for a real QD is depicted. On can observe that inclusion of Coulomb attraction between the electron and hole in a QD structure results in decreasing the transition energy by $\approx$ 10-20 meV [72]. As the electron and hole are confined to the QD the exciton Coulomb energy in the structure is higher than in the bulk semiconductor [72].

The electron and hole wave functions due to their fermionic character must be anti-symmetric in order to overlap in the QD. This results from the Pauli exclusion principle [73] and introduces an additional type of interaction known as exchange interaction [67, 74]. The spin Hamiltonian for an exciton in the absence of magnetic field is given

$$\mathcal{H}_{exchange} = a_z J_{hh,z} \times J_{e,z} + \sum_{i=x,y,z} b_i J^3_{hh,i} \times J_{e,i}. \tag{1.34}$$

In the Eq.(1.34) the excitonic states are distinguished by the total angular momentum m in the z direction, $m = J_{e,z} + J_{h,z} = \pm 1, \pm 2$ with the electron spin $J_{e,z} = \pm 1/2$ and the hole spin $J_{hh,z} = \pm 3/2$, [67]. The exchange energy contributes to a splitting resulting in the separation of bright and dark excitons by an energy value $\delta_0 = 1.5a_z + 3.375b_z$ typically of order 100 - 200 μeV [67, 68, 74]. Additionally, the dark and bright excitonic states split even further from each other by the amount of energy

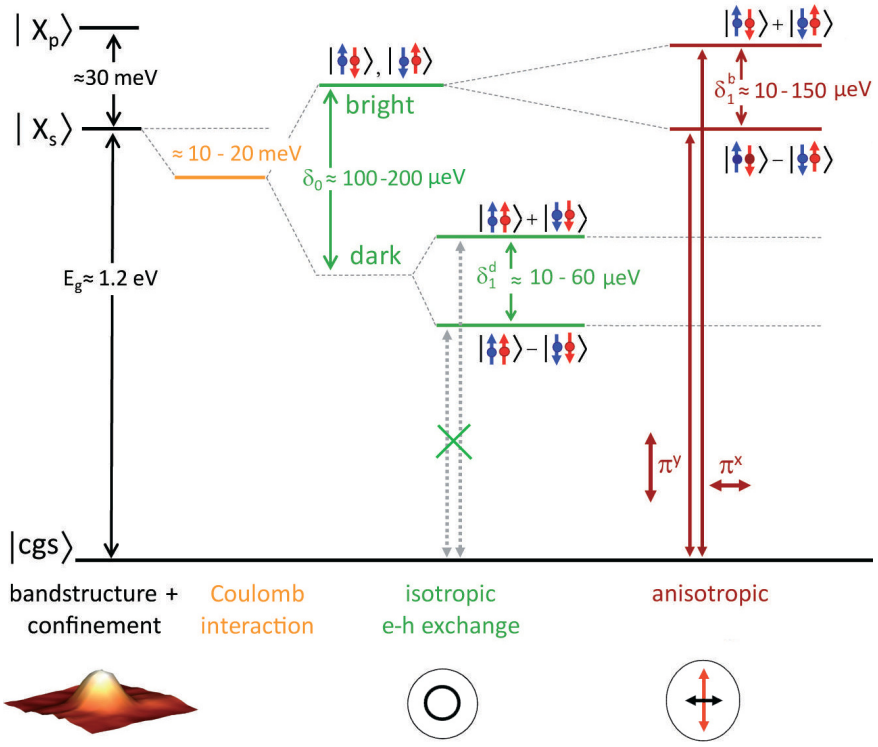

Figure 1.14: Graphical representation of excitonic fine structure and corresponding optical transition in a QD. The energy spectrum undergoes modification caused by the Coulomb interaction and the reduction of rotational symmetry of confinement. Taken from Ref.[30].

$\delta_1^d = 0.75(b_x + b_y)$ for dark state and $\delta_1^b = 0.75(b_y - b_x)$ for bright one [67, 68, 74]. The anisotropic exchange splitting of the bright exciton is completely absent in the perfectly symmetric structures. In such a QD $b_x = b_y$ which yields pure spin states $|\downarrow\Uparrow\rangle$ and $|\uparrow\Downarrow\rangle$ in contrast to the dark states which always hybridise [30]. In most real life cases, QD self-assembly results in a slightly elliptical structures, therefore $b_x \neq b_y$ and the bright exciton energy splits as $\delta_1^b \neq 0$ [68]. In this case eigenstates are linear combinations of symmetric and antisymmetric pure states as the angular momentum is not a good quantum number anymore [30]. As the result of these mixed states polarisation selection rules are lifted and the possibility of linearly polarised optical transitions ($\pi^{x(y)}$) arise.

1.4.4 External electric fields

The exciton consist of a positively charged hole and a negatively charged electron, which form an electric dipole $\mathbf{p} = e\mathbf{d}$, where $\mathbf{d}$ is the displacement vector pointing

from the negative charge to the positive charge, which couples to applied electric field $\mathbf{F}$ [59, 75]. The interaction of the electric field and dipole moments results in an energy shift proportional to $\Delta E = \mathbf{p} \cdot \mathbf{F}$ which provides an empirical tool for the precise tuning of the energy spectrum in QDs.

The exciton dipole moment is the sum of the intrinsic dipole moment $\mathbf{p}_{int}$ and applied electric field driven dipole moment. The first contribution depends entirely on the atomistic properties of the QD structure. It results from the asymmetry of the confining potential in the growth direction caused by In atom concentration gradients and strain driven piezoelectric fields [76, 77]. This induces the hole localisation at the top of the structure close to the In rich apex and the electron at the base [59]. The second contribution results form the electron and hole wave function shift in response to the applied external electric field and is proportional to the product of polarisability β and external electric field and $\mathbf{F}$. In the electric field QD confinement suppresses ionisation of electron-hole pair in contrast to the free exciton [38]. All the above contributions sum up to give the total shift of transition energy, known as quantum confined Stark effect (QCSE) [38, 59, 75], given by equation

$$\Delta E_{QCSE} = E_0 + \mathbf{p}_{int} \cdot \mathbf{F} + \beta \mathbf{F}^2, \tag{1.35}$$

in which E_0 is the transition energy without an external electric field.

Another consequence of an applied external electric field to the QD structure is the effective modification of the potential barrier, which affects the tunnelling rate of carriers out of the structure. In the absence of an applied electric field most of excitons recombine radiatively. However, in the limits of a strong electric field, excitonic lifetimes and recombination rates are controlled by tunnelling processes which can be used to tune the dwell time of charge carriers in the QD [30]. The relationship between the electric field and tunnelling rates Γ_t can be estimated theoretically using Wentzel-Kramers-Brillouin (WKB) method [78–80]. In this approach the one-dimensional square well of width h_w and potential barrier of energy E_b is exploited with an electric field F_z applied perpendicular to the well [30]. The tunnelling rate is then computed using the equation

$$\Gamma_t = \frac{\hbar\pi}{2m^* h_w^2} \exp\left\{-\frac{4}{3\hbar e F_z}\sqrt{2m^* E_b^3}\right\}, \tag{1.36}$$

where m^* is the effective mass. As the electric field term F_z is in argument of the

exponent Eq.(1.36) it can be used to control the tunnelling time of charge carriers over several orders of magnitude [30, 81–84] up to $\approx 1\,\text{ns}$ [85], which corresponds to the radiative recombination time. The effective masses and the potential barriers for the electron and hole in a QD are different, however the above also holds for the exciton lifetime calculation in the QD in the tunnelling regime [30].

The simplicity with which charge carrier flow can be controlled in the QD structure is one of the more important advantages of this nanostructure. This can be achieved by varying the potential difference between the electrodes and their relative position to the dot (Fig. 1.15). In single dots the electrodes are usually placed on the the same layer of the semiconductor and the migration of charge carriers takes places in the plane perpendicular to the growth direction. In this situation, by changing the electric field one can adjust the height and the size of the potential barrier between coplanar dots and control the tunnelling coupling between these structures [86, 87].

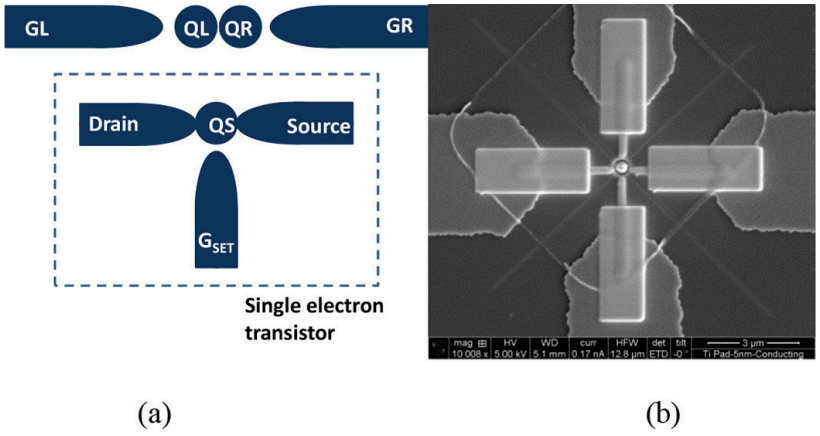

Figure 1.15: (a) A single-electron transistor (SET) coupled to two interacting quantum dots (QL, QR) for quantum-bit (Q-bit) generation and manipulation. (b) A Q-bit device fabricated using a combination of optical lithography, focused ion beam deposition, and atomic force microscope (AFM)-assisted chemical vapour deposition (CVD) of a quantum dot in the middle. QS: Q-bit. G_{SET}: SET channel. Taken from Ref.[88].

1.5 Double quantum dot

Two or more layers of quantum dots grown on the top of each other leads to the formation of vertically stacked quantum structures. The stacked QDs can interact with each other if the thickness of the spacer is small enough, which results in the formation of coupled systems [46, 89–95]. Such molecule-like structures open new possibilities

to investigate coupling effects in low-dimensional quantum dot molecule (QDM) systems and bring us closer to controllable scalability of quantum information processing architecture based on these structures. Coupled quantum nanostructures are a not completely new phenomenon. Previously, the coupling and interaction strength in coupled low-dimensional nanostructures were successfully realised and controlled in double quantum well heterostructures [96–99]. Also, the vertically coupled QDs are not an entirely new idea. The first coupled QD system was successfully fabricated in 1997 using a twofold cleaved edge overgrowth (CEO) technique [100] in which QD structures can be aligned with sub-nanometer precision [101]. The downside of this method is its high complexity and difficulty to implement the method for controlling the coupling in the structure. Therefore it has not been extensively used for vertically stacked structures fabrication. A much more controllable and defect free technique is offered by strain-driven self-assembly of QDM, achieved using Stranski-Krastanow mode, in which the layers of QDs are separated by thin barrier. This method exploits the strain fields in the barrier material originated from the QD in the lower layer which induces the formation of dots in the upper layer aligned to islands underneath [23, 24, 102]. The main advantage of this method is that precise control of the growth parameters allows for very high stacking accuracy and efficiency leading to growth of a significant number of stacked structures at once [45, 102, 103].

1.5.1 Properties of self-assembled vertically stacked quantum dot

The QDM, of which the atomistic model equivalent will be discussed in this thesis, is made of two or three layers of self-organised InGaAs QDs grown on the GaAs substrate using molecular beam epitaxy in the Stranski-Krastanow mode. The process starts with the single InGaAs layer deposited on the GaAs substrate. In the next step the newly formed QDs are capped with GaAs film thin enough to allow strain from the not fully relaxed dots underneath to propagate to the surface. This induces self-assembly of the new layer of QDs preferentially aligned in the vertical direction with the dots in the previous layer. This alignment is stimulated by the fact that the surface potential for In atoms is modified by strain fields preservation, which results in the minimum value directly above the buried QDs [23, 24, 102]. This is a highly efficient process as can be seen at the top of Fig. 1.16. Additionally if the spacer thickness is less that 15 nm, a close to unity stacking probability can be

obtained [45, 102, 103]. In order to achieve such an exceptional stacking efficiency the diffusion length of the In atoms of the surface has to be comparable to the inter-dot separation in the seed layer to allow sufficient material transport to the nucleation regions [30, 103]. The diffusion length can be accurately controlled by varying the thermal conditions in the MBE chamber. If the process is repeated periodically the columns of stacked structures can be grown [45]. The vertically stacked quantum dots

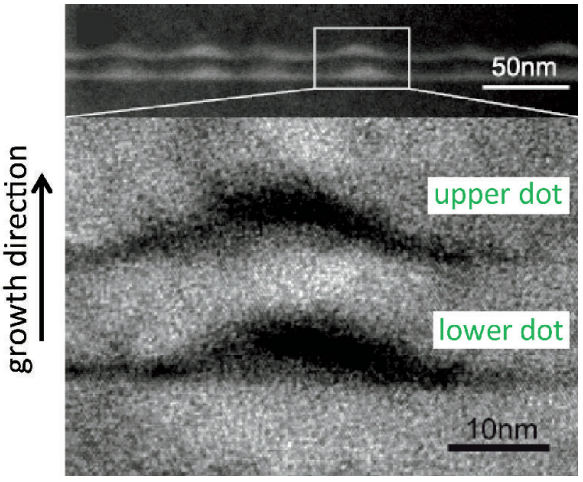

Figure 1.16: XTEM image of a stacked quantum dot molecule (top panel) and close up of single vertically coupled quantum dot system. Taken from Ref.[30].

represent much more complex system compare to single QD which is reflected in e.g. different excitonic states possible to populate a stucture Fig. 1.17. There are two

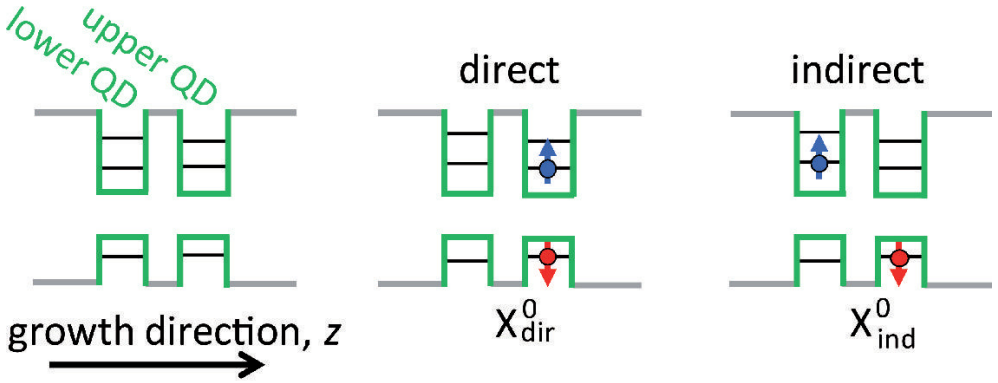

Figure 1.17: Neutral exciton X^0 states in a double quantum dot structure in the absence of an external electric field. There are two distinguishing configurations: electron and hole occupying the same quantum structure (direct X^0) and different structures (indirect X^0). Taken from Ref.[30].

possible configurations of a neutral exciton X^0 in the vertically stacked double dot system. If electron and hole both populate the same quantum dot then the situation is

similar to the exciton in the single dot structure and a direct exciton X^0_{dir} is observed. Alternatively charge carriers can be spatially separated occupying opposite structures resulting in an indirect exciton X^0_{ind}. The separation between the electron and hole wave function in the direct exciton is significantly smaller compared to the indirect exciton. In the first case the displacement of the electron and hole wave functions results from the asymmetry of the confinement in the grow direction and piezoelectric field distribution [59, 76, 77], which localises the electron at the base of the structure while the hole is attracted towards the In-rich apex. In the indirect exciton the wave function's separation is directly related to the inter-dot spacer thickness and for that reason can be large. As a consequence the intrinsic dipole moment carried by an indirect exciton is much larger, which yields much stronger coupling to the external electric field and a greater Stark shift ΔE_{QCSE} compared to the direct exciton [38, 59, 75, 92]. This property allows one to distinguish between direct and indirect excitons and tune them in and out of resonance using external electric fields.

1.5.2 Coupling in vertically stacked quantum dots

If the thickness of a GaAs barrier separating layers of quantum dots is less than 15 nm the quantum states in of the individual dots can interact with each other. The strength of these interactions depends on their relative energy detuning and plays an important role in the coupled states formation [30]. Two interacting states tuned in and out of resonance demonstrate interesting behaviour known as anti-crossing in which energy crossing is avoided. We discuss this phenomenon in more detail for the case of tunnel-coupling of direct and indirect excitons in a vertically coupled system. The coupling mechanism is a consequence of quantum mechanical tunnelling of the charge carriers between the dot through potential barrier. For aligned quantum levels resonant tunnelling leads to strongly coupled states where new eigenstates may occur [92]. As it has already been pointed out the Stark shift for the X^0_{dir} and X^0_{ind} excitons differs, this property can be used to vary the detuning between the two states $\Delta_{dir-ind}$ using an electric field. If the quantum states in the QDM are uncoupled then the eigenstates of $X^0_{dir/ind}$ obey the Schrödinger equation

$$\mathcal{H}^0 \Psi_{dir/ind} = E_{dir/ind} \Psi_{dir/ind}, \tag{1.37}$$

in which $\mathcal{H}^0$ is a hamiltonian of the uncoupled system and $E_{dir/ind}$ is the eigenenergy. For the system in which the two states are coupled by the value κ, the resulting

eigenstates of the interacting system Φ_i are the linear combination of Ψ_{dir} and Ψ_{ind} as follow

$$\Phi_i = \alpha\Psi_{dir} + \beta\Psi_{ind} \qquad with \qquad |\alpha|^2 + |\beta|^2 = 1. \tag{1.38}$$

The Hamiltonian of the coupled system $\mathcal{H}_C = \mathcal{H}^0 + \kappa$ can then be expanded using first order perturbation theory and expressed as [103]

$$\mathcal{H}_C = \begin{pmatrix} E_{dir} & \kappa_{dir-ind}/2 \\ \kappa^*_{dir-ind}/2 & E_{ind} \end{pmatrix}, \tag{1.39}$$

where the coupling matrix element $\kappa_{dir-ind}/2$ ($\kappa^*_{dir-ind}/2$) is given by $\langle\Psi_{dir}|\kappa|\Psi_{ind}\rangle$ [30]. The detuning parameter between the uncoupled states $\Delta_{dir-ind} = E_{dir} - E_{ind}$ can be used to express the eigenvalues of the coupled hamiltonian

$$E_\pm = E_{dir} + (\Delta_{dir-ind} \pm \sqrt{\Delta^2_{dir-ind} + \kappa^2_{dir-ind}})/2. \tag{1.40}$$

Corresponding to Eq.(1.40), eigenstates $\Psi_\pm$ are symmetric and antisymmetric linear combinations of uncoupled states Ψ_{dir} and Ψ_{ind} which form bonded (Φ_+) and anti-bonded (Φ_-) molecular states [30]

$$\Phi_+ = \frac{1}{\sqrt{2}}(\Psi_{dir} + \Psi_{ind}) \tag{1.41}$$

$$\Phi_- = \frac{1}{\sqrt{2}}(\Psi_{dir} - \Psi_{ind}) \tag{1.42}$$

The schematic diagram of tunnel anti-crossing between X^0_{dir} and X^0_{ind} and the electron localisation within the QDM as a function of detuning parameter $\Delta_{dir-ind}$ is plotted in Fig. 1.18. Large values of the detuning parameter results in fact that the energies of coupled states $E_\pm$ and uncoupled states $E_{dir/ind}$ occur simultaneously. A reduction of $\Delta_{dir-ind}$ promotes tunnelling coupling which induces formation of hybridised states. At zero detuning the electron is completely delocalised in all of the structure forming the QDM and the degeneracy of the system is removed. The energy shift between bonding and anti-bonding states is strongly dependent on the separation of the constituent dots and also on the charge carrier's effective mass [92]. At the anti-crossing between bonding and anti-bonding states it is $2\kappa_{dir-ind}$. States in the ideal model system are maximally entangled, however in the real life situation the coupling strength and degree of entanglement are significantly affected by strain, piezoelectric fields and broken symmetry [103–106].

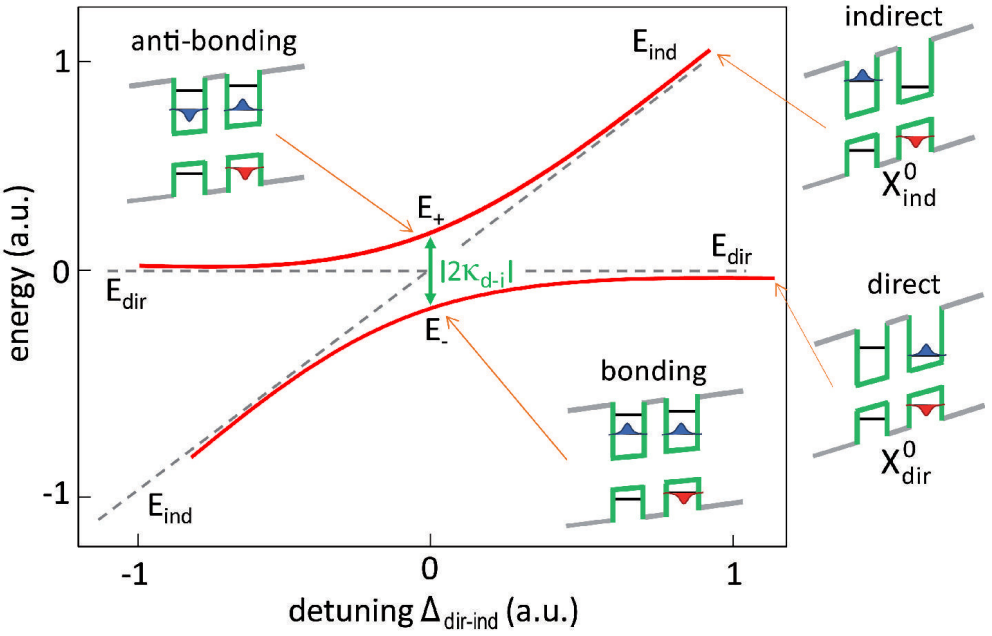

Figure 1.18: Neutral direct and indirect exciton tuned in and out of resonance demonstrates an avoiding crossing behaviour. The energy of the direct exciton is set to zero for simplicity. For $\Delta_{dir-ind} = 0$ the energy levels for electrons in both quantum dots are aligned. As a consequence resonant tunnelling is possible between the dots in a vertically stacked system leading to coupled states with eigenenergies $E_{\pm}$. This yields the formation of hybridised bonding and anti-bonding molecular states shifted by the value of coupling strength constant κ. Taken from Ref.[30].

1.5.3 Characterisation of stacked quantum dots

Similarly to the single QD systems the basic properties of the QDM can be deduced from their interaction with an applied electric field in the form of photoluminescence (PL) spectra. In the Fig. 1.19 emission spectra of a QDM after non-resonant optical wetting layer excitation is plotted [107]. The striking feature of this picture is the strong an anti-crossing behaviour indicating strong coupling in the experimental system. The red and blue curves were obtained using Eq.(1.40) and indicate energy levels corresponding to tunnel anti-crossing between direct and indirect excitons. States in the absence of coupling towards which the eigenstates are converging with an increasing value of detuning parameter are plotted using the dashed line. Depicted in Fig. 1.19, avoiding crossing indicates electron-electron anti-crossing in an exciton. As this results from direct and indirect excitons in the QDM it can be exploited for the identification of spectral lines [92, 107]. As one can see the Stark shift, from direct and indirect exciton can be easily distinguished. There is also additional information possible to extract from the energy spectrum in Fig. 1.19. It can be observed that PL

emission originating from X^0_{ind} decays with increasing detuning and becomes optically more active approaching the anti-crossing region. This effect originates from the variation of the mixing ratio of the levels depending on the detuning. The weak overlap of the electron and hole wave function in indirect excitons makes them optically inactive. Their detection is only possible due to coupling effects and the coupled states emerge brighter proportionally to the contribution of direct excitons.

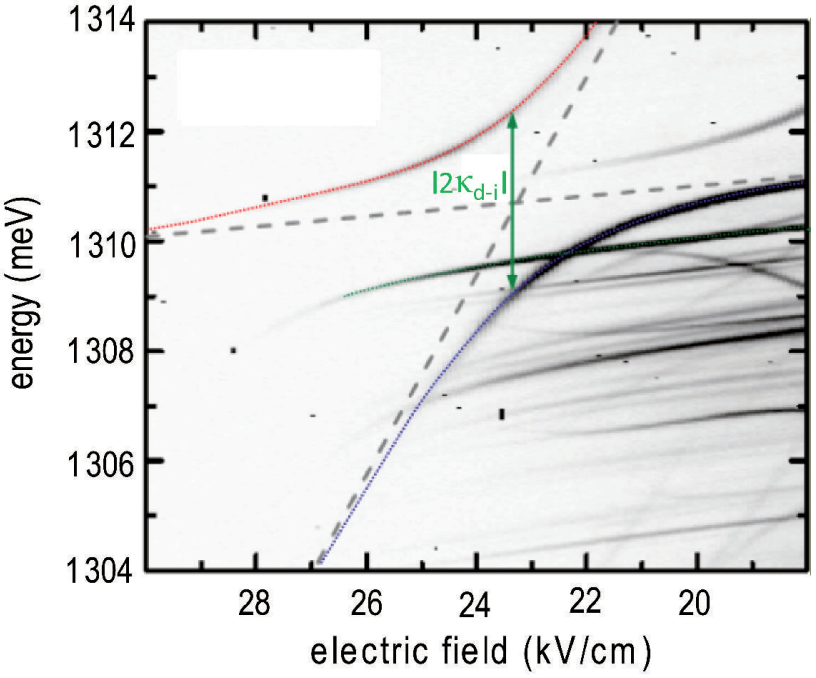

Figure 1.19: PL spectrum as a function of electric field from a vertically stacked double quantum dot obtained due to wetting layer excitation. Taken from Ref.[107].

Vertically stacked quantum dots allow for charge propagation in the growth direction, which can be done by placing electrodes on different layers of the structure one above the other. Adding another electrode to the system allows for the introduction of additional trapping confinement in the plane of the structure. Experimental results, based on the analysis of absorption in the far infrared region of the spectrum, have shown that close to the centre of the structure (where electrons are trapped) the confinement is parabolic [108, 109]. If the single quantum dot is cylindrically symmetric then it demonstrates the structure of a single particle state which is characteristic of a two-dimensional harmonic oscillator. Because of the spatial symmetry of such a dot the electron distribution shows the shell structure and for a small number of charge carriers the energy level population follows Hund's rule for a given symmetry, similar to natural atoms [110–112]. Modulation of an external electric field on an additional electrode allows for the shape of the potential in the plane of the structure to be

changed and as a result the structure of the energy levels also. The impact of the field on the electronic structure can then be investigated by studying electron transport through the dot in terms of a quantum coulomb blockade [113]. A Coulomb blockade originates from the discrete structure of a single particle energy states and Coulomb interactions between electrons confined to the dot. As a consequence of this in low temperatures, of order mK, the single electron current flows through the structure. This phenomenon is the foundation of the single electron field transistor [114], Fig. 1.15.

1.6 Quantum rings

A quantum ring (QR) offers an additional form of geometry for the self- assembly process. A variety of semiconductor compounds have been used to grow QRs such as InGaAS [115], InAs/InP [116], GaSb/GaAs [117] and SiGe/Si [118], however in this thesis only InGaAs structures are considered. The InAs QR structure used in our simulations are of toroidal shape with GaAs in the centre and surroundings. In the following section the method of fabrication of QRs will be introduced together with a discussion of the relative uncertainty of the physical dimension.

1.6.1 Properties of self-assembled quantum rings

In 1997 Garcia *at al.* reported the formation of QR structures characterised by a large lateral extent obtained in the consequence of annealing of quantum dot [115]. This phenomenon triggered significant experimental interest in this structures [115, 119–125]. The geometry of QRs resemble in general that of donut with the central region GaAs rich and a ring of InGaAs around the core. Previous theoretical and experimental work has indicated that QRs, which morphologically originate from quantum dots, demonstrate different electronic and optical properties and behaviour compare to their dot relatives [126–129]. The main difference between rings and dots results from the GaAs barrier material at the rings central region, which strongly affects confining potential and generates strain fields characteristic only for this geometry.

The starting point in the growth of quantum ring structures is a layer of quantum dots, preferably $\approx 10\,\text{nm}$ tall [124], grown using the already described MBE method. Such an ensemble of QDs is capped with a layer of GaAs up to 20 % of the dot's height

[130]. An abrupt change in the annealing conditions lasting between 30-60 seconds results in crater formation in the central area of the dot structure.

The physical properties of QR structures, such as radius, height and landscape scan can be obtained using Atomic Force Microscope (AFM). The earliest samples of the surface QRs were characterised by a large outer radius $\approx 100\,\text{nm}$ and a small height $\approx 2\,\text{nm}$ with the crater formed at the top of initial quantum dot structure.

The most important phase in self-assembly of In atoms from the centre of the dot can be explain as follow. At the annealing temperature In atoms are much more mobile compare to Ga. This explanation can be supported by the characteristic elongation of the QRs along the $[1\bar{1}0]$ direction, which is parallel to preferential direction of In diffusion. The above situation is schematically depicted in Fig. 1.20. However, there is one important detail which shades this picture. QR structures were also reported in compounds which are the members of the same group III, such as InAs/InP [116]. In this situation the diffusion argument cannot be used since atoms are the same and their diffusion rates are equal. An alternative explanation that has been proposed is a de-wetting process which takes place during partial capping of InAs QDs. According to this an additional capping layer may disrupt the equilibrium state formed after dot self-assembly, the formation of the QR can potentially lead to restoring the broken equilibrium and relaxation of the system.

Figure 1.20: Schematic self-assembly of quantum ring structure, a) initial quantum dot is partially capped with GaAs, b) during the annealing phase the In diffuses outwards opening the crater in the top of QD, c) In and Ga atoms mix leading to the QR formation. Taken from Ref.[119].

A system of surface quantum ring structures demonstrates the different properties compared to the quantum rings buried under an additional layer of GaAs. On of the main difference is the lateral sizes of the structure. Furthermore much larger permanent vertical dipoles have been reported which suggests that height of the ring may be much bigger than measured with AFM [126, 129]. Additional measurements of the electronic radii indicate smaller values compared to the lateral radius of the rings identified using AFM [131]. These results are in good agreement with cross-sectional scanning-tunnelling microscopy (X-STEM) data which showed that rings

fully covered with a GaAs layer are smaller but higher compared to the surface rings [120] as theoretical predicted.

The above findings were confirmed theoretically [129] indicating that in order to reproduce the experimental data, theoretically a ring with smaller radius but larger height $\approx 5\,\mathrm{nm}$ is required. Such a model allowed for the reproduction of a dipole moment in the ring structure, which has been found to be opposite in sign to that of the quantum dot [132].

Recent experimental developments in the fabrication of quantum rings, (Fig. 1.21) [122, 133] containing only few electrons have made them an ever increasing topic of experimental and theoretical studies [134]. A QR nanostructure forms an

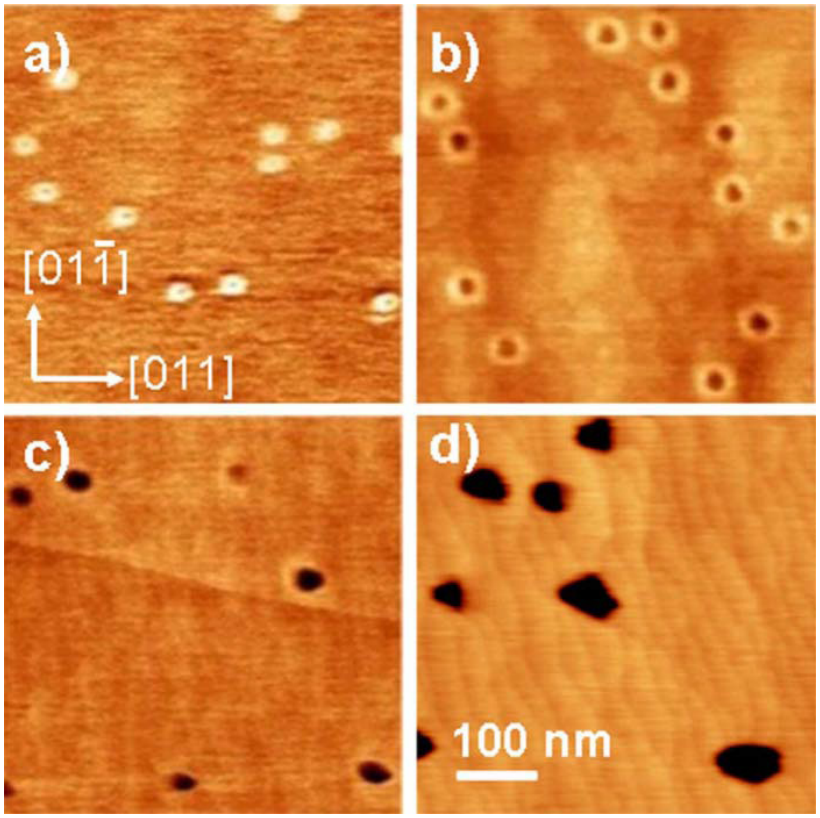

Figure 1.21: AFM images of InAs/GaAs QDs capped with 2 *nm* GaAs followed by (a) 0, (b) 30, (c) 120, and (d) 360 s annealing Ref.[122].

interesting system in which the ground and excited states can be investigated in a few-electron limit. The single electron properties of these systems have been extensively studied from both a theoretical and experimental point of view.

1.6.2 Vertically stacked quantum rings

As has already been mentioned, nontrivial geometry and the possibility of adjusting energy levels, oscillatory strength, polarisability and magnetic properties of QR makes them ideal candidates for the development of new devices [135]. The quantum efficiency and reduction of saturation gain effects in a laser devices can be improved even further by vertically stacking layers of QR's [136]. The process of self-assembly of stacked quantum rings is very similar to that of stacking quantum dots, however much lower density of ring ensembles is needed to overcame the rings overlapping situations [135].

A MBE is used to induce QR self-formation on GaAs (001) semi-insulating substrate. Formation of the quantum structures, growth rate and thermal conditions in the MBE chamber are monitored using reflection high energy electron diffraction. The layers of QRs are manufactured from the layers of QD ensemble using a minimum amount of InAs quantity required for the onset of the 3D transition [135]. Interestingly, due to the strong In segregation and strain propagation in the layers of stacked structures apart of the first spacer ≈ 1.65 Mono Layers (ML), the thickness of the capping layers for the second and following layers decreases to ≈ 1.35 ML [135]. Vertical stacking and quality of its alignment in the growth direction depends strongly on the presence of well defined and separated QRs in the proceeding layer. If ring structures overlap in a first layer the vertical order of rings in the following layers is tilted and sometimes even completely lost. The size of a quantum ring structure increases with the number of layers, however QRs never appear in the second or third layer if there is no QR below on the layer underneath.

"Artificial molecules" formed by vertically coupled quantum rings offer additional degrees of freedom to study new regimes of molecular physics. The use of different compounds, such as GaSb/GaAs may additionally increase the recombination lifetime and significantly enhance luminescence in coupled quantum rings which makes them ideal candidates for luminescence and carrier storage applications [137]. In these systems, coupling between the rings is driven by both Coulomb interaction and inter-ring tunnelling. The latter property can be precisely tuned with high precision during the semiconductor self-assembly process. Proper treatment of exchange-correlation effects in many particle systems is crucial to understand the physics of vertically stacked quantum rings.

As has already been mentioned vertically stacked quantum dot and ring systems open new horizons for the development and fabrication of modern, ultra-fast optoelectronic devices. However ultra-fast devices need ultra-fast signal processing. This leads to the basic concept that even the simplest electronic circuit needs a switch. Switches are one of the most important elements of any electronic device due to their ability to stop, start or redirect the stream of charge, photons or bits. Modern devices, such as multi core computer processors, are capable of performing more than one trillion operations per second [138] and demand small, heat efficient and ultra-fast switches capable of signal processing with the speed of photons. Switching the state of the system using the interaction of matter with a single photon or an external field opens new possible applications in measurements [139] and quantum computing [19].

Excitonic switches are particularly suitable for optoelectronic devices because of their high operating and switching speeds. Switches based on an electron-hole pair system were successfully realised in coupled quantum wells and implemented into such devices as an exciton optoelectronic transistor, excitonic bridge or pinch-off modulator [140]. The main idea of the excitonic switch is direct coupling of photons, which are used in communication to the excitons which act as a operational medium in semiconductor. To do this a photon at the source excites an electron creating an exciton, this composite particle travels in the semiconductor driven by a guide which control the excitons flux then the same photon is released at the drain. This can be done by the introduction of electrodes, resulting in a potential energy gradient that can be controlled by the voltage applied to the electrodes [141]. In this thesis an alternative method of excitonic flux control is described. This approach uses difference between confining potential on two perpendicular crystal directions, which naturally occurred in semiconductors nanostructures. This non-lithographic advantage of self-assembled quantum dot and ring structures over the quantum wells allows for precise exciton probability density distribution control using external electric field oriented along the growth direction.

Similar types of excitonic switch can be realised and controlled using optical coupling in a multiple quantum dot system, which opens new possibilities for optically controlled quantum-dot spins for multi-qubit systems [142]. Stacked quantum dot systems have already been successfully used in lasers [143, 144], high-speed modulators, infrared photodetectors [145] and quantum memory cells [146]. Self-assembled vertically coupled dots are excellent candidates for application in optically controlled

electronic devices, as their complex piezoelectric field, which interacts with the confinement potential and external electric fields [147], allows control of the heavy-hole exciton charge distribution [148]. Introduction of periodic elastic stretching in the vertical direction additionally permits access to light-hole states, which opens the way to dynamic switching not only in the plane of the system but also between heavy hole and light hole excitons [149]. A further advantage is the small dimensions of the device which allows for very dense packing of the detecting or emitting structures in the quantum circuit. At this point we approach the regime where electronic properties of few-particle states govern the device operations from the interaction of confining potentials, strain, Coulomb forces and external fields [150]. Such low-dimension electronic systems are characterised by a modified density of states which enables the development of novel devices characterised by enhanced performance, e.g. quantum dot lasers [151, 152] or light emitters in q-bits for quantum computation devices [153].

The straight forward way to activate an excitonic switch is by creating a photon which activates the switch exciting the electron and creating the exciton. One of the most important advantages of a photon activated switch is its high operational speed. Optically inactive electrons used in typical signal propagation slow the interconnection process at the interface between the optical and electronic parts. This doesn't occur in the case of our excitonic switch, as the signal can be processed simultaneously with optical communication, and can therefore offer the possibility of virtually delay-free signal processing for optical communication.

Other benefits of the excitonic switches are their scalability, high controllability and compactness. The exciton's thermal de Broglie wavelength, which is $\propto 1/\sqrt{T}$, defines the diffraction limit for the dimension of the excitonic switch. Its value is much less than the typical diffraction limit of bulky photonic device, still measured in micrometers. This is a huge advantage given that the thermal de Broglie wavelength at 70 K is $\approx$2 nm, which is considerably less than size of the quantum structure.

In order to describe the quantum effects observed in the above structures the proper quantum mechanical formalism is essential. Additional problems arise from the fact that the quantum structure demonstrate low symmetry, and also one must account for many-body interactions. All of these requirements make the numerical simulations very time and resource-consuming, therefore in many cases simpler models are considered. These simplifications allow for the study of only the most important properties, and some fine properties can simply go unnoticed.

Excitonic switching was first reported by McDonald *et al.* [154] in a single quantum ring structure.

The main objective of this work was to explore the lateral switching of charge probability distribution in single and vertically stacked quantum dots. Simultaneously we aimed to provide the quantitative description of the properties of excitonic complexes in vertically stacked, coupled quantum ring structures with and without an electric field, including the exciton recombination rates. Simulations based on the Open Source, Path Integral Quantum Monte Carlo (PI-QMC) program developed by the Shumway Research Group [155, 156] and two-band effective mass model Hamiltonian derived from a strained, atomistic model of nanostructures calculated using another Open Source program, Qdot-tools [157] gave us the unique opportunity to study Coulomb interacting many particle systems without any approximations. This treatment allowed us to observe novel physical properties, namely excitonic switching of charge distribution, which not been reported so far in the literature.

This thesis is organised in the following manner. The second Chapter is dedicated to the derivation of the Path Integral formalism.

In Chapter 3 the accuracy of the results from the PI-QMC is tested against an analytical, non-perturbative method and compared to the results obtained using alternative simulation techniques such is WKB.

In Chapter 4 the properties of the atomistic model of the quantum structure calculated using a Qdot-tool program are presented. We discuss the impact of strain on the two-band effective mass model Hamiltonian with particular emphasis on heavy hole, light hole and split-off energy. The piezoelectric potential calculated from strain fields is also introduced and its effect on the energy band profile is discussed.

Chapter 5 is dedicated to to explanation of lateral switching behaviour in vertically stacked quantum dots. This phenomenon, initially observed in the single quantum ring structure and accounts for its unique electronic structure [154], is also present in the dot. However it depends strongly on the piezoelectric properties of the structure and can only be observed in multiple quantum dots.

In Chapter 6 the fabrication and properties of vertically stacked quantum rings are introduced. The electronic structure and unique (for the coupled ring system) piezoelectric field distribution is explored together with its impact on the ground state charge probability distribution.

Strain distribution in vertically stacked quantum rings and its impact on the inter-ring tunnelling and recombination rates is further explored in Chapter 7. The effect of the external electric field on the lateral switching of the exciton in the stacked ring is also analysed.

We conclude this thesis in Chapter 8, where the main points of this work are summarised.

Chapter 2

Fundamentals of Path Integral Monte Carlo

2.1 Theory of the PI-QMC approach

In 1959 Richard Feynman amazed the audience at the annual meeting of the American Physical Society when presenting his vision of extreme miniaturisation. He tried to convince the listeners that by using a pen with an atomic size tip it is completely possible to rewrite the whole Encyclopaedia Britannica in an area comparable with a pin head. This was a wonderful dream at that time, closer to science fiction than real life experience. Today we live in that dream. Single atoms can now be manipulated and persuaded to self-assemble into many shapes and structures. Scaling down towards systems of atomic sizes requires physical descriptions which become more and more demanding and sophisticated, going beyond classical theories. In the following chapters it will be demonstrated that Feynman's extraordinary idea, beautiful in its simplicity, scales perfectly well with any system size.

In this chapter the detailed derivation of the Feynman Path Integral formalism necessary for the path integral Monte Carlo (PI-QMC) simulations is presented. This is a collection of the main aspects of the path integral method sourced from many books and on-line publications offering different points of view on essentially the same subject. The basic ideas of Monte Carlo integration and Metropolis algorithm implementation are also outlined. The application of the computation method to the

many-particle discretised path integral permits exact calculations of expectation values for the system of interacting particles. However, some serious limitations to the method must be noted. The most important one, known as the fermion sign problem, is related to simulations for indistinguishable particles e.g. electrons. The sign problem manifests itself as a signal to noise ratio, which vanishes exponentially with inverse temperature and increasing number of particles. It will be demonstrated later that this property results from quantum effects for systems of identical, interacting particles.

Once the technique is introduced a few simple cases will be presented and discussed to highlight the accuracy and consistency of the PI-QMC method with well known, analytically solvable methods.

2.2 Feynman path integral

Before Feynman's dissertation the world of physics could refer to two slightly different formulations of quantum theory. The first case, derived in late 1925, was published in 1926 by Erwin Schrödinger and uses a partial differential equation to describe how the quantum state of some physical system changes with time. The central concepts used in this theorem are the time independent wave function of the system, known as the quantum state or state vector and wave equation governing time evolution of the system. In the second case a matrix representation picture was introduced in 1925 by Werner Heisenberg, whereby the observables are time dependent but, in contrast to Schrödinger's model, the state vectors are constant. In the formulation of quantum mechanics introduced by R. Feynman in 1948 the path integral departs from the principle of least action. It arrives to the same conclusion as Schrödinger but by a different route. In the following sections the single particle derivation of the picture is presented, which can then be extended to more particles.

2.2.1 Classical action

Firstly consider a particle moving in space. The particle moves from point $A(x_a, t_a)$ to point $B(x_b, t_b)$. If one introduces the classical action $\mathcal{S}$ defined as the integral of

the Lagrangian $\mathscr{L}$ of the system

$$\mathcal{S}[x] = \int_{t_a}^{t_b} dt \mathscr{L}(x, \dot{x}), \tag{2.1}$$

where the action is local function of $x(t)$, then the path followed by the particle $x_{cl}(t)$, out of all possible paths, is the one which minimises the classical action $\mathcal{S}$. For an arbitrary confining potential $V(x,t)$ and particle of mass M, the Lagrangian yields,

$$\mathscr{L}(x, \dot{x}; t) = \frac{1}{2} M \dot{x}^2 - V(x,t). \tag{2.2}$$

Using the Calculus of Variations, one can show that the path which minimizes Eq.(2.1) is equivalent to Newton's second law.

2.2.2 Feynman's path integral theory

In quantum mechanics all possible paths contribute to the total amplitude, however they enter it weighted with different phases, defined by the action. In the classical approach only the path which minimises energy contributes.

In the mathematical form one can state that the probability of a particle departing from point x_a at some time t_a and arriving at point x_b at some later time t_b is $P(b,a) = |K(b,a)|^2$, with the amplitude, also called the kernel, K, is given by,

$$K(b,a) = \sum_{all\ paths} \phi[x(t)] \tag{2.3}$$

and is defined in terms of the different contributions $\phi[x(t)]$ from the constituent paths, defined as

$$\phi[x(t)] = A \exp\left\{ \frac{i}{\hbar} \mathcal{S}[x(t)] \right\}. \tag{2.4}$$

In Eq.(2.4), A is a normalisation constant and the action $\mathcal{S}$ corresponds to the classical system. As was mentioned at the beginning of this chapter, Feynman's formulation was not a completely new description of quantum mechanics. One could say that it is rather a fresh look with some things borrowed from Heisenberg and connected to Schrödinger's picture. Eq.(2.3) can be represented in the Heisenberg operator notation by

$$K(b,a) = \langle x_b, t_b | x_a, t_a \rangle . \tag{2.5}$$

The composition property of the operator Eq.(2.5) allows one to split the total displacement of the particle into arbitrary, smaller pieces such that each piece has width τ. Then one can write out, Eq.(2.5), as

$$\langle x_b, t_b | x_a, t_a \rangle \approx \int_{-\infty}^{+\infty} dx_N \, \langle x_b, t_b | x_N, t_N \rangle \, \langle t_N, t_N | x_a, t_a \rangle \,, \tag{2.6}$$

where $t_N \in (t_a, t_b)$. Introduction of the small time step $\tau = t_{j+1} - t_j$ allows one to expand the propagator in the form

$$\begin{aligned} \langle x_b, t_b | x_a, t_a \rangle = \int dx_{N-1} \int dx_{N-2} \ldots \int dx_2 \, \langle x_b, t_b | x_{N-1}, t_{N-1} \rangle \\ \times \langle x_{N-1}, t_{N-1} | x_{N-2}, t_{N-2} \rangle \ldots \langle x_2, t_2 | x_a, t_a \rangle \,. \end{aligned} \tag{2.7}$$

The above equation leads to the observation that if one examine just one of the kernels in this integrand, for instance one starting at the slice i^{th} and ending at the slice $(i+1)^{th}$, separated by the very small interval τ, it will yield the following form (to first order in τ),

$$K(i+1, i) = \frac{1}{A} \exp \left\{ \frac{i}{\hbar} \tau \mathcal{L} \left(\frac{x_{i+1} - x_i}{\tau}, \frac{x_{i+1} + x_i}{2} \frac{t_{i+1} + t_i}{2} \right) \right\}. \tag{2.8}$$

This idea is depicted in Fig. 2.1, where a few possible paths which a particle can follow are drawn together with the most probable classical one (red). One can notice that increasing the number of time slices (reducing τ) makes our calculations more accurate, however significantly complicates the integration procedure. In order to deal with this complication, efficient and accurate approximation is required to propagate the particle in time. Feynman developed that method [158] defining the propagator

$$\langle x_b, t_b | x_a, t_a \rangle \equiv \int_{x(t_b)=x_b}^{x(t_a)=x_a} \exp \left\{ \frac{i}{\hbar} \mathcal{S}[x(t)] \right\} \mathscr{D}x(t), \tag{2.9}$$

where $\mathscr{D}x(t)$ is an operator given by the product of $(N-1)$ differentials (sum over all possible paths from x_a to x_b) and $\mathcal{S}$ is defined in Section (2.2.1). One may argue that the above derivation is not exactly a rigorous formulation of Feynman's idea, and also defining an integral over all possible paths is rather awkward. However it is the intention of this chapter to present an intuitive description of Feynman's picture and its statistical foundations rather than employ previous mathematical analyses.

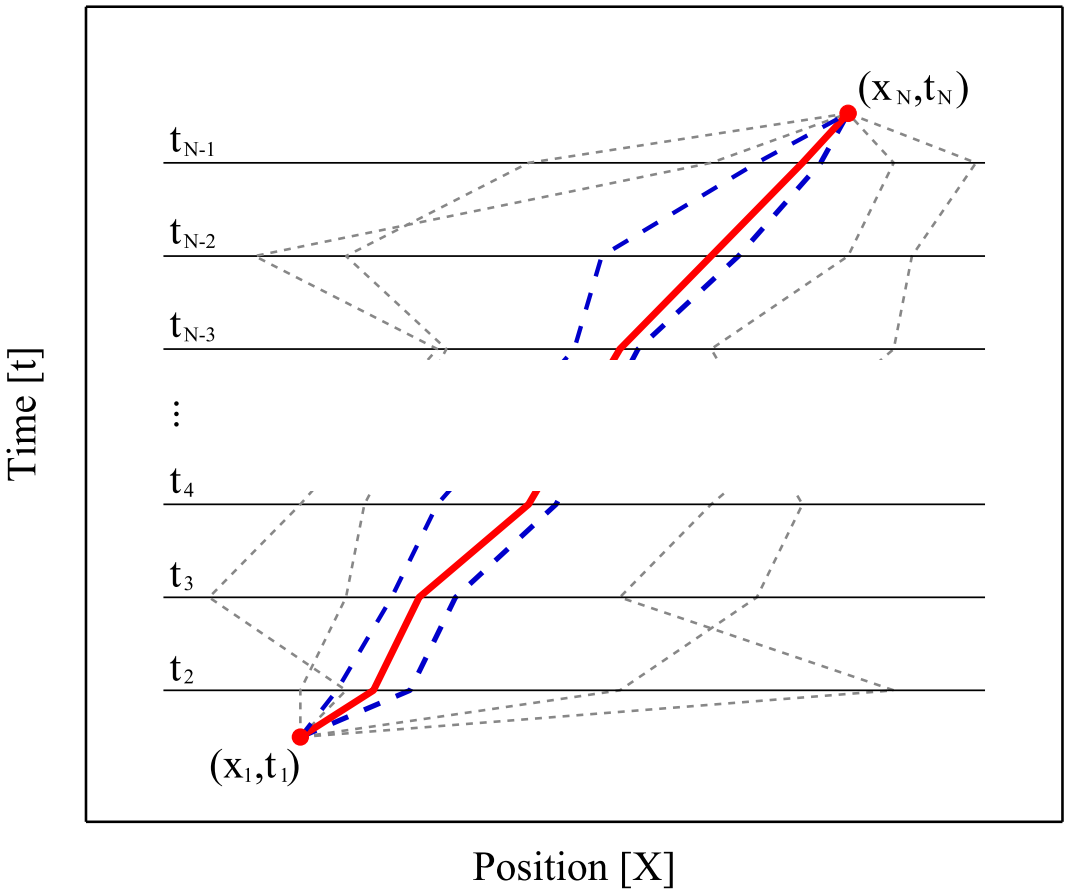

Figure 2.1: Possible paths of a particle in a system. The red line pictures classical trajectory of the particle. All the paths drawn in the picture contribute to the quantum mechanical picture, however the blue paths (dashed) are close to the classical one and have a greater weighting (dotted).

2.2.3 Propagator

In this section the mathematical derivation of the propagator in terms of path integrals is presented. We start by defining the propagator in the form of the Heisenberg operator

$$\langle x_b, t_b | x_a, t_a \rangle = \left\langle x_b \left| \exp\left\{ -\frac{i}{\hbar} \hat{\mathscr{H}}(t_b - t_a) \right\} \right| x_a \right\rangle . \tag{2.10}$$

The time step introduced in Eq.(2.10) can be split into two smaller intervals using the closure relation and identity operator

$$\begin{aligned}\langle x_b, t_b | x_a, t_a \rangle &= \left\langle x_b \left| \exp\left\{ -\frac{i}{\hbar} \hat{\mathscr{H}}(t_b - t_i) \right\} \exp\left\{ -\frac{i}{\hbar} \hat{\mathscr{H}}(t_i - t_a) \right\} \right| x_a \right\rangle \\ = \left\langle x_b \left| \exp\left\{ -\frac{i}{\hbar} \hat{\mathscr{H}}(t_b - t_i) \right\} \right| \int dx_i \left| x_i \times \right\rangle \left\langle x_i \left| \exp\left\{ -\frac{i}{\hbar} \hat{\mathscr{H}}(t_i - t_a) \right\} \right| x_a \right\rangle & \quad (2.11) \\ = \int dx_i K(x_b, t_b; x_i, t_i) K(x_i, t_i; x_a, t_a).\end{aligned}$$

If the time interval is divided even more times, say $M-1$, and we introduce the discrete time period $\tau = (t_b - t_i)/M$, then the propagator in Eq.(2.11) gives

$$\begin{aligned}\langle x_b, t_b | x_a, t_a \rangle &= \left\langle x_b \left| \exp\left\{ -\frac{i}{\hbar} \hat{\mathscr{H}} \tau \right\}^M \right| x_a \right\rangle \\ = \int \cdots \int dx_i \cdots dx_{M-1} K(x_b, t_b; x_{M-1}, t_{M-1}) \cdots K(x_i, t_i; x_a, t_a) & \quad (2.12) \\ = \int \mathscr{D}x(t) \prod_{k=1}^{M-1} K(x_{k-1} \to x_k).\end{aligned}$$

In the above derivation an idea of path integrals becomes apparent, as by introducing larger values of M we split the time-space into even more slices and therefore introduce more possible paths. Now we will connect the above formalism with the actions. Paths of the particle are rather complicated in time and space, however if we take a very short time interval, say close to the position at which the particle is $x_{k+1} = x_k + \gamma$, then the paths can be approximated by a straight line and we can use the Taylor expansion. If the number of time slices goes to infinity, then our local approximation converges to the exact result:

$$\begin{aligned}K(x_{k+1}, t_k + \gamma; x_k, t_k) &= \left\langle x_{k+1} \left| \exp\left\{ -\frac{i}{\hbar} \hat{\mathscr{H}} \cdot \gamma \right\} \right| x_k \right\rangle \\ &= \left\langle x_{k+1} \left| 1 - \frac{i}{\hbar} \hat{\mathscr{H}} \cdot \gamma + \mathscr{O}(\gamma^2) \right| x_k \right\rangle \quad (2.13) \\ &= \langle x_{k+1} | x_k \rangle - \frac{i\gamma}{\hbar} \left\langle x_{k+1} \left| \hat{\mathscr{H}} \right| x_k \right\rangle + \mathscr{O}(\gamma^2).\end{aligned}$$

The third row of Eq.(2.13) can be expanded term by term. First bra-ket yields:

$$\langle x_{k+1} | x_k \rangle = \delta(x_{k+1} - x_k) = \int \frac{dp_k}{2\pi} \exp\left\{ \frac{i}{\hbar} p_k (x_{k+1} - x_k) \right\}. \quad (2.14)$$

In the second term, substitution of an explicit form of the Hamiltonian:

$$\hat{\mathscr{H}} = \frac{\hat{p}^2}{2m} + V(\hat{x}), \tag{2.15}$$

followed by the application of the completeness relation for momentum eigenstates, together with the use of transformation from the momentum to the position representation gives:

$$\begin{aligned}\left\langle x_{k+1} \left| \hat{\mathscr{H}} \right| x_k \right\rangle &= \left\langle x_{k+1} \left| \left(\frac{\hat{p}^2}{2m} + V(\hat{x}) \right) \int \frac{dp_k}{2\pi} \right| p_k \right\rangle \langle p_k | x_k \rangle \\ &= \int \frac{dp_k}{2\pi} \left(\frac{p_k^2}{2m} + V(x_{k+1}) \right) \langle x_{k+1} | p_k \rangle \langle p_k | x_k \rangle \\ &= \int \frac{dp_k}{2\pi} \left(\frac{p_k^2}{2m} + V(x_{k+1}) \right) \exp\left\{ \frac{i}{\hbar} p_k (x_{k+1} - x_i) \right\}.\end{aligned} \tag{2.16}$$

Notice that calculation of a potential only at position x_k results in a break of the symmetry of the problem, however this inconvenience can be corrected by the introduction of an average position $\bar{x} = (x_{k+1} + x_k)/2$. Neglecting the third term in the Taylor expansion of Eq.(2.13) and substituting into it Eqs.(2.14) and (2.16), one finds the propagator for a single time interval, Eq.(2.17)

$$\begin{aligned}K(x_{k+1}, t_{k+1}; x_k, t_k) &= \int \frac{dp_k}{2\pi} \exp\left\{ \frac{i}{\hbar} p_k (x_{k+1} - x_k) \right\} - \frac{i}{\hbar}\tau \int \frac{dp_k}{2\pi} \left(\frac{p_k^2}{2m} + V(\bar{x}) \right) \\ \times \exp\left\{ \frac{i}{\hbar} p_k (x_{k+1} - x_i) \right\} &= \int \frac{dp_k}{2\pi} \exp\left\{ \frac{i}{\hbar} p_k (x_{k+1} - x_k) \right\} \left(1 - \frac{i}{\hbar}\tau \left(\frac{p_k^2}{2m} + V(\bar{x}) \right) \right) \\ &= \int \frac{dp_k}{2\pi} \exp\left\{ \frac{i}{\hbar} p_k (x_{k+1} - x_k) \right\} \exp\left\{ -\frac{i}{\hbar}\tau \hat{\mathscr{H}}(p_k, \bar{x}) \right\}.\end{aligned} \tag{2.17}$$

If one considers M single time interval propagators and substitutes them to Eq.(2.12), this yields Eq.(2.18)

$$\begin{aligned}K(x_b, t_b; x_a, t_a) &= \int \prod_{k=1}^{M-1} dx_k \int \prod_{k=0}^{M-1} \frac{dp_k}{2\pi} \exp\left\{ \frac{i}{\hbar}\tau \sum_{k=0}^{M-1} \left[p_k \left(\frac{x_{k+1} - x_k}{\tau} \right) - \hat{\mathscr{H}}(p_k, \bar{x}) \right] \right\} \\ &= \int \prod_{k=1}^{M-1} dx_k \int \prod_{k=0}^{M-1} \frac{dp_k}{2\pi} \exp\left\{ \frac{i}{\hbar}\tau \sum_{k=0}^{M-1} \left[p_k \dot{x} - \hat{\mathscr{H}}(p_k, \bar{x}) \right] \right\}.\end{aligned} \tag{2.18}$$

Consider the Hamiltonian in the form given in Eq.(2.15), then the integral takes the form

$$\begin{aligned} K(x_N, t_N; x_1, t_1) &= \int \prod_{k=1}^{M-1} dx_k \exp\left\{-\frac{i}{\hbar}\tau \sum_{k=0}^{M-1} V(\bar{x})\right\} \\ &\times \int \prod_{k=0}^{M-1} \frac{dp_k}{2\pi} \exp\left\{-\frac{i}{\hbar}\tau \sum_{k=0}^{M-1} \left(p_k \dot{x} - \frac{p_k^2}{2m}\right)\right\} \\ &= \left(\frac{m}{2\pi i\hbar\tau}\right)^{\frac{M}{2}} \int \prod_{k=1}^{M-1} dx_k \exp\left\{\frac{i}{\hbar}\tau \sum_{k=0}^{N-1} \left(\frac{p_k^2}{2m} - V(\bar{x})\right)\right\}. \end{aligned} \tag{2.19}$$

The terms in the final exponent can be identified as the Lagrangian. If the number of slices, M, is large then the sum can be approximated by the integral. In Section (2.2.1), Eq.(2.1) the relation between the Lagrangian and action was defined, therefore we have

$$\begin{aligned} K(x_N, t_N; x_1, t_1) &= \left(\frac{m}{2\pi i\hbar\tau}\right)^{\frac{M}{2}} \int \prod_{k=1}^{M-1} dx_k \exp\left\{\frac{i}{\hbar}\int_{t_1}^{t_N} \left(\frac{p_k^2}{2m} - V(\bar{x})\right) dt\right\} \\ &= \left(\frac{m}{2\pi i\hbar\tau}\right)^{\frac{M}{2}} \int \mathscr{D}x(t) \exp\left\{\frac{i}{\hbar}\mathcal{S}[x(t)]\right\}, \end{aligned} \tag{2.20}$$

where $\int \mathscr{D}x(t)$ denotes the integration over all possible paths.

As previously stressed in Section (2.2.2) each path contributes to the probability amplitude, however with a differing phase resulting from the classical action S. The classical action dominates the paths, but even paths with much less probability contribute to the overall picture. It can be proved that in the classical limit, the classical action is restored for the classical path. In the classical regime the action is large compared to $\hbar$. This results in rapid oscillations of the phase, which yields significant cancellation of paths. As a result, only the classical path remains.

2.2.4 From the path integral to the Schrödinger equation

Having derived the Feynman propagator, the earlier statement regarding the relationship between the Path Integral and the Schrödinger equation shall now be proved. If both of these pictures are parallel to each other when starting from the path integral formulation, one can retrieve the wave equation governing time evolution of the system in the Schrödinger picture. Firstly the wave function ψ at time t_N is defined in

terms of the Feynman propagator

$$\psi(x_b, t_b) = \int_{-\infty}^{+\infty} K(b, c)\psi(x_a, t_a)dx_a, \tag{2.21}$$

In order to calculate the wave function at time t_b, one can use the knowledge of the state in time t_a. By adding the small value τ to t and using Eq.(2.8) the wave function in some later time can be found:

$$\psi(x_i, t+\tau) = \frac{1}{A}\int_{-\infty}^{+\infty} \exp\left\{\tau\frac{i}{\hbar}\mathcal{L}\left(\frac{x_i - x_{i-1}}{\tau}, x_i\right)\right\}\psi(x_{i-1}, t)dx_{i-1}, \tag{2.22}$$

where the value of normalisation constant A will follow, and the Lagrangian is defined as in Eq.(2.2). The important modification is the introduction of a discrete change in position with time increment τ instead of $\dot{x}$. Substitution of Eq.(2.2) into Eq.(2.22) yields

$$\psi(x_i, t+\tau) = \frac{1}{A}\int_{-\infty}^{+\infty} \exp\left\{\frac{i}{\hbar}\frac{m(x_i - x_{i-1})^2}{\tau}\right\}\exp\left\{-\frac{i}{\hbar}\tau V(x_i, t)\right\}\psi(x_{i-1}, t)dx_{i-1}. \tag{2.23}$$

If the change in position of the particle is small, then the difference $x_i - x_{i-1}$ can be considered as a small displacement η from position x_i. For the infinitesimally small oscillation around x_i, Eq.(2.23) gives

$$\psi(x_i, t+\tau) = \frac{1}{A}\int_{-\infty}^{+\infty} \exp\left\{\frac{im\eta^2}{2\hbar\tau}\right\}\exp\left\{-\frac{i\tau}{\hbar}V(x_i, t)\right\}\psi(x_i + \eta, t)d\eta. \tag{2.24}$$

Power series expansion of Eq.(2.24) to the first order in τ, yields

$$\begin{aligned}\psi(x_i, t+\tau) + \tau\frac{\partial}{\partial t}\psi(x_i, t+\tau) = \frac{1}{A}\int_{-\infty}^{+\infty} \exp\left\{\frac{im\eta^2}{2\hbar\tau}\right\}\left[1 - \frac{i\tau}{\hbar}V(x_i, t)\right] \\ \times\left[\psi(x_i, t+\tau) + \eta\partial_{x_i}\psi(x_i, t+\tau) + \frac{1}{2}\eta^2\partial_{x_i}^2\psi(x_i, t+\tau)\right]d\eta.\end{aligned} \tag{2.25}$$

Now comparing the components of both sides of Eq.(2.25) which contain the same orders of τ results in

$$1 = \frac{1}{A}\int_{-\infty}^{+\infty} \exp\left\{\frac{im\eta^2}{2\hbar\tau}\right\}d\eta. \tag{2.26}$$

Relation (2.26), which is of zeroth order, allows us to calculate the normalisation constant, A, to be

$$A = \sqrt{\frac{2\pi i\hbar\tau}{m}}, \tag{2.27}$$

whereas the first order can be found by equating terms containing τ

$$\psi + \tau\partial_t\psi = \psi - \frac{i\tau}{\hbar}V(x,t)\psi - \frac{\hbar\tau}{2im}\partial_x^2\psi. \tag{2.28}$$

Simple algebra yields Schrödinger equation

$$i\hbar\partial_t\psi = V(x,t)\psi - \frac{\hbar^2}{2m}\partial_x^2\psi = \mathscr{H}\psi. \tag{2.29}$$

2.2.5 Free particle - exact solution

One of the most useful properties of PI-QMC is that by using the products of high temperature density matrices one can compute the low temperature properties of the system. Outlined at the beginning of this chapter, Feynman's path integrals apply to the quantum system at zero temperature. However, that is more than sufficient to demonstrate how the product of classical actions leads to the quantum outcome. We start the solution of this fully analytical problem by deriving the propagator for a free particle in the frame of path integrals. A free particle departing from $(x_a, 0)$ and travelling to point (x_b, t) follows the classical path $x(t) = x_a + t(x_b - x_a)/\tau$. The corresponding classical action for that path is given as

$$\mathcal{S} = \int_0^\tau \frac{m}{2}\left(\frac{t(x_b - x_a)}{\tau}\right)^2 dt. \tag{2.30}$$

The Feynman propagator we want to calculate for the above particle is defined as

$$\begin{aligned} K(x_b,\tau;x_a,0) &= \int_{x_a}^{x_b} dx \exp\left\{\frac{im}{2\hbar}\int_0^\tau dt\dot{x}^2\right\} = \\ &= \lim_{M\to\infty}\left(\frac{m}{2\pi i\hbar\tau}\right)^{\frac{M+1}{2}}\int \mathscr{D}x \exp\left\{\frac{im}{2\hbar\tau}\sum_{j=0}^{M}(x_{j+1}-x_j)^2\right\}, \end{aligned} \tag{2.31}$$

where τ is the discretized time slice $t/(M+1)$, $\mathscr{D}x$ stands for integration over all possible paths and $x_{b+1} = x_0$. Eq.(2.31) is a form of Fresnel integral and yields

$$K(x_b,\tau;x_a,0) = \left(\frac{m}{2\pi i\hbar\tau}\right)^{1/2}\exp\left\{\frac{im(x_b-x_0)^2}{2\hbar\tau}\right\}. \tag{2.32}$$

Eq.(2.32) connects classical action appearing in the phase with the quantum world, which enters through $\frac{i}{\hbar}$. The above solution demonstrates how the quantum propagator emerges from the product of classical actions. For the free particle this result

is exact. However, for non-zero potentials the picture is not so simple. In order to calculate the action the sum of the kinetic and potential energy is integrated. If we deal with the Hamiltonian which has kinetic energy in terms of the form $\frac{\hat{p}^2}{2m}$ the resulting part of action is always the same. It will be demonstrated in Section (2.3) that some sampling techniques use this property extensively, analytically computing the kinetic term and focusing predominantly on Monte Carlo sampling of a potential. It is not a trivial task to sample even a stationary potential $V(x)$ with no explicit time dependency as $x(t)$ is a function of time. The situation is even more challenging when it comes to solving $\int V(x,t)dt$. The intuitive method of tackling such a problem is an approximation, which neglects the time dependency

$$\int_0^\tau V(x,t)dt \approx \tau V(x). \tag{2.33}$$

2.3 Thermal density matrix

In the following section the connection between path integrals and statistical mechanics will be developed. It will be shown that the path integral formalism allows for almost direct application to the computational methods [158]. Applicability of path integrals in the frame of statistical mechanics was successfully proven by Feynman in his analysis of the atomic λ-transition and liquid ^4He [159–161].

We will start with an introduction of the idea of the thermal density matrix and its formulation in statistical mechanics. Then connection between the finite temperature thermal density matrix and imaginary-time path integrals will be outlined.

2.3.1 Properties of the thermal density matrix

The thermal density matrix contains all static properties of a quantum system in thermal equilibrium. The following subsection is devoted to discussing the thermal density matrix formulation in quantum mechanics. We start with defining the density matrix in a canonical ensemble in which any state is defined by set of fixed parameters e.g. number of particles N, volume V, temperature T and dynamic quantities e.g. total energy E.

Any system in thermal equilibrium can be described by a thermal density matrix ρ of the form

$$\rho \equiv \sum_i \exp\{-\beta E_i\} \, |\psi_i\rangle\langle\psi_i|, \tag{2.34}$$

where $\exp\{-\beta E_i\}$ is a weight related to the complete set of energy eigenvectors $|\psi_i\rangle$ with the eigenvalue E_i. Quantity $\beta = 1/k_B T$ is defined in a terms of temperature T and Boltzmann's constant k_B. Knowing that the eigenvalue of the Hamiltonian acting on eigenstate $\hat{\mathscr{H}}|\psi_i\rangle = E_i|\psi_i\rangle$ yields an eigenenergy value, we can rewrite Eq.(2.34) as

$$\rho = \sum_i \exp\left\{-\beta\hat{\mathscr{H}}\right\} |\psi_i\rangle \, \langle\psi_i| = \exp\left\{-\beta\hat{\mathscr{H}}\right\}, \tag{2.35}$$

or in position-space representation

$$\rho(x, x'; \beta) \equiv \left\langle x \left| \exp\left\{-\beta\hat{\mathscr{H}}\right\} \right| x' \right\rangle \equiv \sum_i \exp\{-\beta E_i\} \, \psi_i(x)\psi_i^*(x'), \tag{2.36}$$

where $\exp\{-E_i/kT\}$ is the occupation probability of a state i. One very useful property resulting from Eq. (2.36) is the symmetry of ρ

$$\rho(x, x'; \beta) = \rho^*(x', x, \beta). \tag{2.37}$$

The expression for kernel $K(b, a)$ in terms of an orthogonal basis set of eigenfunctions $\phi_i(x)$ and corresponding eigenenergies E_i is given by,

$$K(x_b, t_b; x_a, t_a) = \Theta(t_b - t_a) \sum_{i=1}^{\infty} \phi_i^*(x')\phi_i(x)^{-iE_i(t_b - t_a)/\hbar} \tag{2.38}$$

where $\Theta(t_b - t_a)$ is the Heaviside step function. Introduction of a new variable, the imaginary time $\tau \equiv it$ yields,

$$K(x_b, \tau_b; x_a, \tau_a) = \Theta(\tau_b - \tau_a) \sum_{i=1}^{\infty} \phi_i^*(x')\phi_i(x)^{-iE_i(\tau_b - \tau_a)/\hbar} \tag{2.39}$$

Assumption that we going forward in time $t_b > t_a$ allows one omit the Θ function. Additionally if we assume that the system is in equilibrium, that is, $\mathscr{H} = \mathscr{T} + \mathscr{V}$ the Hamiltonian is not changing with time and set τ_a to zero, then our kernel yields,

$$G(x_b, \tau_b; x_a, \tau_a) = \sum_i \phi_i^*(x')\phi_i(x)^{-iE_i(\tau_b)/\hbar}. \tag{2.40}$$

The change of notation $K \rightarrow G$ results from the fact that it can be shown G is a Green function for time dependent Schrödinger equation for the imaginary time. If we differentiate G with respect to τ, we obtain

$$\frac{\partial G(b,a)}{\partial \tau_b} = -\frac{1}{\hbar}\sum_i E_i \phi_i^*(x')\phi_i^*(x')^{-iE_i(\tau_b)/\hbar} = -\frac{1}{\hbar}\mathscr{H}_b G(b,a), \tag{2.41}$$

where we used the fact that, $\mathscr{H}\phi_i(x_b) = E_i\phi_i(x_b)$. The Hamiltonian in the above form operates only on functions which exists at time t_b. If one substitute $\tau_b = \hbar\beta$ in Eq.(2.40), then Eq.(2.41) takes on the form of the density matrix,

$$\frac{\partial \rho(b,a)}{\partial \beta} = -\mathscr{H}_b \rho(b,a), \tag{2.42}$$

if one divides both sides of Eq.(2.41) by $\hbar$. The above result is significant, as it allows us to express kernel of a system govern by simple Hamiltonian, which involves only position and momentum coordinates as a path integral. This can be done by building up a product of many kernels, sum over path for the imaginary time approaching zero.

Having defined the thermal density matrix, one can express the expectation value operator $\hat{\mathscr{O}}$ in terms of the density matrix. The expectation value of an operator yields,

$$\left\langle \hat{\mathscr{O}} \right\rangle = \mathscr{Z}^{-1} Tr\left[\rho\hat{\mathscr{O}}\right] = \mathscr{Z}^{-1} Tr\left[\exp\left\{-\beta\hat{\mathscr{H}}\hat{\mathscr{O}}\right\}\right]. \tag{2.43}$$

In the above $\mathscr{Z}$ is the partition function, which normalises density matrix ρ,

$$\mathscr{Z} = \sum_i \exp\left\{-\beta E_i\right\} = Tr\left[\exp\left\{-\beta\mathscr{H}\right\}\right], \tag{2.44}$$

and Tr is the trace of the matrix. In the position representation the expectation value takes the form,

$$\begin{aligned}\left\langle \hat{\mathscr{O}} \right\rangle &= \frac{1}{\mathscr{Z}}\int dx \left\langle x \left| \rho\hat{\mathscr{O}} \right| x \right\rangle \\ &= \frac{1}{\mathscr{Z}}\int dx dx' \rho\left(x,x';\beta\right)\left\langle x' \left| \hat{\mathscr{O}} \right| x \right\rangle \\ &= \frac{1}{\mathscr{Z}}\int dx dx' \rho\left(x,x';\beta\right)\mathscr{O}(x',x),\end{aligned} \tag{2.45}$$

with the partition function defined in the position representation as $\mathscr{Z} = \int dx \rho\left(x,x;\beta\right)$. In order to demonstrate the above properties, let's consider the expectation value of

the position operator, $\hat{x}$,

$$\mathscr{O}(x', x) = \langle x' | \hat{x} | x \rangle = x \langle x' | x \rangle = x\delta(x' - x) \tag{2.46}$$

Eq.(2.46) then yields:

$$\langle \hat{x} \rangle = \frac{1}{\mathscr{Z}} \int dx x \rho(x, x; \beta) . \tag{2.47}$$

It should be noted that according to Eq.(2.36), the diagonal part of the density matrix is always $\rho(x, x, \beta) \geqslant 0$, therefore $\mathscr{Z}^{-1}\rho(x, x; \beta)$ is a correct probability distribution.

We conclude this subsection about thermal density matrix by discussing probably one of the most useful path integrals in the Monte Carlo method, the product property of exponential the function.

If the the thermal density matrix is given for some temperature $T = \sum_i T_i$ $(i = 1, 2, ...)$, then the convolution of two or more density matrices at T_i is a density matrix at a lower temperature. To show that, we use the fact that $\beta = \beta_1 + \beta_2$ and start from Eq.(2.36),

$$\rho(x, x'; \beta) = \left\langle x \left| \exp\left\{ -\beta \hat{\mathscr{H}} \right\} \right| x' \right\rangle \tag{2.48}$$

then, using the product property

$$\exp\left\{ -(\beta_1 + \beta_2)\hat{\mathscr{H}} \right\} = \exp\left\{ -\beta_1 \hat{\mathscr{H}} \right\} \exp\left\{ -\beta_2 \hat{\mathscr{H}} \right\} \tag{2.49}$$

and substituting the definition of the density matrix, this leads to

$$\rho(x, x'; \beta) = \left\langle x \left| \exp\left\{ -\beta_1 \hat{\mathscr{H}} \right\} \exp\left\{ -\beta_2 \hat{\mathscr{H}} \right\} \right| x' \right\rangle . \tag{2.50}$$

Applying the identity operator $|x''\rangle\langle x''|$ to the right side of Eq.(2.50) results in

$$\rho(x, x'; \beta_1 + \beta_2) = \int dx'' \rho(x, x''; \beta_1) \rho(x'', x'; \beta_2) . \tag{2.51}$$

2.3.2 Path integral and the thermal density matrix

Introduced in section 2.3.1, Eq.(2.38) demonstrates an obvious similarity to the definition of the thermal density matrix introduced in Eq.(2.34)

$$K(x_b, t_b; x_a, t_a) = \sum_{i=1}^{\infty} \phi_i^*(x')\phi_i(x)^{-iE_i(t_b - t_a)/\hbar} \tag{2.52}$$

where $t_b > t_a$.

In order to obtain the equilibrium state in statistical mechanics the Hamiltonian of the system must be time independent. Comparison of thermal density matrix Eq.(2.34) and the kernel Eq.(2.52) reveals that they differ only by the argument of the exponent. Substituting β in place of $i(t_2 - t_1)/\hbar$ makes these equations structurally the same. The latter shows that the density matrix can be treated as a kernel with an imaginary time interval $i\beta\hbar$, if care about the sign is taken. Strictly speaking the interval $\beta\hbar$ is not a time, but as it soon will be shown, thinking about it in such a way can help our imagination significantly. We can imagine some particle, initially at some point x' at time $t = 0$, which then arrives to another point in space x after time $t = \hbar\beta$. In Section (2.3.1) the usefulness of the exponent product property was stressed. If this property is used M times, then the density matrix at a temperature T will be expressed in terms of the density matrix at temperature MT, $\exp\left\{-\beta\hat{\mathscr{H}}\right\} = \exp\left\{-\tau\hat{\mathscr{H}}\right\}^M$, with τ defined as β/M. The last expression can be seen as the *time step*. Using the position form:

$$\rho\left(x, x'; \beta\right) = \int dx_1 \cdots dx_{M-1} \rho\left(x, x_{M-1}; \tau\right) \rho\left(x_{M-1}, x_{M-2}; \tau\right) ... \rho\left(x_1, x'; \tau\right), \tag{2.53}$$

we end up with a convolution which can be seen as a *path* of the particle Fig. 2.2, divided on many intermediate slices x_n, which wanders between points x and x. We previously introduced the total probability amplitude $\rho\left(x, x'; \beta\right)$ for a particle travelling between two points as the sum of all possible paths connecting these points in Eq.(2.3). Introducing the *action* in terms of the density matrix:

$$\mathcal{S}(x, x'; \tau) \equiv -\log[\rho(x, x'; \tau)], \tag{2.54}$$

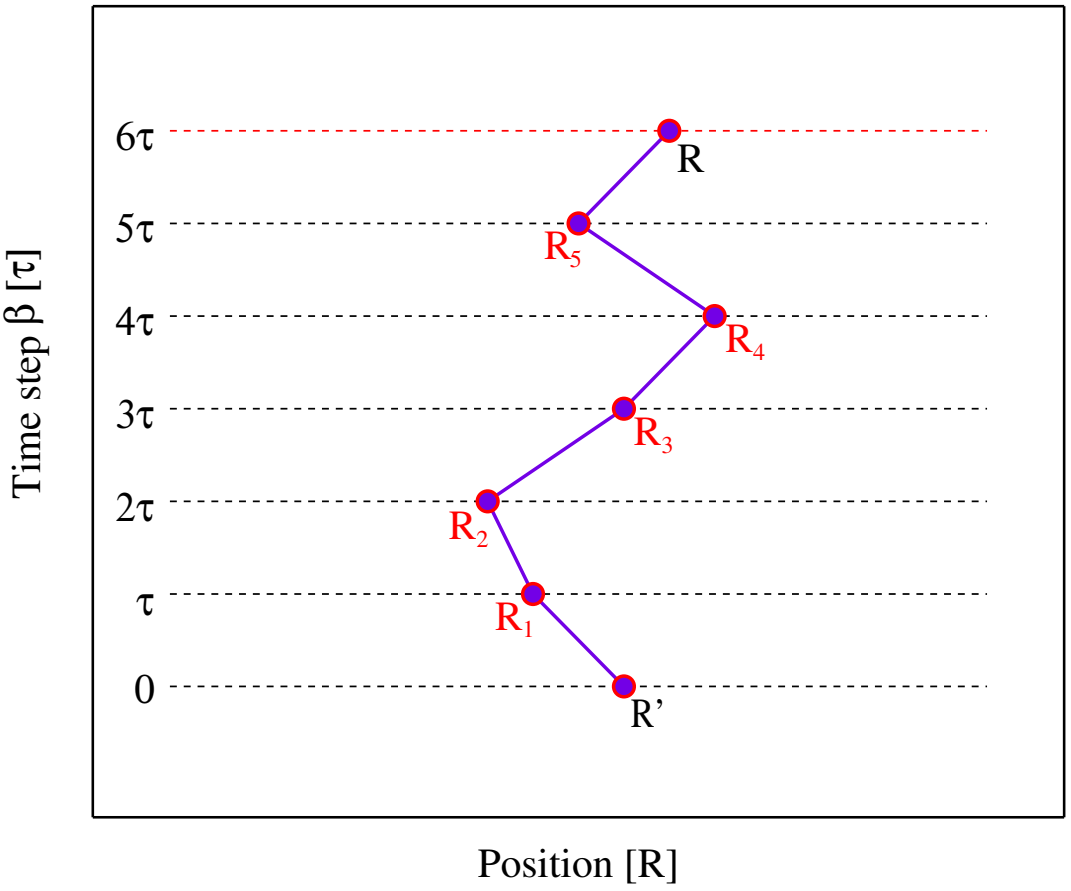

Figure 2.2: A particle travelling between points x' and x. Particle travelling along different, possible path $x_1, ..., x_5$.

where and then substituting to Eq.(2.53)

$$\rho\left(x, x'; \beta\right) = \int dx_1 \cdots dx_{M-1} \exp\left\{-\frac{1}{\hbar}\sum_{m=1}^{M} \mathcal{S}(x_m, x_{m-1}; \tau)\right\}, \tag{2.55}$$

here the sum runs over all possible slices between $x' = x_0$ and $x = x_M$, shown in Fig. 2.2. It it worth noticing that the expression Eq.(2.53), and thereby its discrete time form Eq.(2.55), is *exact* for any $M \geqslant 1$. For the large number of segments, calculation of the limit $M \to \infty$ yields,

$$\rho\left(x, x'; \beta\right) = \int \mathscr{D}x(t) \exp\left\{-\frac{1}{\hbar}\mathcal{S}[x(t)]\right\}, \tag{2.56}$$

with $M\tau = \beta$ and

$$\mathcal{S}[x(t)] = \lim_{\tau\to 0} \sum_{m=1}^{M} \mathcal{S}(x_m, x_{m-1}; \tau), \tag{2.57}$$

$$\mathscr{D}[x(t)] = \lim_{M\to\infty} dx_1 \cdots dx_{M-1}, \tag{2.58}$$

In above expressions $t \in \langle 0, \beta\rangle$ and $x(t)$ stands for continuous path.

2.3.3 Trotter and Feynman-Kac formulas

The path integral method allows us to sample physical properties of the system directly from the thermal density matrix, however to do this an explicit form of density matrix must be derived. A typical Hamiltonian is defined in terms of the kinetic $\hat{\mathscr{T}}$ and potential $\hat{\mathscr{V}}$ energy operators is their sum $\hat{\mathscr{H}} \equiv \hat{\mathscr{T}} + \hat{\mathscr{V}}$. If $\hat{\mathscr{V}}$ represents a lower bounded and sufficiently smooth potential, then time displacement operator can be expressed by

$$\rho(x, x'; \tau) \equiv \exp\left\{-\frac{\tau}{\hbar}\hat{\mathscr{H}}\right\} = \exp\left\{-\frac{\tau}{\hbar}\left(\hat{\mathscr{T}} + \hat{\mathscr{V}}\right)\right\}. \tag{2.59}$$

Eq.(2.59) can be factorised using the Baker-Campbell-Hausdorff equation to the form

$$\exp\left\{-\frac{\tau}{\hbar}\left(\hat{\mathscr{T}} + \hat{\mathscr{V}}\right)\right\} = \exp\left\{-\frac{\tau}{\hbar}\hat{\mathscr{V}}\right\}\exp\left\{-\frac{\tau}{\hbar}\hat{\mathscr{T}}\right\}\exp\left\{-\left(\frac{\tau}{\hbar}\right)^2\hat{\mathscr{G}}\right\}, \tag{2.60}$$

where operator $\hat{\mathscr{G}}$ contains the remaining terms of the series expansion,

$$\hat{\mathscr{G}} \equiv \frac{i}{2}\left[\hat{\mathscr{V}}, \hat{\mathscr{T}}\right] - \underbrace{\frac{\tau}{\hbar}\left\{\frac{1}{6}\left[\hat{\mathscr{V}}, \left[\hat{\mathscr{V}}, \hat{\mathscr{T}}\right]\right] - \frac{1}{3}\left[\left[\hat{\mathscr{V}}, \hat{\mathscr{T}}\right], \hat{\mathscr{T}}\right]\right\} + \cdots}_{O(\tau^3)}. \tag{2.61}$$

The above expression, through $O(\tau^3)$, allows for an approximation of the exact density matrix in $\hat{\mathscr{H}}$ to be the product of the density matrices in $\hat{\mathscr{T}}$ and $\hat{\mathscr{V}}$,

$$\exp\left\{-\frac{\tau}{\hbar}\left(\hat{\mathscr{T}} + \hat{\mathscr{V}}\right)\right\} \approx \exp\left\{-\frac{\tau}{\hbar}\hat{\mathscr{V}}\right\}\exp\left\{-\frac{\tau}{\hbar}\hat{\mathscr{T}}\right\} = \rho_{free}\exp\left\{-\frac{\tau}{\hbar}\hat{\mathscr{V}}\right\}, \tag{2.62}$$

where ρ_{free} is a density matrix for a free particle. Eq.(2.62) can be depicted as an *almost* free particle, slightly perturbed by the vicinity of potential $\hat{\mathscr{V}}$, moving in

infinitesimally small imaginary time interval τ. The latter picture is called a *primitive approximation* due to very simplified assumptions. In order to verify approximation Eq.(2.62) we recall the Trotter derivation [162], which, given that three operators $\hat{\mathscr{T}}$, $\hat{\mathscr{V}}$ and $(\hat{\mathscr{T}}+\hat{\mathscr{V}})$ are self-adjoint and the their spectra are bounded below, [163] yields

$$\exp\left\{-\beta\left(\hat{\mathscr{T}}+\hat{\mathscr{V}}\right)\right\}=\lim_{M\to\infty}\left[\exp\left\{-\tau\hat{\mathscr{V}}\right\}\exp\left\{-\tau\hat{\mathscr{T}}\right\}\right]^{M}. \tag{2.63}$$

The primitive approximation in the position representation takes the form,

$$\begin{aligned}\rho\left(x,x';\tau\right)&=\left\langle x\left|\exp\left\{-\tau\left(\hat{\mathscr{T}}+\hat{\mathscr{V}}\right)\right\}\right|x'\right\rangle\\&\approx\left\langle x\left|\exp\left\{-\tau\hat{\mathscr{V}}\right\}\exp\left\{-\tau\hat{\mathscr{T}}\right\}\right|x'\right\rangle\\&=\int dx''\left\langle x\left|\exp\left\{-\tau\hat{\mathscr{V}}\right\}\right|x''\right\rangle\left\langle x''\left|\exp\left\{-\tau\hat{\mathscr{T}}\right\}\right|x'\right\rangle.\end{aligned} \tag{2.64}$$

Knowing that the potential operator $\hat{\mathscr{V}}$ depends only on position $\hat{\mathscr{V}}=V(x)$ and $|x'\rangle$ is an eigenvector of position operator $\hat{x}$, it is possible to approximate the potential bra-ket of the short-time propagator as,

$$\begin{aligned}\left\langle x''\left|\exp\left\{-\tau\hat{\mathscr{V}}\right\}\right|x'\right\rangle&=\left\langle x''\left|\exp\left\{-\tau V(\hat{x})\right\}\right|x'\right\rangle=\left\langle x''\left|\exp\left\{-\tau V(x')\right\}\right|x'\right\rangle\\&=\exp\left\{-\tau V(x')\right\}\left\langle x''\left|x'\right\rangle=\exp\left\{-\tau V(x')\right\}\delta\left(x''-x'\right).\end{aligned} \tag{2.65}$$

In the next step by substitution of Eq.(2.65) into Eq.(2.64), we obtain the potential in the form of the thermal density matrix,

$$\begin{aligned}\rho\left(x,x';\tau\right)&=\int dx''\left\langle x\left|\exp\left\{\tau\hat{\mathscr{T}}\right\}\right|x''\right\rangle\exp\left\{-\tau V(x')\right\}\delta\left(x''-x'\right)\\&=\left\langle x\left|\exp\left\{\tau\hat{\mathscr{T}}\right\}\right|x'\right\rangle\exp\left\{-\tau V(x')\right\}.\end{aligned} \tag{2.66}$$

Knowing that the exact thermal density matrix ρ is symmetric, it is more efficient to use potential V in a symmetric form by substituting:

$$\exp\left\{-\tau V(x')\right\}\to\exp\left\{-\left(\tau/2\right)\left[V(x)+V(x')\right]\right\}. \tag{2.67}$$

Eq.(2.67) is analogous to introducing the density matrix in the symmetric approximation

$$\exp\left\{-\tau\left(\hat{\mathscr{T}}+\hat{\mathscr{V}}\right)\right\}\approx\exp\left\{-\frac{\tau\hat{\mathscr{V}}}{2}\right\}\exp\left\{-\tau\hat{\mathscr{T}}\right\}\exp\left\{-\frac{\tau\hat{\mathscr{V}}}{2}\right\}. \tag{2.68}$$

Eq.(2.68), as an approximation, is correct to $O(\tau^2)$. It is important to note that the density matrix at temperature T in terms of density matrix at temperature MT, Eq.(2.63) implies that approximation for $\exp\left\{-\beta\left(\hat{\mathscr{T}}+\hat{\mathscr{V}}\right)\right\}$ is valid to τ one order lower than for $\exp\left\{-\tau\left(\hat{\mathscr{T}}+\hat{\mathscr{V}}\right)\right\}$. This is particularly important for the above discussed symmetric approximation,

$$\begin{aligned}\left(\exp\left\{-\tau\left(\hat{\mathscr{T}}+\hat{\mathscr{V}}\right)+O(\tau^3)\right\}\right)^M &= \left(\exp\left\{-\tau\hat{\mathscr{H}}+O(\tau^3)\right\}\right)^{\beta/\tau} \\ &= \exp\left\{-\beta\hat{\mathscr{H}}+\frac{\beta}{\tau}O(\tau^3)\right\} = \exp\left\{-\beta\hat{\mathscr{H}}+O(\tau^2)\right\}.\end{aligned} \tag{2.69}$$

The resulting line of Eq.(2.69) follows from varying τ with β fixed. The main message of the above derivation is that for the convergence of the path integral simulation (limit $\tau \to 0$), the approximation for $\exp\left\{-\tau\hat{\mathscr{H}}\right\}$ has to be correct through $O(\tau)$. In the following step we solve the Bloch equation for a free particle in periodic box of length L in order to obtain ρ_{free},

$$-\frac{\partial\rho_{free}}{\partial\beta} = -\Lambda\nabla^2\rho_{free}(x,x';\beta), \tag{2.70}$$

where $\Lambda = \hbar^2/2m$ and m is a particle mass. Eq.(2.70) describes the diffusion of paths in imaginary time β, to which the solution is well known,

$$\rho_{free}(x,x';\beta) = \frac{1}{(4\pi\Lambda\beta)^{-3N/2}}\exp\left\{-\frac{(x-x')^2}{4\Lambda\beta}\right\} \quad \Lambda\beta \ll L^2. \tag{2.71}$$

The choice of normalisation constant at the front of the Gaussian guarantees,

$$\rho_{free}(x,x';0) = \delta(x-x'). \tag{2.72}$$

The diffusion parameter Λ depends on the mass of the particle. The value of this constant is small for classical particles. Light, quantum particles quickly diffuse in imaginary time, therefore their corresponding value of Λ is large. Another important parameter in Eq.(2.71) is $\sqrt{4\Lambda\beta}$, which describes the width of density matrix. Using relation,

$$\lambda = \frac{h}{\sqrt{2\pi m k_B T}} \equiv \sqrt{4\pi\Lambda\beta}, \tag{2.73}$$

one can define the thermal de Broglie wavelength. If the de Broglie wavelengths become comparable to the distances between particles, quantum many-body effects start to dominate the picture. This length scale can be further adapted to the path

integral formalism by introducing the degeneracy parameter, $n\lambda^N$, in which $n^{-1} \equiv L^N/M$ is a volume per particle and λ^N is the volume occupied by a single path.

The discrete path integral expression for the density matrix within the primitive approximation can then be obtained by merging Eqs.(2.71) and (2.66),

$$\rho(x,x';\beta) = \frac{1}{(4\pi\Lambda\beta)^{3NM/2}} \int dx_1 \cdots dx_{M-1} \times \exp\left\{ -\sum_{m=1}^{M} \left(\frac{(x_m - x_{m-1})^2}{4\Lambda\tau} + \frac{\tau}{2}\left[V(x_m) + V(x_{m-1})\right] \right) \right\}. \tag{2.74}$$

Eq.(2.74) is a more accurate form of Eq.(2.55), which relates the thermal density matrix of the quantum system at any temperature to integrals over the path $x_1 \cdots x_M$ in a classical Maxwell-Boltzmann-like distribution. This idea was first introduced by Feynman, as a mapping of a quantum system on a classical system of interacting *polymers*. In the context of polymer picture, Eq.(2.74) can be interpreted as a description of a chains of *beads* representing the imaginary time propagation of a single particle. All the beads on a chain, Fig. 2.3 are connected by *kinetic links* in such a way, that bead 1 at some time t experiences a potential due to bead 2 at time $t+\tau$ and bead 13 at time $t-\tau$, as shown in Fig. 2.3. In the polymer picture we interpret imaginary time as an additional spatial dimension around the polymer ring. The already mentioned potential differs significantly from the classical perspective as the interactions take place at the same time and only between beads of other chains. One of the biggest advantage of the above picture is the fact that both quantum and polymer system are described by the same partition function. This gives us an opportunity to understand many properties of the quantum system using tools and language of classical statistical mechanics. In order to demonstrate this feature, let us consider the limit $M \to \infty$ in Eq.(2.74),

$$\frac{x_m - x_{m-1}}{\tau} \to \frac{dx(t)}{dt}\Big|_{t=m\tau} \equiv \dot{x}(t)\Big|_{t=m\tau}, \tag{2.75}$$

which leads to an explicit expression for thermal density matrix, known as the Feynman-Kac formula:

$$\rho(x,x';\beta) = \int \mathscr{D}x(t) \exp\left\{ -\int_0^\beta dt \left(\frac{\dot{x}^2(t)}{4\Lambda} + V\left[x(t)\right] \right) \right\}. \tag{2.76}$$

It is worth mentioning that $|x_m - x_{m-1}| \sim \sqrt{\tau}$ as a consequence of the Brownian origin

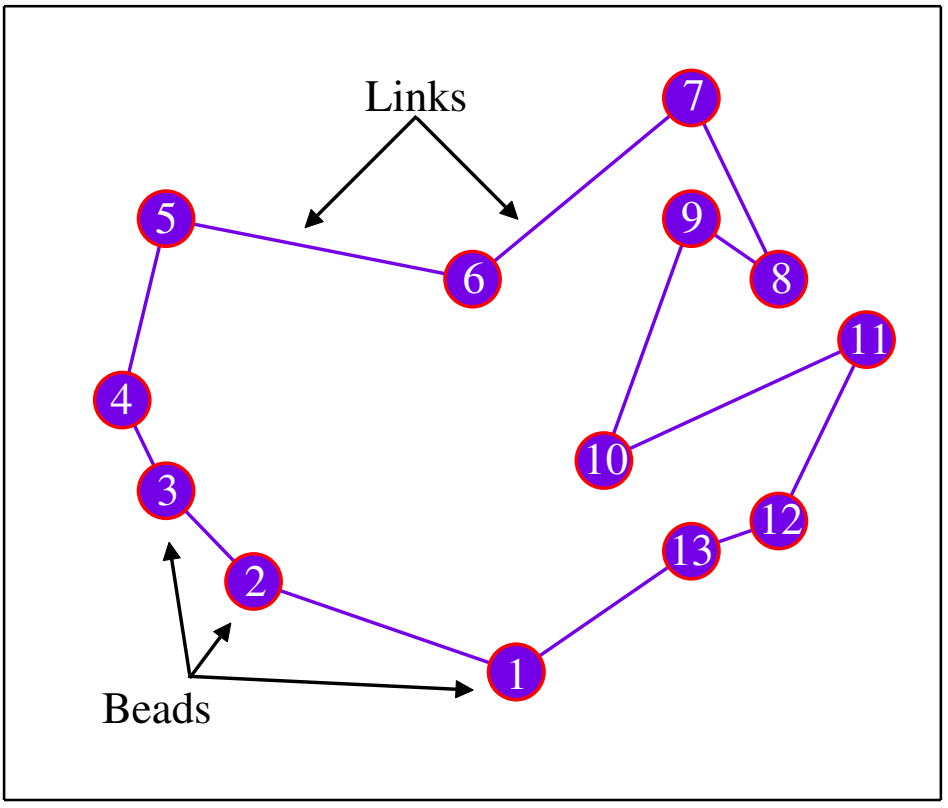

Figure 2.3: Polymer isomorphism. The links represent the kinetic part of the action $(x_m - x_{m-1})^2$. Beads correspond to the thermal density matrices at high temperature T.

of the path $x(t)$. This implies that $\dot{x}(t)$ is infinite everywhere, therefore Eq.(2.76) is not a strict definition and serves more as a mental picture of discrete path integral derived in Eq.(2.74).

One of the very important aspects of the PI-QMC calculation of Eq.(2.74) is the following effect of the convolution property: if $\rho(x, x'; \tau) \geqslant 0 \vee x,\ x'$ for any τ then the same holds for any positive multipliers of τ.

We conclude this subsection with the derivation of an explicit expression for the action $\mathcal{S}[x(t)]$. Comparison of Eqs.(2.76) and (2.56) resembles an integral of the Lagrangian along an imaginary time path, thus the short-time action term Eq.(2.55)

turns into

$$\begin{aligned}\mathcal{S}(x_m, x_{m-1}; \tau) &= \int_{(m-1)\tau}^{m\tau} dt \mathcal{L}(\dot{x}(t), x(t); t) \\ &\approx \frac{(x_m - x_{m-1})^2}{4\Lambda\tau} + \frac{\tau}{2}\left[V(x_m) + V(x_{m-1})\right].\end{aligned} \tag{2.77}$$

Eq.(2.77) is consistent with the action in terms of the density matrix given in Eq.(2.54). Note the fact that both $\mathcal{S}[x(t)]$ and $\mathcal{S}(x_m, x_{m-1}; \tau)$ are dependent on imaginary time, so they do not have anything in common with the mechanical action.

2.3.4 Polymer isomorphism and temperature

The polymer isomorphism picture in the PI-QMC technique is characterised by two extremely useful advantages. The first one is the simplicity with which we can visualise the quantum system. Living in the classical world we often use our intuition to imagine some physical properties; unfortunately, quantum mechanics mostly goes against our common sense. The polymer analogy and path integrals allow us to study the quantum world in the classical, statistical mechanics environment. In Fig. 2.3 a single atom is depicted as a set of thirteen classical particles connected by links. If the temperature is low then the particles, similar to a classical gas, are very slow. The links are heavily stretched and the ring occupies a much bigger volume in position space Fig. 2.4. As a result the uncertainty in the position of the particle increases significantly and the only information we can extract regarding the particle's position in the system is the probability density. The important thing is that even a very delocalised atom can still be distinguished from others as the polymers are well defined. This kind of distinguishable particle is governed by Boltzmann statistics.
With increasing temperature of the system the beads start to oscillate and move faster. The inter-particle separation decreases and at some point all particle are localised upon each other. Uncertainty in the position of the particles goes to zero and we are in the classical system.

The second advantage of the PI-QMC technique is broad computational applicability to quantum liquids. One of the first problems in which polymer isomorphism was successfully applied is the ^{4}He and superfluidity. Let us consider a system assembled of ^{4}He atoms in the superfluid regime. Such a system can by imagined in the

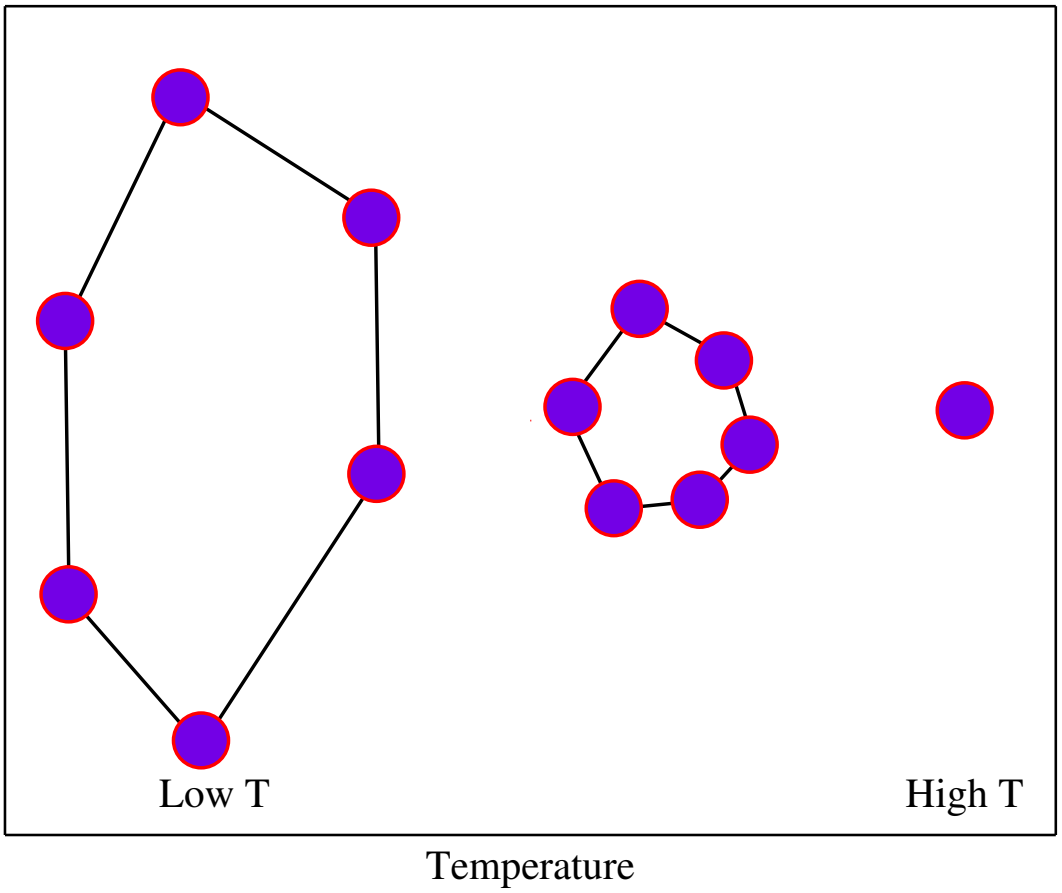

Figure 2.4: Transition between quantum and classical system. Change of the character of the system with varying T.

polymer frame as bead exchange between the atoms. This scenario is almost impossible above the lambda transition, however below it there exists a finite probability that this can occur. In the latter situation, if the temperature is low enough the atoms can share the beads and some polymer rings become attached to other rings. At this point we lose the ability to distinguish the rings as there is no clear indication where constituent rings start and end. The free particle visualised in Fig. 2.4 can be translated into a formal, mathematical expression which clearly show the bridge between quantum and classical world.

2.3.5 Exact solution to simple harmonic oscillator

The harmonic oscillator is one of the simplest models in quantum mechanics. We will use this system in order to verify the correctness of our PI-QMC simulation and also

as a mathematical model of quantum dot. The main advantage of this model system is that quantities such as the energy and the density matrix can be obtain analytically.

We start with the Hamiltonian of a linear quantum harmonic oscillator,

$$\hat{\mathscr{H}} = \frac{\hat{p}^2}{2m} + \frac{1}{2}m\omega^2\hat{x}^2. \tag{2.78}$$

There are two distinguishable terms in Eq.(2.78). The first term corresponds to the kinetic energy of the system and the second one represents the energy stored in the system. The above equation is analogous to the expression for classical harmonic oscillator,

$$E = \frac{1}{2}mv^2 + \frac{1}{2}kx^2, \tag{2.79}$$

if we notice that the Hamiltonian on the left describes total energy of the system, product of mass and velocity yields momentum, and $\omega = \sqrt{k/m}$ is the classical oscillator frequency. Energy levels occupied by the quantum harmonic oscillator are called the energy eigenstates as follows:

$$E_n = \left(n + \frac{1}{2}\right)\hbar\omega, \tag{2.80}$$

where $n = 0, 1, 2, ...$ The energy levels are equally spaced and correspond to a countably infinite number of solutions. For high values of n the period of oscillation gets smaller which is reflected in the wave function behaviour. The ground-state wave function of the one dimension quantum harmonic oscillator is given by,

$$u_0(x) = \left(\frac{m\omega}{\pi\hbar}\right)^{1/4} \exp\left\{\frac{-m\omega x^2}{2\hbar}\right\}, \tag{2.81}$$

which is a Gaussian distribution. With the aid of classical statistical mechanics we can define the partition function of the one-dimensional quantum mechanical oscillator,

$$\mathscr{Z} = \sum_{n=0}^{\infty} \exp\left\{-\beta\hbar\omega\left(n + \frac{1}{2}\right)\right\} = \left[2\sinh\left(\frac{\hbar\omega}{2k_BT}\right)\right]^{-1}. \tag{2.82}$$

Eq.(2.82) can be expanded to an arbitrary number of dimensions D and oscillators N,

$$\mathscr{Z} = \left[2\sinh\left(\frac{\hbar\omega}{2k_BT}\right)\right]^{-ND}. \tag{2.83}$$

With knowledge of the partition function $\mathscr{Z}$ and the Helmholtz free energy $\mathscr{F}$ we can calculate everything else we need,

$$\mathscr{F} = E - TS = -k_B T \ln(\mathscr{Z}) = NDk_B T \ln\left[2\sinh\left(\frac{\hbar\omega}{2k_B T}\right)\right]. \tag{2.84}$$

Using the definition of the mean energy in terms of the trace of the system,

$$\langle H\rangle = -\frac{\partial}{\partial\beta}\ln\left[\sum_x \left\langle x\left|\exp\left\{-\beta\hat{\mathscr{H}}\right\}\right|x\right\rangle\right]. \tag{2.85}$$

Thus we obtain the expression for the total energy of the simple harmonic oscillator

$$E = \frac{ND}{2}\hbar\omega\coth\left(\frac{1}{2}\beta\hbar\omega\right), \tag{2.86}$$

where $\beta = 1/k_B T$. In order to define the thermal density matrix for the quantum harmonic oscillator the imaginary-time propagator of a particle in a harmonic potential is required. In three spatial dimensions this object takes the form

$$K(\mathbf{x},\mathbf{x}';\tau) = \left(\frac{m\omega}{2\pi\hbar\sinh(\omega\tau)}\right)^3 \exp\left\{-\frac{m\omega\left((x^2+x'^2)\cosh(\omega\tau)-2\mathbf{x}\cdot\mathbf{x}'\right)}{2\hbar\sinh(\omega\tau)}\right\}. \tag{2.87}$$

The probability density of the system is defined as the diagonal of the thermal density matrix $\rho(\mathbf{x}) = K(\mathbf{x},\mathbf{x}';\tau)$.

2.4 Coulomb interactions

All theoretical treatments of extremely complex physical phenomena meet some limitations. Unfortunately this also applies to Quantum Monte Carlo methods. One of the more challenging issues are the interaction of two identical particles and the presence of an attractive Coulomb potential. The first case, known as a fermionic sign problem, will be discussed in the following section; here we focus on the Coulomb system and the methods of dealing with it.

The typical Coulomb potential takes the form $-\frac{1}{r}$. This potential is well defined everywhere in space, except at $r = 0$, a non-integrable singularity at which must be handled correctly. We do not know exactly how the system behaves and even more important if the path integral estimators converge.

In this section we outline techniques which we successfully implemented into the Coulomb Action used in PI-QMC numerics in order to overcome this issue.

2.4.1 Analytical approach

One of the most straightforward implementations of Coulomb interactions into the PI-QMC is the one used in [164]. In this technique the analytical form of action is obtained by solving the Schrödinger equation in the centre-of-mass (CM) and relative coordinates (RC) frames. CM can be treated as a movement of a free particle, as the Coulomb interactions enter only into the RC part. Solutions to both terms are well known and yield plane waves for CM, and hydrogen-atom-like solutions to RC. The resulting wave functions and density matrix then allow the construction of a ground state Coulomb density matrix. From this, if the particles are close enough to each other, one can find the expression for an action with the help of Eq.(2.54). As the hydrogenic wave functions were obtained for the ground state of the system, the ground state density matrix can be calculated. The main downside to this method is the fact that in order to maintain the system in the ground level we are limited to the low temperatures.

2.4.2 The pair-product approximation

A much more general method of dealing with many-particles system can be found in pair action. Assuming that the system can be approximated as a hard-sphere-like one, we can find the exact form of action for any two atoms and then expand that to a many body action. In order to find this action we have to check if the potential energy can be split into a pairwise sum of terms,

$$V(R) = \sum_{i<j} v(\mathbf{r}_i - \mathbf{r}_j). \tag{2.88}$$

Applying Eq.(2.76), we observe that what appears is the integration of potential energy along the path. Using the Feynman-Kac formula for the inter-action U_m,

$$\exp\left\{-U_m(R, R'; \tau)\right\} = \left\langle \exp\left[-\int_0^\tau V(R(t))dt\right]\right\rangle, \tag{2.89}$$

we get the expectation value,

$$\exp\left\{-U_m(R,R';\tau)\right\} = \left\langle \prod_{i<j} \exp\left[-\int_0^\tau v(\mathbf{r}_{ij}(t))dt\right]\right\rangle \tag{2.90}$$

which is the exact density matrix for a pair of interacting particles. Eq.(2.90) can be rearranged further, assuming that the $\mathbf{r}_{ij}$'s are uncorrelated [165] leading to,

$$\exp\left\{-U_m(R,R';\tau)\right\} \approx \prod_{i<j} \left\langle \exp\left[-\int_0^\tau v(\mathbf{r}_{ij}(t))dt\right]\right\rangle. \tag{2.91}$$

Now it is apparent that the $\langle r_{ij}\rangle$ is the interacting part of the exact action for a pair of atoms, therefore we can define the pair-product action as,

$$U(R,R';\tau) = \sum_{i<j} u(\mathbf{r}_{ij},\mathbf{r'}_{ij};\tau). \tag{2.92}$$

$u(\mathbf{r}_{ij},\mathbf{r'}_{ij};\tau)$ is the exact action to the two body problem, which must be calculated.

The above approximation, by definition, is exact for two particles. If τ is sufficiently small, this approximation is correct as most inter-particle collisions involve two atoms at a time. The sum of pairwise interactions U is accurate to τ^2. The errors in U result from three and more body correlations. In a homogeneous system the correlation effect is low, as other atoms in different directions have opposite correlations, therefore a significant number of many-body effects cancel. This consideration leads to the conclusion that significant errors can occur in the situation when three particles come to close proximity. If two-body interactions dominate then the pair product will be error free to the lowest order in a density expansion of action [165].

2.4.3 Matrix-squaring method

Using the matrix-squaring method the exact pair action can be computed [166]. We start by separating the pair density matrix into the centre-of-mass and relative coordinates parts. If, for simplicity, we consider only the density matrix for a single particle in an external potential and expand the relative part in terms of the contributions from all partial waves [166] for a spherical central potential, then,

$$\rho_R(\mathbf{r},\mathbf{r}';\tau) = \frac{1}{4\pi r r'}\sum_{l=0}^{\infty}(2l+1)\rho_l(r,r';\tau)P_l(\cos(\theta)), \tag{2.93}$$

where θ is the angle between $\mathbf{r}$ and $\mathbf{r}'$ and P_l are Legendre polynomials. Each pair density matrix for a one-dimensional particle subjected to a potential is defined by partial wave components with an additional centrifugal term [167]. These partial wave components fulfil the Bloch equation,

$$-\frac{\partial\rho(x,x';t)}{\partial t} = \left\{-\lambda\frac{d^2}{dr^2} + \tilde{v}_l(x)\right\}\rho(x,x';t), \tag{2.94}$$

and are subject to the boundary conditions $\rho_l(r,r';t) = \delta(r-r')$ and $\rho_l(0,r';t) = 0$. One can then define the effective potential $\tilde{v}_l(r)$ in the form:

$$\tilde{v}_l(r) = v(r) + \frac{\lambda}{r^2}l(l+1). \tag{2.95}$$

At this point the pair density matrix ρ_l can be expanded in terms of eigenfunctions [132],

$$\rho_l(r,r';\tau) = \sum_n \phi_n^*(r)\exp\{-\tau E_n\}\phi_n(r') + \int_0^\infty dk\phi_k^*(r)\exp\{-\tau E_k\}\phi_k(r'). \tag{2.96}$$

All partial waves are Green's functions. Applying the convolution technique to the lower temperature pair matrices, which were obtained using the matrix-squaring method [168], leads to,

$$\rho_l(r,r';\tau) = \int_0^\infty dr''\rho_l(r,r'';\frac{\tau}{2})\rho_l(r'',r';\frac{\tau}{2}). \tag{2.97}$$

The main idea behind the matrix-squaring method is that if one squares the thermal density matrix k-times then the resulting temperature drops down by a factor of 2^k. Squaring of one-dimensional integrals for all values of r, r' and l is not the most efficient way. The process can be significantly improved by repeated application of kinetic and potential operators to a uniform grid in r and r' using a fast Fourier transform [169]. The main idea of matrix-squaring is to get a pair density matrix at some τ, in a form which can be fast and easily computed in the Monte Carlo computer simulation.

In the situation in which one deals with small τ and large x, summation over the partial waves to find the pair density matrix, Eq.(2.93) is far too lengthy (the number of partial waves required is of the order of $r/\sqrt{\lambda\tau}$).

In order to overcome this inconvenience, one can consider the special case of a

Coulomb potential in which the only term needed to get the relative coordinates pair density matrix is $l = 0$ [170]. We then introduce three vectors,

$$q = (|\mathbf{r}| + |\mathbf{r}'|)/2, \quad s = |\mathbf{r} - \mathbf{r}'|, \quad z = |\mathbf{r}| - |\mathbf{r}'|\,, \tag{2.98}$$

defined as $\mathbf{r} = \mathbf{r}_i - \mathbf{r}_j$ and $\mathbf{r}' = \mathbf{r}'_i - \mathbf{r}'_j$, and $l = 0$ allows one to write the diagonal:

$$\rho_r(\mathbf{r}, \mathbf{r}; \tau) = -\frac{1}{8\pi}\frac{\partial^2}{\partial s^2}\rho_{l=0}(z + s, z - s; \tau)|_{s=0}, \tag{2.99}$$

and off-diagonal elements separately,

$$\rho_r(\mathbf{r}, \mathbf{r}'; \tau) = -\frac{1}{8\pi s}\frac{\partial}{\partial s}\rho_{l=0}(z + s, z - s; \tau). \tag{2.100}$$

Defined in Eq.(2.98) distances s and z are small, comparable to the thermal de Broglie wavelength Λ_r [167], therefore one can use the power series expansion of potential action [171]:

$$u(x_r, x'_r; \tau) = \frac{u_0(x; \tau) + u_0(x'; \tau)}{2} + \sum_{k=1}^{n}\sum_{j=0}^{k} u_{kj}(q; \tau) z^{2j} s^{2(k-j)}. \tag{2.101}$$

We can distinguish two terms in Eq.(2.101). The first one is called end-point action, and the remaining terms are off-diagonal corrections to this action. Using a least-square fit to the partial wave expansion, the function $u_{kj}(q)$ can be tabulated and use during the Monte Carlo simulations.

In our simulations the PI-QMC numerics are used. A high temperature approximation to the pair density matrix is implemented together with an analytical power series expansion, and the fast Fourier transform of the kinetic and potential operators are hard-coded into the software [172].

2.5 Thermodynamic properties

In the previous sections we showed how to simulate the quantum system at a finite temperature. We derived a way to discretise such a system and the methods to evolve it to the equilibrium state. At this point we need to develop a set of tools which will help us to take a look into the system's behaviour and analyse its physical properties. In the following subsections, the estimators coded into the PI-QMC software will be

discussed. The properties that the PI-QMC code is capable of computing include: thermal and virial energy, density, pair correlation function and static polarisation. We conclude with a short discussion of errors affecting the estimators.

2.5.1 Energy

The expectation value of the quantum mechanical energy of the system is one of the most frequently calculated properties in PI-QMC simulations. One of the method of finding E is differentiation,

$$\langle E\rangle_T \equiv -\frac{1}{\mathscr{Z}}\frac{\partial \mathscr{Z}}{\partial \beta}. \tag{2.102}$$

The canonical partition function $\mathscr{Z} \equiv \int dx \rho(x, x; \beta)$ is given by

$$\mathscr{Z} = \left(\frac{Nm}{2\pi\hbar^2\beta}\right)^{N/2} \int dx_1 \cdots dx_N \exp\left\{-\beta V_C\right\} \tag{2.103}$$

with propagator potential V_C,

$$V_C \equiv \sum_{j=1}^{N}\left[\frac{Nm}{2\hbar^2\beta^2}(x_j - x_{j+1})^2 + \frac{1}{N}V(x_j)\right], \tag{2.104}$$

where $x_{N+1} \equiv x_1$. The above expression can be interpreted as the quantum path integral, which is equivalent to a classical expectation value of N harmonically interacting beads in the vicinity of external potential V [173]. The energy is then defined in the form:

$$\langle E\rangle_T = \frac{1}{\mathscr{Z}}\left(\frac{Nm}{2\pi\hbar^2\beta}\right)^{N/2} \int dx_1 \cdots dx_N \epsilon_T \exp\left\{-\beta V_C\right\}, \tag{2.105}$$

with the Barker estimator $\epsilon_T = \langle K\rangle_T + \langle \bar{V}\rangle_T$ where,

$$\langle \bar{V}\rangle_T = \frac{1}{N}\sum_{j=1}^{N} V(x_j) \tag{2.106}$$

and

$$\langle K\rangle_T = \frac{N}{2\beta} - \frac{Nm}{2\hbar^2\beta^2}\sum_{j=1}^{N}(x_j - x_{j+1})^2. \tag{2.107}$$

The pre-fraction $1/\mathscr{Z}$ can be seen as an average over all paths and energy, and so Eq.(2.105) can be then calculated using the Monte Carlo method. If $x_1 \cdots x_N$ are sampled with respect to V_C, then ϵ_T is the thermodynamic estimator for the energy

E. In general, convergence of thermodynamic estimator ϵ_T to E is rather slow as the mean square fluctuation in the thermodynamic estimator increase as $N/2\beta^2$. An alternative way of calculating the energy estimator of the system is the virial energy. In this estimator the energy calculation is based on the potential energy, which doesn't fluctuate significantly over the time-slice. The main advantage of this estimator is a much faster convergence and hugely reduced variance for small values of τ, compared to the K_T. The virial energy can be obtained by elimination of the kinetic part during the integration by parts over the path variable [165]. The estimator itself takes the form

$$\epsilon_T = \langle K \rangle_V + \langle \bar{V} \rangle_T$$

where,

$$\langle K \rangle_V = \frac{1}{2N} \sum_{j=1}^{N} x_j V'(x_j). \tag{2.108}$$

The convergence of the virial estimator is better compared to the thermodynamic one, however the applicability of the virial estimator is limited to the smooth, slowly varying and bound potentials.

2.5.2 Density and pair correlation function

Scalar operators like the pair density matrix and pair correlation function are amongst the most straightforward to compute. In PI-QMC all time-slices are equivalent. The pair correlation function $g_{\alpha,\beta}$ between two particles α and β is given,

$$g_{\alpha,\beta}(\mathbf{r}, \mathbf{r}') = \frac{1}{n_\alpha(\mathbf{r}) n_\beta(\mathbf{r}')} \left\langle \sum_{i,j} \delta(\mathbf{r}_i - \mathbf{r}) \delta(\mathbf{r}_j - \mathbf{r}) \right\rangle. \tag{2.109}$$

In Eq.(2.109) the average over all paths and over links k is taken. The pair correlation function estimator can be used to obtain properties of the system that depend on the relative separation of the two particles. Once the separation is calculated, information like angular and radial separation probability between charge carriers can be computed. These quantities contain the statistical information of the different inter-particle separations and spatial distribution.

2.5.3 Polarization

The static polarisation of a molecule is defined as,

$$\mathbf{P} = \alpha_{\mu\nu}\mathbf{E}. \tag{2.110}$$

In the above equation, $\mathbf{E}$ stands for the applied electric field and $\alpha_{\mu\nu}$ is the molecular static polarizability tensor in the directions μ and ν. In most of our simulations, e.g.: excitons and bi-excitons, we deal with diatomic molecules. This simplifies the polarizability tensor to two components, parallel $\alpha_{||}$ and perpendicular, $\alpha_{\perp}$. The polarizability estimator, defined as:

$$\alpha_{\mu\nu} = E_{\nu}^{-1} \sum_{l} \langle eX_{\mu}(l) \rangle \,, \tag{2.111}$$

allows us to find the static polarizability of the l^{th} particle in direction μ, placed at $X_{\mu}(l)$ in an applied electric field of strength E_{ν} in direction ν.

2.5.4 Errors of large scale sets of PI-QMC simulation data

Path Integral Quantum Monte Carlo estimators are averaged over substantial sets of datapoints, therefore finding the error in an estimator is very important. The most frequently calculated error in all of our simulations is the standard error,

$$error = \frac{\sigma}{\sqrt{N}}. \tag{2.112}$$

Here N is a number of data-points and σ is the standard deviation. This kind of error, decreasing proportionally with $\sqrt{N}$, can be successfully lowered by more frequent data sampling, longer runs or multi-cpu parallel calculations.

Another source of errors is the Metropolis algorithm, which we will discuss in the next section. In the ideal situation all measurements should be independent. Unfortunately, in Metropolis calculations a new configuration is generated out of the previous, leading to autocorrelation,

$$R_A(k) = \frac{1}{(N-k)\sigma_A^2} \sum_{i=1}^{N-k} (A_i - \bar{A})(A_{i+k} - \bar{A}),$$

where $\sigma_A^2 = \frac{1}{N}\sum_i A_i^2 - \bar{A}^2$ and standard deviation of the mean $\bar{A} \approx \sqrt{\frac{1+2\tau_A}{N}}\sigma_A$, for $(\tau_A \ll N)$. Note that, as defined in Eq.(2.112), the standard error underestimates the errors bars. We minimise these errors by running the PI-QMC simulations long enough for the correlations to decay, then statistical sampling takes place.

2.6 Path integrals for Fermi and Bose statistics

The main difference between Fermi and Bose statistics is the symmetry of the wave functions, given by the spin-statistics theorem. According to this theorem, the wave function is symmetric or anti-symmetric when two identical particles are exchanged,

$$\Psi_{B/F}(R) = (\pm 1)^{\mathscr{P}} \Psi_{B/F}(\mathscr{P}R). \tag{2.114}$$

In Eq.(2.114), $\mathscr{P}$ is any of the $\mathscr{N}!$ permutations of the particle labels in x with the same spin, $(+)$ refers to (B)osons and $(-)$ to (F)ermions. Any additional internal degrees of freedom, e.g.: spin, are also permuted [171].

If one defines the wave function describing the distinguishable particle $\Psi_D(R)$, then the odd or even parity can be obtained by acting with the symmetric or anti-symmetric operator on the $\Psi_D(R)$,

$$\Psi_{B/F}(R) = \frac{1}{\mathscr{N}!}\sum_{\mathscr{P}} (\pm 1)^{\mathscr{P}} \Psi_D(\mathscr{P}R). \tag{2.115}$$

Using these states one can construct the density matrix for the system of bosons or fermions,

$$\rho_{B/F}(R, R'; \beta) = \frac{1}{\mathscr{N}!}\sum_{\mathscr{P}} (\pm 1)^{\mathscr{P}} \rho_D(R, \mathscr{P}R'; \beta). \tag{2.116}$$

It is possible to symmetrise or anti-symmetrise Eq.(2.116) with respect to the first, second or both arguments. They are equivalent yielding the same physical observable. The implementation of parity into the path integral takes place by summation over all $\mathscr{P}$ permutations. This concept requires summation over all possible permutations

of final position R' and integration over all configurations of the paths,

$$\begin{aligned}\rho_{B/F}(R,R';\beta) = \frac{1}{\mathscr{N}!}\sum_{\mathscr{P}}(\pm 1)^{\mathscr{P}}\int\cdots\int dR_1 dR_2\cdots dR_{M-1}\\ \rho_D(R,R_1;\tau)\rho_D(R_1,R_2;\tau)\cdots\rho_D(R_{M-1},\mathscr{P}R';\tau)\\ = \frac{1}{\mathscr{N}!}\sum_{\mathscr{P}}(\pm 1)^{\mathscr{P}}\int_{R\to\mathscr{P}R'} dR_t\exp\{-\frac{1}{\hbar}\mathcal{S}[R_t]\}.\end{aligned} \tag{2.117}$$

and will be further explored in section 2.8.2.

2.7 Monte Carlo technique

Sampling is an essential element of any path integral Monte Carlo numerics. In the classical picture the interacting atoms of a liquid or gas are visualised as point like particles in the container. Through iterative solving of Newton's equations for interacting bodies one can study the time evolution of the system. When the iterations are repeated over a long time, the system achieves the thermal equilibrium state. The same situation takes place in the quantum system, with the difference that instead of a point-like representation of atoms we use, as already mentioned, polymer isomorphism. Thermal equilibrium for a system of polymer rings, (beads connected by kinetic links) can also be reached by moving beads and whole necklaces in the simulation box. The manner in which the displacement is performed is called sampling.

In Eq.(2.74) in Section (2.3.3) the thermal density matrix of a many-body system was derived, however in order to calculate a large number of multi-dimensional integrations we must use the stochastic numerical technique. One can imagine $\rho(R,R';\beta)$ as a probability distribution, which should be sampled according to the distribution resulting from the action. This distribution nevertheless differs from the classical liquid analogue, as the beads on the path are connected by kinetic links. This fact is reflected in the long correlation times, which cause slow convergence making classical methods inapplicable.

In the early days Monte Carlo methods were used predominantly to find integrals which were unsolvable analytically. Nowadays the Monte Carlo category includes all sorts of statistical tools and techniques [174], and is widely applicable to a whole spectrum of problems. In this section the theory of Monte Carlo integration is outlined from a statistical point of view.

2.7.1 Monte Carlo Integration

The easiest method of numerical integration involves the computation of a definite integral of the form,

$$F = \int_a^b f(x)dx. \tag{2.118}$$

One of the possible ways of dealing with Eq.(2.118) is use of the mean value theorem known from elementary calculus,

$$F_m = \lim_{N\to\infty} \frac{(b-a)}{N} \sum_{l=0}^{N} f(x_l). \tag{2.119}$$

In this approach the area under a curve between points a and b is divided into N parts, and x_l completely covers the integration interval. For a large number of slices N, F_m approaches the exact value F, and the error in this approximation is defined as $(b-a)\sigma_f/\sqrt{N}$, where σ_f is the variance. In order to evaluate Eq.(2.119) using Monte Carlo integration, one needs to consider its values at N-numbers of $\{x_l\}$, randomly selected from the interval $[a, b]$. One of the most challenging tasks is to generate a proper set of random numbers.

Accuracy and efficiency of Monte Carlo integration can be further improved by application of more advanced methods, such as Simpson's rule or Gaussian quadrature, in which the weighted average of the points is used [175]:

$$F_m = \frac{(b-a)}{N} \frac{\sum_{l=0}^{N} w_l f(x_l)}{\sum_{l=0}^{N} w_l} \tag{2.120}$$

These methods result in accurate values for the integrals as long as the dimension (D) of the system is small, namely $D < 8$. The efficiency and accuracy for higher dimension systems decreases as N^D. To overcome this inconvenience, having a probability distribution, one can choose from it randomly the points x_l using the Monte Carlo technique. Random selection of $x_l's$ from the interval $[a, b]$, yields the solution to Eq.(2.118) given by,

$$F_m = (b-a)\bar{f} = \frac{(b-a)}{N} \sum_{l=0}^{N} f(x_l) + O(\frac{1}{\sqrt{N}}). \tag{2.121}$$

Here $\bar{f}$ is a mean value of f over the set of sampled points $\{x_l\}$. We see that the Monte Carlo error gets smaller as $\sqrt{N}^{-1}$ and does not depend on the dimension of

the system any more. According to the central limit theory, the set of all integrals for different $\{x_l\}$ will follow the Gaussian distribution [176]. The uncertainty in the solution to the integral comes from the standard deviation σ_m calculated for different F_m,

$$\sigma_m = \sqrt{\frac{\frac{(b-a)}{N}\sum_{l=0}^{N} f^2(x_l) - F_m^2}{N-1}}. \tag{2.122}$$

2.7.2 Importance sampling

There are however some cases in which the integration is inefficient, even if we have the set of the proper, uniform random numbers. This can be due, for example, to the significant weight of the function in only some intervals, as in the case of a Gaussian distribution with the largest contribution close to the central peak. To avoid such a situation and improve efficiency a smarter sampling method is required, which will use random numbers but with their density enhanced in the most interesting regions. In this "importance sampling method" the non-uniform distribution function $\pi(x)$ is introduced from which a points are sampled. We require $\pi(x) > 0$ and to well approximate $f(x)$ in the regions of interest. Once the distribution function $\pi(x)$ is set the random variable x can be sampled from $\pi(x)$. At this point integral Eq.(2.119) can be computed by choosing the points from $\pi(x)$,

$$F = \int_a^b dx \pi(x) \frac{f(x)}{\pi(x)} = \int_a^b dp \frac{f(x(p))}{\pi(x(p))}. \tag{2.123}$$

Using the above expression, in which $\pi(x)$ is derived from some function $p(x)$ with a change of integration variable, Eq.(2.119) can be expressed,

$$F \approx \frac{(b-a)}{N} \sum_{l}^{N} \frac{f(x(p_l))}{\pi(x(p_l))}. \tag{2.124}$$

The important observation is that the integration is more efficient now, however the error still decreases in the $\frac{1}{\sqrt{N}}$ ratio. The non-uniform distribution mentioned above can be obtained in many ways. The most popular method is the Metropolis algorithm, outlined in the following subsection.

2.7.3 Metropolis Monte Carlo

In the Metropolis algorithm [177] a random walk of points, spread according to a proper probability distribution, is introduced. We start with some starting point in configuration or phase space, then the next possible point is selected. A move to this new point is then accepted or refused by the Metropolis algorithm.

In order to derive the Metropolis algorithm let us focus on the probability density ρ at two points $\mathbf{X} = \{x_1, x_2, \cdots\}$ and $\mathbf{X}' = \{x_1', x_2', \cdots\}$ in the configuration space specified by the integration variables and limits. As before, one can define the probability distribution function $p(\mathbf{X})$ in this space. The probability density function $\pi(\mathbf{X})$ for continuous distribution yields,

$$\pi(\mathbf{X}) = \frac{dp(\mathbf{X})}{d\mathbf{X}} \geqslant 0. \tag{2.125}$$

We require that the mean number of samples at $\mathbf{X}$ and $\mathbf{X}'$, averaged over a large number of trial steps, fulfils the condition $\rho(\mathbf{X}) = \rho(\mathbf{X}')$. Having that, the transition probability $T(\mathbf{X} \to \mathbf{X}')$ for a trial move from $\mathbf{X}$ to $\mathbf{X}'$ can be found. The obvious condition is that in thermal equilibrium mean numbers of accepted transitions from $\mathbf{X}$ to $\mathbf{X}'$ is completely cancelled by the number of reverse moves,

$$\pi(\mathbf{X})(\mathbf{X} \to \mathbf{X}') = \pi(\mathbf{X}')(\mathbf{X}' \to \mathbf{X}). \tag{2.126}$$

This random walk through the phase space [178] allows us to sample any distribution resulting from detailed balance [179]. Eq.(2.126) can be separated into two parts, $T(\mathbf{X} \to \mathbf{X}') = t(\mathbf{X} \to \mathbf{X}')A(\mathbf{X} \to \mathbf{X}')$. With this separation, the probability of a trial move is given by $t(\mathbf{X} \to \mathbf{X}')$ and the probability of acceptance of that move is $A(\mathbf{X} \to \mathbf{X}')$. Knowing these two quantities one can write the acceptance probability,

$$A(\mathbf{X} \to \mathbf{X}') = \min\left|1, \frac{\pi(\mathbf{X}')t(\mathbf{X}' \to \mathbf{X})}{\pi(\mathbf{X})t(\mathbf{X} \to \mathbf{X}')}\right|. \tag{2.127}$$

The Metropolis Monte Carlo method is one of the most efficient techniques of sampling of configuration space. If one selects the probability of a trial move to be the symmetric matrix $t(\mathbf{X} \to \mathbf{X}') = t(\mathbf{X}' \to \mathbf{X})$, then the acceptance probability yields,

$$A(\mathbf{X} \to \mathbf{X}') = \begin{cases} \frac{\pi(\mathbf{X}')}{\pi(\mathbf{X})} & \text{for } \pi(\mathbf{X}) < \pi(\mathbf{X}') \\ 1 & \text{for } \pi(\mathbf{X}) \geqslant \pi(\mathbf{X}'). \end{cases} \tag{2.128}$$

Therefore in the Metropolis algorithm, the probability of acceptance of a trial displacement can be given in terms of the ratio of the probability distribution function at each point of configuration space,

$$A(\mathbf{X} \to \mathbf{X}') = \min \left| 1, \frac{\pi(\mathbf{X}')}{\pi(\mathbf{X})} \right|. \tag{2.129}$$

We can notice that the probability depends only on the previous value, therefore we deal with a Markov process. Once the acceptance A is obtained, we can sample the path by making a set of displacements according to T. Acceptance of these moves depends on A.

2.7.4 Single moves

The simplest realisation of the Metropolis algorithm is a single slice move, in which only one bead of the path is moved at the time. This can be imagined as a randomly selected bead moved some random distance from its initial position. The new configuration is checked against the Metropolis acceptance condition and accepted if the move lowers the energy of the paths, or is refused otherwise,

$$\mathbf{X_k^{new}} = \begin{cases} \mathbf{X_k^{trial}}, & \text{for } \frac{\rho(\mathbf{X}_l,\mathbf{X'}_k;\tau)\rho(\mathbf{X'}_k,\mathbf{X}_m;\tau)}{\rho(\mathbf{X}_l,\mathbf{X}_k;\tau)\rho(\mathbf{X}_k,\mathbf{X}_m;\tau)} \geqslant \text{random number} \\ \mathbf{X}_k, & \text{otherwise.} \end{cases} \tag{2.130}$$

The freshly accepted coordinates become the new starting point and the process is repeated. We create a random walk through the phase space until thermal equilibrium for the ground state is reached. This is a Markov chain, as every next move depends on the previous coordinate of the bead.

2.7.5 Free particle sampling

In the Metropolis Monte Carlo simulations, any transition probability is permitted as long as the ensemble averages equals the time averages, or in the other words as long as it is ergodic. The situation is a little different for the free particle. We can find the acceptance probability corresponding to the single bead displacement of a free

particle polymer chain in the absence of external confinement [132],

$$A(\mathbf{X}_k \to \mathbf{X}_l) = \min\left[1, \frac{T(\mathbf{X}_k \to \mathbf{X}_l)}{T(\mathbf{X}_l \to \mathbf{X}_k)} \exp\{-\Delta\mathbf{S}_{kinetic}\}\right], \tag{2.131}$$

where the change of kinetic action $\Delta\mathbf{S}_{kinetic}$ is defined,

$$\begin{aligned}\Delta\mathbf{S}_{kinetic} &= \frac{m}{2\hbar^2\tau}\left[(\mathbf{X}_{l-1} - \mathbf{X}_m)^2 + (\mathbf{X}_m - \mathbf{X}_{l+1})^2 - (\mathbf{X}_{l-1} - \mathbf{X}_l)^2 - (\mathbf{X}_l - \mathbf{X}_{l+1})^2\right] \\ &= \frac{m}{\hbar^2\tau}\left[(\mathbf{X}_m - \overline{\mathbf{X}}_l)^2 - (\mathbf{X}_m - \overline{\mathbf{X}}_l)^2\right].\end{aligned} \tag{2.132}$$

Here $\overline{\mathbf{X}}_l = \frac{\mathbf{X}_{l+1}+\mathbf{X}_l}{2}$. Using Eq.(2.132), one can observe that the optimal transition probability for a free particle is the one that precisely cancels with this difference [132],

$$A(\mathbf{X}_l \to \mathbf{X}_m) = \min\left[1, \frac{\exp\left\{\frac{m}{\hbar^2\tau}\left(\mathbf{X}_l - \overline{\mathbf{X}}_l\right)^2\right\}\exp\left\{\frac{m}{\hbar^2\tau}\left(\mathbf{X}_m - \overline{\mathbf{X}}_l\right)^2\right\}}{\exp\left\{\frac{m}{\hbar^2\tau}\left(\mathbf{X}_m - \overline{\mathbf{X}}_l\right)^2\right\}\exp\left\{\frac{m}{\hbar^2\tau}\left(\mathbf{X}_l - \overline{\mathbf{X}}_l\right)^2\right\}}\right]. \tag{2.133}$$

It is apparent that in the neighbourhood of $\overline{\mathbf{X}}_l$ the transition probability follows a Gaussian distribution. In the Monte Carlo language this means that for a set of non-interacting particles all moves resulting from the above distribution are accepted. The main advantages of the free particle sampling are the high efficiency of simulations and a speed up of the convergence.

2.7.6 Displacement moves

In most of our simulations we deal with systems containing interacting particles in very complex confinements, like multiple quantum rings or coupled dots. The movements of beads in these structures, which are characterised by the high potential difference between minima, usually have a low acceptance probability which slows convergence and decreases efficiency significantly. To overcome this problems we introduce an additional type of move which will sample the troublesome regions more frequently, improving the acceptance ratio and therefore speeding up the convergence. In the displacement moves method instead of moving a single bead we displace whole paths in the configuration space. As the states of the kinetic links remain unchanged we do not adjust the relative positions between the beads and so the only action we are

required to compute is the difference in potential action between the old and new positions of the polymer chain.

2.7.7 Multilevel sampling

Detailed study of complex potentials and low temperature simulations requires a much bigger number of beads in order to sample the system more accurately. In this case sampling the path phase space with only single moves affects the efficiency and slows down the computation time meaningfully, as the average move is of the order $\sqrt{\hbar^2\tau/2m}$ and depends on time.

One of the methods of dealing with this problem is the introduction of multi-level moves. A significant increase in efficiency and convergence time is obtained by moving many slices at the same time. We achieve this by separating the path into $k+1$ levels containing $j = 2^k - 1$ beads. To illustrate this process let us consider the case of $k = 3$. This gives us 4 levels and $j = 5$, $\{\mathbf{X}_{l+1} \cdots \mathbf{X}_{f-1}\}$ beads to be sampled, as the coordinates of the 1^{st}, $\mathbf{X}_l$ and 7^{th}, $\mathbf{X}_f$ beads remain fixed in the space. In the first step we move the $\mathbf{X}_{l+3}$ bead, which in this example is the middle one. The move of the bead in the highest level is accepted with the probability,

$$A(\mathbf{X}_l \to \mathbf{X}_m) = \min\left[1, \frac{T(\mathbf{X}_m \to \mathbf{X}_l)P(\mathbf{X}_m)}{T(\mathbf{X}_l \to \mathbf{X}_m)P(\mathbf{X}_l)}\right] \tag{2.134}$$

At this point one can use free particle sampling, as P and T are the density matrices with the larger time step, $2^k\tau$. The process starts again if the move is not accepted. Acceptance of the trial move leads to moving lower level beads. This process lasts as long as beads in all levels are moved and detailed balance is maintained.

2.8 Path integral methods for Fermions

Path integral Monte Carlo simulations of bosons, e.g. excitons or liquid ^{4}He, are highly efficient. This is because Boltzmann weights for such a system are strictly positive for all path configurations and can be easily mapped into a classical partition function of a chain of polymers. On the other hand for fermions there are configurations resulting in negative weights which cannot be mapped.

In the following section the origins of the fermion sign problem will be outlined and compared to the Bose distribution and a practical method of dealing with this difficulty in PI-QMC simulations will be given.

2.8.1 Fermionic sign problem

In Section (2.3.1) the operator expressions Eq.(2.43) and Eq.(2.44) for a quantum system with Hamilton operator $\hat{\mathscr{H}}$ were defined. These operators expression need to be evaluated in order to compute the thermal averages of the observable $\mathscr{O}$. The problem scales exponentially, however Monte Carlo simulations allow us to map the quantum picture to a classical one. The evaluation of partition function $\mathscr{Z}$, Eq.(2.44) can be done with help of a Taylor expansion [180],

$$\begin{aligned}\mathscr{Z} &= Tr \exp\left\{-\beta\hat{\mathscr{H}}\right\} = \sum_{l=0}^{\infty} \frac{(-\beta)^l}{l!} Tr\hat{\mathscr{H}}^l \\ &= \sum_{l=0}^{\infty} \sum_{\mathbf{i}_1,\cdots,\mathbf{i}_l} \frac{(-\beta)^l}{l!} \left\langle i_1 \left| \hat{\mathscr{H}} \right| i_2 \right\rangle \left\langle i_2 \left| \hat{\mathscr{H}} \right| i_3 \right\rangle \cdots \left\langle i_l \left| \hat{\mathscr{H}} \right| i_1 \right\rangle \\ &\equiv \sum_{l=0}^{\infty} \sum_{i_1,\cdots,i_l} p(i_1,\cdots,i_l) \equiv \sum_k p(k).\end{aligned} \tag{2.135}$$

In the above expression l is the order of expansion and $\{|i_l\rangle\}$ form a complete basis set. One can state configurations in the form of the sequences $k = (i_1, \cdots, i_l)$ of l basis states [181]. These configurations then contribute with the weight $p(k)$, defined as the corresponding product of the matrix elements of $\hat{\mathscr{H}}$ and $\frac{(-\beta)^l}{l!}$ [181]. The same method can by applied to Eq.(2.43), which yields the classical-like form,

$$\langle\hat{\mathscr{O}}\rangle = \mathscr{Z}^{-1} Tr\left[\mathscr{O}\exp\left\{-\beta\hat{\mathscr{H}}\right\}\right] = \mathscr{Z}^{-1}\sum_k A(k)p(k). \tag{2.136}$$

There are two possible outcomes: $p(k) > 0$ and $p(k) < 0$. In the first case we deal with system of bosons, therefore we can map it to a classical chain of polymers. The $p(k) < 0$ outcome is characteristic of a fermionic system, governed by the Pauli exclusion principle, in which two fermions were exchanged.

It is common practice to sample such a system with respect to the Bose statistics, and instead of negative weights use the absolute values, $|p(k)|$. Then the sign $s(k) \equiv$

sign $p(k)$ can be passed to the quantity one is going to sample:

$$\langle\hat{\mathscr{O}}\rangle = \frac{\sum_k A(k)p(k)}{\sum_k p(k)} = \frac{\frac{\sum_k A(k)s(k)|p(k)|}{\sum_k |p(k)|}}{\frac{\sum_k s(k)|p(k)|}{\sum_k |p(k)|}} \equiv \frac{\langle As\rangle'}{\langle s\rangle'}. \tag{2.137}$$

Eq.(2.137) allows one to perform the Monte Carlo simulations, however the price for that is an exponential increase in the signal/noise ratio with the growing number of particles and $1/k_BT$. This can be clearly demonstrated by considering the mean value of the sign $\langle s\rangle = \frac{\sum_k p(k)}{\sum_k |p(k)|}$, in which numerator is a fermionic partition function and the denominator is a bosonic partition function used for sampling. It was demonstrated in Sect.(2.3.1), that partition functions are exponentials of the corresponding free energy, therefore the above mean value is a exponential of the difference $\Delta E_{ratio} = E_F - E_B$ of these free energy densities, $\langle s\rangle = \frac{\sum_k p(k)}{\sum_k |p(k)|} = \exp\{-\beta N \Delta E_{ratio}\}$ [181]. If one estimates the relative error in this method of sampling:

$$\frac{\Delta s}{\langle s\rangle} = \frac{1}{\langle s\rangle}\sqrt{\frac{\langle s^2\rangle - \langle s\rangle^2}{M}} = \frac{\sqrt{1-\langle s\rangle^2}}{\langle s\rangle\sqrt{M}} \sim \frac{\exp\{\beta N \Delta E_{ratio}\}}{\sqrt{M}}, \tag{2.138}$$

it become obvious that using this approach the inefficiency of fermionic simulations grows exponentially.

2.8.2 Fixed-node approximation

Many-body interacting fermions at finite temperature are in the centre of interest of condensed matter physics and chemistry, however from a computational point of view this is a rather difficult problem. In order to overcome the lack of exact techniques, which properly scale with the number of particles and operate low temperature, we frequently turn to approximations. One of the most accurate is the fixed-node approximation [182, 183], which can be efficiently implemented into the PI-QMC code method.

In order to derive the fixed-node approximation we start by rewriting the many-body density matrix for an imaginary-time path integral, Eq.(2.74) in a slightly different form,

$$\rho_F(R,R';\beta) = \Omega\sum_{\mathscr{P}}(-1)^{\mathscr{P}}\int_{\mathscr{P}R'}^{R} dR \exp\left\{-\int_0^\beta dt\left[\frac{1}{4\Lambda}\left(\frac{dR}{dt}\right)^2 + V(R(t))\right]\right\}, \tag{2.139}$$

where Ω is a constant and $V(R(t))$ is a potential. The density matrix for fermions, Eq(2.139) is a solution to the time dependent Schrödinger equation:

$$\frac{d\rho_F(R,R';\tau)}{d\tau} = \left[\Lambda \sum_i \nabla_i^2 + V(R)\right] \rho_F(R,R';\tau), \tag{2.140}$$

with the initial condition [182],

$$\rho_F(R,R';0) = \sum_{\mathscr{P}} \frac{(-1)^{\mathscr{P}}}{N!} \delta(\mathscr{P}R - R). \tag{2.141}$$

The idea behind this approximation is rather simple: one restricts a set of solutions that the program can accept only to positive contributions, which then can be treated in the frame of the Bose statistics, free of negative signs.
If we are interested in a wave-function of a system, then the trial wave-function is considered in a form of a Slater determinant, and the fixed-node action computes the minimum energy many-body wave-function that has the same nodal surface as the input one. These fixed-node solutions can be further improved by using more accurate trial wave-functions containing, for example, back-flow.

There are many realisations of the fixed-node method. The ground-state fixed-node quantum Monte Carlo simulations are based on restriction of the Hilbert space only to the wave-functions which share nodes with a trial wave-function. As this is variational approximation, energies computed this way are higher compared to exact energies obtained from exact ground state nodes. Any approximation is a trade of one quantity for another. In this case one gets a very good deal as approximately 90% of the correlation energy is recovered. Therefore, this makes fixed-node calculations excellent techniques for *ab initio* simulations of solids and molecules [184–186].

2.8.2.1 Restricted path integrals

The most straight forward implementation of the fixed-node approximation is by restricting the path to only particular positive contributions. This can be done by the introduction of a reference point R^* on the path that characterises the nodes of $\rho_F(R,R^*;t) = 0$. Therefore to enforce the *node-avoiding* path, the algorithm is allowed to accept only the solutions for which $\rho_F(R,R^*;t) \neq 0$ for $0 < t \leqslant \beta$.

Restricting the integral:

$$\rho_F(R^*, R_\beta; \beta) = \int dR_0 \rho_F(R_0, R^*; 0) \oint_{R_{0\beta} \in \mathscr{X}(R^*)} dR_t \exp\{-\frac{1}{\hbar}\mathcal{S}[R_t]\} \tag{2.142}$$

$$= \frac{1}{\mathscr{N}!} \sum_{\mathscr{P}} (-1)^{\mathscr{P}} \oint_{\mathscr{P}R^*_\beta \in \mathscr{X}(R^*)} dR_t \exp\{-\frac{1}{\hbar}\mathcal{S}[R_t]\}, \tag{2.143}$$

(where $\mathscr{X}(R^*)$ is a nodal surface with respect to R^*) results in the situation that the path does not touch or cross the node. Permutation $\mathscr{P}$ applied to R^* does not affect nodal restriction $\mathscr{X}(R^*) \equiv \mathscr{X}(\mathscr{P}R^*)$, as $\rho_F(R, R^*; \beta) = 0$, which yields $\rho_F(R, \mathscr{P}R^*; \beta) = 0$. This latter property leads to an equivalent form of Eq.(2.143),

$$\rho_F(R^*, R_\beta; \beta) = \frac{1}{\mathscr{N}!} \sum_{\mathscr{P}} (-1)^{\mathscr{P}} \oint_{\mathscr{P}R^*_\beta \in \mathscr{X}(\mathscr{P}R^*)} dR_t \exp\{-\frac{1}{\hbar}\mathcal{S}[R_t]\}, \tag{2.144}$$

$$= \frac{1}{\mathscr{N}!} \sum_{\mathscr{P}} (-1)^{\mathscr{P}} \oint_{R^* \to \mathscr{P}R_\beta \in \mathscr{X}(R^*)} dR_t \exp\{-\frac{1}{\hbar}\mathcal{S}[R_t]\}. \tag{2.145}$$

In the above expression the entire path was permuted by $\mathscr{P}^{-1}$, and so the summation index changed, knowing that $\mathscr{P}^{-1}$ and $\mathscr{P}$ have the same sign.

Eq.(2.145) can be simplified even more if the diagonal elements of $\rho_F(R, R^*; 0)$ are considered. This is a consequence of the odd permutations, which always cross a node since $\rho_F(R^*, R^*; 0) = -\rho_F(R^*, \mathscr{P}_{odd}R^*; 0)$. Then Eq.(2.145) yields,

$$\rho_F(R, R; \beta) = \frac{1}{\mathscr{N}!} \sum_{\mathscr{P}_{even}} \oint_{R \to \mathscr{P}R \in \mathscr{X}(R^*)} dR_t \exp\{-\frac{1}{\hbar}\mathcal{S}[R_t]\}. \tag{2.146}$$

The situation is more complicated if off-diagonal density matrix elements are examined. In this case odd permutations lead to negative contributions resulting in the open path, which are out of the scope of this thesis.The restricted path integral method is exact if the exact fermion density matrix is used as the restriction, a detailed proof of which can be found in [187].

2.8.3 Trial density matrix

The exact fermionic density matrix guarantees the exact results, however the exact matrices are known only for a few systems. In every day simulations trial density matrices $\rho_T(x, \mathbf{R}'; \beta)$, calculated from single particle density matrices by a Slater

determinant, are used,

$$\rho_T(R,R';\beta) = \begin{vmatrix} \rho_1(r_1,r'_1;\beta) & \cdots & \rho_1(r_N,r'_1;\beta) \\ \cdots & \cdots & \cdots \\ \rho_1(r_1,r'_N;\beta) & \cdots & \rho_1(r_N,r'_N;\beta) \end{vmatrix}, \tag{2.147}$$

We outline this method on the example of a system of two fermions which have spin 1/2. If we neglect magnetic fields, spin-orbit coupling and relativistic effects then the Hamiltonian of the system is spin independent. Therefore the magnetisation of the system is described by a good quantum number m, as the spin component in the $\hat{z}$ direction S_z can be quantised. If one consider ensembles with fixed magnetisation m, then the density matrix is a product of spin up and spin down density matrices,

$$\rho_T(R,R';\beta) = \left|\left|\rho_1(r_i,r'_j)\right|\right|_{i,j\in\uparrow} \left|\left|\rho_1(r_i,r'_j)\right|\right|_{i,j\in\downarrow}. \tag{2.148}$$

Complete antisymmetrization and then projection of magnetisation m yields only the states, which again can be written as Slater determinants, however with relabelled particles. At this point we focus only on the unpolarised systems with $m = 0$ and $N_\uparrow = N_\downarrow$. Constraining the nodes indicates the positive sign of each determinant all along the paths, as situations when the signs are changed at the same time do not contribute.

In our simulations different extensions of this type of nodes are used. This is necessary to properly treat the pairing mechanisms responsible for forming for example, excitons, trions and biexcitons in semiconductors at finite temperature.

In our studies the above trial density matrix was widely applied using, among other things, a: free particle (FP) nodes, simple harmonic oscillator (SHO) nodes and ground state (GS) nodes to simulations of interacting electron and electron-hole pairs in an atomistic model of semiconductor nano-structures.

In our model the density matrix of a single free particle is used. It is derived from exact eigenfunctions of the Hamiltonian, which are given by the plane waves,

$$\Psi_n(\mathbf{R}) = \frac{1}{\sqrt{V}} \exp\{-i\mathbf{k_n}\cdot\mathbf{R}\}, \tag{2.149}$$

where k-vector $\mathbf{k_n} = 2\pi\mathbf{n}L^{-1}$ and $\mathbf{n}$ is a N-dimensional integer vector. If one considers a periodically repeated box of size L with a volume $V = L^N$, then the density matrix

for a FP is given by,

$$\rho(R, \mathbf{R}'; \beta) = \frac{1}{V} \sum_{\mathbf{n}} \exp\{-\beta\Lambda {\mathbf{k_n}}^2 + i\mathbf{k_n} \cdot (\mathbf{R} - \mathbf{R}')\} \tag{2.150}$$

$$= (4\pi\Lambda\beta)^{-\frac{N}{2}} \sum_{\mathbf{n}} \exp\left\{-\frac{(\mathbf{R} - \mathbf{R}' - \mathbf{nL})^2}{4\Lambda\beta}\right\} \tag{2.151}$$

$$\approx (4\pi\Lambda\beta)^{-\frac{N}{2}} \exp\left\{-\frac{(\mathbf{R} - \mathbf{R}')^2}{4\Lambda\beta}\right\} \quad \text{if} \quad \Lambda\beta \ll L^2. \tag{2.152}$$

Calculated this way, $\rho(\mathbf{R}, \mathbf{R}'; \beta)$, Eq.(2.151) is then used in Eq.(2.148). If the high temperature case is considered then the nodal surface for the interacting system approaches that for a FP. Additionally for a low density system the exchange effects can be safely neglected as enforcement of the nodes doesn't affect the paths significantly, therefore its exact shape is not important. The FP nodes become exact in the limit of high density due to the domination of the kinetic energy component of the system over the potential one. On the other hand, high density and high degeneracy limits of the interacting system may have a strong impact on the fermionic density matrix.

2.8.4 Further improvement of fixed-node approximation - the double reference point

When the temperature of the system increases, the FP nodes approximation converges to the exact fermionic nodal surface. The introduction of an additional reference point can help enforce the nodes by taking the sign of $\rho_T(R, R^*; \beta)$ instead of $\rho_T(R, R^*; 2\beta)$.

The convolution function allows us to represent $\rho(R, R^*; 2\beta)$ for a fermionic system in terms of $\rho(R, R^*; \beta)$,

$$\rho_F(R_\beta, R'_\beta; 2\beta) = \int dR^* \rho_F(R_\beta, R^*; \beta)\rho_F(R'_\beta, R^*; \beta). \tag{2.153}$$

If we imagine one path running from R^* to R_β and the second from R^* to R'_β, then Eq.(2.153) can be understood as an integer over all possible pairs of paths. The same reference point R^* can be used in the computation of the restricted path integral for both fermionic density matrices. To do this, one needs to set time to zero at R^*, then the time must increase towards R'_β and R_β up to β. If the explicit form of fermionic

density matrix is use, as defined in Eq.(2.143), then Eq.(2.153) yields,

$$\rho_F(R_\beta, R'_\beta; 2\beta) = (\mathscr{N}!)^{-2} \int dR^* \sum_{\mathscr{P}\mathscr{P}'} (-1)^{\mathscr{P}+\mathscr{P}'} \oint_{\mathscr{P}R^*_\beta \in \mathscr{X}(R^*)} dR_t \exp\{-\frac{1}{\hbar}\mathcal{S}[R_t]\} \times \oint_{\mathscr{P}'R^* \to R'_\beta \in \mathscr{X}(R^*)} dR_t \exp\{-\frac{1}{\hbar}\mathcal{S}[R_t]\} \tag{2.154}$$

$$= (\mathscr{N}!)^{-2} \sum_{\mathscr{P}\mathscr{P}'} (-1)^{\mathscr{P}+\mathscr{P}'} \int dR^* \oint_{R^* \to \mathscr{P}R_\beta \in \mathscr{X}(R^*)} dR_t \exp\{-\frac{1}{\hbar}\mathcal{S}[R_t]\} \times \oint_{R^* \to \mathscr{P}'\mathbf{R}'_\beta \in \mathscr{X}(R^*)} dR_t \exp\{-\frac{1}{\hbar}\mathcal{S}[R_t]\} \tag{2.155}$$

$$= (\mathscr{N}!)^{-1} \sum_{\mathscr{P}} (-1)^{\mathscr{P}} \int dR^* \oint_{R^*_\beta \in \mathscr{X}(R^*)} dR_t \exp\{-\frac{1}{\hbar}\mathcal{S}[R_t]\} \times \oint_{R^* \to \mathscr{P}R'_\beta \in \mathscr{X}(R^*)} dR_t \exp\{-\frac{1}{\hbar}\mathcal{S}[R_t]\}. \tag{2.156}$$

In the above derivation, Eq.(2.145) was used. It was also noticed that the above path integral can be calculated as a pair of independent factors, therefore we were able to replace the double sum over the permutations with a single one. Eq.(2.156) can be read as a single path integral of the form $\rho_F(R_\beta, R'_\beta; 2\beta)$. If we set the reference point R^* in the middle of the path, then the path starts at R_β and ends at $\mathscr{P}R'_\beta$ going though R^*. We check the nodes by selecting the time argument in the following way,

$$t_{reference} = \begin{cases} t, & \text{for} \quad 0 \leqslant t \leqslant \frac{\beta}{2} \\ \beta - t, & \text{for} \quad \frac{\beta}{2} \leqslant t \leqslant \beta. \end{cases} \tag{2.157}$$

From Eq.(2.157) it can be seen that one must compute the trial density matrix only up to $\beta/2$. It is important to notice that in the above, the time doubling method requires an additional treatment of the sign problem after every complete iteration step.

2.8.5 Nodes for two identical fermions

In this section we analyse the restricted path integral technique in detail and prove that the solution is exact if the nodes are known. We focus our attention on two

identical, non-interacting fermions for which the exact nodes are defined as,

$$\rho(\mathbf{r}_1, \mathbf{r}_2, \mathbf{r}_1^*, \mathbf{r}_2^*; \beta) \equiv \begin{vmatrix} \rho_1(\mathbf{r}_1, \mathbf{r}_1^*; \beta) & \rho_1(\mathbf{r}_1, \mathbf{r}_2^*; \beta) \\ \rho_1(\mathbf{r}_2, \mathbf{r}_1^*; \beta) & \rho_1(\mathbf{r}_2, \mathbf{r}_2^*; \beta) \end{vmatrix} = 0, \tag{2.158}$$

where the free particle density matrix defined in Eq.(2.152) is used. Eq.(2.158) yields the solution of the form,

$$(\mathbf{r}_1 - \mathbf{r}_2) \cdot (\mathbf{r}_1^* - \mathbf{r}_2^*) = 0. \tag{2.159}$$

If one introduces the relative coordinates $\mathbf{r} = \mathbf{r}_1 - \mathbf{r}_2$ and relative reference point $\mathbf{r}^* = \mathbf{r}_1^* - \mathbf{r}_2^*$, then the node is a plane at $\mathbf{r}$=0, which is perpendicular to the relative reference vector. In this section only closed paths ending in the reference point $\mathbf{r}(\beta) = \mathbf{r}^*$ will be considered. We have two possibilities in the case of permutations, as paths have to start at $\mathbf{r}^*$ or $-\mathbf{r}^*$. There are three possible path configurations:

1. The path avoids the node ⇒ begins and ends at $\mathbf{r}^*$, Fig. 2.5(a).
2. Path begins and ends at $\mathbf{r}^*$, crossing the node an even number of times, Fig. 2.5(b).
3. Path crosses the node an odd number of times ⇒ starts at $-\mathbf{r}^*$, Fig. 2.5(c).

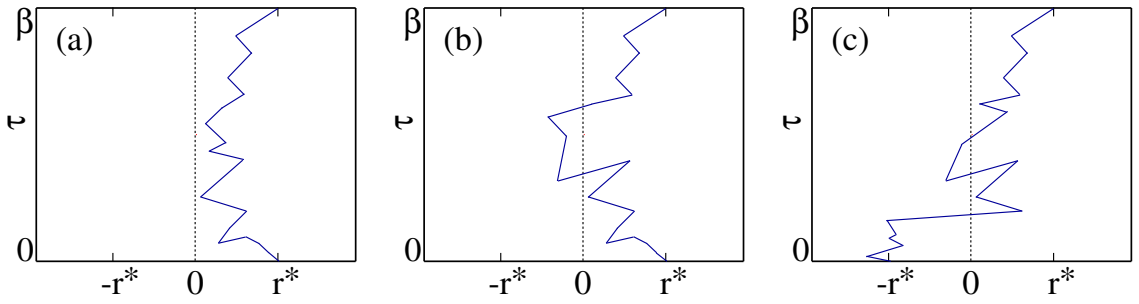

Figure 2.5: The nodal constraint for paths. (a) node avoiding path, (b) even number of node $\mathbf{r} = 0$ crossing and (c) involving permutations, odd number of nodes crossing require that path start at $\mathbf{r}(0)$=$-\mathbf{r}^*$.

Different types of paths have distinct physical meanings. If a system of distinguishable particles is considered there is no need for the nodal surface as permutations cannot take place, this corresponds to paths in Fig. 2.5(a) and Fig. 2.5(b). If a bosonic system is considered, we do not have to worry about minus signs and nodes as we sum over all permutations. This changes if a fermionic system comes into play. In this case the restricted path integral technique or direct fermion methods can be

used on an equal basis, as long as the exact nodes are applied. The main difference between these approaches is that in the direct method the path is not restricted, instead all positive and negative permutations are taken into account and summed up including those from Fig. 2.5(c). Restricted path integrals rely on the nodal structure which basically discards any permutations appearing in the two particle system and potentially leading to the negative results. In this case only the situation depicted in Fig. 2.5(a) is possible as Fig. 2.5(b) and Fig. 2.5(c) cancel each other.

2.8.6 Nodal action

The restricted path integral method clearly assumes that paths do not cross the nodes, which form infinite potential barriers and also the length of the path is reasonably short. This is done by checking the sign of the determinant at each time slice and discarding the configurations for which one is negative. The accuracy of this method depends on the number of slices used in the simulation. If a greater number of slices is introduced we can find that previously accepted paths are now rejected due to crossing and recrossing the node within a much bigger slice, which wasn't detected earlier and resulted in the errors. We fix this problem by introducing the nodal action U_N in our PI-QMC simulation.

In order to derive the nodal action U_N we consider one more time the exact solution to the problem introduced in Section 2.6 and described by Eq.(2.116), together with the nodal constraint discussed in Subsection 2.8.5. For the fermionic system the density matrix yields,

$$\rho(\mathbf{r}, \mathbf{r}^*; \beta) = \rho_D(\mathbf{r}, \mathbf{r}^*; \beta) - \rho_D(-\mathbf{r}, \mathbf{r}^*; \beta). \tag{2.160}$$

One can note that if $\mathbf{r} = \mathbf{r}^*$, then the first term in Eq.(2.160) is a diagonal density matrix element and as such, is bigger than the second term. Using Fig. 2.5, the first matrix corresponds to the situations in Fig. 2.5(a) and (b) and the second one in Fig. 2.5(c). From Eq.(2.160) one can see that the second term can be considered as a mirror image of a particle with a minus sign with respect to the nodal line $\mathbf{r} = 0$. It is clear that matrix $\rho_D(\mathbf{r}, \mathbf{r}^*; \beta)$ and its mirror image $\rho_D(-\mathbf{r}, \mathbf{r}^*; \beta)$ fulfil the Bloch equation, and if summed up, return zero at the node.

The most important parameter required to derive the nodal action is the charge image separation from the nodal line. If the small value of τ is considered we can

assume the nodal line between two time slices is flat. Then the action difference for the system with and without a node reads,

$$\Delta \exp\{-U_N^i\} = \exp\{-(U_{node}^i - U_{free}^i)\} = \frac{\rho(\mathbf{r}_{i-1}, \mathbf{r}_i; \tau) - \rho(\mathbf{r}_{i-1}, \mathbf{r}_i - 2\mathbf{d}_i; \tau)}{\rho(\mathbf{r}_{i-1}, \mathbf{r}_i; \tau)}, \quad (2.161)$$

where d_i is a separation from the node at time slice i with the mirror image at point $\mathbf{r}_i - 2\mathbf{d}_i$. The nodal action can be reformulated in terms of the nodal separation at the two slices with help of the free particle ρ_{free},

$$\exp\{-U_N^i\} = 1 - \exp\left\{-d_i d_{i-1} \Lambda\tau\right\}. \quad (2.162)$$

Using the Newton-Raphson method the nodal separation can be approximated,

$$d_i = \frac{\rho_T(\mathbf{R}_i, \mathbf{R}^*; \beta)}{|\nabla_{\mathbf{R}} \rho_T(\mathbf{R}_i, \mathbf{R}^*; \beta)|}. \quad (2.163)$$

One can simplify the above expression using a matrix form of ρ_T, namely $\rho_{ij} = \rho_1(r_i, r_j^*; \beta)$ and its derivatives $||\rho_{ij}||'$,

$$||\rho_{ij}||' = ||\rho_{ij}||^2 \sum_{ij} \rho'_{ij} \rho_{ji}^{-1}, \quad (2.164)$$

then the inverse-distance-squared to the node reads,

$$\frac{1}{d^2} = \sum_i \left(\sum_j (\nabla_{x_i} \rho_{ij})^2 \rho_{ji}^{-1} \right)^2. \quad (2.165)$$

The internal energy of a system is also affected due to an additional term in the nodal action,

$$E_N = -\frac{dU_N}{d\tau} = -\frac{1}{1 - \exp\{-y\}} \frac{dy}{d\tau} \quad (2.166)$$

where $y \equiv \left(\frac{d_{i-1} d_i}{\Lambda\tau} \right)$. Then $-dy/d\tau$ can by estimated from,

$$-\frac{dy}{d\tau} = \frac{y}{\tau} - \frac{y d d_i}{d_i d\tau} - \frac{y d d_{i-1}}{d_{i-1} d\tau} \approx \frac{y}{\tau}. \quad (2.167)$$

Calculation of the derivatives of the distances to nearest node d_i introduces additional numerical effort, however in Eq.(2.167) the change in the separation between the mirror image and the node with imaginary time is omitted, simplifying simulations.

2.8.7 Excitonic recombination rates in the frame of two-band effective mass model

In the following, the square of the matrix element present in the equation for the recombination rate will be derived in the path integral form. We then depart from the electron-hole recombination in the effective mass model using a path integral formalism and we will end up showing that the recombination rate is a ratio of the thermal trace and radiative configurations of the electron-hole pairs [188] (Fig. 2.6). The two-band effective mass model Hamiltonian is given by

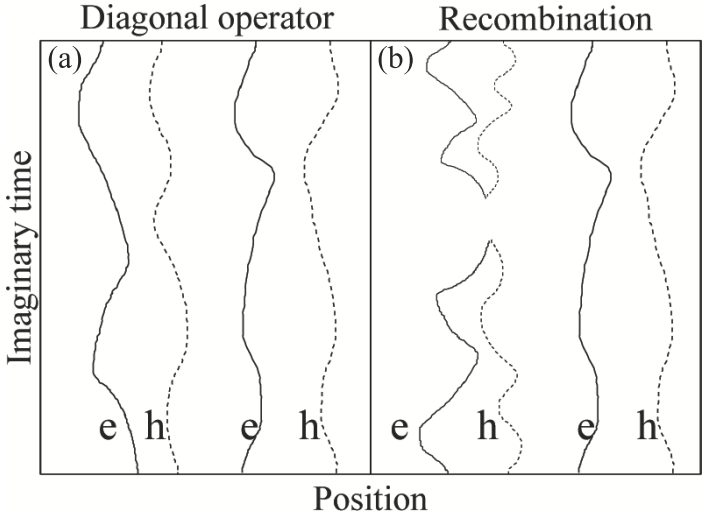

Figure 2.6: Visualisation of path-integral calculated for bi-exciton recombination rates Ref.[188]. The recombination rates are expressed in the form of a ratio of path integrals with (a) diagonal and (b) radiating constraints, based on Eq. (2.174).

$$\hat{\mathscr{H}} = \sum_{n_e} \left(\frac{\hbar^2}{2m_e^*} \nabla^2_{\mathbf{r}_e} + V_e(\mathbf{r}_e) \right) + \sum_{n_h} \left(\frac{\hbar^2}{2m_h^*} \nabla^2_{\mathbf{r}_h} + V_h(\mathbf{r}_h) \right) + \frac{1}{2} \sum_{i \neq j} \frac{q_i q_j}{\epsilon r_{ij}}, \qquad (2.168)$$

where V_e and V_h are the confining potentials for the electron and hole respectively with anisotropic effective mass for the hole. As it was pointed in the previous chapters of this thesis the PI-QMC gives us tools to obtain the thermal density matrix directly from Eq.(2.168) without using single-particle or variational wave functions. Our approach gives us the exact solution which is free of the problems involved with finding a basis set or variational solution.

The recombination rate of an exciton which generates a photon is the sum of the rates of all possible recombination processes. Let's define the state Φ_i^α which is made of N electron-hole pairs. This state decays into the Φ_l^α state with $N-1$

excitons. The exciton recombines generating a photon with energy $\hbar\omega$, momentum $\hbar\mathbf{k}$ and polarisation $\hat{\lambda}$ in the medium with refractive index approximately $\sqrt{\epsilon}$ with the rate given by [188]

$$\frac{d\Gamma^{\alpha}_{\mathbf{k}\hat{\lambda}}}{d\Omega} = \frac{n\omega e^2}{hc^3} \left| \left\langle \Phi^{\alpha}_{l} \left| \mathbf{j}_{\mathbf{k}\hat{\lambda}} \cdot \hat{\lambda} \right| \Phi^{\alpha}_{i} \right\rangle \right|^2 , \tag{2.169}$$

which results from Fermi's golden rule. Typically, photons carry less energy than the energy difference between conduction and valence band ($\approx 1 - 3\,\mathrm{eV}$), however the wavelength is usually much longer than the structure size ($\approx 5 - 50\,\mathrm{nm}$) [188]. This allows us to assume the $\mathbf{k} \to 0$ in the current operator $\mathbf{j}_{\mathbf{k}\to 0,\hat{\lambda}}$. In the semiconductor structures the recombination rate is usually estimated using an envelope function. In this method the single-particle wave functions are approximated as a product of envelope and Bloch functions. Using the Bloch function in the form $\phi(\mathbf{r}) = \psi(\mathbf{r})u(\mathbf{r})$ the current operator can be represented in a form of delta function on an envelope and current operator $\mathbf{j} = \frac{\mathbf{p}}{m}$ on Bloch function. Now the Kane parameter,

$$E_{\mathbf{p}} = 2 \left| \langle c.b. \left| \mathbf{p} \right| v.b. \rangle \right|^2 , \tag{2.170}$$

which describes the momentum matrix element between the Bloch function for conduction (cb) and valence (vb) bands can be introduced. Knowing that the most important transitions takes place in the energy range significantly smaller than the energy band gap which is given by the Coulomb interactions, the standard assumption $\hbar\omega \approx E_{gap}$ can be justified. With this approximation, the recombination rate due to α transition within the envelope function framework can be expressed as [188]

$$\Gamma^{\alpha} = \frac{2nE_{gap}E_{\mathbf{p}}e^2}{3\hbar^2 c^3 m} \left| p^{\alpha}_{N} \right|^2 , \tag{2.171}$$

where $^{\alpha}_{N}$ is the point contact matrix element defined as

$$p^{\alpha}_{N} = \int \psi^{\alpha^*}_{N}(\mathbf{R}_N)\psi^{\alpha}_{N-1}(\mathbf{R}_{N-1})\delta^3(\mathbf{r}_{e,N} - \mathbf{r}_{h,N})d^{3N}\mathbf{R}_N . \tag{2.172}$$

In Eq.(2.172) the integral estimates the overlap between initial and final envelope functions.

2.8.8 The recombination rates in the Feynman path integral formulation

Carefully derived in the above section, Eqs.(2.171) and (2.172) are rather difficult to use in a process of the estimation of recombination rates. In recombination rates the correlations between significant number of interacting particles are very important, therefore many-particle initial and final states must be dealt with accurately. As we already emphasised, the rate results from the sum of all possible transitions of which the number in a many particle-system is large. Only simplified systems such as harmonic oscillators allow for exact treatment of the above problems, however any matrix element and recombination rate yields an approximation due to a wave function used in the calculations. Different methods lead to the different results depending on the initial conditions. The variational approach reported in [189] results in a good treatment of correlation effects for a single transition from bi-exciton to exciton, but unfortunately can only be successfully applied to perfectly spherical quantum dot structures. A path integral implementation of the recombination rates which will be derived below takes into account all correlations in the initial and final states. We aim to express Eqs.(2.171) and (2.172) in the path integral formalism. To do this we calculate the square of the point contact matrix element,

$$|p_N^\alpha|^2 = \int\int \rho_N^\alpha(\mathbf{R}_N, \mathbf{R'}_N)\rho_{N-1}^\alpha(\mathbf{R'}_{N-1}, \mathbf{R}_{N-1})\delta(\mathbf{r}_{e,N} - \mathbf{r}_{h,N})\delta(\mathbf{r}_{e',N} - \mathbf{r}_{h',N})d\mathbf{R}_N d\mathbf{R'}_N, \tag{2.173}$$

where ρ_N^α and ρ_{N-1}^α are the density matrices describing the initial and final states. We expect that the electrons and holes are in thermal equilibrium before they recombine [190]. Then the thermal density matrix of N excitons, $\rho(\mathbf{R}_N, \mathbf{R'}_N; \beta)$, can be introduced. The summation over all final states requires $\rho_{N-1}(\mathbf{R'}_{N-1}, \mathbf{R}_{N-1}) = \delta^{3(N-1)}(\mathbf{R}_{N-1} - \mathbf{R'}_{N-1})$, as the final state is free to take on any value. Substituting the above delta-function into Eq.(2.173) and integrating with respect to $\mathbf{R'}_N$ then using Eq.(2.171), one can get the radiative recombination rate as the function of temperature,

$$\Gamma_N(\beta) = \frac{2nE_{gap}E_{\mathbf{p}}e^2}{3\hbar^2c^3m}\left\langle |p_N|^2 \right\rangle_\beta, \tag{2.174}$$

where

$$\langle |p_N|^2 \rangle_\beta = \frac{1}{\mathscr{Z}_N}\int\int \rho_N(\mathbf{R}_N, \mathbf{R'}_N; \beta)\delta(\mathbf{R'}_{N-1} - \mathbf{R}_{N-1})\delta(\mathbf{r}_{e,N} - \mathbf{r}_{h,N}) \times\delta(\mathbf{r}_{e',N} - \mathbf{r}_{h',N})d\mathbf{R}_N d\mathbf{R'}_N. \tag{2.175}$$

In Eq.(2.175) the ρ_N is normalised by a partition function for N excitons, $\mathscr{Z} \equiv Tr(\rho_N)$.

The real-space path integral form of the thermal density matrix in Eq.(2.175) is given by [191],

$$\rho(\mathbf{R}_N, \mathbf{R'}_N; \beta) = \int_{\substack{\mathbf{R}_N(0)=\mathbf{R'}_N \\ \mathbf{R}_N(\beta)=\mathbf{R}_N}} \mathscr{D}\mathbf{R}_N(t) \exp\left\{-\frac{1}{\hbar}\int_0^\beta \hat{\mathscr{H}} dt\right\}. \tag{2.176}$$

The above derivation leads to the conclusion that both $\mathscr{Z}_N$ and $\langle|p_N|^2\rangle_\beta$ can be expressed in the path integral which differ only by constraints on the paths [188],

$$\mathscr{Z}_N = \int_{diagonal} \mathscr{D}\mathbf{R}_N(t) \exp\left\{-\frac{1}{\hbar}\int_0^\beta \hat{\mathscr{H}} dt\right\}, \tag{2.177}$$

$$\mathscr{Z}_N\langle|p_N|^2\rangle_\beta = \int_{radiating} \mathscr{D}\mathbf{R}_N(t) \exp\left\{-\frac{1}{\hbar}\int_0^\beta \hat{\mathscr{H}} dt\right\}. \tag{2.178}$$

In case of Eq.(2.177) the diagonal constraint is $\mathbf{R}_N(0) = \mathbf{R}_N(\beta)$ (Fig. 2.6(a)). The radiating condition is a trace over non-radiating electron-hole pairs, $\mathbf{R}_{N-1}(0) = \mathbf{R}_{N-1}(\beta)$, and pairing of decaying particles, $\mathbf{r}_{e,N} = \mathbf{r}_{h,N}$ and $\mathbf{r}_{e',N} = \mathbf{r}_{h',N}$, Fig. 2.6(b) [188].

At this point it can be useful to analyse the dependency of the recombination rates in the path integral formalism on the strength of the confinement in the structure. Lets take the $t = 0$ time-slice in imaginary time. If the diagonal boundary conditions are considered then the path integral samples diagonal elements of the thermal density matrix in the position basis [188]. If the system is made of the electron-hole pairs not interacting through the Coulombic potential then the electron and hole sample the probability density functions of the ground state free-particle system. For the radiating case, the charge carriers are forced to meet, however two distinguished points $t = 0_-$ and $t = 0_+$ may be sampled. This leads to $\langle|p_N|^2\rangle_\beta \sim 1$ as the effects cancel and is characteristic for strong confining potentials [188]. When the confinement is weak the particles form an exciton. If the boundary conditions are considered electron and hole samples product of the structure volume $\mathrm{Vol}_{\,\mathrm{struct}}$ and exciton volume $\sim a_X^3$. For the radiating constraint the $\mathrm{Vol}_{\,\mathrm{struct}}$ sampled at $t = 0_-$ and $t = 0_+$ may not be exactly the same, thus $\langle|p_N|^2\rangle_\beta \sim \mathrm{Vol}_{\,\mathrm{struct}}/a_X^3$ which is typical for a weak confinement with the structure dimension less that the wavelength of emitted radiation.

The picture becomes more complicated for a bi-exciton which is made of two

excitons from which one can be radiatively constrained and the other diagonally constrained. If the potential of the structure is strong we expect cancellation of boundary constraint effects like previously in the single exciton, and $\Gamma_{XX}/\Gamma_X \approx 2$, as the electron-hole pairing contribute to the recombination rates. Weak confinement results in a scenario in which the exciton in diagonal boundary condition forms a bi-exciton with the electron-hole pair in the radiating boundary condition, with the radius of the bi-exciton a_{XX}. One may expect the reduction of the relative rate proportional to $\Gamma_{XX}/\Gamma_X \approx 2a_{XX}^3/\mathrm{Vol}_{\,\mathrm{struct}}$, as the factor related to the volume of the structure is suppressed by binding.

2.8.9 Implementation of the recombination rates into the PI-QMC

The PI-QMC is able to directly sample the recombination rates expression derived in the above section. In order to calculate the $\langle|p_N|^2\rangle_\beta$ thermal density matrix containing radiating and diagonal elements is defined in the following manner,

$$\widetilde{\rho}(\mathbf{R}_N, \mathbf{R'}_N) = \rho_{rad}(\mathbf{R}_N, \mathbf{R'}_N) + \rho_{diag}(\mathbf{R}_N, \mathbf{R'}_N) \tag{2.179}$$

where the radiative constraint is given by

$$\rho_{rad}(\mathbf{R}_N, \mathbf{R'}_N) = \rho_N(\mathbf{R}_N, \mathbf{R'}_N)\delta(\mathbf{R}_{N-1} - \mathbf{R'}_{N-1})\delta(\mathbf{r}_{e,N} - \mathbf{r}_{h,N})\delta(\mathbf{r}_{e',N} - \mathbf{r}_{h',N}) \tag{2.180}$$

and diagonal

$$\rho_{diag} = \rho_N(\mathbf{R}_N, \mathbf{R'}_N)\delta(\mathbf{R}_N - \mathbf{R'}_N). \tag{2.181}$$

The probability of finding the system in either state can be expressed as,

$$P(rad_{state}/diag_{state}) = \int \frac{\rho_{rad/diag}(\mathbf{R}_N, \mathbf{R'}_N)d\mathbf{R}_N d\mathbf{R'}_N}{\int \widetilde{\rho}(\mathbf{R}_N, \mathbf{R'}_N)d\mathbf{R}_N d\mathbf{R'}_N}, \tag{2.182}$$

as radiative and diagonal sets do not overlap in the configuration space. Eq.(2.175) combined with Eq.(2.182) yields the ratio which can be computed using the PI-QMC numerics,

$$\langle|p_N|^2\rangle_\beta = \frac{P(radiating)}{P(diagonal)}. \tag{2.183}$$

Computing the recombination rates using the PI-QMC technique involves expansion of the thermal density matrix ρ_N with finite number of imaginary time-slices in the

configuration space ($\mathbf{R}_N^{(0)} = \mathbf{R}_N, \mathbf{R}_N^{(1)}, \cdots \mathbf{R}_N^{(n)} = \mathbf{R'}_N$), with n being the number of time-slices. Then the multilevel Metropolis algorithm is used to sample the probability distribution $\widetilde{\mathscr{Z}^{-1}}\widetilde{\rho}$. We estimate the probability of finding the system in the radiating or diagonal state using relative frequencies defined as x_{rad} and $x_{diag} = 1 - x_{rad}$ of radiative or diagonal path configurations present in the Markovian chain. This yields the relationship $\langle |p_N|^2 \rangle_\beta \approx x_{rad}/x_{diad}$ which, substituted into Eq.(2.174), gives the radiative recombination rate,

$$\Gamma_N(\beta) = \frac{2nE_{gap}E_{\mathbf{p}}e^2}{3\hbar^2c^3m}\frac{x_{rad}}{x_{diag}}. \tag{2.184}$$

In the above expression the excitonic energies obtained from E_{gap} simulations are used in order to find the recombination rates.

2.8.10 Summary

The above chapter was dedicated to the theory of the path integral formulation of quantum mechanics and its connection to statistical mechanics. We demonstrated that the Metropolis Monte Carlo method can be successfully applied to numerical sampling of the thermal density matrix, and is capable of effective dealing with complex, many body systems. The origin of the fermion sign problem was outlined and practical methods of efficient simulation of such a system explained with particular emphasis on the fixed node technique. The electron-hole recombination process was explained and its interpretation in the path integral picture derived. Finally implementation of the recombination rate into the PI-QMC was presented.

Chapter 3

PI-QMC vs. analytical methods

In this chapter an analytical method used for verification of our numerical results is presented and discussed in detail. This is cross-section of information sourced from research publications in which a shifted 1/N expansion was developed and successfully improved in order to be able to handle problem from different field of physics and quantum chemistry. A huge advantage of this method is that low-lying energy levels of an arbitrary dimensional system can be quickly calculated using a simple analytical form and the strength of the Coulomb interaction of particles can be tuned through effective Bohr radius and the oscillator characteristic length. It will be demonstrated that the results of the simulations obtained using the PI-QMC algorithm are in excellent agreement with an algebraic solution of the Schrödinger equation performed using a highly flexible and broadly applicable method known as the shifted 1/N Expansion [192].

We start with the derivation of the method for a single particle in an arbitrary spherically symmetric potential. Then more advanced cases will be analysed and the analytical recursive relation used in our calculations presented. We conclude the Chapter with a comparison of results from the PI-QMC simulations and direct calculations in Mathematica using the shifted 1/N technique.

3.1 Solution of the Schrödinger equation with the shifted 1/N expansion

The Shifted 1/N expansion method has been developed quite recently and has already found many applications in different fields of theoretical physics, due to its ability to enable fast and accurate calculations of the energy and wave functions of a quantum system [192]. The main idea of the method is based on the semiclassical theory of spin systems [192] known from solid-state physics, in which the spin is used as the expansion parameter. The 1/N expansion goes further and instead of spin, deals with the coordinate space system [193] and was initially developed for solving problems in quantum field theory.

One of the most important advantages, among many others, is the fact that in the shifted 1/N method we do not expand with respect to a coupling constant, but instead all coefficients of expansion are a functions of this constant. This is a very important difference compared to the coupling-constant perturbation approach [192],which is mostly valid only for weakly coupled systems. The shifted 1/N expansion is valid for a broad range of coupling values, in which even leading orders of the expansion can be characteristic for the physics of the system. Finally, in this technique we are not limited to the class of problems described by a Hamiltonian made of the sum of two terms: a directly solvable and a small perturbing one. This latter together with clear algebraic recursion, allows for the fast calculation of the ground states of the system.

3.1.1 The Hamiltonian framework

A system of two interacting particles of effective mas m^* confined to a three-dimensional parabolic potential of frequency ω is described by the time-independent Schrödinger equation,

$$\mathscr{H} = -\frac{\hbar^2}{2m^*}\nabla_1^2 + \frac{1}{2}m^*\omega^2\mathbf{r}_1^2 - \frac{\hbar^2}{2m^*}\nabla_2^2 + \frac{1}{2}m^*\omega^2\mathbf{r}_2^2 + \frac{q_1 q_2}{4\pi\epsilon_0\epsilon\,|\mathbf{r}_1 - \mathbf{r}_2|}, \tag{3.1}$$

where ϵ is the static dielectric constant. At this point it is convenient to define two length-scales characteristic for the problem, which we will find very useful later during the derivation of the recurrence relation. The first one is the oscillator characteristic length $l_0 = \sqrt{\hbar/m^*\omega}$ and the second one the effective Bohr radius $a_0^* = 4\pi\epsilon_0\epsilon\hbar^2/m^*e^2$.

The equation of motion (3.1) can be decoupled to centre-of-mass (CM)

$$\mathscr{H}_{CM} = -\frac{\mathbf{P}^2}{2\mathscr{M}} + \frac{1}{2}\mathscr{M}\omega^2 R^2, \tag{3.2}$$

and the relative coordinates (rel) motion,

$$\mathscr{H}_{rel} = -\frac{\mathbf{p}^2}{2\mu} + \frac{1}{2}\mu\omega^2 r^2 + \frac{e^2}{4\pi\epsilon_0\epsilon|\mathbf{r}_{rel}|}. \tag{3.3}$$

For the CM we define $\mathscr{M} = 2m^*$, $\mathbf{P} = \mathbf{p}_1 + \mathbf{p}_2$, with corresponding coordinates $\mathbf{r}_{CM} = (\mathbf{r}_1 + \mathbf{r}_2)/2$ and $Q = 2e$. Similarly for the relative motion $\mu = m^*/2$, $\epsilon = 4\pi\epsilon_0\epsilon$, $\mathbf{p} = (\mathbf{p}_1 - \mathbf{p}_2)/2$ with $\mathbf{r}_{rel} = \mathbf{r}_1 - \mathbf{r}_2$ and $q = e/2$.

The centre-of-mass motion Eq.(3.2) is described by the Schrödinger equation for a particle of mass $\mathscr{M}$ in a three-dimensional parabolic potential. The solution to this problem yields eigenenergies of the form,

$$E_{CM} = \left(2N_{CM} + L_{CM} + \frac{3}{2}\right)\hbar\omega \tag{3.4}$$

where $N_{CM} = 0, 1, 2, ...$ and $L_{CM} = 0, \pm1, \pm2, ...$. The equation of relative motion does not possess a straight-forward analytical solution, therefore the shifted 1/N expansion method will be applied. We start with rewriting Eq.(3.3) in the operator notation,

$$\mathscr{H}_{rel} = -\frac{\hbar^2}{2\mu}\left[\frac{1}{r}\frac{\partial}{\partial r}\left(r\frac{\partial}{\partial r}\right) + \frac{1}{r^2}\frac{\partial^2}{\partial\phi^2}\right] + \frac{1}{2}\mu\omega^2 r^2 + \frac{e^2}{\epsilon r}. \tag{3.5}$$

If one introduces an factorised wave function of the form $\Phi(r,\phi) = 1/\sqrt{r}\eta(r)\exp\{im\phi\}$ and acts upon it with Eq.(3.5), the following new radial form is produced,

$$\frac{d^2\eta(r)}{dr^2} + \left(-\frac{l^2 - \frac{1}{4}}{r^2} - \frac{\mu^2\omega^2 r^2}{\hbar^2} - \frac{2^2}{\hbar^2\epsilon}\frac{1}{r}\right)\eta(r) = -\frac{2_{n_r,l}}{\hbar^2}\eta(r), \tag{3.6}$$

in which $l = 0, \pm1, \pm2, ...$ is the azimuthal quantum number. The introduction of the new variable $r = \sqrt{2}l_0 z$ in Eq.(3.6) simplifies the relative part even more,

$$\frac{1}{2l_0^2}\frac{d^2\eta(z)}{dz^2} + \left[\frac{2\mu E_{n_r,l}}{\hbar^2} - \frac{l^2 - \frac{1}{4}}{2l_0^2}\frac{1}{z^2} - \frac{2\mu e^2}{\sqrt{2}l_0\hbar^2\epsilon}\frac{1}{z} - \frac{\mu^2\omega^2 2l_0^2}{\hbar^2}z^2\right]\eta(z) = 0. \tag{3.7}$$

Multiplication of both sides by $2l_0^2$ gives:

$$\frac{d^2\eta(z)}{dz^2} + \left[\frac{2l_0^2 m^* \omega E_{n_r,l}}{\hbar^2\omega} - \frac{l^2-\frac{1}{4}}{z^2} - \frac{\sqrt{2}l_0 m^* e^2}{\hbar^2\epsilon}\frac{1}{z} - \frac{m^{*2}\omega^2 l_0^4}{\hbar^2}z^2\right]\eta(z) = 0, \tag{3.8}$$

and identifying the already introduced effective Bohr radius a_0^* and the oscillator characteristic length l_0 yields,

$$\frac{d^2\eta(z)}{dz^2} + \left[\mathscr{E} - \frac{l^2-\frac{1}{4}}{z^2} - z^2 - \mathscr{C}\frac{1}{z}\right]\eta(z) = 0, \tag{3.9}$$

with $\mathscr{E} = 2E_{n_r,l}/\hbar\omega$ and coupling parameter $\mathscr{C} = \sqrt{2}l_0/a_0^*$. This latter parameter is especially important as it provides information about the relative strengths of the Coulomb and confining potentials. Based on this ratio, two interaction regimes can be defined, firstly in which the dots' potential dominates $l_0 \ll a_0^*$ and therefore the Coulomb interaction is weak and can be treated as a perturbation. The second case $l_0 \gg a_0^*$ considers the situation in which the Coulomb potential contributes most to the energy of the system. As it is apparent from the above discussion the confining and Coulomb potentials are coupled to each other, making Eq.(3.9) analytically unresolvable, forcing us to use an approximation technique.

The shifted $1/N$ expansion, in which N is the number of spatial dimensions, is a powerful method of solving problems involving interacting particles in arbitrary spherically symmetric, power-law potentials. It provides exceptionally accurate and intuitive analytical expression of the energy eigenvalues and wave functions of the Schrödinger equation [194, 195].

3.1.2 Shifted 1/N expansion method

We begin with rewriting the radial Schrödinger equation in $N-$ *spatial* dimensions with an arbitrary, spherically symmetric potential $\hat{V}(r)$,

$$\left\{-\frac{\hbar^2}{2m}\left(\frac{d^2}{dr^2} + \frac{N-1}{r}\frac{d}{dr}\right) + \frac{l(l+N-2)}{2r^2} + \hat{V}(r)\right\}\phi(r) = E\phi(r), \tag{3.10}$$

where $\hat{V}(r)$ is defined as,

$$\hat{V}(r) = r^2 + \frac{\mathscr{C}}{r}, \tag{3.11}$$

Setting $\xi(r) = r^{(N-1)/2}\phi(r)$ and shifted variable $\bar{k} \equiv N + 2l - a$, in which the l is an angular momentum and a an additional degree of freedom, to be defined yields the form,

$$\left[-\frac{\hbar^2}{2m}\frac{d^2}{dr^2} + \frac{\bar{k}^2\left[1-(1-a)/\bar{k}\right]\left[1-(3-a)/\bar{k}\right]\hbar^2}{8mr^2} + V(r)\right]\xi(r) = E\xi(r). \quad (3.12)$$

In order to successfully apply the $1/\bar{k}$ expansion and get reasonable results, we have to suitable define the potential in large energy limit [194]. For increasing values of $\bar{k}$, l behaves like $\bar{k}^2$, therefore it is reasonable to look for a potential which follows a similar pattern. In other words, we are looking for an effective potential which does not change with $\bar{k}$ for large values of $\bar{k}$ and provides reasonable zeroth-order classical results [195]. These conditions can be met by applying the following modification to Eq.(3.12),

$$-\frac{\hbar^2}{2m}\frac{d^2\xi(r)}{dr^2} + \bar{k}^2\left[\frac{\left[1-(1-a)/\bar{k}\right]\left[1-(3-a)/\bar{k}\right]\hbar^2}{8mr^2} + \frac{V(r)}{Q}\right]\xi(r) = E\xi(r), \quad (3.13)$$

in which the constant Q rescales the potential and will be defined below. At this point we attempt to systematically expand Eq.(3.13) in terms of $1/\bar{k}$. We notice that the effective potential,

$$V_{eff}(r) = \frac{\hbar^2}{8mr^2} + \frac{V(r)}{Q} \quad (3.14)$$

has the biggest impact on the energy of the system. We assume that $V(r)$ is a slowly varying potential and that $V_{eff}(r)$ has a minimum at $r = r_0$ and bound states are well-defined [196]. If this is the case, then the following relation holds,

$$4mr_0^3V'(r_0) = \hbar^2 Q, \quad (3.15)$$

in which r_0 is the explicit solution to the equation,

$$N + 2l - 2 + (2n+1)\sqrt{3 + \frac{r_0V''(r_0)}{V'(r_0)}} = \sqrt{\frac{4mr_0^3V'(r_0)}{\hbar^2}}. \quad (3.16)$$

Knowing the value of r_0, Q can be computed from Eq.(3.15). Once the value of r_0 is found, the largest contribution to the energy is given by

$$\bar{k}^2V_{eff}(r_0) = \frac{\bar{k}^2}{r_0^2}\left[\frac{\hbar^2}{8m} + \frac{r_0^2V(r_0)}{Q}\right]. \quad (3.17)$$

The next contribution in the expansion is of order $\bar{k}$ and is given by, [196]

$$\frac{\bar{k}}{r_0^2}\left[\left(n+\frac{1}{2}\right)\hbar\omega-\frac{(2-a)\hbar^2}{4m}\right], \tag{3.18}$$

Introduced at the beginning of this section, the shifting parameter a, is defined in such a way to cancel this contribution i.e.

$$a=2-\frac{2(2n+1)m\omega}{\hbar}. \tag{3.19}$$

The subsequent terms contributing to the energy of the system are computed by shifting the centre of coordinates to $r=r_0$ using the following form [196],

$$x=\frac{\sqrt{\bar{k}}}{r_0}(r-r_0), \tag{3.20}$$

Substitution of the above equation into expression Eq.(3.13) and expanding about $x=0$ in a power series of x [196], results in

$$\begin{aligned}\left[-\frac{\hbar^2}{2m}\frac{d^2}{dx^2}+\frac{\bar{k}\hbar^2}{8m}\left[1+\frac{3x^2}{\bar{k}}-\frac{4x^3}{\bar{k}^{3/2}}+\frac{5x^4}{\bar{k}^2}-\cdots\right]-\frac{(2-a)\hbar^2}{4m}\left[1-\frac{2x}{\bar{k}^{1/2}}+\frac{3x^2}{\bar{k}}-\cdots\right]\right.\\ \left.+\frac{(1-a)(3-a)\hbar^2}{8m\bar{k}}\left[1-\frac{2x}{\bar{k}^{1/2}}+\frac{3x^2}{\bar{k}}-\cdots\right]\right.\\ \left.+\frac{r_0^2\bar{k}}{Q}\left[V(r_0)+\frac{V''(r_0)r_0^2x^2}{2\bar{k}}+\frac{V'''(r_0)r_0^3x^3}{k\bar{k}^{3/2}}+\cdots\right]\right]\xi(r)=\frac{Er_0^2}{\bar{k}}\xi(r).\end{aligned} \tag{3.21}$$

Eq.(3.21) is of the form of the Schrödinger equation, which was rigorously solved in Appendices A and B of [196] leading to the shifted 1/N algorithm. In this thesis only the most important steps resulting in the analytical form of the energy eigenvalues are presented. The energy eigenvalues in the form of a large-N expansion can be obtained using the following relation,

$$E_{n,l}=\frac{\bar{k}}{r_0^2}\lambda_n, \tag{3.22}$$

in which, $\lambda_n=\lambda_n^{(0)}+\lambda_n^{(1)}+\lambda_n^{(2)}+\lambda_n^{(3)}+\cdots$, with $n=0,1,2,....$ Successive contributions to the λ_n are given in Appendix A of this thesis, and without proceeding into the derivations we present here the steps which we followed in order to compute the quantities in question.

Having set the number of spatial dimensions, the orbital angular momentum l

and radial quantum number n, Eq.(3.16) were used to determine r_0. In the next step the Q was found using Eq.(3.15). These parameters allowed us to quantify the ω in Eq.(A.8). Using Eq.(3.19) the shifting parameter was computed. Using the above set of input data, the values in Eq.(A.2) and Eqs.(A.9)-(A.18) were calculated and substituted into Eqs.(A.3)-(A.6) to obtain the energy Eq.(3.22).

3.2 Results

In this section results obtained from the PI-QMC simulations will be compared to the shifted $1/N$ analytical calculations in order to demonstrate reliability of the PI-QMC algorithm. We begin with the simple harmonic oscillator, then the case of two interacting electrons will be presented. More tests run against different analytical methods can be found in [132].

3.2.1 Two indistinguishable interacting electrons in a parabolic potential

In the atoms which contain more than one electron, according to the Pauli's exclusion principle, electrons which occupy the same quantum state must differ at least by one quantum number. This means that if one considers a quantum system containing two indistinguishable interacting fermions neglecting their spin, then the only configuration allowed for the system is one electron in the ground state and the second one in the first excited state.

In following test case a GaAs/$In_{1-x}Ga_xAs$ quantum dot was considered, with the dielectric constant set to 12.5. Two identical electrons with effective mass $0.067\,m_e$ were confined in an isotropic, harmonic potential of strength $\hbar\omega = 30\,\text{meV}$ which resulted in the ratio of the Coulomb potential to the harmonic confinement $\mathscr{C} = \sqrt{2}l_0/a_0^* = 1$. In a non-interacting system this latter parameter is $\mathscr{C} = 0$. The energy values calculated using the shifted 1/N expansion were compared against the PI-QMC simulations with Simple Harmonic Oscillator nodes and the exact calculations obtained with the Wontzel-Kramers-Brillouin (WKB) double parabola method [197] and collected in Table 3.1.

$\mathscr{C}=0$			$\mathscr{C}=1$			
$\|n,m\rangle$	$E_{n,m}$	PI	$\|n,m\rangle$	PI	1/N	WKB
$\|0,0\rangle$	30	-	$\|0,0\rangle$	-	51.35	52.43
$\|0,1\rangle$	60	-	$\|0,1\rangle$	-	72.79	72.83
Energy [meV]	90	89.88±0.09		126.90±0.09	124.14	125.26

Table 3.1: Comparison of energy for $\mathscr{C}=0$ two non-interacting interacting and $\mathscr{C}=1$ Coulomb interacting electrons calculated using fixed node PI-QMC, shifted 1/N expansion and WKB methods

One can see that for a system of two identical non-interacting electrons the result obtained from the PI-QMC simulations is in excellent agreement with the analytical value. The energy value obtained for the interacting particle is in very good agreement with the WKB method and shifted 1/N expansion. A small overshoot of the energy value can be accounted for by the finite temperature value of the simulation which can result in thermal excitation of the particles. The analytical calculation doesn't account for thermal effects. An additional discrepancy can stem from the fixed nodes approximation, which, as an approximation, can influence the thermodynamic estimators calculated for the system.

3.2.2 Conclusions

In this chapter the non-perturbative, shifted 1/N expansion technique has been described and applied to the test examples. The analytical shifted 1/N expansion method used to calculate the energy values of the test systems demonstrates very good agreement with the PI-QMC simulation results and previous data presented in [132]. Additionally our simulations for Coulomb interacting electrons in a harmonic potential have shown the PI-QMC technique is able to accurately reproduce not only the results obtained from shifted 1/N method but also those obtained from WKB simulations.

Chapter 4

Properties of atomistic model (In,Ga)As nanostructures

4.1 Introduction

Self-assembled InGaAs/GaAs quantum dots are one of the most commonly studied nanostructures, due to their broad applicability ranging from single photon sources to quantum computing [198]. An abrupt change of conditions during the growing process can result in the formation of a quantum ring structure [115].

The quantum ring has been grown in many different semiconductor compounds such as InGaAs [116], InAs/InP [117], GaSb/GaAs [118] and SiGe/Si [119]. Nanostructures modelled and presented in this thesis are limited to InGaAs multiple quantum dots and rings. The rings discussed here are, in their shape, similar to a donut with a GaAs inner region, which generates almost toroidal confinement surrounded by a cylindrically symmetric InGaAs matrix.

In this chapter detailed atomistic models will be introduced and differences between them compared. We conclude with the discussion of piezoelectric properties of those structures and its impact on the electronic structure of the stacked nanostructure. The results from this chapter will lead into the path integral simulations in remaining chapters of this thesis,

4.2 Computational models

The Path Integral Quantum Monte Carlo method is capable of the direct sampling of the density matrix of charge carriers in arbitrary confining potentials. To obtain a realistic picture of these potentials the atomistic model is constructed such that the modelled quantum structure is as close as possible to the physical one. In such a model the individual atoms are taken into consideration, and both electron and hole confining potentials are computed as a shift from their relaxed bulk values due to the strain fields.

In our simulations, atomistic models are limited to only two bands, one conducting and one valence. However this simplification is largely compensated for by our ability to construct realistic shapes and sizes of nano-structures, including the effect of random alloy fluctuation, piezoelectric potentials and a correctly captured point group symmetry.

Strain can be used to tune the properties of semiconductor structures and devices. One of the most commonly used methods is to grow a semiconductor over-layer on top of another layer of substrate, even if their lattice constants are not the same. As a result the over-layer can experience the large strain fields, maintaining long range atomic ordering in the matrix of the substrate [199]. The explanation of this process and initial theory of epitaxial growth was first introduced in [200]. According to this, the epitaxial growth take place as long as the lattice mismatch is less than around 10 %.

Strain fields can be seen as a reaction to the relatively small dislocation of atoms in the crystal. As will be demonstrated in the following chapters, the strain significantly affects the electronic properties of the semiconductor structures, for instance: energy band gap, effective masses of charge carriers and the lattice constant.

In this section the theoretical background of atomistic model development is presented and its implementation in PI-QMC numerics discussed. The importance of piezoelectric potentials resulting from the strain fields and their positive impact on the two band model used here is also commented on in detail.

4.2.1 Strain evaluated from atomistic structure

The intuitive way of describing the strain is a picture of a crystal structure made of cubic cells, which undergo deformation, e.g. stretching. The deformation results in a relative change in position between these unit cells, and the strain fields are formed. However the same mechanisms affects the unit cells itself as the position of the atoms in the cell also change. In Fig. 4.1 the positions of the atoms in the unstrained unit cell are compared to the strained one. It is apparent that no matter if the unit cell is

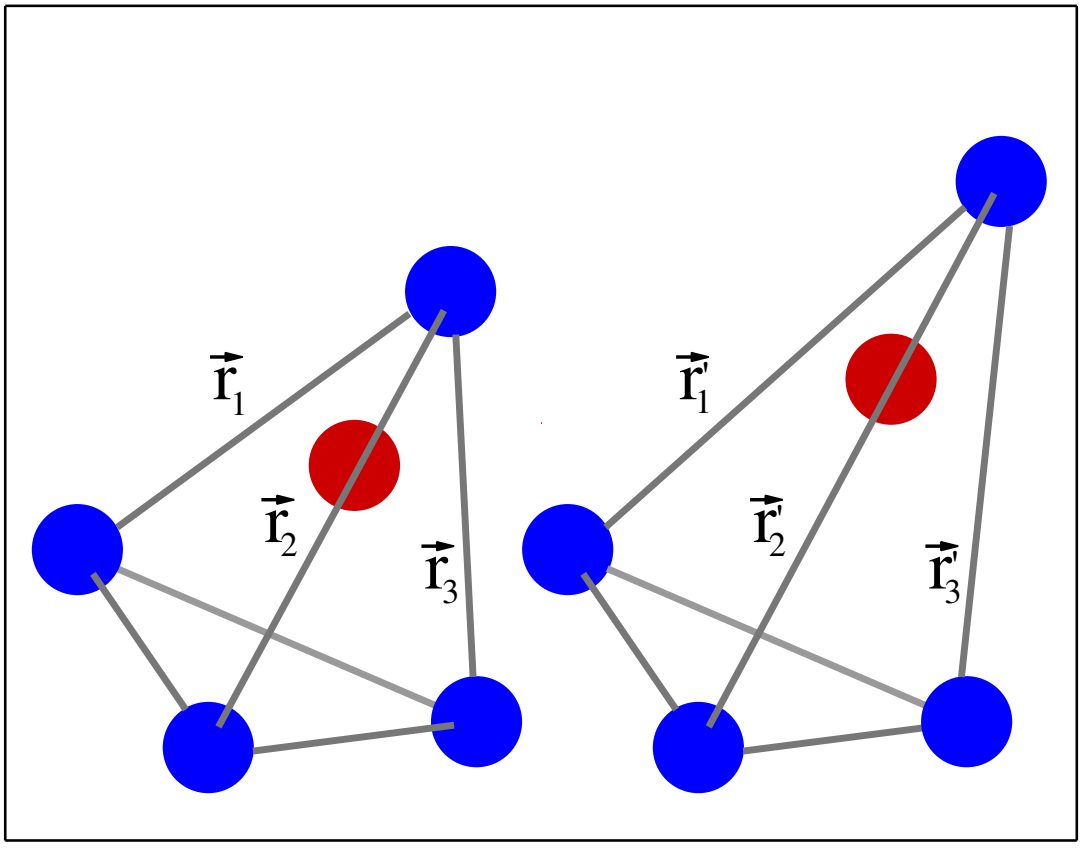

Figure 4.1: Comparison of the unstrained and strained unit cell (tetrahedron).

strained or not, all atoms are always inside the structure. This is very useful observation because a comparison of the strained cell lattice vectors to the lattice vectors of an unstrained tetrahedron allows us to identify the components of the strain tensor.

Independently of the crystal structure the relation between the strained and unstrained axes is governed by the system of six linear equations,

$$\begin{pmatrix} 1+\epsilon_{xx} & \epsilon_{xy} & \epsilon_{xz} \\ \epsilon_{yx} & 1+\epsilon_{yy} & \epsilon_{yz} \\ \epsilon_{zx} & \epsilon_{zy} & 1+\epsilon_{zz} \end{pmatrix} \begin{pmatrix} a \cdot x_i \\ a \cdot yi \\ a \cdot z_i \end{pmatrix} = \begin{pmatrix} a \cdot x'_i \\ a \cdot y'_i \\ a \cdot z'_i \end{pmatrix} \quad i = 1,2,3 \quad , \tag{4.1}$$

where ϵ_{ij} are the deformation coefficients and a is lattice constant of the unstrained crystal. In Eq.(4.1) the diagonal elements relate the length of the strained and unstrained axes and the off-diagonal elements describe the angles. Strain components, known also as the deformation coefficients, are commonly expressed in the form,

$$\epsilon = \begin{pmatrix} \epsilon_{xx} \\ \epsilon_{yy} \\ \epsilon_{zz} \\ 2\epsilon_{yz} \\ 2\epsilon_{zx} \\ 2\epsilon_{xy} \end{pmatrix}. \tag{4.2}$$

For the Zinc-Blende structure, $\epsilon_{yz} + \epsilon_{zy} = 2\epsilon_{yz}$. There are three distinguished forms of strain depending on the orientation of the force in the crystal, which play an extremely important role in quantum self-organised nano-structures. If one considers arbitrary strain tensor ϵ, then we can decompose it into three separate tensors as follows,

$$\begin{aligned} \begin{pmatrix} \epsilon_{xx} & \epsilon_{xy} & \epsilon_{xz} \\ \epsilon_{yx} & \epsilon_{yy} & \epsilon_{yz} \\ \epsilon_{zx} & \epsilon_{zy} & \epsilon_{zz} \end{pmatrix} &= \frac{1}{3} \begin{pmatrix} \epsilon_{xx}+\epsilon_{yy}+\epsilon_{zz} & 0 & 0 \\ 0 & \epsilon_{xx}+\epsilon_{yy}+\epsilon_{zz} & 0 \\ 0 & 0 & \epsilon_{xx}+\epsilon_{yy}+\epsilon_{zz} \end{pmatrix} \\ &+ \frac{1}{3} \begin{pmatrix} 2\epsilon_{xx}-(\epsilon_{yy}+\epsilon_{zz}) & 0 & 0 \\ 0 & 2\epsilon_{yy}-(\epsilon_{zz}+\epsilon_{xx}) & 0 \\ 0 & 0 & 2\epsilon_{zz}-(\epsilon_{xx}+\epsilon_{yy}) \end{pmatrix} \\ &+ \begin{pmatrix} 0 & \epsilon_{xy} & \epsilon_{xz} \\ \epsilon_{yx} & 0 & \epsilon_{yz} \\ \epsilon_{zx} & \epsilon_{zy} & 0 \end{pmatrix}. \end{aligned} \tag{4.3}$$

where the first 1/3 tensor with constant diagonal elements describes the change in the volume of the unit cell and is known as the hydrostatic component, and the remaining two shear components correspond to the change of shape of the cell. Using Eq.(4.3)

one can define two important quantities which will be extensively discussed in this thesis,

$$\begin{aligned} \epsilon_{bi} &= \epsilon_{zz} - \frac{1}{2}(\epsilon_{yy} + \epsilon_{xx}) \\ \epsilon_{hyd} &= \epsilon_{xx} + \epsilon_{yy} + \epsilon_{zz}. \end{aligned} \tag{4.4}$$

In the above, the equivalent expression ϵ_{bi} stands for bi-axial strain, which is measured in the growth direction and compared to the in-plane one, while ϵ_{hyd} is the hydrostatic strain which estimates the volume change in the unit cell. Definitions in Eq.(4.4) are very important, which will be demonstrated in the coming chapters, as electron and hole confinement is strongly affected by the hydrostatic strain, compared to the properties of the bands in a bulk semiconductor. Additionally the valence band properties also depend on the biaxial strain which makes our model even more complicated.

4.2.2 Valence force field method

The use of an atomistic model allows us to define the precise shape and size of the nanostructure from which the strain and stress can be computed. In order to obtain these quantities the nanostructure is numerically assembled atom-by-atom, including those located in the surrounding material. To do this the atoms are mapped on to the Zinc-Blende crystal structure, which usually has a bulk material lattice constant. In our simulations we follow the convention that the As anion is located at the (0,0,0) coordinate of the unit cell, with the In and Ga cations at (1/4,1/4,1/4) of the length of the unit cell. Then the crystal direction [111] is defined by the vector between these two positions [201]. All the above steps, including computing relaxed structures and related energy band offsets, are carried out by the **Qdot-tools** package [157]

The quantum nanostructure of interest, e.g. dot or ring is placed on the wetting layer modelled as a quantum well in the supercell filled with the GaAs matrix. The simulation cell must be large enough to allow the strain to completely decay at the boundaries. This is important, as we study our structures in periodic boundary conditions and potential interactions between the images in neighbouring supercells can result in significant error. The quantum structures discussed in this thesis are made of InAs buried in GaAs. An important difference between these two chemical compounds is a 7 % lattice mismatch which results in a highly strained system. The parameters of the strain-relaxed structure are obtained using the Valence Force

Field (VFF) model [202], in which the energy caused by the strain is represented as a few-body potential between the atoms,

$$E = \frac{1}{2}\left(\sum_{i,j} V_2(r_{ij}) + \sum_{i,j,k} V_3(\Theta_{ijk}) + \cdots\right), \tag{4.5}$$

where the two-atom bond stretching potential, Fig.(4.2(a)) is described as,

$$V_2(r_{ij}) = \frac{3}{8}\alpha_{ij}\frac{(r_{ij}^2 - d_{ij}^2)^2}{d_{ij}^2} \tag{4.6}$$

and three-atom bond bending potential, Fig.(4.2(b)) is defined by,

$$V_3(\Theta_{ijk}) = \frac{3}{8}\beta_{ijk}\frac{\left(r_{ij}r_{ik}\cos(\theta_{ijk}) - d_{ij}d_{ik}\cos(\phi_{ijk})\right)^2}{d_{ij}d_{ik}}. \tag{4.7}$$

In the above expression θ_{ijk} is an angle between $\mathbf{r}_{ij}$ and $\mathbf{r}_{ik}$ and $\phi_{ijk} = \cos^{-1}(1/3)$ is the equilibrium tetragonal bound angle in the Zinc-Blende crystal. The coefficients α_{ij} and β_{ijk} depend on the local environment in the crystal and are fitted to the elastic parameters of the bulk crystal. In Table 4.1 the parameters used in all of our atomistic models are presented [203].

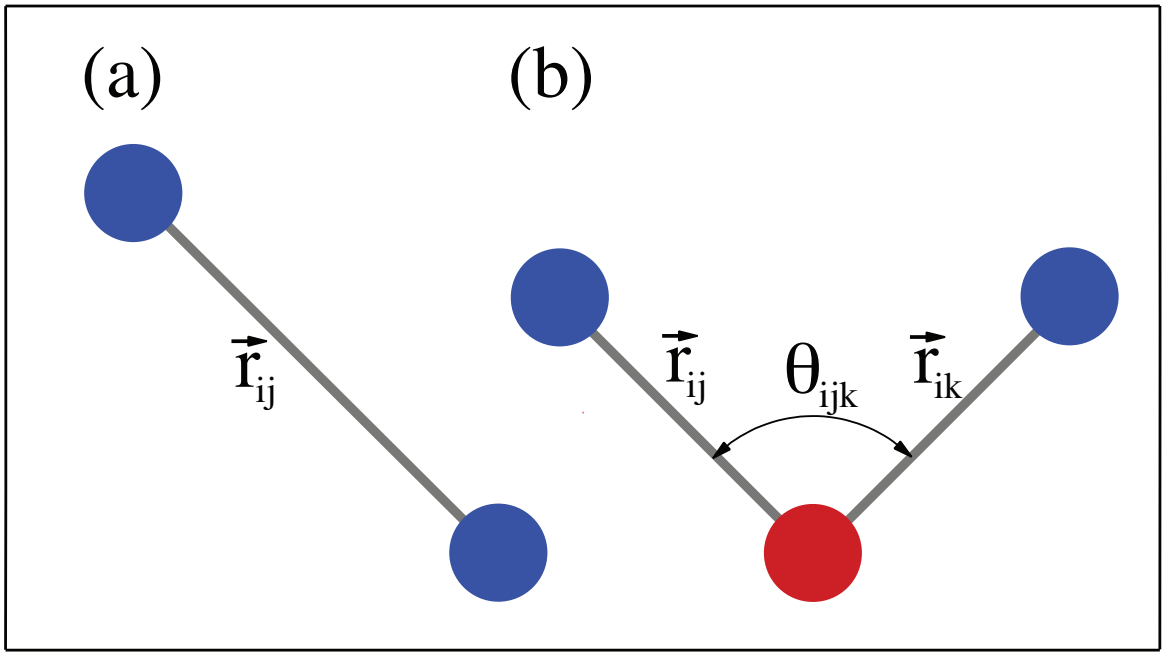

Figure 4.2: Visualisation of two-atom bond stretching (a) and three-atom bond bending (b) potentials.

Compound	$\alpha_{ij}(Ha)$	$\mathrm{d}_{ij}(a_0)$	$\beta_{ijk}(Ha)$	$\cos(\phi_{ijk})$
GaAs	0.026311	4.62595	0.0061122	-0.33333
InAs	0.022454	4.97625	0.0039129	-0.33333
InGaAs	-	-	0.0050125	-0.35021

Table 4.1: VFF parameters.

In order to extract realistic physical information, such a system must undergo relaxation during which the atoms find their equilibrium positions. This is achieved by the application of the conjugate gradient minimisation technique [204]. This method is based on the fact that strain energy can be modelled as a fourth-order, relative position dependent, polynomial. If we assume that atoms are displaced by a factor γ along the conjugate vector $\mathbf{r}_i$ at each minimization step, $\mathbf{v}_i = \mathbf{v}_i + \gamma \mathbf{r}_i$, then the minimal strain energy can be computed by applying a line minimization of the energy along $\mathbf{r}_i$.

4.2.3 Strain effects on semiconductor bands approximation

Once the structure is relaxed, atomic positions and residual forces are used to compute the stress tensor at each atom. The obtained values of strain and composition profile are then mapped to the grid, whose spacing corresponds to the material lattice constant, in such a way that one grid point contains 8 atoms. Using the strain-stress relation, based on continuum elasticity theory, the strain fields are mapped from the stress values. In the final step each 8 atom unit cell is used to calculate the composition and strain dependent band offset.

As already mentioned, the two-band effective mass model is used in all our simulations. The strain modified conduction band offset is defined in terms of the diagonal elements of the hydrostatic strain tensor multiplied by the deformation potential, and the energy of the unstrained conduction band edge [205] as follows,

$$V_c(i,j,k) = E_c + a_c(\epsilon_{xx} + \epsilon_{yy} + \epsilon_{zz}), \tag{4.8}$$

where V_c is strain modified confining potential, E_c the unstrained bulk energy level of the conduction band edge and $a_c Tr\epsilon$ is trace of strain. In Fig. 4.3 the conduction band energy and composition profile of Fig. 4.3a a vertically stacked dot and Fig. 4.3b

a quantum ring is shown. In our calculation of the valence band offset the anisotropy

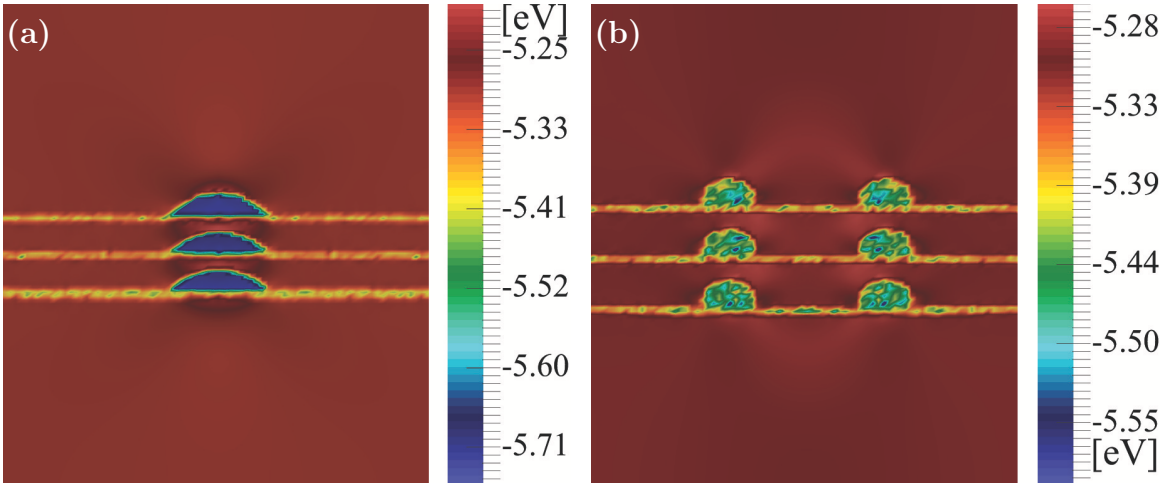

Figure 4.3: Cross section along [110] direction of electron confinement potential for (a) vertically stacked elliptical dot and (b) ring.

of the strain is included [205], in such a way that heavy hole, light hole and spin-orbit coupling effects are accounted for,

$$V_v^s = a_v(\epsilon_{xx}+\epsilon_{yy}+\epsilon_{zz})$$
$$-b\left[\begin{pmatrix}-2&0&0\\0&1&0\\0&0&1\end{pmatrix}\epsilon_{xx}+\begin{pmatrix}1&0&0\\0&-2&0\\0&0&1\end{pmatrix}\epsilon_{yy}+\begin{pmatrix}1&0&0\\0&1&0\\0&0&-2\end{pmatrix}\epsilon_{zz}\right] \tag{4.9}$$
$$-\sqrt{3}d\left[\begin{pmatrix}0&-1&0\\-1&0&0\\0&0&0\end{pmatrix}\epsilon_{xy}+\begin{pmatrix}0&0&0\\0&0&-1\\0&-1&0\end{pmatrix}\epsilon_{yz}+\begin{pmatrix}0&0&-1\\0&0&0\\-1&0&0\end{pmatrix}\epsilon_{zx}\right].$$

The deformation parameters used in Eqs.(4.8) and (4.9) can be found in Table (4.2). Additionally, linear interpolation of the deformation potentials between different com-

Compound	e_c	e_v	a_c	a_v	b	d	$split\text{-}off$
GaAs	-5.29	-6.92	-7.17	1.16	-1.90	-4.23	0.34
InAs	-6.13	-6.67	-5.08	1.00	-1.55	-3.10	0.38

Table 4.2: Deformation parameters.

pounds in a structure allows for the inclusion of random alloying effects, which makes

our model reasonably close to the real nano-structures. At present the PI-QMC method is limited to only the two-band effective mass model Hamiltonian, and because of this restriction only the bottom of conduction and the top of the valence band (heavy hole), (see Fig. 4.4) can be used. Even with this simplification our atomistic

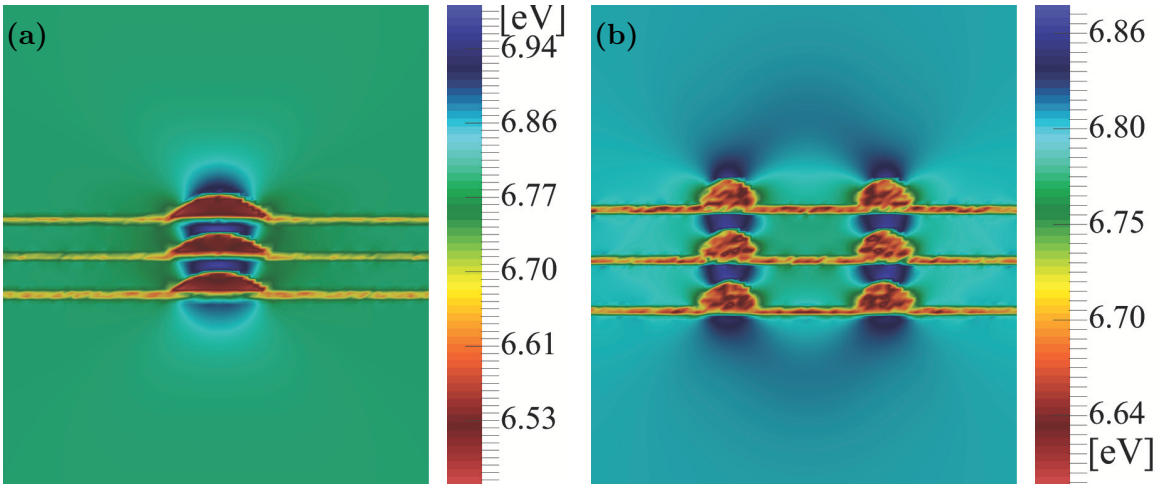

Figure 4.4: Cross section along the [110] direction of the hole confinement potential for vertically stacked elliptical (a) dots and (b) rings.

models are still much more accurate compared to the analytical potentials. One of the most important properties, which plays paramount role in the results discussed in this thesis, is an accurate treatment of the crystal lattice. Because the atomistic models used in our studies are numerically assembled following the Zinc-Blende structure the resulting symmetry is maximally C_{2v}, as the properties depending on the [110] and $[1\bar{1}0]$ directions in the crystal are significantly different. This is completely lost in the analytical and continuum elasticity based approaches to e.g. $In_{1-x}Ga_xAs$ alloys. An additional advantage results from the fact that these potentials can be directly loaded into the PI-QMC simulations.

4.2.4 Valence band structure.

The two-band, effective mass model Hamiltonian used in our PI-QMC simulation, due to its simplicity, does not account for band degeneracy and spin-orbit effects.

In order to analyse the impact of the degenerate bulk valence bands on our calculations we start with a brief outline of this phenomenon. For now we neglect spin-orbit coupling. In Zinc-Blende structure semiconductor at the $\mathbf{k} = 0$ point the conduction band (cb) has s-type symmetry with orbital angular momentum $m = 0$.

The valence band on the other hand has p-type symmetry with $m = 1$, resulting in triple degeneracy $m_l = 0$ and ± 1. In order to fully treat the situation one must develop a description of the effective mass of the hole including contributions from the degeneracy. This can be done in the framework of the Luttinger Hamiltonian [206],

$$\mathscr{H} = Ap^2\mathscr{I} + B(\mathbf{p} \cdot \mathbf{L})^2, \tag{4.10}$$

where A and B are constants and $\mathscr{I}$ is a 3×3 unitary matrix. Diagonalization of Eq.(4.10) yields two energy eigenvalues, $E_1(p) = Ap^2$ for $L_Z = 0$ and two-fold degenerate $E_h(p) = (A + B)p^2$ for $L_Z = \pm 1$. These two quadratic terms give the pair of parabolic branches, which are characterised by different effective masses and known as the heavy and light holes (hh) and (lh) respectively [207]. Apart from their different masses the additional distinction between hh and lh is a projection of the orbital momentum $\mathbf{L}$ on the orientation of $\mathbf{p}$. This projection is equal to 0 for lh and ± 1 for hh. Inclusion of the spin while spin-orbit coupling is neglected simply doubles these states [207].

The picture gets more complicated when spin-orbit interaction is involved. Contributions from spin-orbit coupling yields an energy relative to $\mathbf{L} \cdot \mathbf{S}$. At this point $\mathbf{L}$ and $\mathbf{S}$ are not conserved on their own, however their sum $\mathbf{J} = \mathbf{L} + \mathbf{S}$ still holds this property, where J^2 has $j(j + 1)$ eigenvalues with $|l - s| \leq j \leq l + s$. The solution to these eigenvalues is a combination of states. Conduction band $l = 0$ is not affected as $j = s = 1/2$, however the valence band $l = 1$ splits into $j = 1/2$ and $j = 3/2$ states, resulting in the fine structure of spectral lines. At the top of the band ($\mathbf{k} = 0$). An argument similar to the one for the effective mass leads to the conclusion that there must be a additional four-fold degeneracy $j = 3/2$, $J_Z = \pm 1/2, \pm 3/2$ separated by energy gap ΔE from the two-fold degenerate state $j = 1/2$, $J_Z = \pm 1/2$. This gap is known as the spin-orbit splitting and in GaAs is approximately 0.3 eV [207].

4.2.4.1 Heavy hole, light hole and split-off energy bands

Here we will discuss how big an impact the heavy hole (hh), light hole (lh) and split-off (so) bands have on our results, namely if we simulate the heavy or light hole. The allowed bands in the crystal structure are closely related to the discrete energy levels of the atom. When individual atoms are close to each other these levels split and form a band structure. In general these energy levels are degenerate, which greatly affects

the band energy spectrum. Using the following equations [208]

$$\mathscr{H}_s = \begin{pmatrix} a_c e & 0 & -v^* & 0 & -\sqrt{3}v & \sqrt{2}u & u & -\sqrt{2}v^* \\ 0 & a_c e & \sqrt{2}u & \sqrt{3}v^* & 0 & v & -\sqrt{2}v & -u \\ -v & \sqrt{2}u & -p+q & -s^* & r & 0 & \sqrt{3/2}s & -\sqrt{2}q \\ 0 & \sqrt{3}v & -s & -p-q & 0 & r & -\sqrt{2}r & \sqrt{1/2}s \\ -\sqrt{3}v^* & 0 & r^* & 0 & -p-q & s^* & \sqrt{1/2}s^* & \sqrt{2}r^* \\ \sqrt{2}u & v^* & 0 & r^* & s & -p+q & \sqrt{2}q & \sqrt{3/2}s^* \\ u & -\sqrt{2}v^* & \sqrt{3/2}s^* & -\sqrt{2}r^* & 1/\sqrt{2}s & \sqrt{2}q & -a_v e & 0 \\ -\sqrt{2}v & -u & -\sqrt{2}q & 1/\sqrt{2}s^* & \sqrt{2}r & \sqrt{3/2}s & 0 & -a_v e \end{pmatrix} \tag{4.11}$$

where

$$\begin{aligned} p &= a_v(\epsilon_{xx}+\epsilon_{yy}+\epsilon_{zz}), \\ q &= b[\epsilon_{zz} - \frac{1}{2}(\epsilon_{xx}+\epsilon_{yy})], \\ r &= \frac{\sqrt{3}}{2}b(\epsilon_{xx}-\epsilon_{yy}) - id\epsilon_{xy}, \\ s &= -d(\epsilon_{xz}-i\epsilon_{yz}), \\ u &= \frac{-i}{\sqrt{3}}P_0\sum_j e_{zj}\partial_j, \\ v &= \frac{-i}{\sqrt{6}}P_0\sum_j (e_{xj}-ie_{yj})\partial_j. \end{aligned} \tag{4.12}$$

the shift of the lh energy with respect to the hh due to biaxial strain was calculated. The electron and hole experience different confining potentials in [110] and [1$\bar{1}$0] directions. Similarly, in a coupled-structure confinement varies not only on two perpendicular diagonals but also from dot to dot. In Fig. 4.5 the valence band of a single and triple dot is compared. The hh ground and first excited state and strained lh band edge is also indicated. Values of confining potential in the triple dot system are different in all three structures. Therefore, for clarity of the diagram the confinement potential in the triple dot is averaged over the height of the In containing layers. We also averaged confining potential over [110] and [1$\bar{1}$0] directions for the single and triple dot structure. In the single structure the impact of the lh can also be neglected as the lh branch is localised in the surrounding matrix away from the dot. It is evident that in the triple dot the biaxial strain drives the lh band edge away from the ground and the first excited state and we can safely assume that the ground state

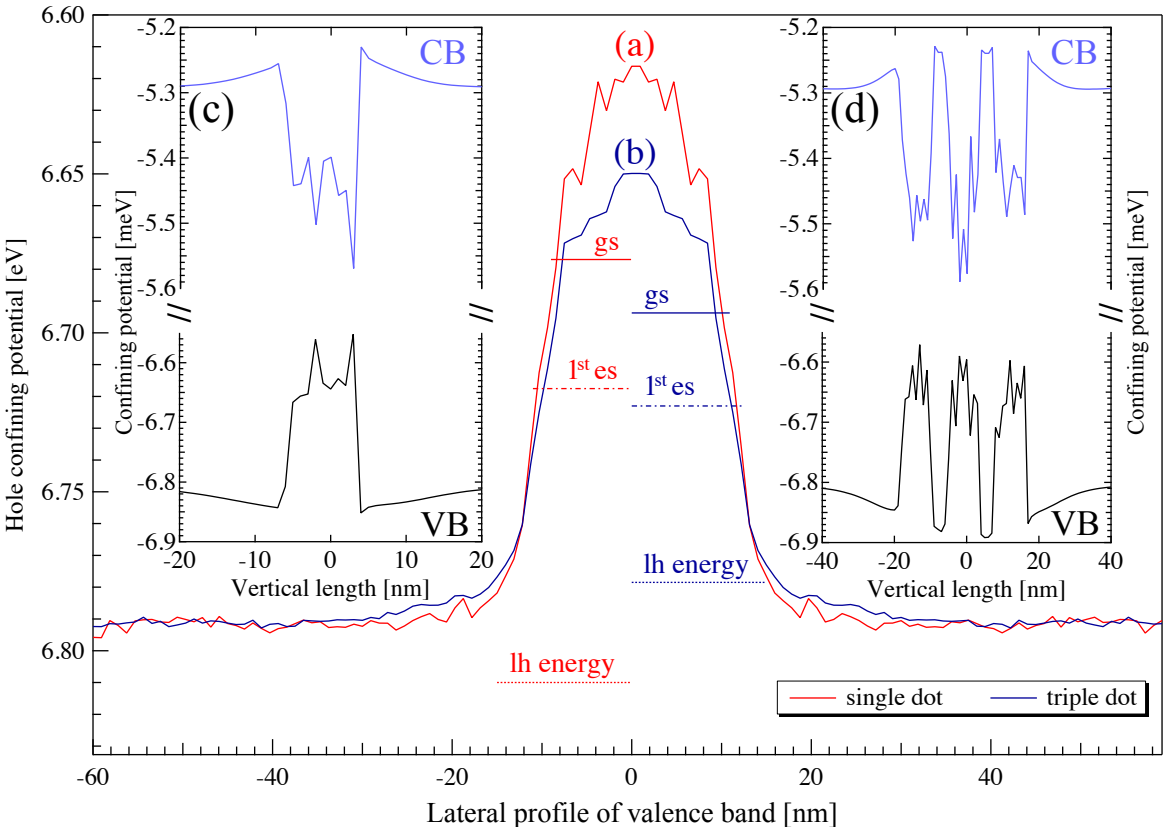

Figure 4.5: Valence band profile of (a) single dot and (b) triple dot across the dot structures averaged over the vertical extent, and over [110] and [1$\bar{1}$0] directions. Also indicated are the light-hole energy calculated from the biaxial strain shift and the ground state (gs) and the first excited state (1^{st} es) of the single particle heavy-holes. Insets (c) and (d) shows the conduction and valence band profile in the growth direction along the axis of the dot.

remain unaffected. It is worth to mention that in both types of structures the spin-orbit splitting energy band $\Delta = 0.3\,\text{eV}$ [207] greatly exceeds the range of confining potential and similarly to the lh branch, do not affect our calculations.

We conclude therefore that in the single and coupled quantum structures due to significant strain and translational symmetry breaking the contribution from hh-lh mixing can be neglected. These calculations clearly show that with the correct treatment of strain, piezoelectric potentials and composition profile, even our simplified two-band effective mass model Hamiltonian can provide accurate insight into the physics of advanced semiconductor nanostructures. Finally, we want to emphasise that this conclusion is in excellent agreement with [146, 149] that hh dominates in InGaAs dot structures.

4.3 Symmetry properties of confining potentials

Physically realistic models of nanostructures require the consideration of random alloy fluctuations. This element additionally complicates the picture, particularly affecting the charge localisation produced of confining potentials computed from strained stacked structures. The effect of random alloying results in the complete breaking of any underlying symmetry of the system and the possibility of spontaneous charge localisation close in the In-rich areas. This effect can be partially diverted and the C_{2v} symmetry reimposed, resulting in averaging areas of large alloy concentration over the structure. From a computational point of view this process can be understood as a calculation of the mean alloy profile from many random samples [132]. This approach greatly improves the PI-QMC simulations efficiency of sampling, as when obtained this way the confining potentials are significantly smoother with the underlying C_{2v} symmetry maintained. The C_{2v} point group symmetry is based on two perpendicular mirror planes [110] and $[1\bar{1}0]$ crossing each other at the C_2 axis. This demands that the structure defined in this symmetry must be symmetric under 180 ° rotation or reflection. The atomistic model of nanostructures used in this thesis meets this requirement by permutation of the coordinate system in order to obtain reflections, which are then averaged along the mirror planes generating a structure with C_{2v} symmetry. It was already emphasised that we endeavour to obtain atomistic models of nanostructures which are as realistic as possible. This is reflected in the stacked structures having shape asymmetry, in the [001] vertical direction. Vertically asymmetric structures provide important differences in the strain profile and strain affected confinement potentials due to the volume difference between the base and the top of the nanostructure. As apparent from the Hamiltonian for a strained valence band, Eq.(4.9), biaxial strain ϵ_{bi} predominantly affects hole confinement and significantly increases towards the apex and base of the structures. It will be demonstrated later that interplay between the size of the dot base and the strength of the biaxial strain in this area tends to localize holes in the lowest regions of the quantum structure. On the other hand electrons are not sensitive to the biaxial strain component and their probability distribution spreads over the entire volume of the artificial molecule.

4.4 Piezoelectric contribution

The piezoelectric effect is characteristic for crystals that lack a centre of inversion e.g. Zinc-Blende structures. This effect originates from stress-induced finite charge density polarisation and, as it will be demonstrated, plays an extremely important role in InGaAs stacked quantum structures. Using the reduced polarisation introduced in [209] the piezoelectric response can be expressed in terms of the stress up to the second-order,

$$p_\mu = \sum_i \tilde{e}^0_{\mu i}\eta_i + \frac{1}{2}\sum_{ik} \tilde{B}_{\mu ik}\eta_i\eta_k, \tag{4.13}$$

with the reduced proper piezoelectric tensor of the form,

$$\tilde{e}^0_{\mu i} = \frac{d}{d\eta_i}p_\mu = \tilde{e}^0_{\mu i} + \sum_k \tilde{B}_{\mu ik}\eta_k. \tag{4.14}$$

In the above equations η_i stands for the strain tensor in the Voigt form, $\tilde{e}^0_{\mu i}$ is the piezoelectric tensor of the unstrained material and $\tilde{B}_{\mu ik}$ is a tensor of rank five which contains Cartesian coordinates μ and strain index i, k [209]. Knowing the strain field distribution $\eta_i(\mathbf{r})$ one can calculate the piezoelectric charge density from the divergence of of the total polarisation,

$$\rho(\mathbf{r}) = -\nabla \cdot (\mathbf{P} + \mathbf{Q}), \tag{4.15}$$

where $\mathbf{P}$ is given by

$$\begin{pmatrix} P_x \\ P_y \\ P_z \end{pmatrix} = \begin{pmatrix} e_{11} & e_{12} & e_{13} & e_{14} & e_{15} & e_{16} \\ e_{21} & e_{22} & e_{23} & e_{24} & e_{25} & e_{26} \\ e_{31} & e_{32} & e_{33} & e_{34} & e_{35} & e_{36} \end{pmatrix} \begin{pmatrix} \epsilon_{xx} \\ \epsilon_{yy} \\ \epsilon_{zz} \\ 2\epsilon_{yz} \\ 2\epsilon_{zx} \\ 2\epsilon_{xy} \end{pmatrix}. \tag{4.16}$$

The InAs/GaAs semiconductor is characterized by the Zinc-Blende crystal structure, therefore only $e_{14} = e_{25} = e_{36}$ are non-zero piezoelectric coefficients which yields

simpler form of the matrix

$$\begin{pmatrix} P_x \\ P_y \\ P_z \end{pmatrix} = \begin{pmatrix} 0 & 0 & 0 & e_{14} & 0 & 0 \\ 0 & 0 & 0 & 0 & e_{14} & 0 \\ 0 & 0 & 0 & 0 & 0 & e_{14} \end{pmatrix} \begin{pmatrix} \epsilon_{xx} \\ \epsilon_{yy} \\ \epsilon_{zz} \\ 2\epsilon_{yz} \\ 2\epsilon_{zx} \\ 2\epsilon_{xy} \end{pmatrix}. \tag{4.17}$$

Derivation of the second order piezoelectric tensors in the frame of density functional theory [209] indicates that the second order polarization can be equally important in the InAs/GaAs heterostructure materials as the linear tensor. The second order polarization described by the last term in Eq.(4.13) depends on three non-zero coefficients B_{114}, B_{124}, B_{156} leading to the second order polarization tensor

$$\mathbf{Q} = 2B_{114} \begin{pmatrix} \epsilon_{xx}\epsilon_{yz} \\ \epsilon_{yy}\epsilon_{xz} \\ \epsilon_{zz}\epsilon_{xy} \end{pmatrix} + 2B_{124} \begin{pmatrix} \epsilon_{yz}(\epsilon_{yy}+\epsilon_{zz}) \\ \epsilon_{xz}(\epsilon_{xx}+\epsilon_{zz}) \\ \epsilon_{xy}(\epsilon_{xx}+\epsilon_{yy}) \end{pmatrix} + 4B_{156} \begin{pmatrix} \epsilon_{xz}\epsilon_{xy} \\ \epsilon_{yz}\epsilon_{xy} \\ \epsilon_{yz}\epsilon_{xz} \end{pmatrix}. \tag{4.18}$$

In order to compute the resulting piezoelectric potentials in the structure Poisson's equation is solved using relation,

$$\rho(\mathbf{r}) = -\epsilon_0 \nabla \cdot [\epsilon_r(\mathbf{r}) \nabla V_p(\mathbf{r})], \tag{4.19}$$

where ϵ_0 is a dielectric constant in vacuum and $\epsilon_r(\mathbf{r})$ is a material dependent static dielectric constant. The change in the piezoelectric potential is next found using,

$$\Delta V_p(\mathbf{r}) = -[\epsilon_0 \epsilon_r(\mathbf{r})]^{-1} \rho(\mathbf{r}) + [\epsilon_r(\mathbf{r})]^{-1} \nabla V_p(\mathbf{r}) \nabla \epsilon_r(\mathbf{r}), \tag{4.20}$$

The real three-dimensional charge density distribution is described by the first term of Eq.(4.20). The remaining term of Eq.(4.20), refers to the fact that the dielectric constant is different between two or more compounds of In(Ga)As, which leads to the additional small charge polarisation [210]. In computing the piezoelectric potentials the Fast Poisson solver, an algorithm developed by Peter McDonald, former member of Semiconductor Theory Group, is used [132]. In our PI-QMC code a constant value of the dielectric constant across the quantum structure is taken, therefore the last term of Eq.(4.20) is neglected.

The two terms in Eq.(4.13) are equally important in the case of In(Ga)As quantum structures [209, 210] due to the fact that they contribute to the total piezoelectric potential with opposite signs. Moreover, in highly strained vertically coupled structures the quadratic term is the leading one as multilayer, three-dimension confining and piezoelectric potentials interact strongly. The linear contribution to the piezoelectric field results in a similar-to-quadruple potential. This term possess a significant impact on the structural symmetry of a stacked structure reducing it from C_{4v} or $C_{\infty v}$ to C_{2v} [211–213].

Chapter 5

Lateral exciton switching in vertically stacked quantum dots

5.1 Introduction

This thesis is dedicated to lattice mismatched structures, in which the lattice constants of the two compounds that form the nanostructure are different. We consider here InAs and GaAs, which are commonly used in the growth of quantum dots and rings, and are characterized by lattice constants differing by ≈7 % [214]. The most common method for self-assembly of high quality quantum nanostructures is the Stranski-Krastanow (SK) growth mode. In this technique the surface morphological instability resulting from the relaxation of strain energy in lattice mismatched heterostructures is used to drive spontaneous nucleation, leading to the formation of coherent quantum structures [215]. The SK in-situ method is superior compared to other techniques, such as lithography, because the resulting structures are defect free but as the process relies on spontaneous relaxation the structures are formed randomly and their size varies. Different island sizes lead to significant broadening of optical transition energies, limiting practical applications [216]. The size non-uniformity problem can be overcome introducing multilayer structures. In this configuration buried quantum dots not only induce the nucleation and growth process of similar dimension dots in subsequent layers (Fig. 5.1), but also stimulate vertical alignment in the growth direction [23, 217–219]. Neighbouring QDs are strongly coupled, which leads to the formation of quantum dot molecules (QDM) with new and interesting properties, resulting from inter-dot interactions [220]. In this Chapter we report the novel

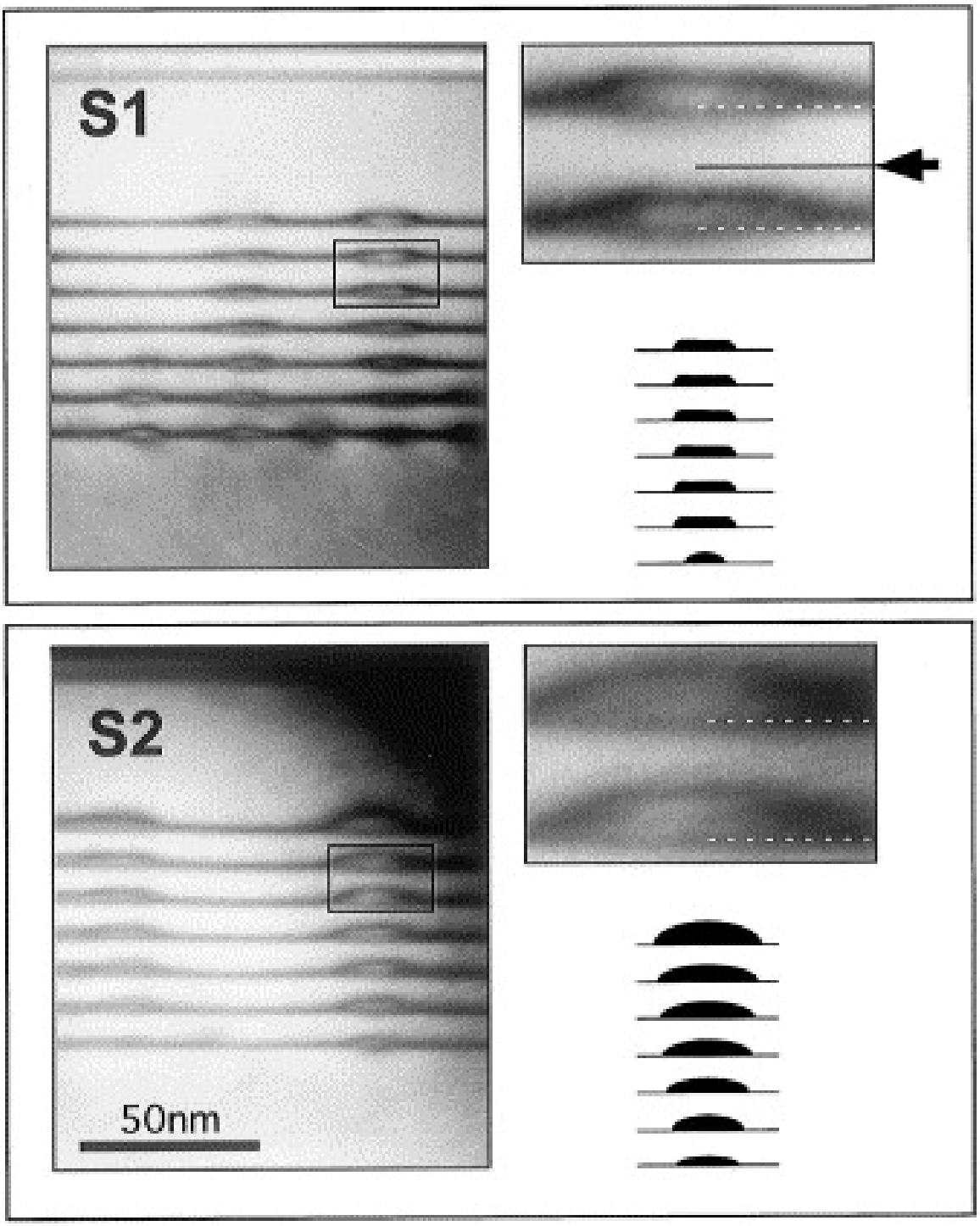

Figure 5.1: Cross-sectional TEM images of two samples of vertically stacked quantum dots. The right-hand side of the image shows magnification of the selected areas and a schematic of the trend in the TEM contrast for typical dot columns observed in the corresponding structure. For the sample S1, the arrow indicates the position of the Indium-flush plane Ref.[221].

exciton-based switch, theoretically realised in a coupled quantum dot using PI-QMC

simulations. The impact of an electric field (parallel to the growth direction) on exciton PL spectra is investigated and used to determine the lateral switching of exciton charge distribution in the coupled dots. Switching of the probability density of Coulomb interacting electron-hole systems in the plane perpendicular to the applied electric field and built-in dipole moment allow insight into the relative localisation of charge carriers in the semiconductor nanostructure. This plays a significant role when new devices assembled from densely packed interacting quantum structures are designed.

This Chapter has the following structure: in the following section the details of our atomistic model of the nanostructure are discussed. We start with discussion of the results of the lateral switching in a single dot and then we compare them to the triple dot structure explaining the physics of the excitonic switching. We end with some conclusions and a roadmap of further studies.

5.2 Atomistic model of vertically stacked quantum dot

Dimensions used in the atomistic model of a quantum dot and considered in this thesis is shown in Fig. 5.2. The single structure is a 4 -nm-tall $In_{0.5}Ga_{0.5}As$ truncated-conical dot of a base radius 10.2 nm and top radius 7.2 nm, located on a 0.9 nm thick $In_{0.3}Ga_{0.7}As$ wetting layer. A typical model contains approximately 17×10^6 atoms placed in a random alloy structure as described in [222], immersed in a GaAs matrix. The coupled system, Fig. 5.2, is formed by stacking single structures in the vertical direction with separation 3.4 nm between the top and the base of the adjacent dots.

The valence force field method [202] is used to relax the atoms to their equilibrium positions. These relaxed positions and residual forces are then used to compute the stress tensor for each atom. Finally, using continuum elasticity theory we map the stress to the strain fields [203]. The valence and conduction band energies shifts are extracted from the strain profile and included in the two band effective mass model Hamiltonian. Quantum dots are formed from the significant difference between the energy band gaps of InAs and GaAs. Lattice mismatch strain generates strong piezoelectric potentials (see Fig. 5.3), which contribute to a shift of the valence and conduction bands Fig. 5.4 and, as it will be shown, significantly perturb the electronic

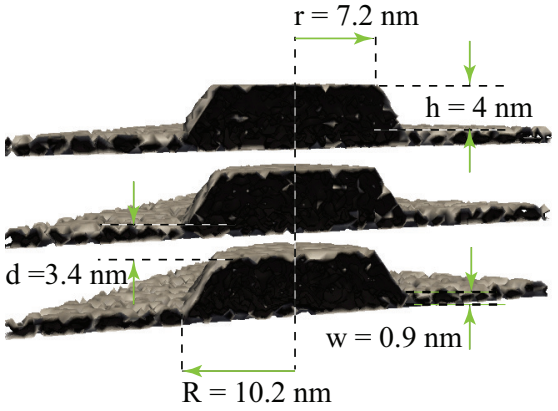

Figure 5.2: Cross-section of the atomistic model of vertically stacked quantum dot used in PI-QMC simulations.

states. In order to account for this perturbation the piezoelectric fields are carefully calculated up to the second order and included in all simulations.

5.3 Single dot case

Optical properties of single quantum dots are well known and can be considered as a reference point in an investigation of more complicated nano-structures. Studies of artificial atoms [223] consisting of multiple dots were preceded by the detailed analysis of the confined exciton in a single dot with and without a vertical electric field. Such a field can be easily introduced to the system by embedding nano-structures inside of an intrinsic layer of a *n-i-p* junction. This method offers addition benefits like the injection of charge carriers from the doped layers [146].

5.3.1 Charge distribution in single dot structure with and without the external electric field

Electrons and holes which form an exciton are subject to different confining potentials in the growth direction. This results in a spatial separation of electrons and holes producing a permanent dipole moment [126, 224–226]. The dipole couples to the external electric field. The dipole couples to any external electric field which will pull (push) the electron-hole system apart (together) in the vertical direction and affects its oscillator strength and mutual Coulomb attraction. The size of the dipole depends strongly on the dot composition profile, in particular on the In concentration [129].

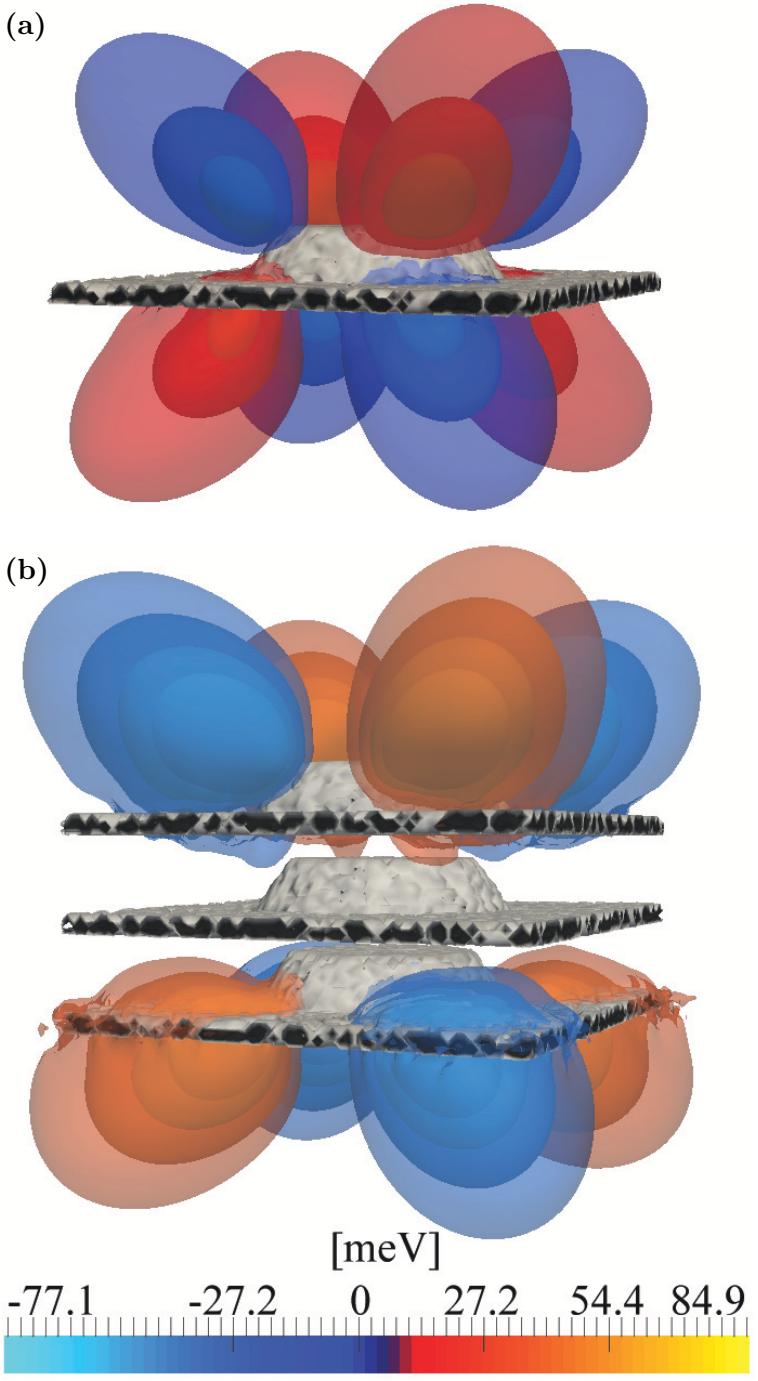

Figure 5.3: Comparison of piezoelectric potentials in the form of iso-surfaces for (a) single and (b) triple system.

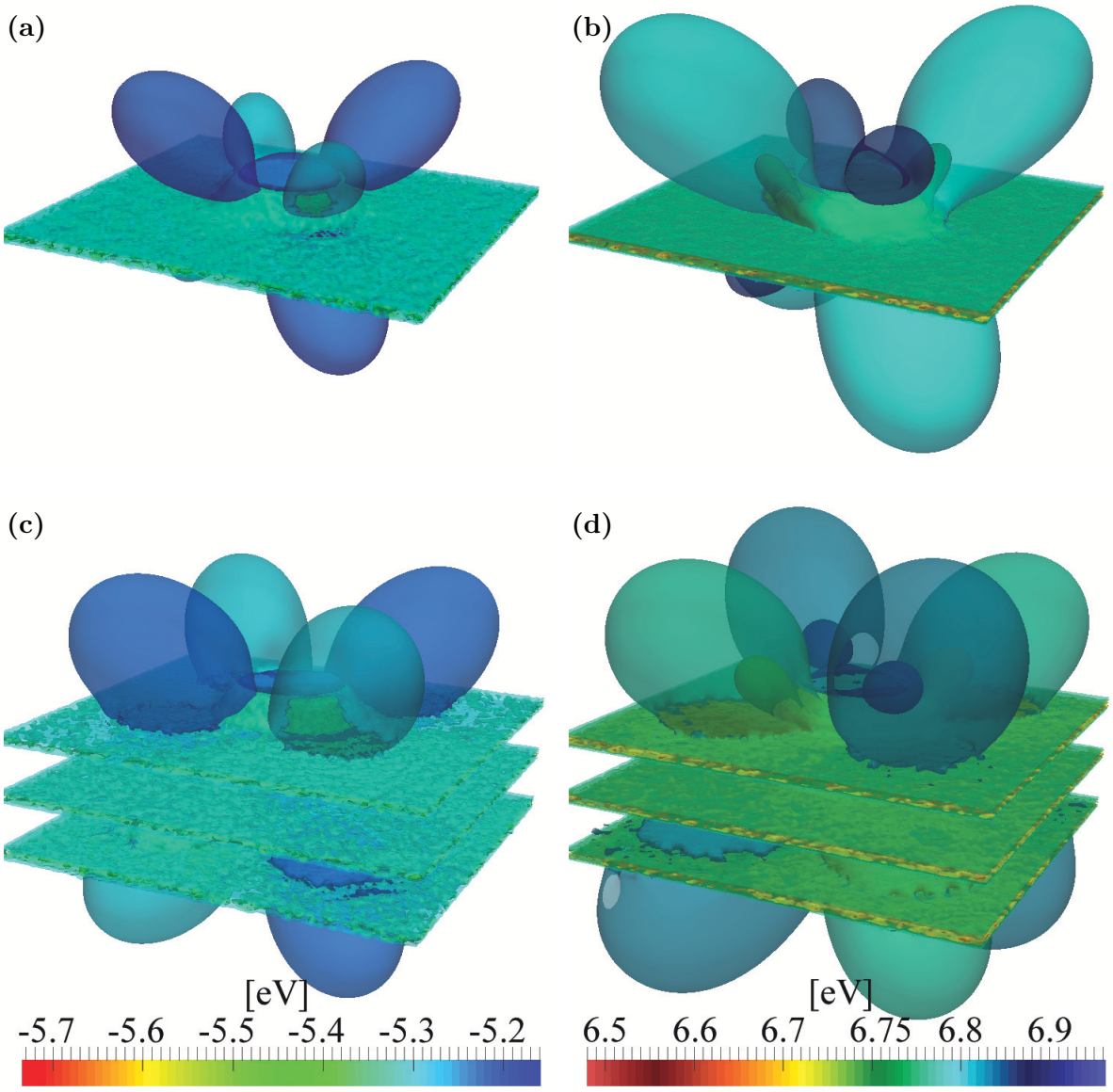

Figure 5.4: Strain and piezoelectric field modified conduction band in (a) single and (c) triple dot structure. Valence band of (b) single and (d) triple atomistic model quantum dots is also presented.

We theoretically studied the influence of two opposite orientations of a static electric field E along the growth direction on the single particle and bound states in a quantum dot Fig. 5.5. The Path integral technique allowed us to explore the impact of the field (0 to $\pm 80\,\mathrm{kV/cm}$) on the charge distribution of Coulomb interacting particles over a broad range of temperatures. The charge density distribution can be obtained directly from sampling the thermal density matrix of the system during the PI-QMC simulation.

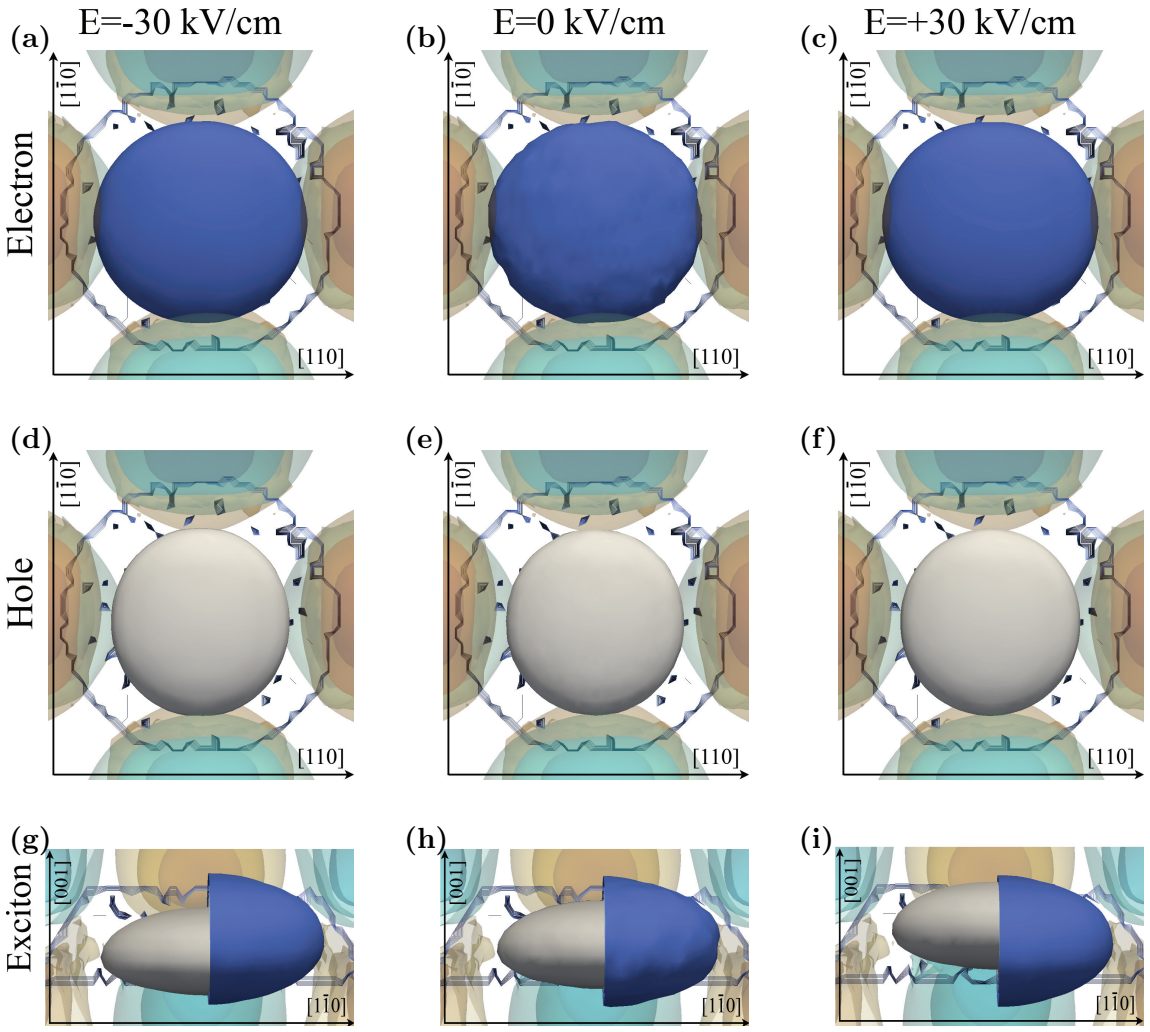

Figure 5.5: Single quantum dot. Cross-section of the single particle and exciton probability distributions (volumetric plot) with and without vertical ([001]) electric fields at 10 K. The piezoelectric potential and the outline of the quantum dot structure are also included.

In Fig. 5.5 the probability distribution of the electron, hole and exciton is compared for different values of external electric field. In Figs. 5.5a - 5.5c the probability distribution of the ground state electron is plotted in the [110] direction. One can see that strength and orientation of the electric field does not affect the probability distribution of the charge carrier. In all three cases the electron distribution profile is slightly elliptical indicating, already pointed out fact, that confinement in the [110] and [1$\bar{1}$0] differ. In Figs. 5.5d - 5.5f the probability distribution for the hole is depicted. One can see that also in this case the probability distribution is uniform irrespectively of the electric field orientation.

The slice through the centre of a single dot in the [1$\bar{1}$1] direction, Figs. 5.5g - 5.5i,

shows the charge density profile of the heavy-hole exciton as a function of the applied field. It is clearly visible that the quantum dot has an inverted (electron-over-hole) permanent dipole moment even with 0 kV/cm applied electric field. This indicates a strong In atom concentration gradient. The above result is in excellent agreement with experimental data reported by *Warburton et al.* [126], and indicates that our atomistic model correctly reflects properties of real self-assembled quantum dot. This effect originates from the biaxial strain distribution, which changes with the height of the structure. At the bottom of the dot the biaxial strain is large and positive, while at the apex the situation changes leading to the swap of the sign of the strain. The hole confining potential includes a contribution proportional to the biaxial strain, therefore the potential well experienced by the hole is deeper towards the base of the dot, promoting localisation of the hole wave function in that region [129]. The piezoelectric potential adds to the strain fields and perturbs the valence band, amplifying the localisation of the hole wave function in the [110] direction, Fig. 5.4b. The conduction band is very weakly affected by biaxial strain, allowing the electron charge distribution to be delocalised in the structure and even tunnel into the barrier material. The piezoelectric potential interacts with the conduction band, but, as shown in Fig. 5.4a, the minima are shallower and appear to not directly overlap with the confining potential in the structure. The vertical electric field applied to the system stretches the electron-hole pair reducing the exciton binding energy. The orientation of the E field also has a significant impact on the polarity of the exciton in the single quantum dot as shown in Fig. 5.5g and 5.5i.

In summary, we have shown that the interplay between the electric field and piezoelectric potential with an exciton in a single, self-assembled quantum dot is insufficient to induce spatial localisation of the charge distribution in the plane perpendicular to an applied field. We conclude that the difference in confinements for an electron and a hole on the $[1\bar{1}0]$ and [110] diagonals is compensated for by the piezoelectric field, which suppresses a change in the localisation of the exciton probability distribution in the lateral direction.

5.4 The linear response theory

Lateral switching phenomenon which we are discussing in the next section can be identified by computing the polarizability of the exciton. The PI-QMC simulations

allow for estimation of these polarizabilities using linear response theory. This perturbative approach gives us insight into how the system will respond to an external vertical electric field in its absence, or in other words we look for the value of α in the Stark effect using the perturbation expansion,

$$E = E_0 - Fd - \frac{1}{2}\alpha F^2. \tag{5.1}$$

In Eq.(5.1) E_0 is energy of the system in the absence of an external electric field F and d is the permanent dipole. Applicability of the above technique results from dipole fluctuations due to the thermal excitations of the system. The linear response theory relates those fluctuations to the polarizability of the exciton. It follows from the above that the time order temperature correlation function can be expressed in the form [132]

$$\chi_{dd}(\tau) = -\frac{1}{\hbar}\langle d(\tau)d(0)\rangle, \tag{5.2}$$

where the dipole operator d at imaginary time τ and 0 is thermally averaged. We note that the Hamiltonian is not time dependent, however differences in time cannot be neglected. This lets us Fourier transform Eq.(5.2) into imaginary frequency given by Matsubara frequencies $\omega_n = 2\pi n/\beta\hbar$ as follows,

$$\chi_{dd}(i\omega_n) = \int_0^\beta e^{i\omega_n\tau}\chi_{dd}(\tau)d\tau. \tag{5.3}$$

In the limit $\lim_{i\omega_n\to\infty}$, using analytic continuation [132] the frequencies converge to the real axis,

$$\alpha(\omega) = \lim_{i\omega_n\to\omega_n+i0^+} -\chi_{dd}(i\omega_n). \tag{5.4}$$

During the PI-QMC simulation the correlation data Eq.(5.2) are obtained and Fourier transformed resulting in Matsubara frequencies. Those Fourier transformed data, (Eq.(5.4)) have a Lorentzian form in the imaginary axis direction and the best fit to this data is estimated using the least squares method [132]. The simplest case is the simple harmonic oscillator as all dipole transitions possesses the same energies, therefore only one Lorentzian is sufficient for best fit to data. More complicated systems are usually a linear combination of these functions and in most situations two Lorentzians are enough to obtain good fit. The polarizability value for the given system is then a point at which the best fit line crosses the real axis. This method provides excellent accuracy as discussed in [132].

5.4.1 The recombination rates and the quantum-confined Stark effect

Electron and hole probability densities overlap. This is a property of the few-body state in semiconductor nanostructures and may be computed using effective mass parameters. The steady-state's occupation, driven by continuous photo-excitation of the nanostructure, can be analysed by calculating the rates of photoluminescence (PL), Fig. 5.6. These radiative recombination rates are calculated using the PI-QMC

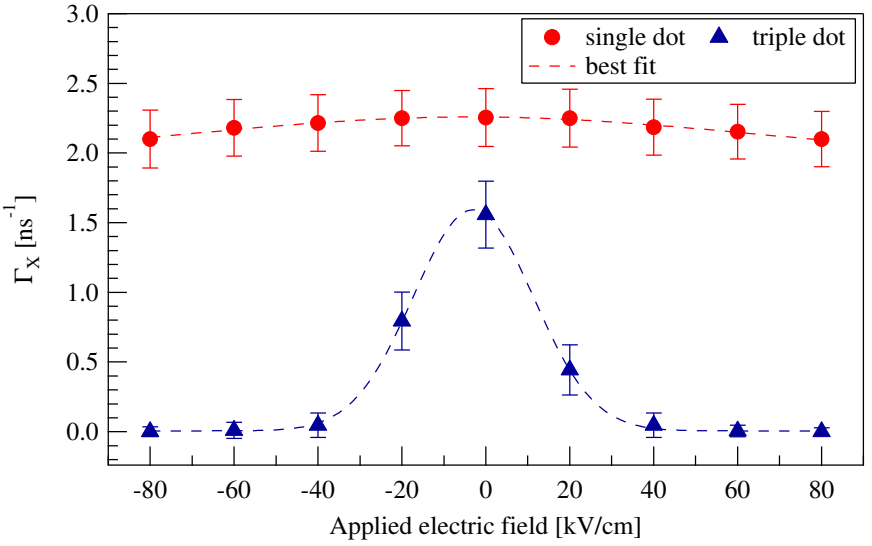

Figure 5.6: Exciton recombination rates as a function of applied electric field in the vertical direction with the lines of best fit. The error bars arise from the statistical uncertainty of the PI-QMC calculation.

technique [188], as will be discussed in Chapter 7 and can be experimentally measured using time-resolved methods [227]. The rate of recombination depends on two important factors: the relative spatial distribution of the electron and hole, and the semiconductor compound dipole moment which affects recombination rates through Fermi's golden rule. In a single quantum dot (Figs. 5.5a-5.5f) in-plane probability density distribution, which is the wave function squared, of an exciton is unaffected by the orientation of the vertical electric field. This indicates that the electron and hole wave function can spread significantly in entire volume of a single dot structure resulting in their smaller overlap. Such a distribution results from the fact that the difference between the confining potential in the [110] and [1$\bar{1}$0] is rather small and insufficient to induce stronger localisation of the particles in one direction. This result was further confirmed by examining the lateral polarizability and energy fluctuation

of PL emission from the exciton observed by the Quantum Confined Stark Effect (QCSE) Fig. 5.7. The QCSE for a single and triple dot structure differs significantly. The triple dot structure demonstrates a much larger shift, compared to the single dot, and a strong non-parabolic dependence on the inter-band transition energy on the applied electric field. The single dot shows conventional, almost quadratic dependence on the applied external field observed in many other types of single quantum dots. We account this discrepancy for significantly stronger strain fields present in the triple dot system which affects energy bands structure and which results in a charge carriers dynamics. In Fig. 5.7 due to the different energy range for the single and triple system this distribution looks almost linear compared to the triple dot. The results presented here are in very good agreement with other theoretical calculations, for comparison see [228].

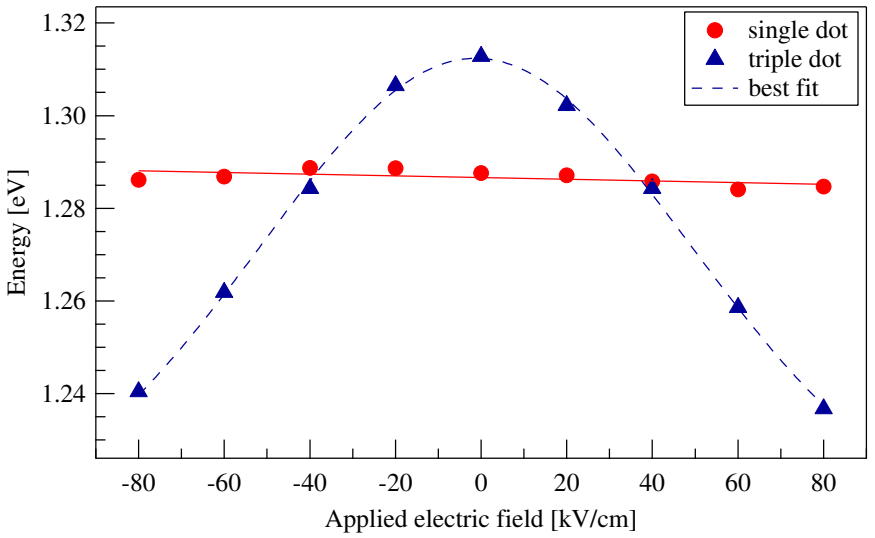

Figure 5.7: Comparison of energies of PL emission for an exciton as a function of applied external electric field in single and triple quantum dot. The electric field is oriented in the [001] direction.

In Chapter 7 the confinement limits associated with size of the quantum system will be outlined in details. Here we only point out that both the single and vertically stacked quantum dots used in our simulations are much larger than the average excitonic Bohr radius (≈13 nm in GaAs) which place them in the weak confinement limit. In such a case single particle energies are dominated by the Coulomb interactions and excitons forms composite particles whose dynamics are governed by potential fields in the dot structure. In the single dot the wave functions of the electrons and holes are strongly localised in the structure and every unit cell of the dot contributes to the exciton's oscillatory strength. This effect, known as a super-radiant effect [229], leads

to an increase of oscillatory strength and results in the high recombination rate Fig. 5.6 as the electron and hole are nearby. The recombination lifetime is given by [229]

$$\frac{1}{\tau} = \frac{2n\pi e^2 f_{osc}}{3\lambda_{PL}^2 \epsilon_0 c m_0}, \tag{5.5}$$

where n is the refractive index (3.5 for GaAs), f_{osc} is the transition oscillator strength, λ_{PL} is the emission wavelength. In the weak confinement limit the electron and hole wave function the overlap is small which decreases even further with increasing E-field pulling the electron and hole in opposite directions. This reduces recombination rates and is clearly reflected in the size of the error bars for a single quantum structure, which can be interpreted from the uncertainty principle point of view. As we observe that the electron and hole are localised in the dot, the uncertainty in their position decreases, therefore the uncertainty in the recombination rate must increase. As the electric field stretches the exciton in the vertical direction and forces it to oscillate, the localisation of the electron and hole becomes more uncertain and the error in the recombination rate starts to decrease. Also due to the charge and the effective mass they respond differently to the strain fields in quantum dots [150] in particular the biaxial strain which predominantly affects the confinement of the hole. Piezoelectric extrema on the other hand are located outside the island (Fig. 5.3b) and their perturbing impact on the confining potentials, and therefore the ground-state wave functions of the particles is minimal. These observations seems to be consistent with the experimental results by *Dalgarno et al.* [229] however our systems differ significantly.

5.5 Lateral switching in coupled quantum dots

In this section a system made of two and three, vertically stacked quantum islands will be discussed. Such a structure demonstrates the new, interesting phenomenon of lateral switching of charge distribution, not reported in literature so far.

In Fig. 5.8 the probability distribution of the electron, hole and exciton in a triple quantum dot is presented. We compare the single particle states Figs. 5.8a - 5.8f plotted in the [110] plane (top view) with Figs. 5.8g - 5.8i the bound states plotted in the $[1\bar{1}1]$ plane with and without the static electric field. In contrast to the single dot, the most striking feature of the triple quantum dot system is a strong,

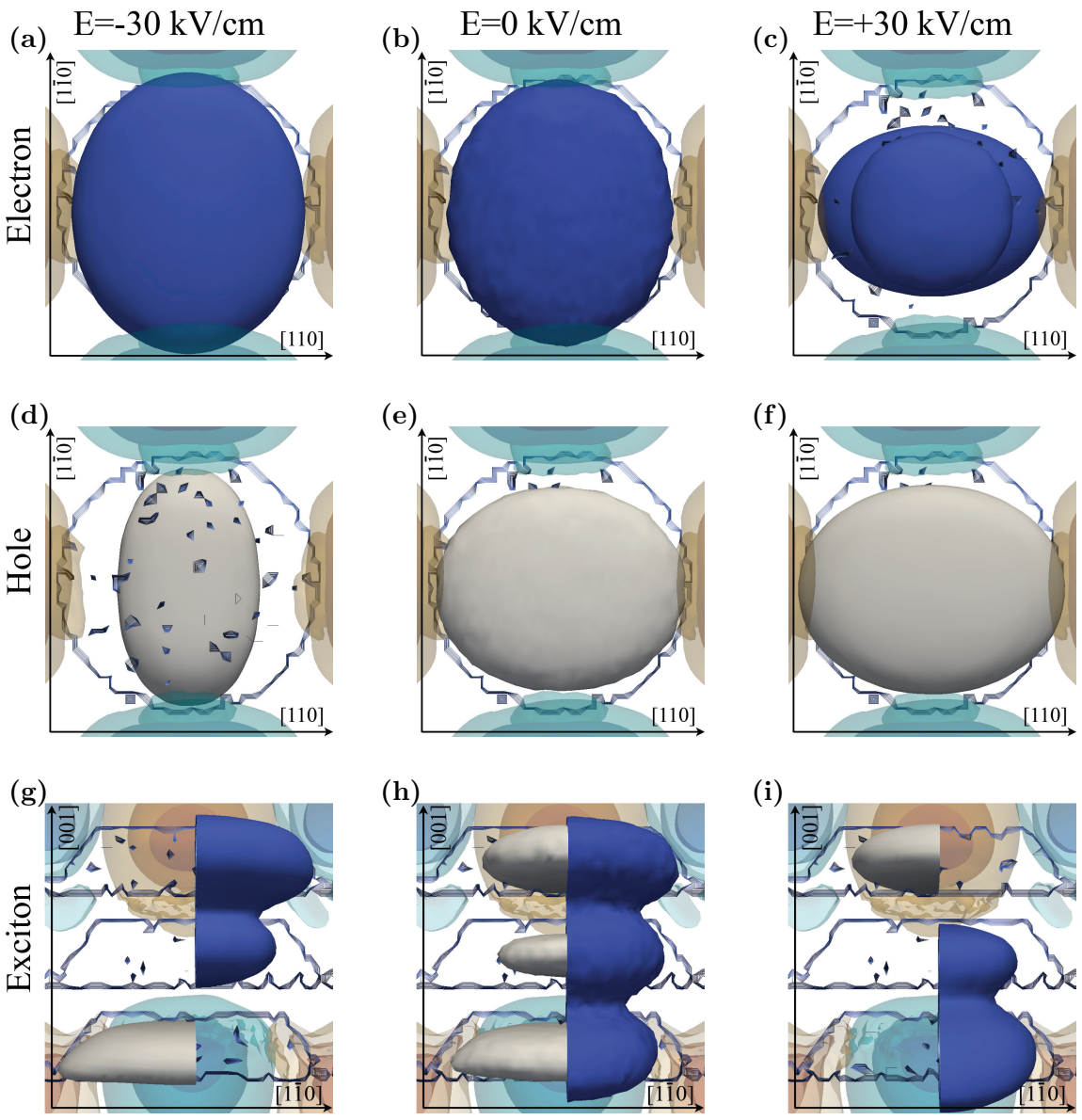

Figure 5.8: Coupled quantum dot. Cross-section of the single particle and exciton probability distributions (volumetric plot) with and without vertical ([001]) electric fields at 10 K. The piezoelectric potential and the outline of the quantum dot structure are also included.

diagonal localisation of the charge distribution which we can accurately switch in the plane of the quantum dot by changing the direction of the perpendicular electric field. It is important to note that probability distribution in the top island for both the electron and the hole is rotated by 90 degrees at two different fields compared to the bottom one (see Figs. 5.8g and 5.8i). In fact we are looking through all three quantum structures from the top, therefore we see the residues of the distribution in the middle and bottom quantum dots.

Compared to the single quantum dot the much larger volume of alloy in the coupled structure induces a stronger piezoelectric potential. The piezoelectric field perturbs the confinement for the electron and hole, Figs. 5.4c and 5.4d. An interesting characteristic of the triple dot system is that the piezoelectric field originating from the central dot is cancelled by fields from the top and bottom structures. This leads to the symmetry along the [110] and [1$\bar{1}$0] diagonals for the middle dot. The piezoelectric potential penetrates into the top and bottom structures creating local minima and maxima in the dot confining potential, Figs. 5.4c and 5.4d.

In Fig. 5.8b the top view of the electron charge probability distribution is compared to the electron distribution in the vertical cross-section Fig. 5.8h in the absence of an external electric field. We see strong delocalisation of the electron probability density in the whole dot volume, Fig. 5.8b. Additionally coherent tunnelling of the electron result in delocalised molecular states which manifests itself as a simultaneous probability density distribution in all three quantum dots and inter dot barrier [148], Fig. 5.8h. According to [148] this distribution corresponds to a bonding state. The electron in the triple dot structure can be in the one of the three basis states in which the particle is in one dot or another [148]. The tunnelling of the electron between three dots results in formation of molecular states that are symmetric and antisymmetric superposition of these basis states. The hole charge distribution however, is stronger confined to the central region of the dot, Fig. 5.8e. In Fig. 5.8h it is also apparent that the hole charge distribution is shifted toward the base of each dot with the highest probability to be found in the top and bottom quantum islands, additionally the hole probability density distribution is completely suppressed in the inter dot barrier which corresponds to antibonding state [148]. As already indicated, the confinement differs in all three structures and also along diagonals in the plane of the dots. The top and bottom dots are characterised by deeper wells compared to the middle one. The repelling action of positive piezoelectric lobes and different strength of confinement on the diagonals naturally favours localisation of the hole in

an outer dot, as much more energy is required to overcome the barrier and transit to the central structure. This is clearly visible in Fig. 5.8h. A zero electric field promotes the occurrence of strong electron-hole wave function overlap, which results in the radiative recombination (Fig. 5.6) and higher oscillator strength direct exciton, as the electron and hole occupy the same dot structure, Fig. 5.8h.

A vertical [001] electric field applied to the structure polarises the exciton in the growth direction and creates a localisation of the charge distribution on two planes [110] and [1$\bar{1}$0], perpendicular to the static electric field. It also tilts the energy bands resulting in the shift of excitonic emission lines due to the Quantum Confined Stark Effect. This manifests itself in a vertical and lateral switching of the ground state probability distribution between two diagonals and a field driven transition to a spatially indirect exciton, as positive and negative charges are attracted by opposite structures, Figs. 5.8g and 5.8i. In Figs. 5.8a and 5.8d the electron and hole elongated charge distribution is shown for -30 kV/cm. Changing the orientation to +30 kV/cm rotates the distribution 90°, Figs. 5.8c and 5.8f in the plane of the quantum dot. It is apparent from comparison of distributions for different values of an electric field in Fig. 5.8 that the switching of the charge distribution is not equal on two diagonals for both charge carriers. The lateral switching is much more pronounced for the hole than for the electron, due to the fact that the hole undergoes much stronger localisation in the dot than the lighter electron. Moreover the electron is not susceptible to biaxial strain, which dominates the quantum island, therefore its distribution in the structure is approximately uniformly spread between all three dots.

The lateral switching originates from the complex strain profile of coupled structures and the corresponding piezoelectric potentials penetrating the dots. Calculations of the electron-hole recombination rate Fig. 5.6 and energy Fig. 5.7, for different values of gate voltage show high oscillator strength, particularly for the small values of the electric field between ±30 kV/cm. For the stronger static electric potentials, e.g. ±80 kV/cm, the fields overcome the Coulomb attraction and dissociate the exciton. At this point the electron and hole occupy different structures, wave functions do not overlap any more and the oscillator strength drops essentially to zero. This is also clearly reflected in the recombination rate, which completely disappears (Fig. 5.6) as both the dipole moment and the charge spatial separation is large.

As the exciton transition goes from spatially direct to indirect, the oscillator strength varies for different values of the external field. Due to the different potentials

on planes [110] and [1$\bar{1}$0] the measured oscillator strength is not symmetric around the 0 kV/cm point, as the exciton is attracted by local minima and maxima in top and bottom structure in a different way. Changing the direction of the electric field in the vertical direction lowers the energy on one of the diagonals and promotes the lateral switching between the [110] and [1$\bar{1}$0] directions, Fig. 5.8. As a result, an increase in the lateral polarizability tangential to the direction of the confining potential is observed Fig. 5.9. It is important to notice that the lateral switch operates only for

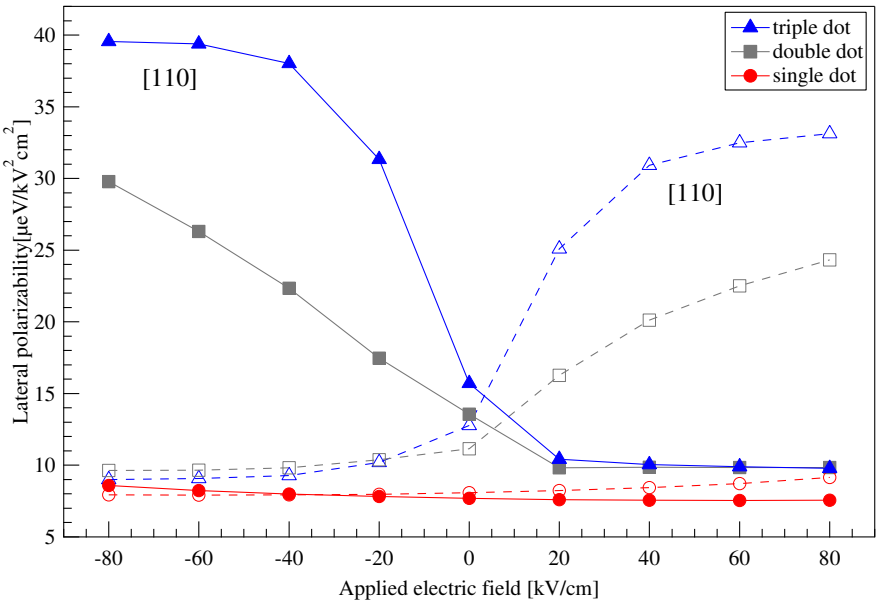

Figure 5.9: Comparison of lateral polarizability calculations of exciton in the [110] and [1$\bar{1}$0] direction versus applied vertical electric field for different heterostructures.

values of electric field in the range ±30 kV/cm. Stronger fields, more than ±40 kV/cm, break the exciton. The unbounded charge carriers are then attracted and trapped by the piezoelectric extrema and the lateral polarisability remains constant in the triple dot structure. Orientation of vertical electric field still swaps their spatial distribution in the triple quantum dot molecule, however the lateral switching is not possible anymore, due to its Coulombic nature.

The situation is a little different in a double dot, in which the lateral switching is preserved even for higher values of E. The smaller volume of the alloy in a double dot creates a weaker piezoelectric potential which attracts the charges. The electron and the hole are able to tunnel between the top and bottom structures as the dots are relatively close. The sum of the piezoelectric and confining potentials is however strong enough to preserve the Coulomb interaction and sustain the lateral switching. When the orientation of the external electric field is changed the polarizability in the

$[1\bar{1}0]$ direction is much larger. It is clear, Fig. 5.9, that the response of the exciton to the electric field in a single dot is extremely weak compared to the multiple structures. This is caused by the electron and the hole occupying of the same structure. The small vertical separation between the electron and the hole create much a weaker dipole, which in addition is tightly bound by the confining potential of the single quantum dot. A coupled structure's bright states can be examined experimentally by measuring the lateral polarisability of the exciton, which determines the sensitivity of excitonic energy to an electric field, Fig. 5.9, and can be use to confirm the lateral switching phenomenon.

5.5.1 Electron-hole pair correlation function

Further insight into the electron-hole distribution in the single and coupled quantum dot systems can be obtained from the pair correlation function $g(r)$. In Fig. 5.10 pair correlation data are plotted for the single and triple dot, for two different values of temperature with and without an electric field. We study two opposite values of the electric field at $\pm 30\,\mathrm{kV/cm}$. As before, we start with the single dot system without an electric field and compare it to the coupled structure. In Fig. 5.10b the pair correlation function (PCF) for the single and triple system is plotted for 10 K and 70 K without an electric field. The exciton in the single dot is strongly bound by the Coulomb interaction and the structures vertical extent. Therefore the particle separation is equal to the physical height of the structure which is 4 nm. This separation can often be slightly greater, as the electron is free to tunnel into the surrounding material, and the hole favours the bottom of the structure in order to stay away from areas of high biaxial strain. Increase of the temperature of the system only weakly affects the electron and hole separation in a single structure due to the finite quantum well depth. Higher temperatures provide more kinetic energy to particles in the system and weaken the Coulomb interaction. This allows the charge distribution to spread in and even outside the dot. On the other hand this effect is counterbalanced by the confinement of the island, and the difference between the PCF for single dot at 10 and 70 K is negligible. The PCF of a triple dot structure without an electric field, Fig. 5.10b, shows some additional features not present in the single quantum dot. At 10 K we see two distinguishable maxima at 4 nm and 12 nm, Fig. 5.10b. The first, lower maximum, corresponds to the direct exciton when the particles occupy the same structure. The second one indicates the indirect exciton when the electron and the

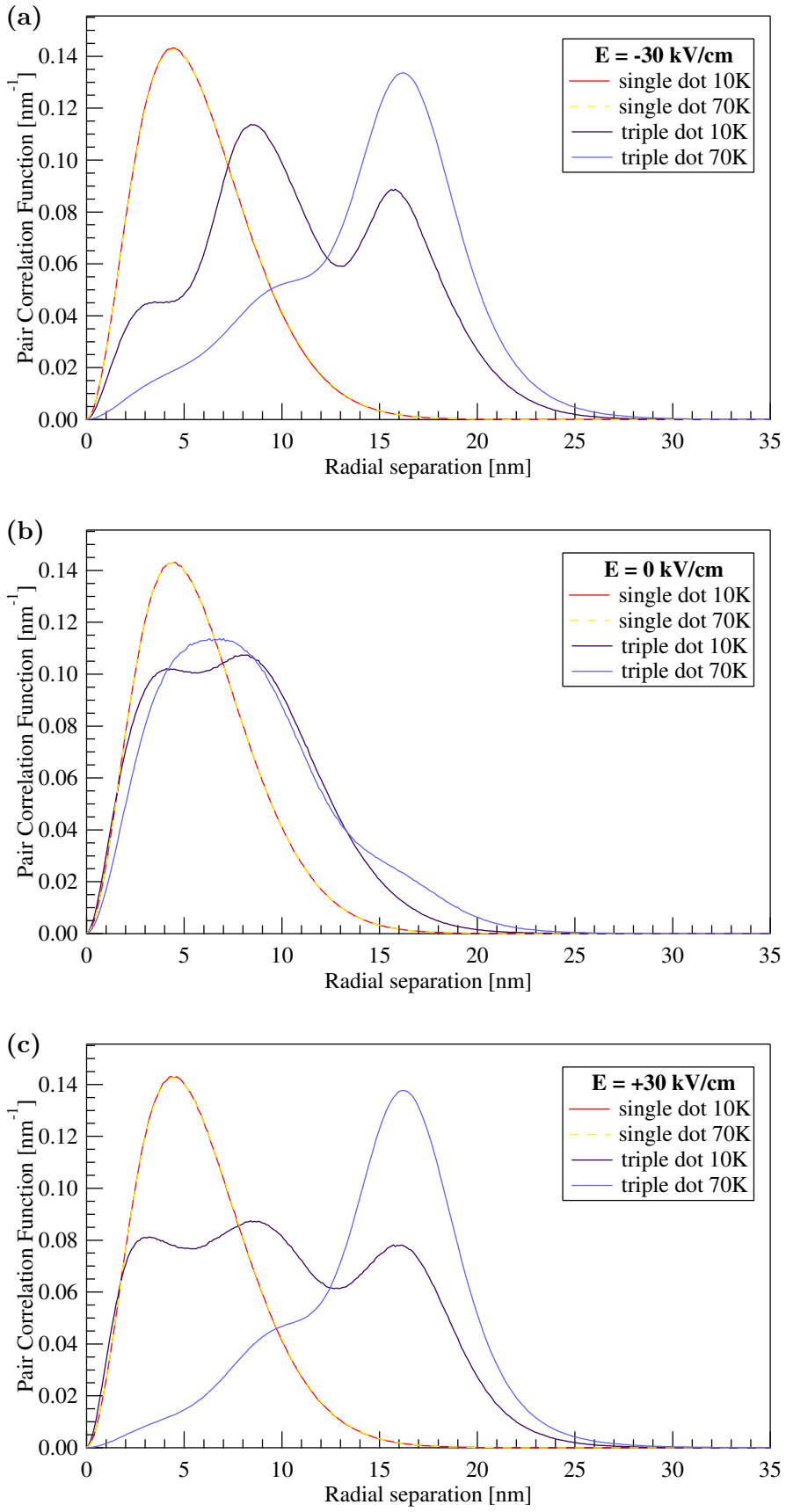

Figure 5.10: Pair correlation function for the single and triple quantum dot in the presence of the electric field ±30 kV/cm at temperature 10 and 70 K.

hole remain in the top and bottom dots respectively. At 70 K the thermal energies of the electron and the hole are higher, therefore we see a smooth curve with the maximum slowly varying over the whole structure height. The increase of thermal energy excites the electron-hole pair and makes them more mobile. We can observe a more uniform distribution of charge density over the cross-section of the whole coupled structure. Moreover, a small secondary maximum at a distance of ≈ 17 nm indicates a finite probability of finding the exciton outside the coupled dot.

The application of a vertical electric field to the system affects the single and multiple structures in completely different ways, Figs. 5.10a and 5.10c, particularly for low temperatures. The plot of the PCF for the single quantum dot does not change when the external field is applied. The strong confining potential of the structure keeps the exciton localised in the dot. The hole, which is much heavier than the electron, occurs towards the base of the quantum dot. The electron on the other hand is delocalised in the whole structure, including tunnelling into the barrier material. The positive hole and the negative electron form the electric dipole. In the single dot system the electric dipole moment is comparable to the height of the structure. Application of an external electric field stretches/compresses the electron-hole pair in the vertical direction. Changing the orientation of the field flips the system's overall polarity, however the electron-hole separation is only marginally affected. The system's response to the rise of temperature from 10 to 70 K is also marginal.

The coupled quantum dots are far more sensitive to the change of environmental conditions compared to the single one, Fig. 5.10a. We see that even small alterations, e.g. the orientation of static field, yields substantial variations in the charges' relative position. For T=10 K and E=+30 kV/cm the most energetically favourable configurations the one in which the electron and hole are confined to neighbouring dots. The charge carriers tunnel between the middle and bottom (top) quantum dot, however the lowest to middle transition dominates. This effect is a consequence of the biaxial strain distribution. Coupled dot structures can be seen from two points of view. As the structure is assembled from three dots separated by a GaAs barrier, each constituent dot is characterised by the In concentration, with a maximum at the apex. The hole prefers to stay away from the region of high concentration and therefore is localised at the base of the quantum dots. If the quantum post [146] resemblance is considered, then coupled dots form a single tall structure. This structure contains relatively more In at the apex than at the base. This clearly shows the apparent similarities between quantum posts and coupled dots. The electric field creates a dipole by

stretching the exciton towards the top and base of opposite dots, promoting inter-dot tunnelling. In the low temperature limit and for a positive E-field, the electron and the hole tend to occupy neighbouring structures, Fig. 5.10c, in this case the bottom and the middle dot. When the sign of E is negative the occupancy of the middle and top dots dominates. In both configurations the middle dot is always populated with the highest probability and by the electron. This indicates the important role of the biaxial strain, which is the strongest in the middle structure, and the piezoelectric field which is absent in the middle dot. As the temperature of the system increases the electron and hole experience thermal excitation. That energy allows them to overcome confinement of the structures and localise themselves on the top and bottom structures in the form of an indirect exciton.

5.5.2 Temperature dependence

One of the difficulties with lateral excitonic switches is the limited exciton life-time and temperature dependent exciton binding energy. The exciton lifetime is rather short, approximately 2 ns in direct gap semiconductors like InGaAs. Another problem results from the temperature of the system which affects the exciton binding energy, as $\approx E_{binding}/k_BT \approx 1$, at room temperature. In the following section we present a study of single and coupled dot systems in a broad temperature range of 10 to 310 K.

In Fig. 5.11a the ground state energy of the system of single and coupled dots as a function of temperature expressed as energy is compared. The temperature dependence of the experimentally measured band gap energy for bulk InGaAs has been removed. This is a necessary adjustment as the difference in band gap energy for ΔT=300 K is about 8 meV [230]. We see that the curves for opposite orientation of the electric fields cross each other. By inspection of Fig. 5.11a we observe that the temperature value at which this feature appears is the same for both the single and double systems. Triple dots require more thermal energy to follow this pattern, and also the curve separation before and after crossing is less pronounced. We attribute this to the existence of an additional potential, which is experienced by the charge carrier when the electric field forces it toward the base of the dot. This is especially apparent in the single structure. We observe the monotonic increase in the thermal energy of the interacting particle as the system gets hotter. When the thermal energy of the system overcomes the Coulomb attraction the exciton dissociates and the probability of finding the electron and hole in the structure drops rapidly. In Fig. 5.11b

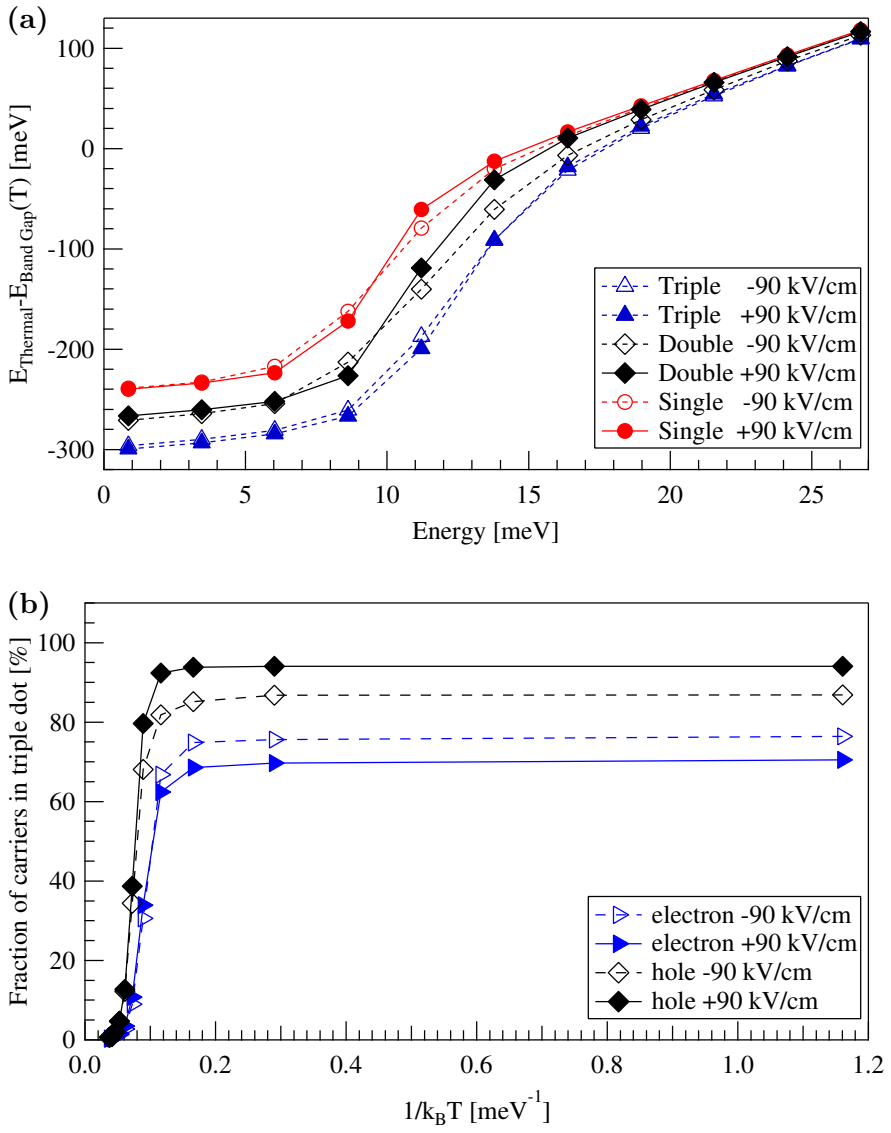

Figure 5.11: (a) Comparison of ground state energy of a single, double and triple quantum dots. We consider two opposite orientations of electric field $\pm 90\ kV/cm$. In (b) the percentage of the charge carriers in the quantum dot structure vs. temperature in the form of energy is presented.

the fraction of charge carriers remaining within the structure is shown for electron and hole for two opposite orientations of electric field. The percent of the distribution in the coupled dots shows that, even for relatively low temperatures, charge carriers are not completely confined to the dot regions. We notice that the rate of leaking of the electron and hole out of the structure depends on the orientation of electric field, which was already observed in the energy case. We conclude that the presence of a potential well in the form of a wetting layer plays a significant role in the tunnelling process, trapping both electron and hole when the electric field acts opposite to the

growth direction.

The exciton in the quantum dot exhibits a large binding energy due to the fact that charge carriers are strongly confined in all three spatial dimensions. In our single dot at low temperature the electron and hole wave functions strongly overlap each other due to the fact that the size of the structure is comparable to the excitonic Bohr radius. The presence of the electric field polarises the electron-hole system in the [001] direction, lowering the overlap between the wave functions of the charge carriers. When the temperature increases, intuitively we expect a decrease of the binding energy as the charge carriers acquire more kinetic energy. However we observe the opposite phenomenon here. When the temperature increases the wave functions of electron and hole overlap significantly more due to the finite size of the confining well, however the overall energy of the system is still not sufficient to free the particles from the confining potential, hence the binding energy increases. This effect is even stronger in the case of zero electric field as an absence of an induced electric dipole allows the excitonic wave function to spread within the whole region. In Fig. 5.12a the binding energy for the single and triple dot system in an electric field is compared to one without an electric field Fig. 5.12b. We see that for the single dot the increase of binding energy is much more pronounced as the wave function can only slightly penetrate into the barrier material.

In the triple dot system the wave function of the electron and hole may spread over the whole structure, reducing the Coulomb interaction and lowering the binding energy due to the vertical tunnelling of charge carriers. The coupled dot system undergoes a slightly different process, however the picture is consistent with the single dot. In the presence of zero electric field the electron wave function is spread in all three structures and the hole wave function, affected by strong, non-uniform biaxial strain, prefers the top and bottom structures. When the temperature is raised the holes overcome the strain and tunnel between the structures. Their wave functions overlap in all dots adding to the overall binding energy, inset Fig. 5.12b. The applied electric field effectively suppresses tunnelling, polarising the electron and hole into the top and bottom dots.

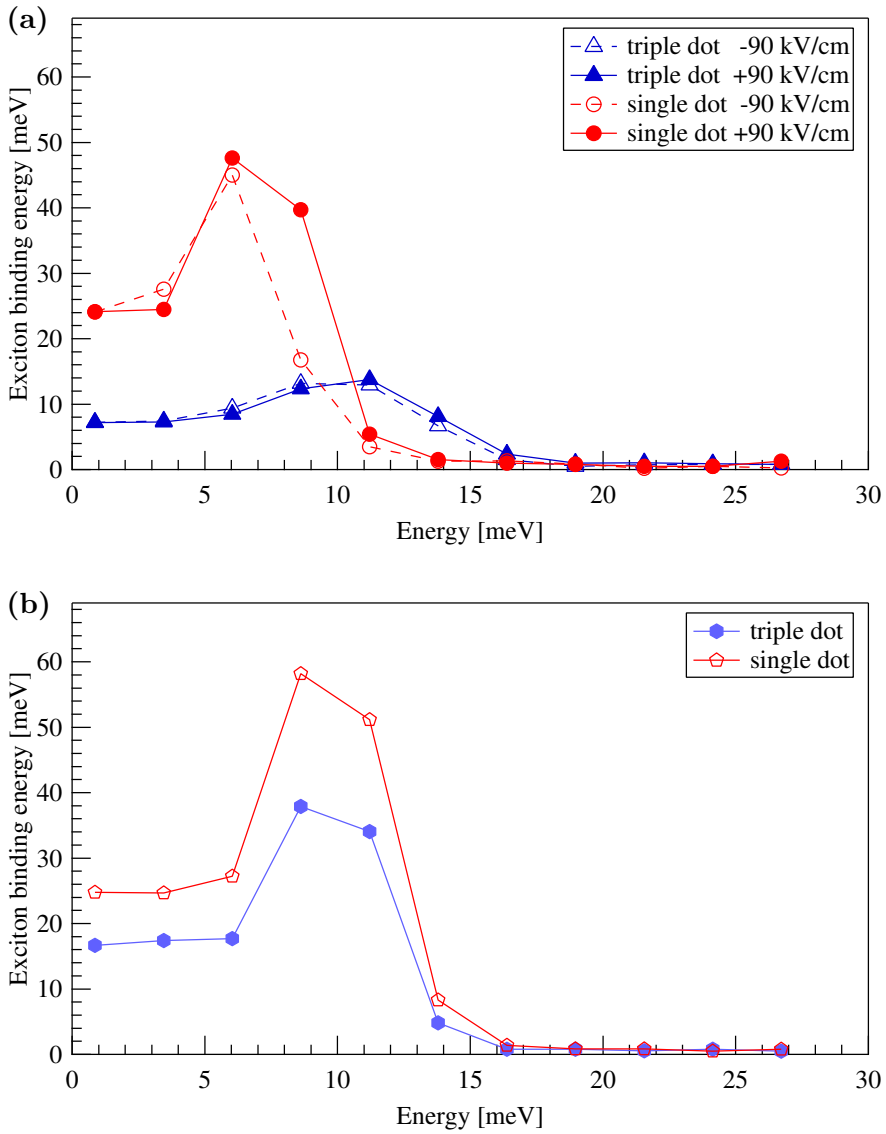

Figure 5.12: (a) Comparison of exciton binding energy in a single and triple dot structure as a function of temperature in the form of energy for two opposite orientations of electric field. (b) the exciton binding energy results without external field.

5.6 Conclusions

We used the Path Integral Quantum Monte Carlo method to study a heavy-hole exciton in an atomistic model of single and multiple quantum dot. We have showed that an exact treatment of the electron-hole Coulomb potential, as well as a full description of the strain and piezoelectric field uncovers new, exciting phenomenon of lateral switching. We found that the lateral switching of the charge distribution in the vertical electric field, previously reported for quantum rings, is clearly present and

highly tunable in the system of stacked quantum dots. On the other hand it cannot be observed in a single quantum dot structure. We investigated the lateral switching in dots of different shapes, sizes and composition profiles. It was found that this generic phenomena is caused by the interplay of piezoelectric field deformation of conduction and valence bands and the Coulomb interaction. Moreover the lateral switching does not depend on the geometry of quantum structure but on the overall volume of the alloy in the system. Switching was observed for applied fields sufficiently small that exciton dissociation was not a factor. The localised probability distribution functions for the electron and the hole are in excellent agreement with the pair correlation data as well as the lateral polarizability. Calculations of the recombination rate indicate a bright exciton particularly for small values of the E field, whose polarizability can be observed experimentally.

Chapter 6

Vertically stacked coupled quantum rings

6.1 Introduction

A Quantum Ring (QR) is a term describing a doubly-connected nanostructure of ring-like shape [231]. Charge carriers and quantum fields in QRs experience unusual density of states, and display novel physical properties which differ significantly from singly-connected nanostructures e.g. quantum dots [231].

There are a large number of publications treating various aspects of the physical properties of QRs, including studies of the finite width of the structure [232], mesoscopic properties of strongly coupled polarons [233] and theoretical and numerical modelling of self-organised QRs [234].

In this Chapter we focus on results of modelling exciton complexes in vertically stacked semiconductor quantum ring (VSR). We start with the detailed analysis of strain fields and the corresponding piezoelectric potential. Then the effect of vertical separation on the electronic properties of the VSR will be discussed and its impact on the recombination rates of exciton and biexciton investigated. The effect of a vertical electric field will be then analysed, with particular emphasis on the Stark effect and the mechanism of lateral switching.

6.1.1 Vertically stacked quantum rings

This thesis is entirely devoted to multiple coupled structures. Engineering of the strain fields in stacked structures allows for the vertical order of growth of InGaAs QRs (Fig. 6.1). It has already been established, based on the recent experimental data on vertical order growth of InGaAs VSDMs and VSRMs [217, 231, 235–237], that the strain field originating in the bottom layer of quantum structures can be transferred to the above layers. If the proper composition profile and thickness of the spacer layer is used, the preferential nucleation of sites in the higher layers is achieved. This approach allows to acquire both vertical correlation and anti-correlation of the VSRs during the growth in the [001] direction [231]. In Fig. 6.1 a sample of three vertically stacked quantum rings grown on the GaAs substrate is presented. One can see that the top QR isn't buried in the GaAs matrix and its size and alignment slightly differ from the remaining two structures. As found in [135] one of the most important parameters which has a critical impact on the vertical alignment is the spacer thickness. It was experimentally found that a GaAs spacer thickness $\leqslant$6 nm guarantees uniform strain transfer between the layers of the InGaAs QR which results in formation of a structure which is very similar in shape and dimensions.

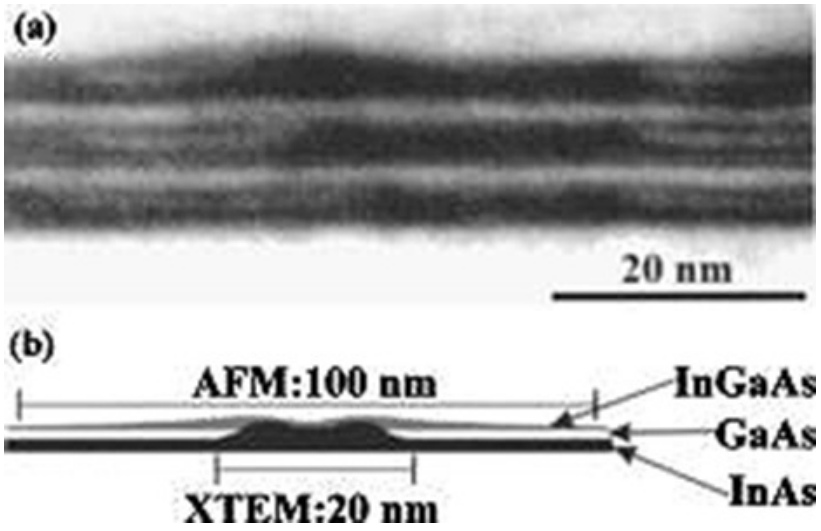

Figure 6.1: The (002) dark field XTEM of a sample with three stacks of QRs with 3 nm GaAs spacer between them, showing clear vertical ordering of the QRs. (b) Scheme of the proposed material distribution of a single QR depicted from XTEM measurements Ref.[135].

6.2 Electronic structure of strain in vertically stacked ring structures

In this Section the atomistic model of a triple quantum ring will be introduced. We begin with detailed analysis of the strain fields present in our structure and the resulting piezoelectric potential. Then impact of the inter-ring separation on exciton (X) properties and inter-ring tunnelling will be discussed with particular attention to the importance of the Coulomb interaction and recombination rate of the electron-hole pairs in absence of an external electric field. We conclude this Chapter with an analysis of the impact of an external, vertical electric field on the system will be described including the excitonic switching phenomenon and quantum confined Stark effect.

The model of a vertically stacked ring used in this work is based on a cross-sectional scanning tunnelling microscopy (X-STM) analysis by Garcia *at al.* [238]. According to this an average height of a single QR is about $h \approx 4$ nm. The inner r and outer R radii of the alloy $In_{30}Ga_{70}As$ QR structure were estimated to be ≈ 8 nm and ≈ 15 nm respectively (Fig. 6.2). We vary the inter-ring separation d from 0 to 12.5 nm. The reason for the choice of this separation was discussed above; the impact of spacer thickness on the homogeneity of consecutive structures in the higher layers.

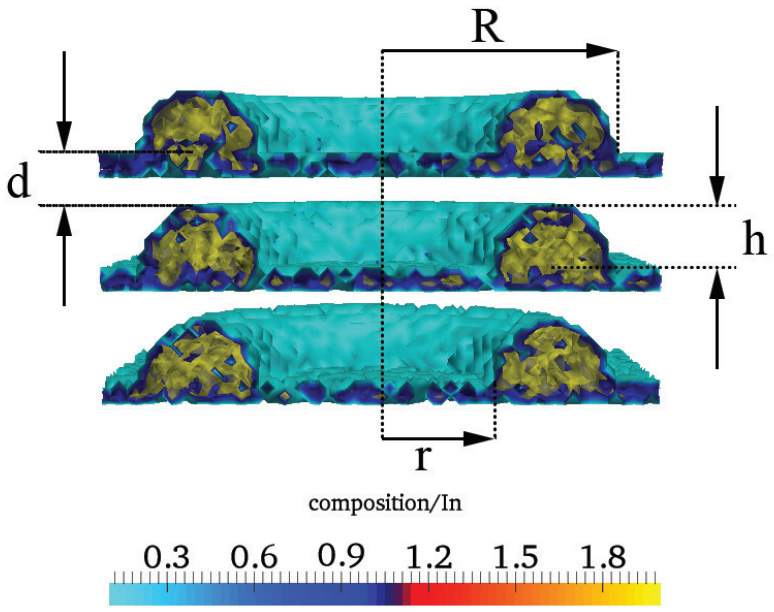

Figure 6.2: In atoms per volume concentration profile of cross-section of VSR used in our analysis. The model ring shown has following parameters d =3.4 nm, $h \approx 4$ nm, r =8 nm and R =15 nm .

We start with the strain distribution analysis in a coupled quantum ring. In Fig. 6.3 the strain components in the x-y plane through the centre of the triple ring structure are presented. The normal strain components ϵ_{xx}, ϵ_{yy} and ϵ_{zz} are plotted in Figs. 6.3a, 6.3b, 6.3c and compared to shear ϵ_{yz} strain Fig. 6.3d. By inspection of Figs. 6.3a - 6.3c one can see that the normal strain components have rotational symmetry about the z-axis. On other hand the shear strain distribution clearly lacks this feature (Fig. 6.3d). As one can see in Figs. 6.3a - 6.3c, distribution of ϵ_{xx}, ϵ_{yy} and ϵ_{zz} contributions in the [100] direction is almost identical across the structure and simulation cell, and plotting its values on [110] and $[1\bar{1}0]$ diagonals does not change the picture. The normal strain component in the growth direction ϵ_{zz} is also symmetric but the tensile strain reaches higher values than for other two. As apparent in Figs. 6.3a, 6.3b and 6.3c the compressive strain is entirely localised in the ring structures and wetting layers. Tensile regions are formed mainly above and below the rings with some additional areas in the core of the structures due to Poisson's ratio. This is the result of burying the structure in the GaAs matrix material which reduces the energy and induces formation of the new quantum ring layers [239]. The distribution of the shear strain (Fig. 6.3d) is significantly different. As one can see, this component resulting from angular distortion of the crystal structure is dominating, the boundary region between the InGaAs ring and GaAs barrier material. As it will be shown in the following section these are the regions from which the piezoelectric potential originates. The first order piezoelectric potential

$$\mathbf{P} = \begin{pmatrix} P_x \\ P_y \\ P_z \end{pmatrix} = \begin{pmatrix} 0 & 0 & 0 & e_{14} & 0 & 0 \\ 0 & 0 & 0 & 0 & e_{14} & 0 \\ 0 & 0 & 0 & 0 & 0 & e_{14} \end{pmatrix} \begin{pmatrix} \epsilon_{xx} \\ \epsilon_{yy} \\ \epsilon_{zz} \\ 2\epsilon_{yz} \\ 2\epsilon_{zx} \\ 2\epsilon_{xy} \end{pmatrix}, \tag{6.1}$$

is related to linear polarizability entirely through the shear strain components while the second order polarizability contains contributions from both normal and the shear strain coefficients

$$\mathbf{Q} = 2B_{114} \begin{pmatrix} \epsilon_{xx}\epsilon_{yz} \\ \epsilon_{yy}\epsilon_{xz} \\ \epsilon_{zz}\epsilon_{xy} \end{pmatrix} + 2B_{124} \begin{pmatrix} \epsilon_{yz}(\epsilon_{yy} + \epsilon_{zz}) \\ \epsilon_{xz}(\epsilon_{xx} + \epsilon_{zz}) \\ \epsilon_{xy}(\epsilon_{xx} + \epsilon_{yy}) \end{pmatrix} + 4B_{156} \begin{pmatrix} \epsilon_{xz}\epsilon_{xy} \\ \epsilon_{yz}\epsilon_{xy} \\ \epsilon_{yz}\epsilon_{xz} \end{pmatrix}. \tag{6.2}$$

In Fig. 6.4a, detailed distribution of the normal component inside the vertically stacked ring is plotted in two different configurations. The strain distribution inside the ring at the distance $\bar{r}$ =11.5 nm from the centre along the line parallel to the growth direction is presented in Fig. 6.4a while in Fig. 6.4b the normal strain components along the y-axis averaged over the vertical extent of the structure is shown. As one can see Figs. 6.3d and 6.4a the shear strain is stronger in the top and bottom rings which has a significant impact on the piezoelectric field distribution. In Fig. 6.4,

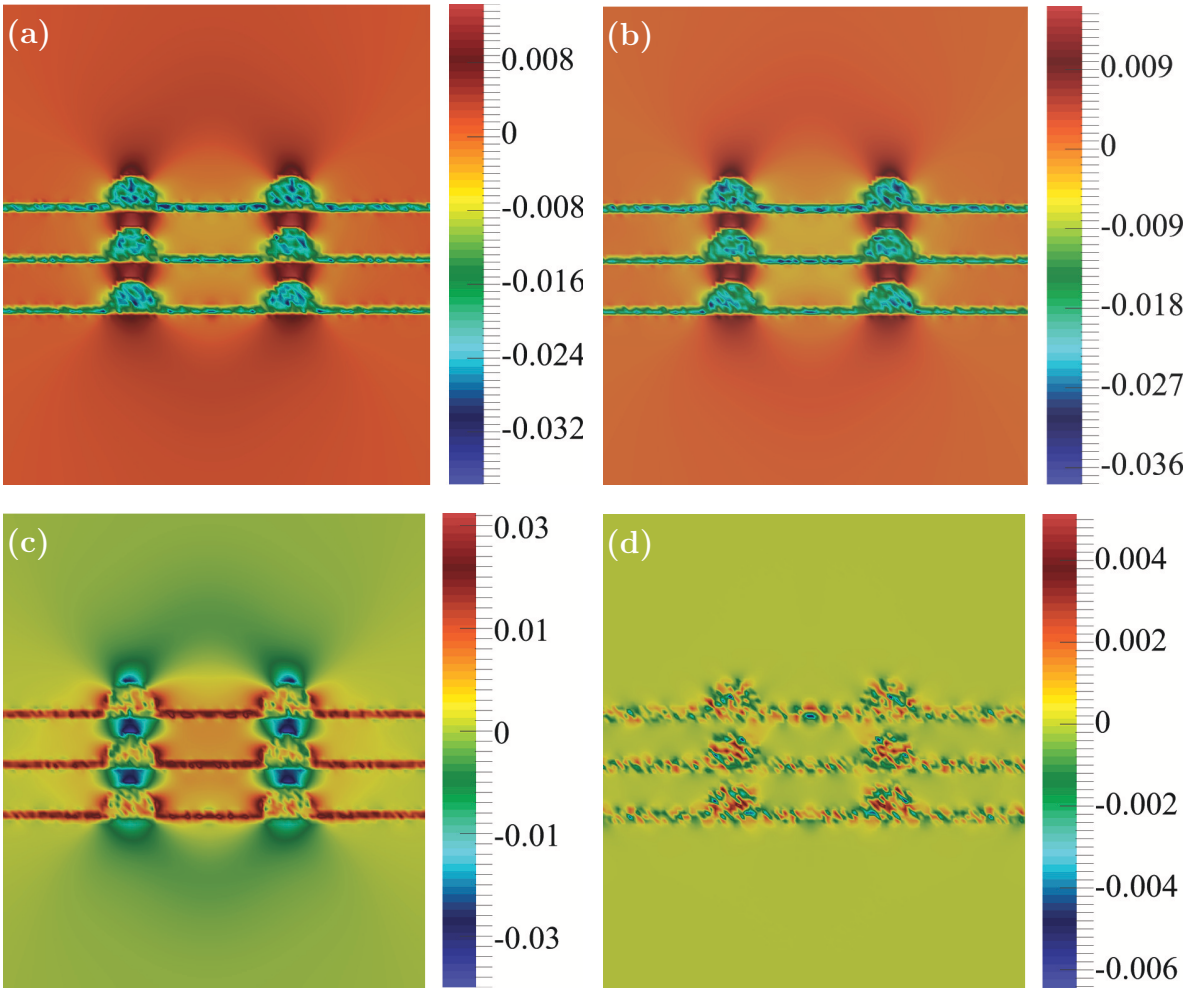

Figure 6.3: The normal strain components in the x-y plane through the centre of stacked quantum ring. (a) ϵ_{xx}, (b) ϵ_{yy}, (c) ϵ_{zz} and (d) ϵ_{yz}.

detailed distribution of the normal component inside the vertically stacked ring is plotted in two different configurations. One can see that ϵ_{xx} and ϵ_{yy} strain values are negative and almost identical in the bottom and middle rings indicating that the rings undergo compression in these directions. The top ring shows stronger contraction in the ϵ_{xx} direction. The sign of the strain changes in the surroundings of the structures

and in the wetting layers, however tensile strain between the structures is dominating the picture. The ϵ_{zz} contribution shows compressive strain between the structures which penetrates into the barrier material. In the quantum ring distribution the ϵ_{zz} is opposite compare to ϵ_{xx} and ϵ_{yy} with the strongest contribution in the bottom ring. The shear strain component appears only at the interface of the structure and the wetting layer quickly decaying to zero in the GaAs matrix. In fact, all components discussed here converge to zero at the barrier, which demonstrates that our atomistic structure is properly relaxed. In Fig. 6.4b the normal strain components along the

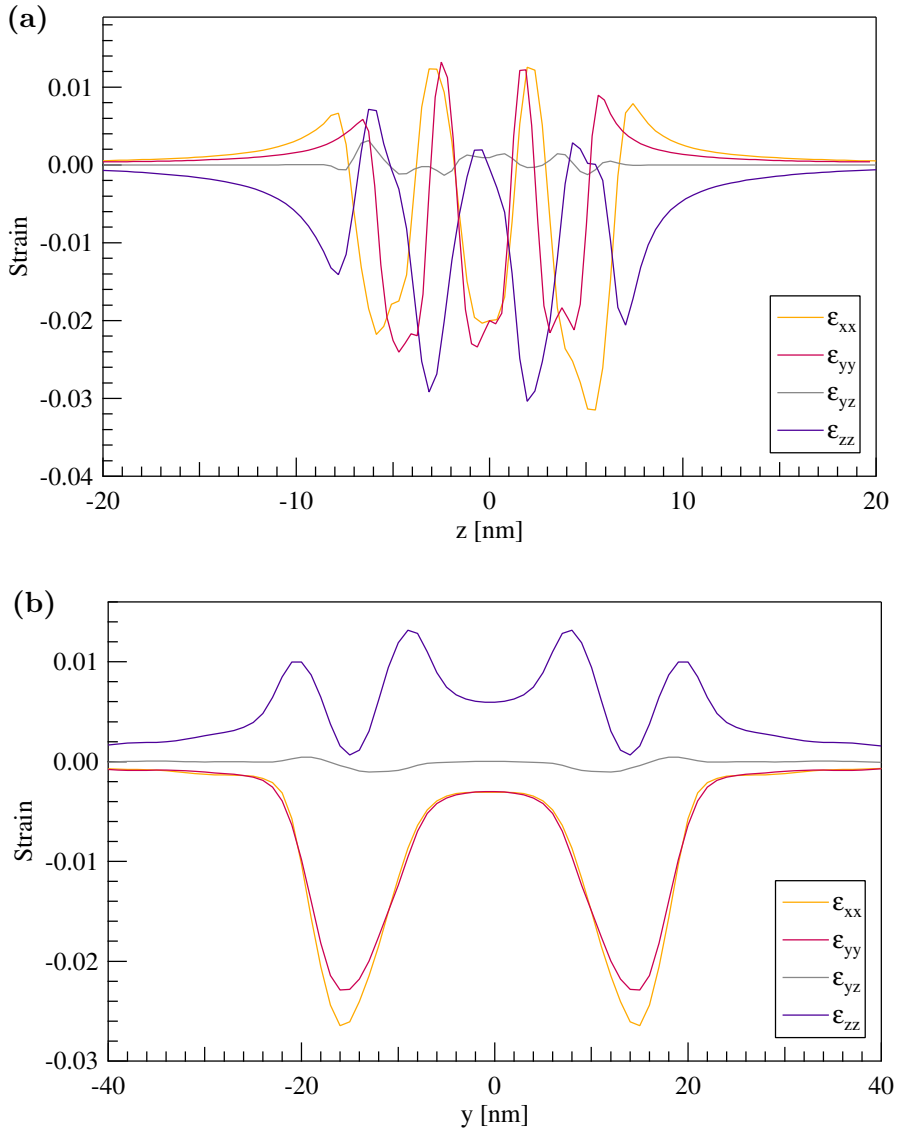

Figure 6.4: Comparison of normal strain components in (a) the [001] and (b) in the [010] directions. In panel (a) strain is plotted along the line at a mean radius $\bar{r}$ =11.5 nm and parallel to the growth direction. The inter-ring separation d =3.4 nm.

y-axis averaged over the vertical extent of the stacked structure are depicted. The apparent feature of the plot is axial symmetry of all components. This results from the fact that the atomistic model is an ideal circle. In this scan the compressive character of ϵ_{xx} and ϵ_{yy} is even more pronounced. One can notice that these contributions decrease from the centre of the ring towards the outer radius, showing a minimum at the boundary region then an increase to zero in the wetting layer. The ϵ_{zz} component demonstrate tensile nature and is mainly localized close to the inner radius of the structure and at the boundary between ring and the surroundings.

Biaxial and hydrostatic strain contributions on two perpendicular diagonals of the simulation cell are visualised in Figs. 6.5a, 6.5b and 6.5c, 6.5d respectively. The biaxial ϵ_{bi} and hydrostatic ϵ_{hyd} strain components are particularly important in self-assembled quantum structures as those are responsible for deformation of conduction and valence band edges and also shifting the heavy and light hole energy levels in stacked structures. One can notice that biaxial strain takes higher values inside the top and bottom quantum ring towards the base of the nanostructure, extending to the core region of the ring. Such a distribution indicates that the hole will be localised mostly in the top and bottom structures towards the ring base with more uniform probability distribution in the middle structure. On the other hand electrons, which are more sensitive to the hydrostatic strain, will be uniformly de-localised in all three structures as the hydrostatic strain component is mostly constant in ring and the barrier material. In Fig. 6.6 the biaxial and hydrostatic strain along the line perpendicular to the growth direction at the distance $\bar{r}$ =11.5 nm from the centre of the ring is plotted. It is apparent that biaxial and hydrostatic strain components are characterised by opposite signs however the absolute values are similar. Both components are almost identical in the middle structure indicating uniform distribution of the charge carrier probability density. The biaxial strain is much stronger in the bottom ring, forcing the hole to localise mostly in this structure towards the wetting layer. The hydrostatic strain component is very similar in the top and bottom rings sightly increasing toward the top structure which promotes de-localisation of the electron between all three rings. The above tendency is even more pronounced in Fig. 6.6b, in which the cross-section along the y-axis averaged over the ring height and vertical extent of the structure is shown. One can see that the hydrostatic strain is rather uniform and almost symmetric in the ring material, quickly decaying to zero in the GaAs surroundings and core region. As it was already mentioned this stimulates the uniform probability distribution of electrons in all three vertical structures. The biaxial strain demonstrates non-zero

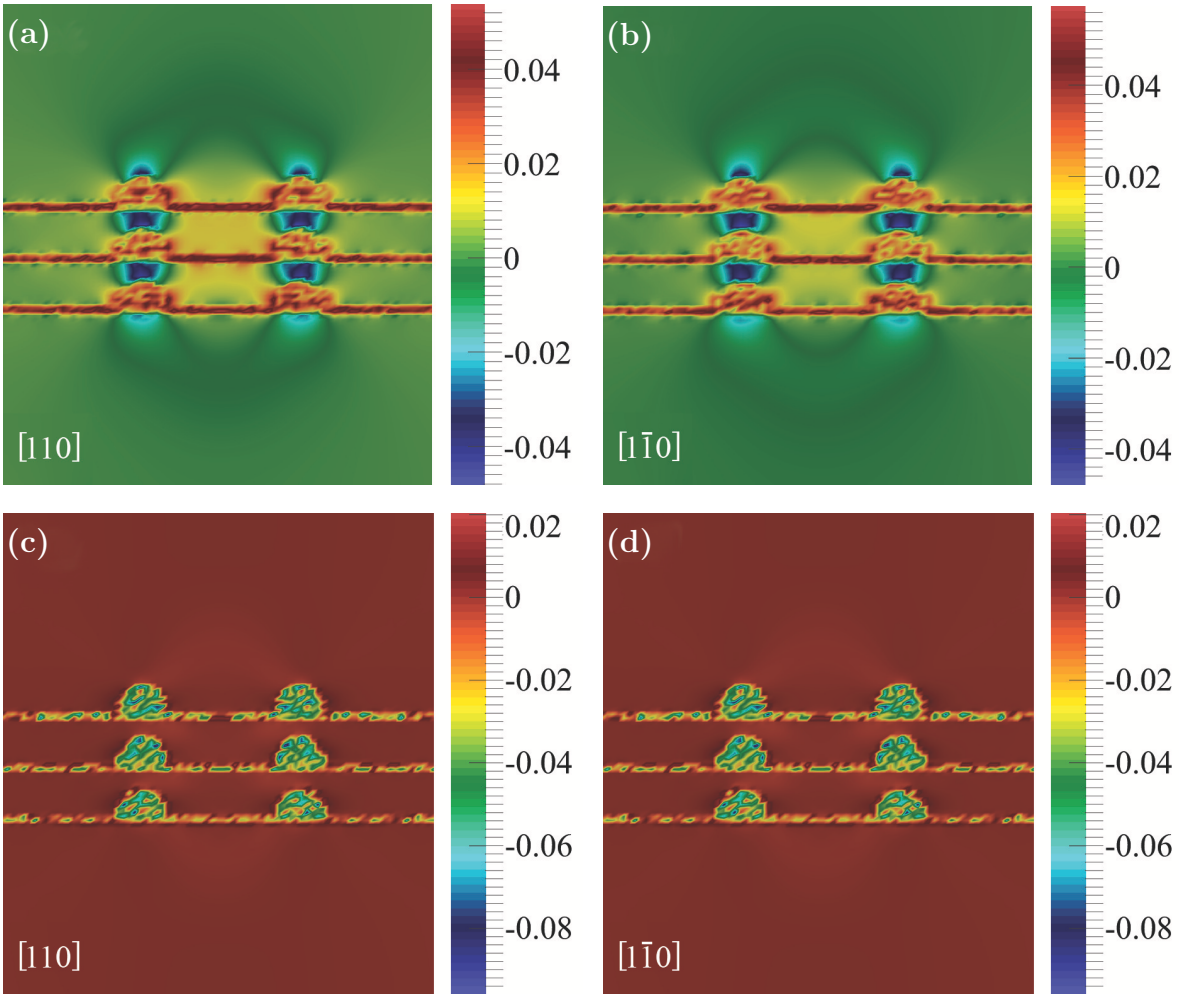

Figure 6.5: Biaxial and hydrostatic strain profile in the [110] and [1$\bar{1}$0] direction through the centre of stacked quantum ring. Fig. (a) biaxial strain ϵ_{bi} in the [110] direction, (b) biaxial strain ϵ_{bi} in the [1$\bar{1}$0] direction, (c) hydrostatic strain ϵ_{hyd} in the [110] direction and (d) hydrostatic strain ϵ_{hyd} in the [1$\bar{1}$0] direction.

value in the central region of the ring and two distinctive peaks, one towards the centre and the second one near the outer perimeter with a minimum between them. This suggests that the hole will localise in the ring structure with the highest probability distribution between the two discussed peaks.

6.3 Piezoelectric fields in stacked rings

There are not many detailed studies of piezoelectric potentials in the single quantum ring and even less regarding multiple systems. Piezoelectric properties of quantum rings were first analysed by Barker *at al.* [129] and much later by Yu-Min *at al.* [239]

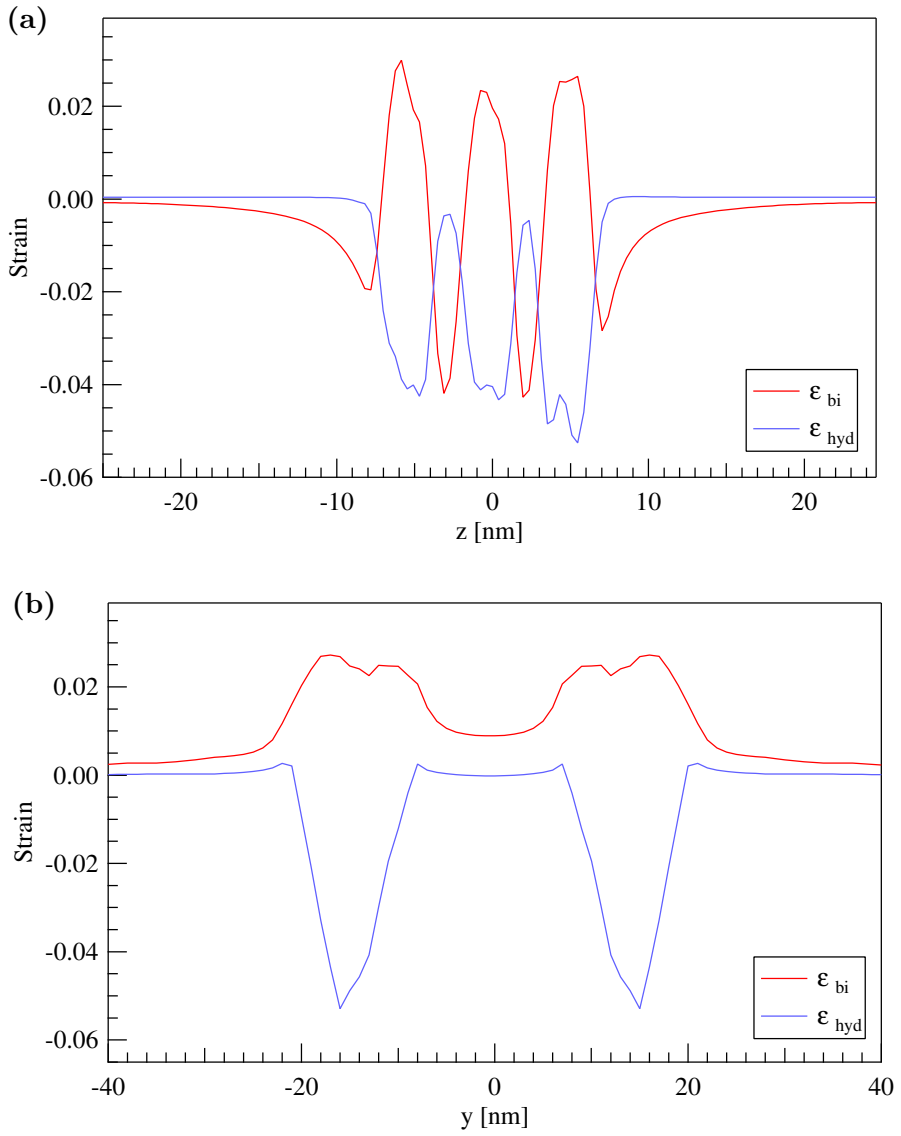

Figure 6.6: Biaxial and hydrostatic strain in (a) the [010] direction averaged over the height and vertical extent of the structure and over two diagonals and (b) in [010] direction. The inter-ring separation d =3.4 nm.

in the frame of a continuum method of describing the structure, however both works are limited to single rings only. In the work by BoYong *at al*. [240] the system of three identical rings with rectangular cross-section and without wetting layer is investigated using finite element methods.

Presence of the atomistic strain in a crystal lattice of this structure creates a piezoelectric field. This piezoelectric potential is much more complex than in the quantum dot discussed earlier due to the GaAs core, but surprisingly similar in case of vertically stacked dots. The distribution of the piezoelectric potential in a stacked structure is very sensitive to the ring separation. For closely spaced rings one can

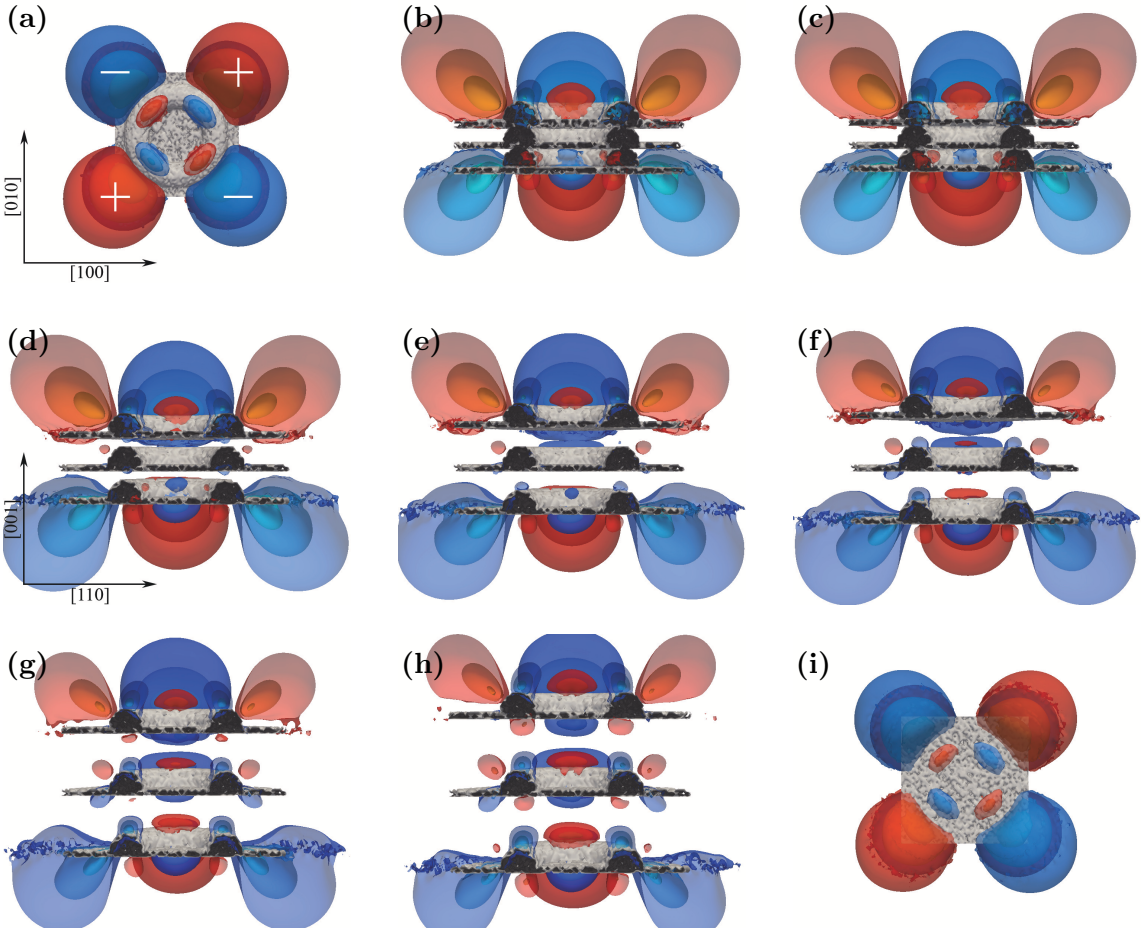

Figure 6.7: The iso-surface representation of the piezoelectric potential profile in a stacked quantum ring as a function of ring separation. (a) Top view (top to bottom). Figs. (b) - (h) are plotted in the [111] plane which is rotated 90∘ with respect to the top view Fig. (a). Ring separation plotted: (b) d=0 nm, (c) d=1.1 nm, (d) d=3.4 nm, (e) d=5.6 nm, (f) d=7.9 nm, (g) d=10.2 nm, (h) d=12.4 nm. In Fig. (i) the ring structure from the bottom view is depicted.

observe the distribution characteristic for a single tall structure, with sixteen lobes originating from the top and bottom regions and penetrating into the ring and surroundings (Fig. 6.7b). With increasing ring separation piezoelectric potential occurs in the top and bottom structures, almost completely decaying in the middle ring (Figs. 6.7d, 6.7e) up to the critical separation, which will be discussed in detail in Chapter 7. Further enlargement of the barrier between the rings yields reduction of the inter-ring interaction and formation of the piezoelectric regions in the middle structure (Figs. 6.7f, 6.7g and 6.7h), however those regions are much smaller than in the top and bottom rings. This indicates that the presence of the other rings, even at a greater

distance relaxes the strain fields in the middle structure. Large external lobes spreading into the GaAs matrix are similar to those observed in the quantum dots, however the set of inner lobes resulting from the barrier material in the rings centre makes the ring properties unique (Figs. 6.7). As shown in Fig. 6.7, external piezoelectric regions are localised outside the ring structure as was observed in the quantum dots, however the inner piezoelectric lobes penetrate into the ring e.g. Fig. 6.7d. As it will soon be demonstrated, the distribution of piezoelectric fields has significant impact on the confinement potential of the rings. Additionally, the distribution of piezoelectric regions destroys the rotational symmetry of the structure and spatially separates charge carriers, localising them in the regions of lowered potentials.

The impact of piezoelectric potentials on the charge carrier distribution in the stacked structure is one of the most important threads of this thesis, therefore we discuss it in more details on a system with separation of 3.4 nm. In Fig. 6.8 the overall piezoelectric potential (top row), second and first order (middle and bottom row respectively) contributions are shown on two perpendicular diagonals. One can see that the first order piezoelectric potential is equally strong in both diagonal planes including strong piezoelectric regions inside the core barrier. The distribution of the piezoelectric potential outside the ring is very similar to that in stacked quantum dots. The second order piezoelectric contribution is very small compared to the first order, and localised mainly in the ring structure, predominantly over and beneath the structure, locally penetrating into the core region. The second order contribution to the piezoelectric field has opposite sign compared to the first order, which leads to the reduction overall piezoelectric potential inside the rings, particularly in the middle structure. The piezoelectric potential in the [110] plane changes sign every 90 degrees. This will lead to the periodic raising and lowering of the potential for the electron and hole in the ring and additionally change the charge's localisation in the growth direction of the structure. As will be shown, these properties result in the characteristic change of electron and hole behaviour in the vertically stacked structures.

6.4 Exciton ground state probability distribution

The influence of biaxial and hydrostatic strain and the first and second order piezoelectric fields on the charge carrier distribution is even clearer in the confining potential

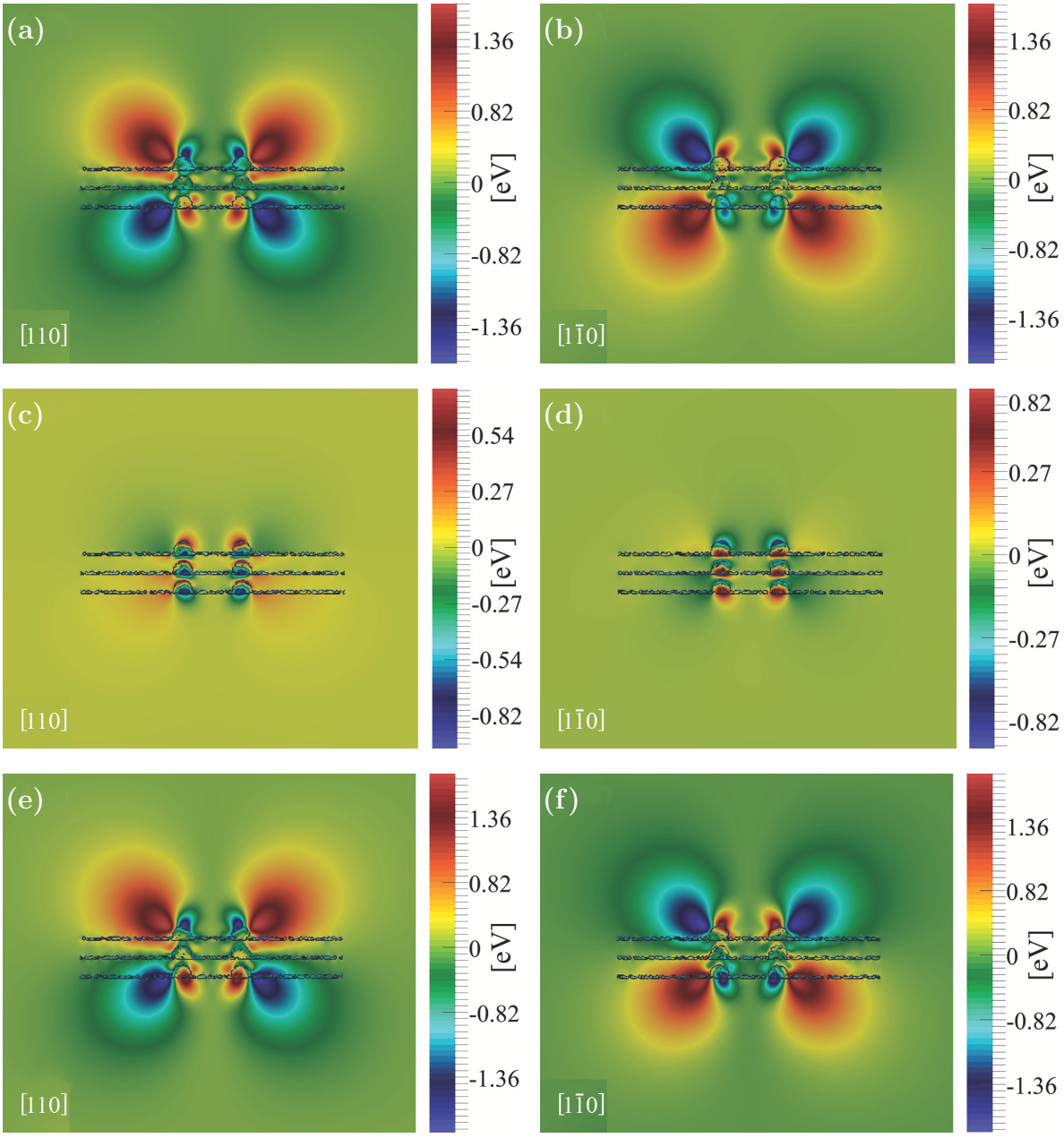

Figure 6.8: Piezoelectric potential profile in the [110] and [1$\bar{1}$0] direction through the centre of stacked quantum ring. (a) and (b) 1^{st} and 2^{nd} order, (c) and (d) 2^{nd} order only, (e) and (f) 1^{st} order only.

distributions shown in Fig. 6.9. In order to match the C_{2v} symmetry we symmetrise these potentials. This step smoothes the confining potentials and also increases the speed and efficiency of simulations. Inclusion of the piezoelectric potential significantly modifies the conduction and valence band profile, introducing positive and negative regions inside and outside of the structure. Those fields act as effective potential wells attracting electrons and holes and promoting localisation of the charge carriers. The

ring cross-section shows that the structure is wider at the bottom and rounded at the top. This vertical asymmetry will have an impact on the charge carrier confinement and observed probability density distribution. One should expect that a greater volume at the middle and bottom of the ring will result in localisation of both charge carriers, preferably in that region. Strain and confinement potential in the [110] and

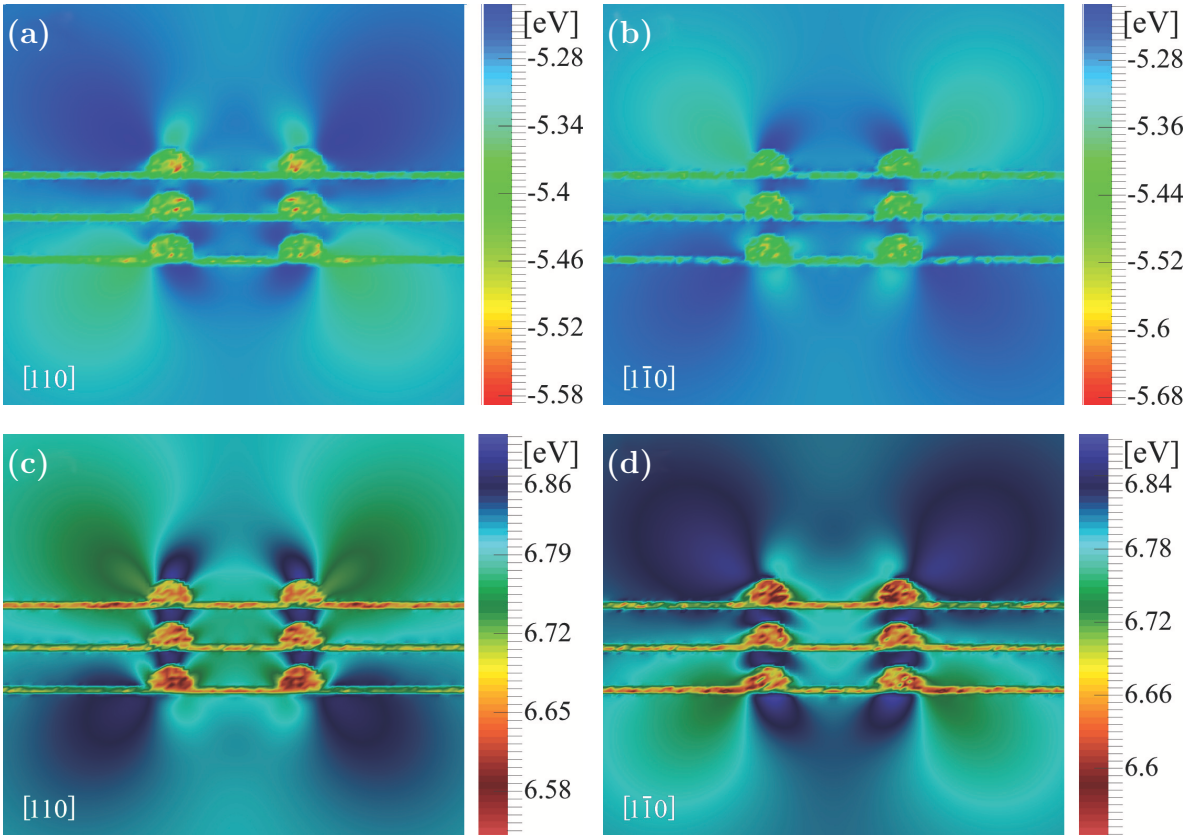

Figure 6.9: Plot of conduction band edge potential profile (a) in the [110] and (b) in the [1$\bar{1}$0] and valence band edge potential profile (c) in the [110] and (d) in the [1$\bar{1}$0] direction through the centre of stacked quantum ring derived from strain fields with piezoelectric domain.

[1$\bar{1}$0] directions are different due to the characteristics of the underlying crystal lattice geometry. This difference varies significantly between all three structures and will induce the electron and hole localisation on one of these two diagonals. However which one is more likely to demonstrate stronger confinement cannot be deduced from the strain and potential. The ground state probability distribution obtained from the PI-QMC simulations for a non-interacting electron and hole shows that electron is delocalised in all three rings and also penetrates the wetting layer and barrier material, particularly in the bottom structure, Figs. 6.10b and 6.10f. The electron preferably aligns in the [110] direction in the bottom ring and in the [1$\bar{1}$0] direction in the middle

and top structure. However, the probability distribution indicates that finding the electron in the top ring is smaller when compare to the other two rings. It is also apparent that the probability distribution in the middle ring is much more uniform around the ring than in the remaining two. Free particle hole probability distribution is predominantly localised in the top and bottom quantum ring on two perpendicular planes with a small chance of finding the hole in the middle ring (Figs. 6.10c and 6.10g). Explanation of such a distribution can be given by analysing the confinement

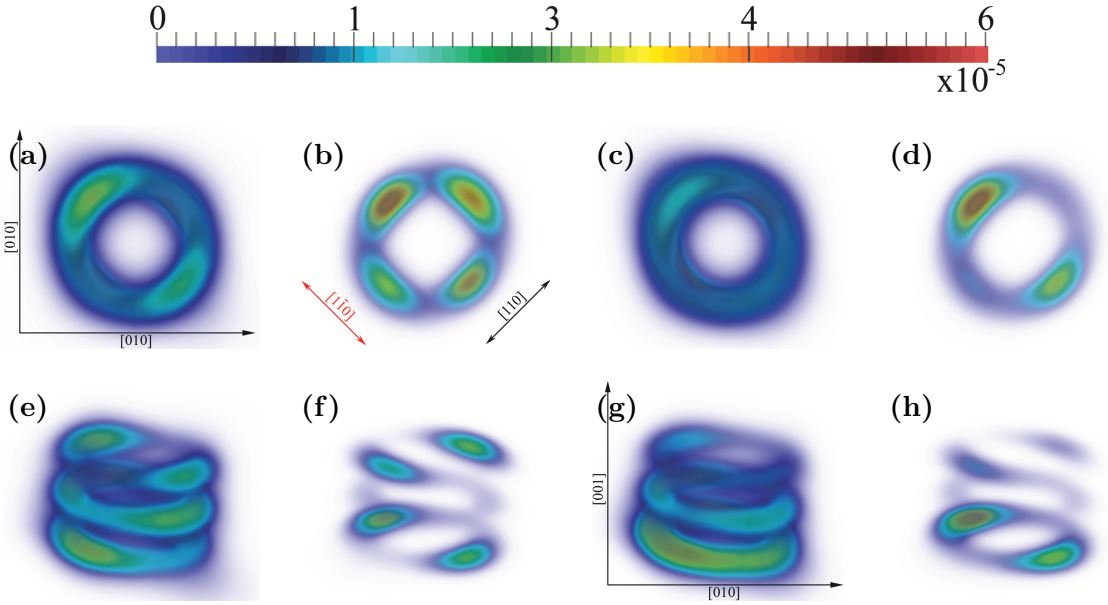

Figure 6.10: Probability density distribution in [001] and [111] plane of single particle and excitonic states in stacked ring. Top view (a) single particle electron, (b) single particle hole, (c) electron in exciton, (d) hole in exciton. Top view (e) single particle electron, (f) single particle hole, (g) electron in exciton and (h) hole in exciton.

profile for the electron and hole. In Fig. 6.12 the average conduction and valence band are presented in two distinct configurations. In Fig. 6.11a the conduction band averaged over the ring height and vertical extent of the In containing structure is plotted on the [110] and [1$\bar{1}$0] plane, and Fig. 6.11b shows the valence band profile. It is apparent that the potential experienced by the hole in the [1$\bar{1}$0] direction is a few meV lower than on [110], which should promote localisation of the hole in this plane. However this is not exactly consistent with the probability distribution shown in Fig. 6.12. In the electron case average difference between two perpendicular diagonals is not so sharp compared to the hole. One should expect therefore that the electron probability distribution will be rather uniform around all the rings. Once again the mean probability distribution does not reflect our expectations.

A better understanding of the electron and hole probability distribution preferences can be acquired by analysing the confining potentials for each ring, instead of averaging them over the extent in the growth direction. It is reasonable to expect that the presence of the other rings and spacer will differently affect the strain profile in the system and therefore the energy band edge deformation. In Figs. 6.12a the conduction and 6.12b valence band averaged over the height of each ring are plotted for a stacked structure. Again in this analysis we focus on the system with a rings separation of 3.4 nm. It is clearly visible that both conduction and valence band significantly varies not only on two perpendiculars planes but also between the rings. For clarity of the diagrams the conduction and valence band edges in the middle and top structure are offset from their original values by 0.1 eV and 0.2 eV respectively.

As it was already mentioned the valence band is highly susceptible to the change of biaxial strain. In Fig. 6.6a the biaxial strain along the line located at $\bar{r} = (R-r)/2$ and parallel to the growth direction is shown for a coupled structure. It is clearly visible that the presence of the top and bottom rings lowers the value of the biaxial component of the strain in the middle ring. Lower value of the ϵ_{bi} results in the smaller difference between the valence band on the [110] and $[1\bar{1}0]$ diagonals. In Fig. 6.6b the biaxial strain averaged over the height and vertical extent of the structure in the [010] direction through the centre of the ring is shown. One can see that the strain in the core region of ring is higher than its value in the barrier material with two distinct peaks close to the inner and outer circumference. These should increase the height of the barrier at the outer radius and lower it near the core allowing the hole to be localised more strongly towards the central region of the ring. This can be seen in Fig. 6.10g as a more uniform probability distribution in the middle ring. Furthermore the piezoelectric potential in this structure is very weak compared to the top and bottom rings Fig. 6.7d and apparently insufficient to promote localisation of the dot. The valence band edge in the top and bottom ring is much more complex compared to the middle one. The presence of the GaAs matrix material over and beneath the top and bottom rings, unbalanced by any other structures results in the much higher values of biaxial strain Fig. 6.6a. The difference between confinement on two diagonals is much more pronounced and even greater in the top structure. Also one can see that the potential towards the centre of the ring is lower near the inner radius due to the inner piezoelectric lobes. This will allow the hole probability distribution to spread into the core region. Inclusion of piezoelectric fields creates additional potential wells outside the ring which trap the hole (Figs. 6.10c and 6.10g). The conduction band

(Fig. 6.12a) shows similar properties to those discussed above, however the electron, with much smaller mass compared to the hole, is able to escape from trapping regions more often than the heavy hole. The electron is still attracted by these areas as it is clearly shown in Figs. 6.10b and 6.10f but its probability distribution is delocalised in all three structures. Another reason for such a behaviour is the fact that the hydrostatic strain which affects the electron is much more uniform when compared to the bi-axial one (Fig. 6.6b). As it can be seen in Fig. 6.6a the hydrostatic strain in the bottom and middle ring have very similar values, while it is much stronger in the top structure. This relationship can be observed in Fig. 6.10f as a smaller probability of finding the electron in the top structure.

In the more realistic Coulomb interacting case (Figs. 6.10e and 6.10i) the hole strongly localises on the $[1\bar{1}0]$ diagonal in the bottom ring due to the weaker bi-axial strain and on the [110] diagonal in the top ring. One can see that, similar to the single particle, the probability distribution of localisation in the middle and top ring is small. Piezoelectric fields in the top and bottom ring together with the bi-axial strain which lowers the potential in the core, promotes localisation toward the centre of the ring. The heavy hole attracts the electron to the regions in which the hole is localised in order to form an exciton. As shown in Figs. 6.10d and 6.10h the highest probability of finding an exciton is in the bottom structure while the lowest in the top one. An electron in the top and middle ring occupies most of the volume of the ring with preferable localisation in the $[1\bar{1}0]$ direction. On the other hand a hole in the top ring localises in the [110] direction and does not display any obvious localisation preferences in the middle ring. This observation leads to the conclusion that the piezoelectric field in the top ring has much bigger impact on the electron probability distribution than the Coulomb interaction. Similarly in the middle structure, as the hole is almost absent here, the electron is attracted by the piezoelectric field originating from the top structure and localises in the $[1\bar{1}0]$ plane.

6.5 Conclusions

In this Chapter properties of vertically stacked InGaAs quantum rings calculated using an atomistic model were analysed. An example ring system separated by 3.4 nm of GaAs barrier was considered, including a wetting layer. It was found that the presence of the significant amount of strain in the structure affects the band edge

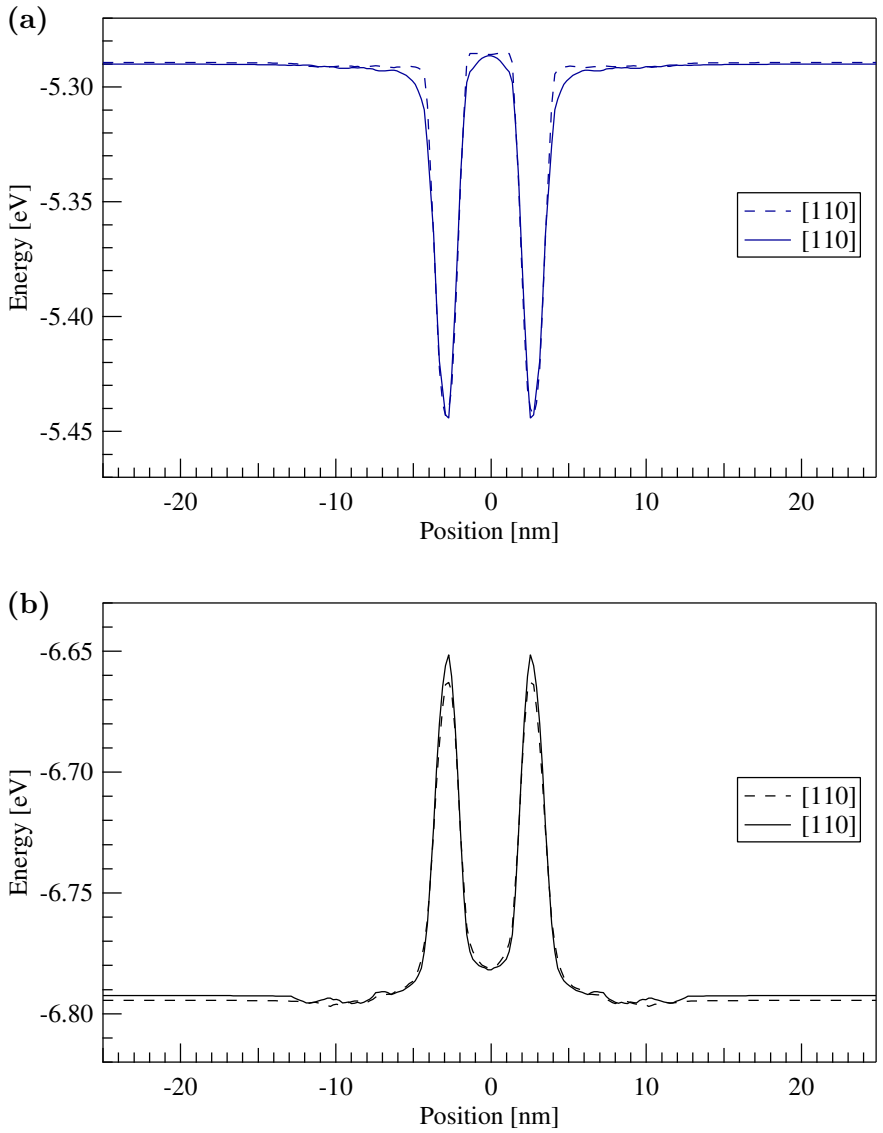

Figure 6.11: (a) Conduction band averaged over height of the rings and vertical extent. (b) Valence band averaged over height of the rings and vertical extent. Conduction and valence band edge potential profile in the [110] and [1$\bar{1}$0] direction through the centre of stacked quantum ring.

for electron and hole, promoting localisation of charge carriers on the [110] or [1$\bar{1}$0] diagonal. Strain induced compression and distortion of the crystalline structure leads to charge acquisition which results in generation of substantial piezoelectric fields. Strength and piezoelectric potential distributions strongly depend on the inter-ring separation. Additionally these fields break rotational symmetry of the system and modify the conduction and valence bands introducing regions which can trap charge carriers and localise them even stronger. These properties can be use to tailor the electronic characteristics of the system. The results clearly indicate that strain and

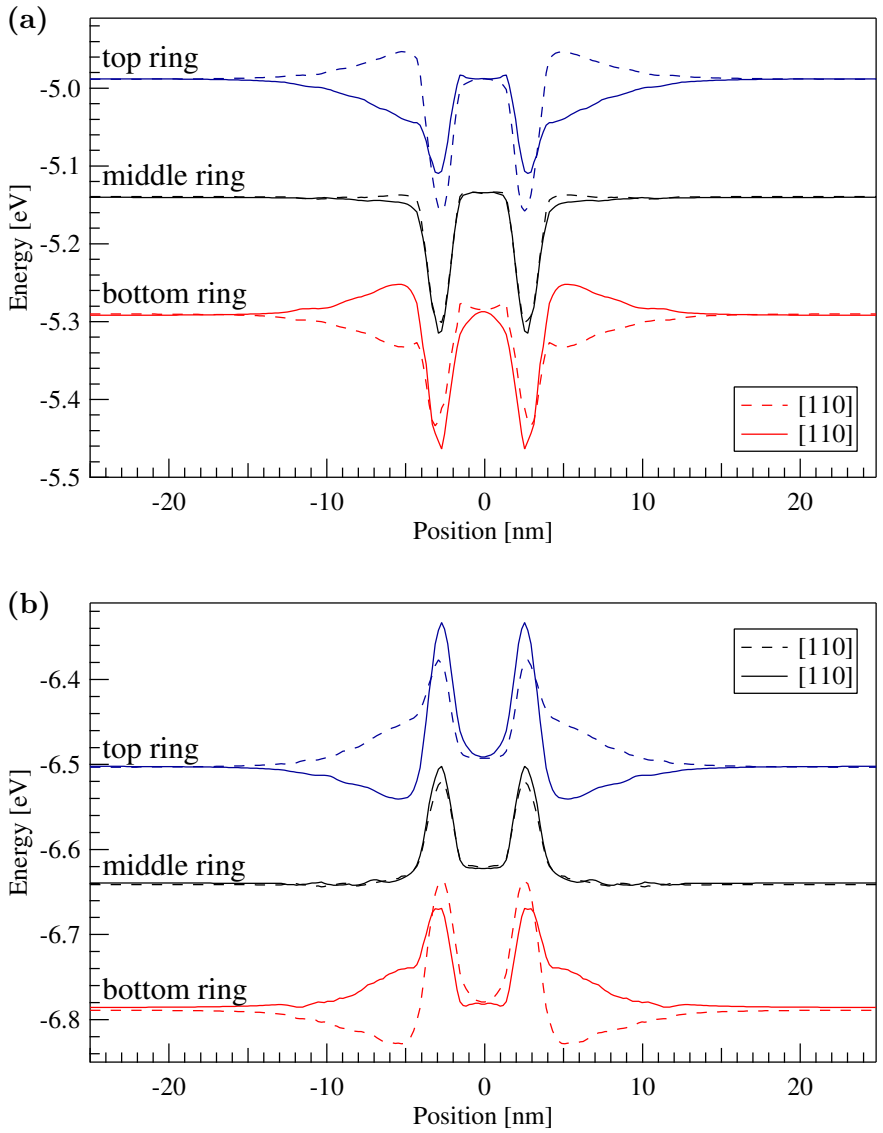

Figure 6.12: (a) Conduction band averaged over height of the rings and vertical extent. (b) Valence band averaged over height of the rings and vertical extent. Conduction and valence band edge potential profile in the [110] and [1$\bar{1}$0] direction through the centre of stacked quantum ring. The band profile is offset by 0.1 eV (middle ring) and 0.2 eV (top ring) with respect to original values.

piezoelectric potentials are very important for charge carrier distribution and optical characterisation of InGaAs stacked quantum rings.

Chapter 7

Coupling regimes and recombination rates

7.1 Introduction

Control of coupling between the quantum states and structures is one of the main objectives in designing and developing modern semiconductor devices. The ability to adjust the strain and piezoelectric field as well as the vertical extent of the structure reveals new possibilities of controlling electron-hole inter-ring tunnelling and recombination rates in vertically stacked quantum ring systems. In this Chapter the results of the study of the effects of non-uniform strain, ring separation and Coulomb interaction on the electronic structure and recombination rates of the system will be presented. We start by distinguishing two coupling regimes in vertically stacked quantum rings with different spacer thickness and then discuss their impact on recombination rates.

7.2 Strain and tunnel coupling in stacked rings

The excitonic system in the stacked quantum dot exhibit high binding energy which significantly varies with temperature. The large binding energy results from the fact that the electron and hole are confined in all three spatial directions. Additionally, large strain fields, which, due to the fact that In atoms concentration is non-uniform in the quantum structure and extends to the GaAs surroundings, affects the charge carriers mobility and distribution. Interplay between these factors can result in a

complex hybridisation between excitonic and single-particle states stemming from the multiple islands in the coupled dot structure [241].

Quantum rings morphologically originate from quantum dots, therefore, apart from some obvious differences due to the shape and piezoelectric potential distribution, one can expect similar interesting phenomenon. In this section the impact of non-uniform strain field, piezoelectric potential and Coulomb interactions on the inter-ring tunnelling will be analysed. In Fig. 7.1 the probability distribution of a Coulomb interacting electron, Figs. 7.1a, 7.1b and hole Figs. 7.1c, 7.1d in the triple ring is plotted for two ring separations for comparison. One can observe that the electron and hole are confined to the entire volume of the structure. For small separation of the rings (Figs. 7.1a) the electron is delocalised in all three rings, and the low value of confinement in the barrier, (see Fig. 7.2a) can be easily overcome by this light and mobile particle. The hole, which is much more massive compared to the electron, demonstrates weaker predispositions to spread between all structures even that vertical profile of the valence band (Fig. 7.2b) is varying substantially slower than conduction one. Greater ring separation localises the hole in the bottom structure (Fig. 7.1d) and slightly suppresses electron delocalisation (Fig. 7.1b) in all three rings.

In Fig. 7.3a the variation of confining potential experienced by the electron in all three rings and inter-ring barrier (Fig. 7.3b) is plotted. We can see in Fig. 7.3a that the depth of potential well is different in all three structures, which is particularly apparent for small ring separation. The most steady increase can be seen in the middle structure. Satellite rings show a much higher rate of potential change which is especially well visible in the top ring. When the spacer thickness decreases from 3.4 nm to 1.1 nm the confinement potential for the electron becomes shallow in the middle and top structure and almost constant in the top rings, attracting the electron to those lower energy regions. The potential in the barrier between the rings Fig. 7.3b shows similar change in the confining energy. This picture is consistent with probability distribution pattern plotted in Fig. 7.1a and 7.1b. The effective potential for holes follows the trend discussed for electrons, however confinements in the top and middle ring are much more similar than for electrons. The GaAs barrier between the rings is substantially higher than for electrons and almost linearly increases in the barrier material between the bottom and middle ring (Fig 7.4b). The middle-top ring potential barrier is even higher, mainly for small rings separation, which can explain the probability distribution in Fig. 7.1d.

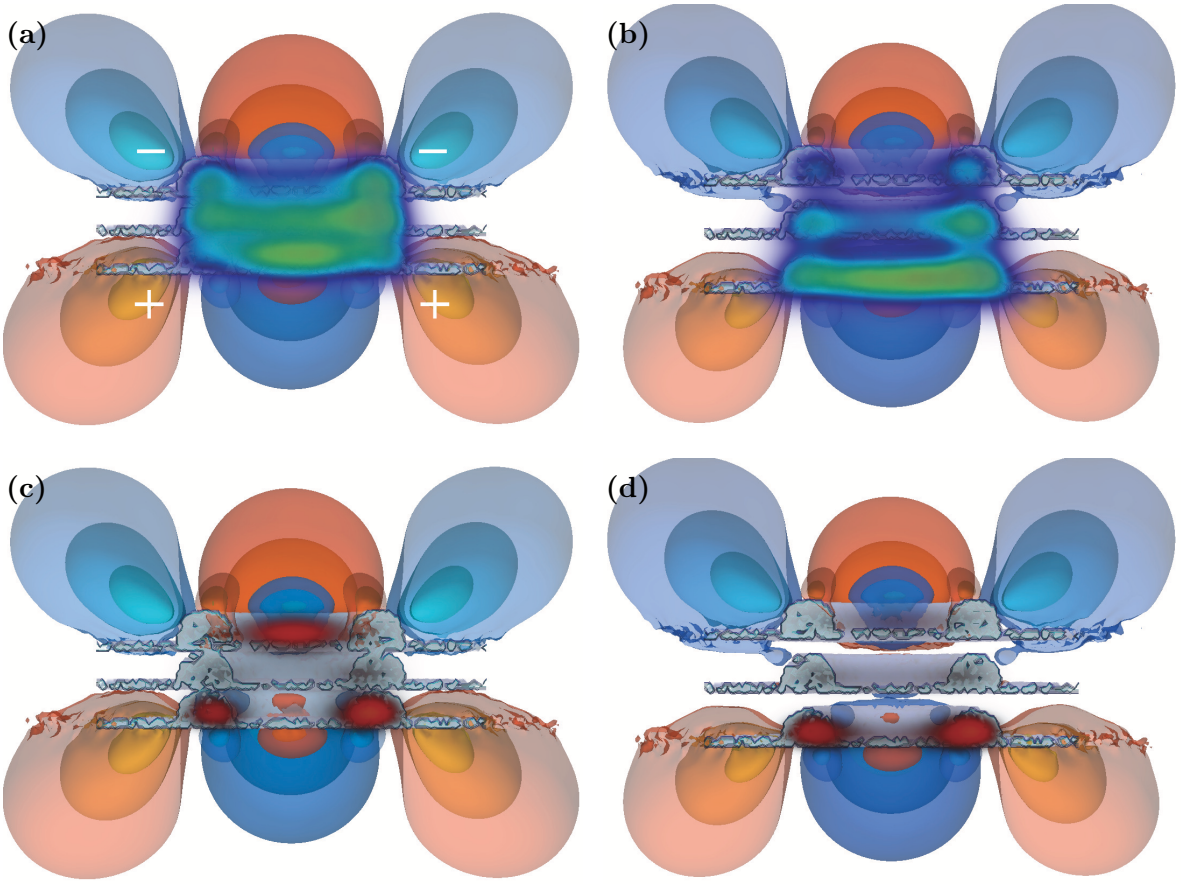

Figure 7.1: The electron and hole probability distribution in stacked quantum ring for different ring separation. Volumetric plot of (a) electron in the ring separated d=1.1 nm, (b) electron in the ring separated d=3.4 nm, (c) hole in the ring separated d=1.1 nm, (d) hole in the ring separated d=3.4 nm.

A discussed above, the confinement energies in the ring structures and barriers can be explained by analysing the Fig. 7.6a biaxial and Fig. 7.6b hydrostatic strain distribution as a function of spacer thickness. The conduction band is mostly affected by the hydrostatic strain which shifts the energy levels of the unstrained conduction band. As one can see in Fig. 7.6b, ϵ_{hyd} in the top and middle rings increases abruptly while decreasing in bottom ring between 0 nm to 1.1 nm thickness. It can be explained in the following way: for 0 nm separation the top of the middle ring is merged with the bottom of the wetting layer of the neighbouring ring, the crystal structure is compressed and the strain energy gathered in the structure is large. When the GaAs barrier is formed the middle structure can relax and the strain energy is partially dissipated. Growing inter-ring distance allows for even greater relaxation and for large separations ϵ_{hyd} reaches a constant value. In the top ring the overall strain energy, which also includes contributions from the middle and bottom rings, quickly converges

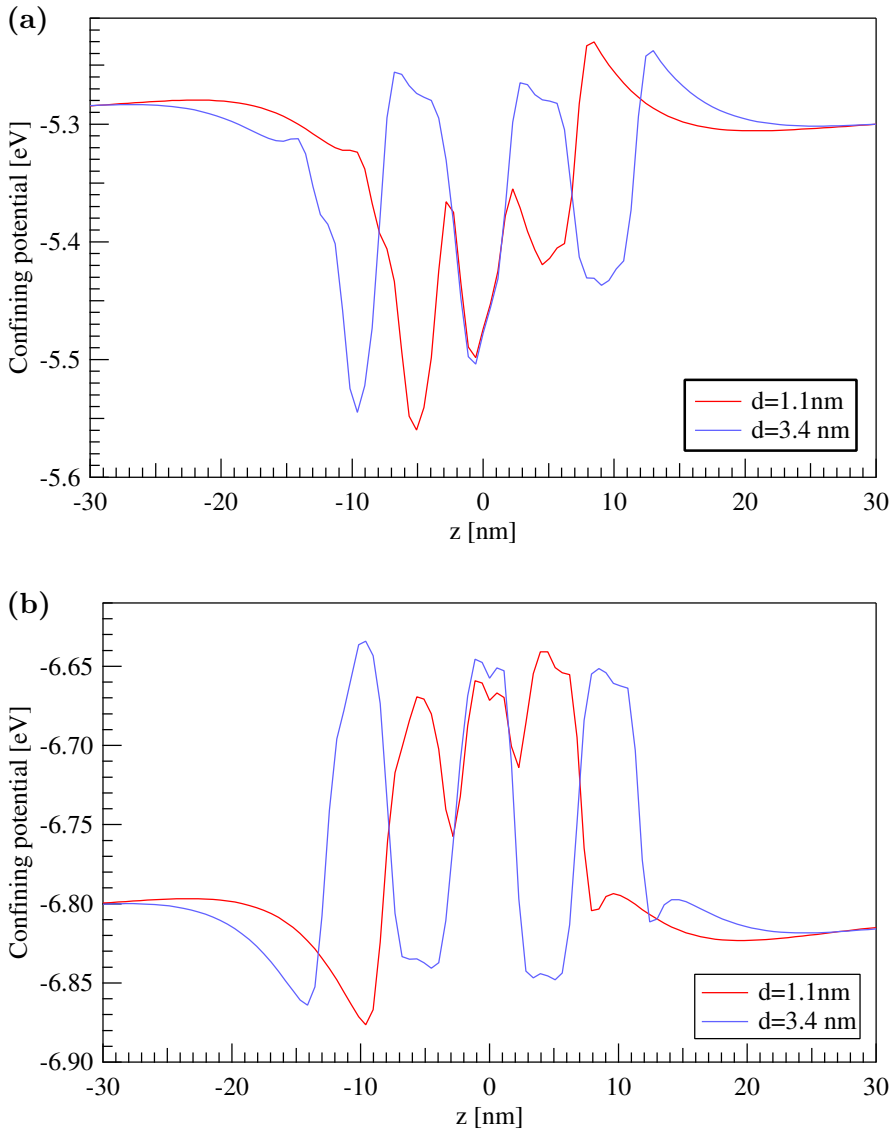

Figure 7.2: Comparison of (a) conduction and (b) valence band profile for two different rings separations.

to the constant value in the GaAs matrix. The bottom ring is squeezed between the wetting layer and middle rings therefore the strain drops down initially and then oscillates with ring separation. Biaxial strain originates from stretching the crystal structure in the growth direction and plays an important role in the vertical ordering of the quantum rings. As a superposition of shear and normal strain contributions it affects predominantly the hole, for which the degeneracy of the heavy and light hole bands at the Γ point is lifted. As the result the top band is moved to a lower hole energy and become similar to the heavy hole, while the other band moves higher in energy. As a consequence the band degeneracy is removed. This is well reflected in the Fig. 7.6a in which one can see almost linear increase of ϵ_{bi} up to 3.4 nm then

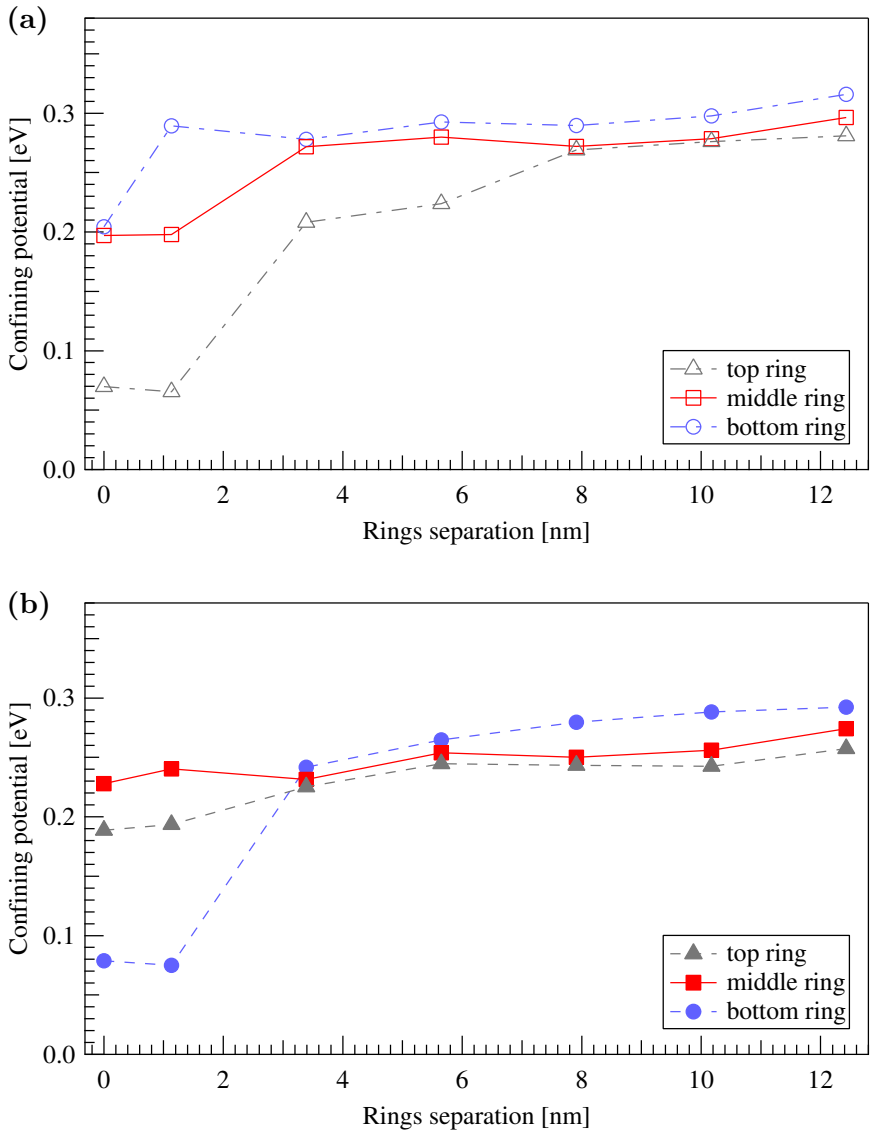

Figure 7.3: Variation of a confinement inside the top, middle and bottom ring for (a) electron and (b) hole as a function of ring separation.

small drop for 5.6 nm follow by virtually constant value for a larger separations. The significant difference of the strain value in the top, bottom and middle rings and also increasing amount of energy required to overcome the barrier between the rings (Fig. 7.4b) localises the hole in the bottom ring most of the time (Fig. 7.1d). In Fig. 7.5a the ground $1s^+$ hole and Fig. 7.5b the ground $1s^+$ electron state are plotted as a function of ring separation for the non-interacting case. In both cases one can notice fast convergence to the single ring energy value. As it was already pointed out, non-uniform strain and asymmetric confinement makes the effective potential wells in the satellite rings deeper or shallower with respect to the central structure. This is not an obstacle for the ground state electrons, which due to their small mass

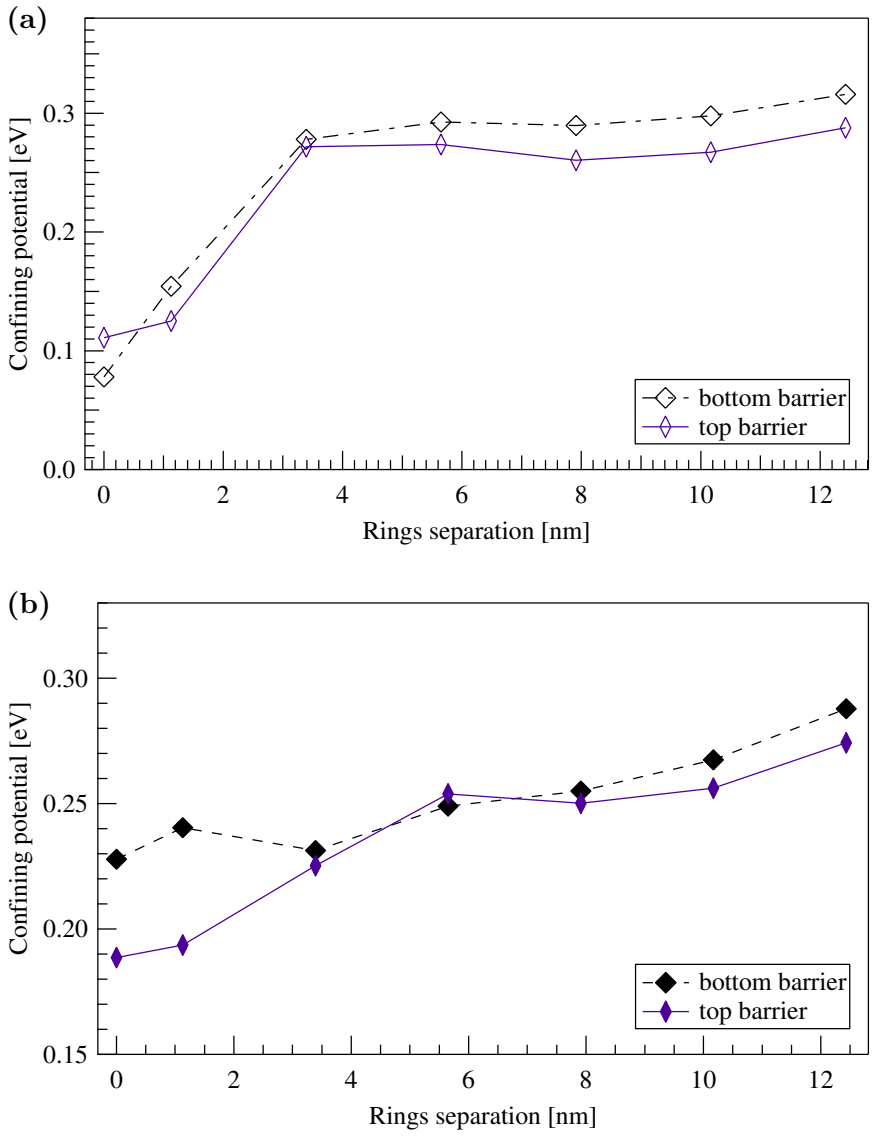

Figure 7.4: Variation of a confinement in the barrier between the rings for (a) electron and (b) hole as a function of ring separation.

and high mobility easily populate all three structures. Also the inter-ring barrier for the electron is characterised by steep, uniformly increasing energy which can be overcome by these charge carriers. The $1s^+$ probability distribution for the hole is predominantly localised in a bottom or eventually top ring. For small separations the energy difference between the bottom and remaining rings is significant. Also, increasing biaxial strain prevents inter-ring migration, however this is not exactly consistent with Fig. 7.1c. The explanation stems from the presence of piezoelectric potentials whose negative regions attracts the positive hole, giving it the boost of energy necessary to compensate the potential difference. Comparison of the ground state energy values for the free electron and hole (Figs. 7.5a and 7.5b) shows a

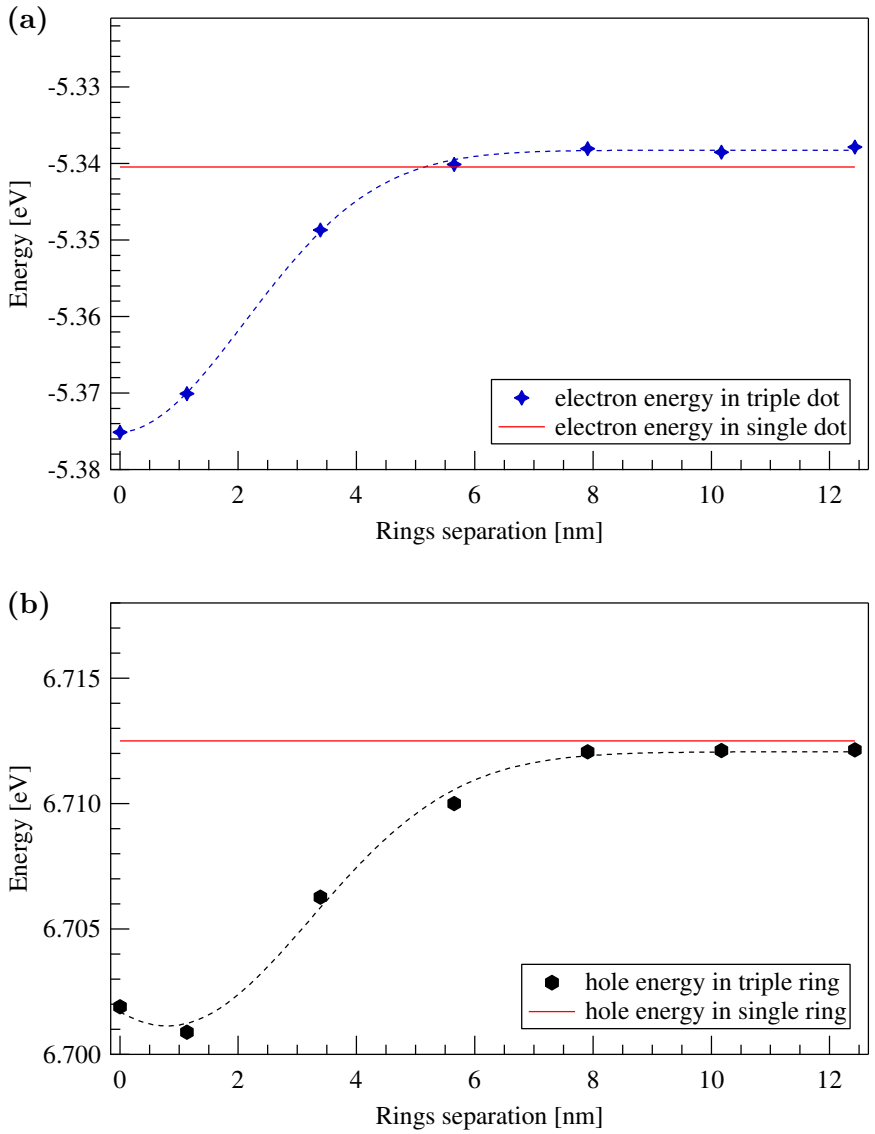

Figure 7.5: Plot of (a) hole and (b) electron energy vs. ring separation in stacked quantum ring. Red horizontal line indicates the electron and hole energy in single ring.

continuous increase for separation greater than 1.1 nm implying that the impact of strain on valence band is larger than on the conduction one.

In Figs. 7.7a and 7.7b the ground state energy of the free particle, exciton and bi-exciton system are plotted for different ring separation. In all three cases the striking feature is a steady increase of the energy of the system crowned with a prominent maximum at 7.9 nm and slow decrease for the larger separations. As this behaviour is present in both the interacting and non-interacting case, this yields that the origin of this phenomenon is directly related to the properties of the vertically stacked ring structure and not the particles in the system. This observation allows us to identify

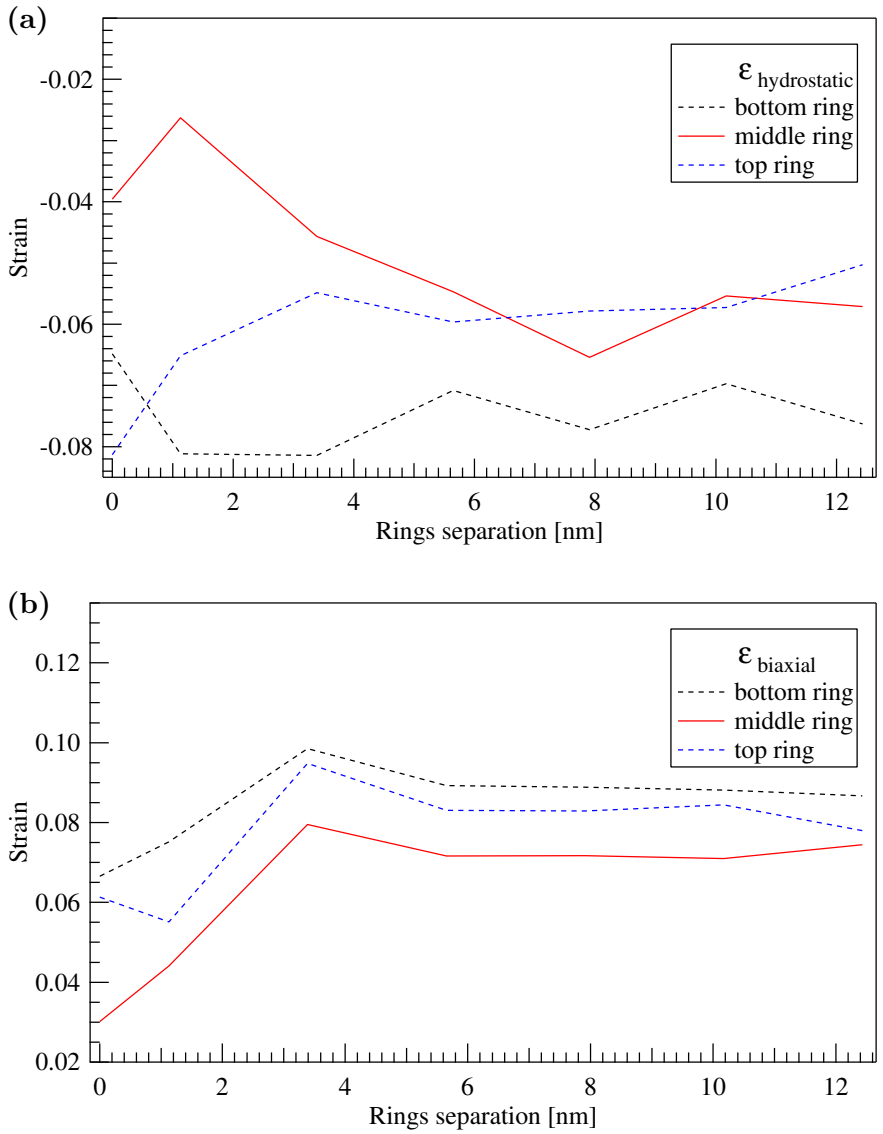

Figure 7.6: Variation of (a) hydrostatic and (b) biaxial strain in the top, middle and bottom structure vs. ring separation in stacked quantum ring.

two coupling regimes, namely tunnelling and strain coupling. In the first regime particles freely tunnel through the inter ring barrier. As one can see in Figs. 7.8a and 7.8b, both exciton and bi-exciton systems are strongly affected by tunnel coupling for ring separation $\leqslant$7.9 nm. The discrepancy in the figures results from the fact that in Fig. 7.8a electron-hole Coulomb energy is plotted while in Fig. 7.8b the exciton-exciton Coulomb energy is depicted. It is clear that Coulomb interactions play an important role in the tunnel coupling process. For small separations the Coulomb energy is small as the electron and hole mostly occupy the same structure but with increasing separation the interaction energy increases as the direct exciton becomes an indirect one localised in different structures. Additionally, piezoelectric fields attract

the electron and hole in an opposite directions, thus the Coulomb system not only must withstand increasing potential in inter-rings barriers but also piezoelectric potential. As a consequence the Coulomb energy increases to the maximum value and when strain coupling takes over the energy drops rapidly to the level characteristic for closely spaced rings as suppressed tunnelling confines the exciton to the same structure. This process is well reflected in the pair correlation function presented in Fig. 7.9. One can see that with increasing ring separation, distance d between electron and hole becomes comparable with a single ring height while for a closely spaced structure d is of order 9-18 nm (Fig. 7.9a). For the non-interacting case picture is more chaotic (Fig. 7.9b). For most ring-separations, due to the strain, the hole is confined to the bottom or top ring. The electron is delocalised all over the structure with finite probability of finding it even in the GaAs matrix. For this reason, the average separation of charge carriers is comparable with total structure vertical extent. These calculations are in excellent agreement with experimental results (black symbols in Fig. 7.7a) presented in [135] and also consistent with simulations reported in [241]. However the tunnelling coupling regime obtained in [241] is much smaller compare to ours. We conclude that this difference arises from a much simpler model of the ring's system with uniform and symmetric potential across all three vertical structures. Also excluding the piezoelectric domain from the model will lead to suppression of tunnelling coupling earlier than in our model. Finally, the In concentration gradient and random alloying profile included in our model results in much stronger strain fluctuation between the rings than assumed in [241].

7.3 Recombination rates in stacked quantum rings

In semiconductor nanostructures charge can be carried by both the electrons in the conduction band and holes in the valence band. The electrons and holes can be introduced to the system by diffusing from their reservoirs. This can be achieved by using over-doped semiconductors or an ionised dopant originating from material surrounding a potential well [242]. Alternatively the electron and hole pairs can be generated by radiative excitation in which a photon of energy greater than the energy band gap is absorbed in the valence band of semiconductor. Photons are generated by laser pulses which allows for control of the electron and hole concentrations as with excitation, recombination takes place, decreasing number of excitons [243, 244].

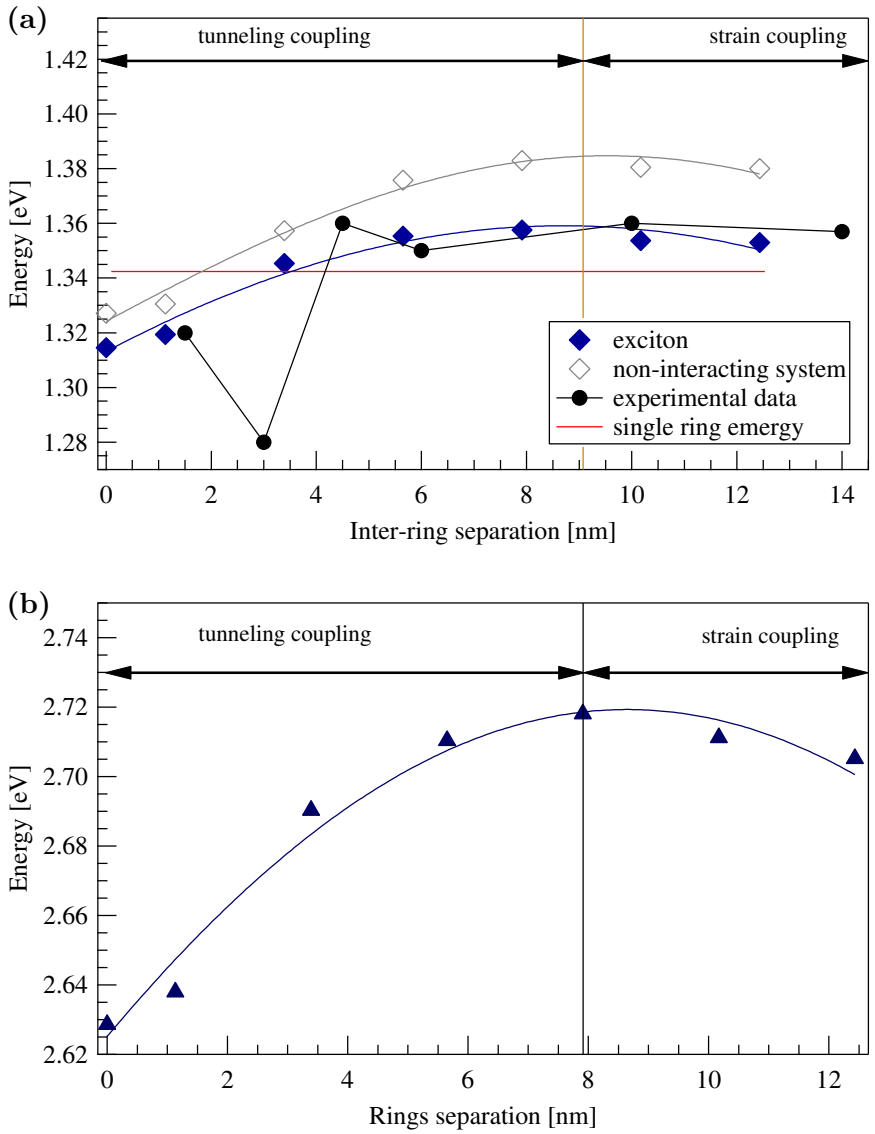

Figure 7.7: Plot of (a) hole and (b) electron energy vs. ring separation in stacked quantum ring. Red horizontal line indicates the electron and hole energy in single ring.

The electron and hole carry an opposite charge, therefore the Coulomb interaction between them is attractive in nature. Because of this, the electron and hole can form bound states with the centre-of-mass free to move in quantum wires [245–247], unlike a system of two identical electrons. Excitons are also observed in quantum wells, dots and rings [248–252].

Due to the quantum confinement effect the energy of an exciton in a quantum nanostructure is higher than in a bulk semiconductor of the same type [253]. Additionally, recombination energy depends strongly on a quantum state of an exciton. The excitonic states in which recombination take place by emission of a photon are called

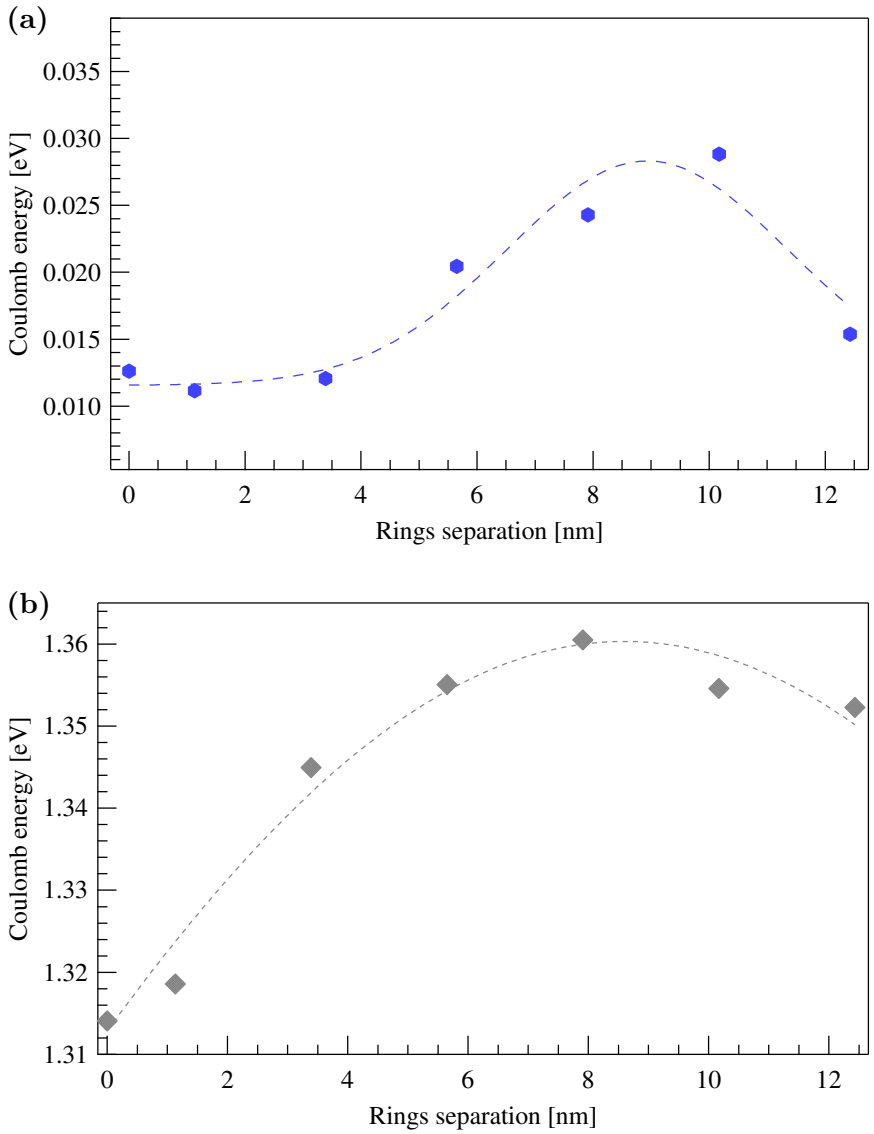

Figure 7.8: Change of Coulomb energy for (a) exciton and (b) bi-exciton in vertically stacked quantum ring with inter-ring distance. For the exciton the Coulomb energy is calculated as difference between non-interacting and interacting system. In bi-exciton case we plot interaction energy between two excitons in the system.

optically active states, unlike the optically inactive states in which the recombination energy is dissipated through phonons in the crystal structure.

The recombination rates can be analysed in two different regimes which should clearly influence the bi-exciton to exciton recombination ratio. In the first case, if the electron and hole confinement potential is large, then the excitonic wave function can be treated as a product of the electron and hole wave functions in the structure, weakly affected by the particles Coulomb interaction. This results in the matrix element of the electron and hole wave functions which is present in the recombination rates

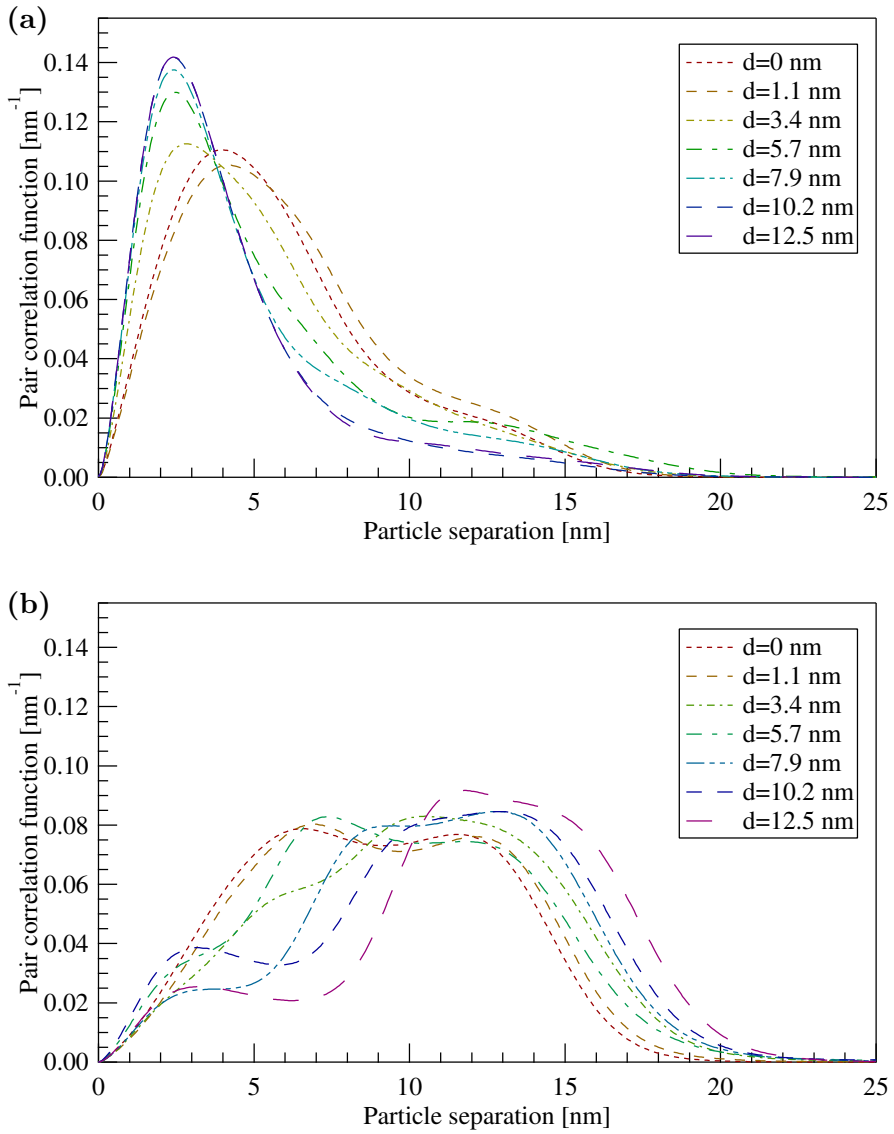

Figure 7.9: Comparison of pair correlation functions for (a) Coulomb interacting and (b) free particle system as a function of quantum rings separation.

and which is identical for bi-exciton and exciton. Because of the number of allowed recombination ways, the bi-exciton should recombine at two times the exciton rate [188]. On the other hand if charge carriers are confined in a weak potential, which is characterised by the binding energy of the exciton being much higher compared to the single-particle level separation in the structure, then the electron-hole pair form a strongly bounded bulk-like quasi-particle. As a consequence the confinement energy decays as the structure gets larger compared to the exciton radius. Also the dominating factor in the dipole matrix element originates from the above quasi-particle which does not depend on the structure size. The formed quasi-particle is described by a coherent wave function spread in the volume of the quantum structure. As a result

the radiative matrix elements add up constructively for excitonic decay. This leads to an increase in the radiative decay rate of the exciton with the structure size, as long as the structure size is less than the wavelength of the emitted radiation. This does not occur in the bi-exciton as the resulting state of the recombining exciton holds off constructive "interference" and lowers the bi-exciton to exciton recombination ratio.

Stacked nanostructures are in the intermediate limit. In this regime the excitonic wave functions are, in general, difficult to separate except for some special models, such as a harmonic potential [254]. Nevertheless, coherently spreading many-particle wave functions result in an increase in decay rates as the size of the system increases [188].

In this section the path integral description of recombination rates will be briefly outlined and its implementation into the PI-QMC technique explained. Then the results for the recombination rates of the exciton and bi-exciton in a self-assembled, vertically coupled quantum ring structure will be presented. We discuss the impact of vertical ring separation on radiative decay rate at a finite temperature in the absence of external electric field.

7.4 Calculation of the recombination rates in stacked rings

In this sections results obtained from calculations of recombination rates in vertically stacked quantum rings will be presented and compared with PL experimental data presented in [255]. We conduct these simulations at 10 K, therefore we assume only recombinations in the ground state. In Fig. 7.10a the absolute recombination rate Γ_X for the exciton is plotted. In the system of unseparated vertically stacked quantum rings the coherent volume of the system is larger compared to the one with an inter-ring barrier. The wetting layer contributes to the overall coherent volume increasing the effective size of the ring. In this virtually single tall structure the heavy hole is mostly confined to the top and bottom structure but the electron is delocalised in the entire volume therefore the electron and hole wave functions overlap and the exciton recombines. When the distance between the three structures increases and the GaAs barrier is formed Γ_X drops due to vertical separation of the charge carriers. The electron still is able to tunnel both laterally and vertically in the system but the hole

affected by biaxial strain, predominantly remains in one of the rings. In this situation the recombination takes place only when the electron wanders to that ring. As long as the system remains in the tunnelling coupling regime the particle can tunnel through the GaAs inter-ring barrier and the coherent volume increases almost linearly. In practice, only the electron is able to overcome the piezoelectric potential and barrier potential between the rings and in the core region, but this is sufficient to frequently occupy the same structure as a dot.

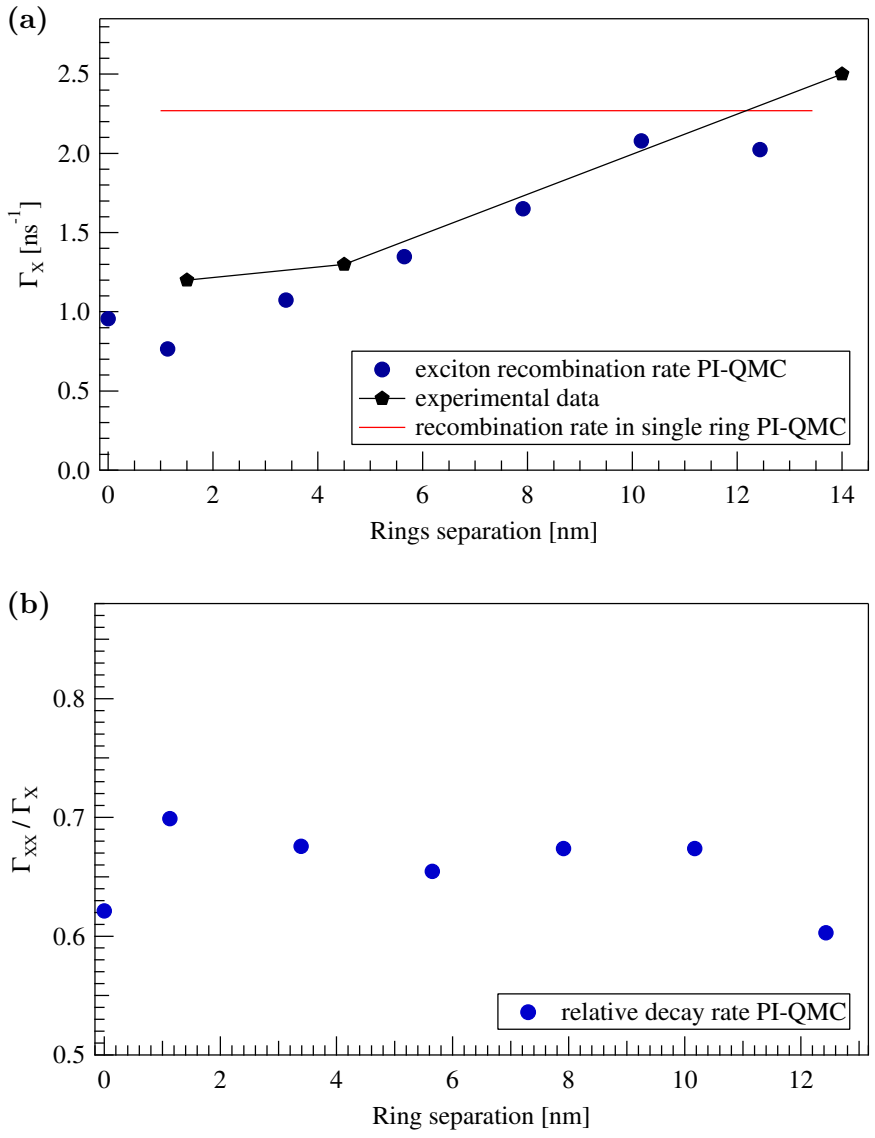

Figure 7.10: Path integral calculation of recombination rates for stacked quantum rings. In (a) the absolute decay rate of exciton is plotted together with experimental data from Ref.[255]. In (b) the relative decay rate of bi-exciton and exciton is shown.

In Fig. 7.10b the relative recombination rates Γ_{XX}/Γ_X of the bi-exciton is depicted. On can notice that the situation is opposite compared to that for the exciton.

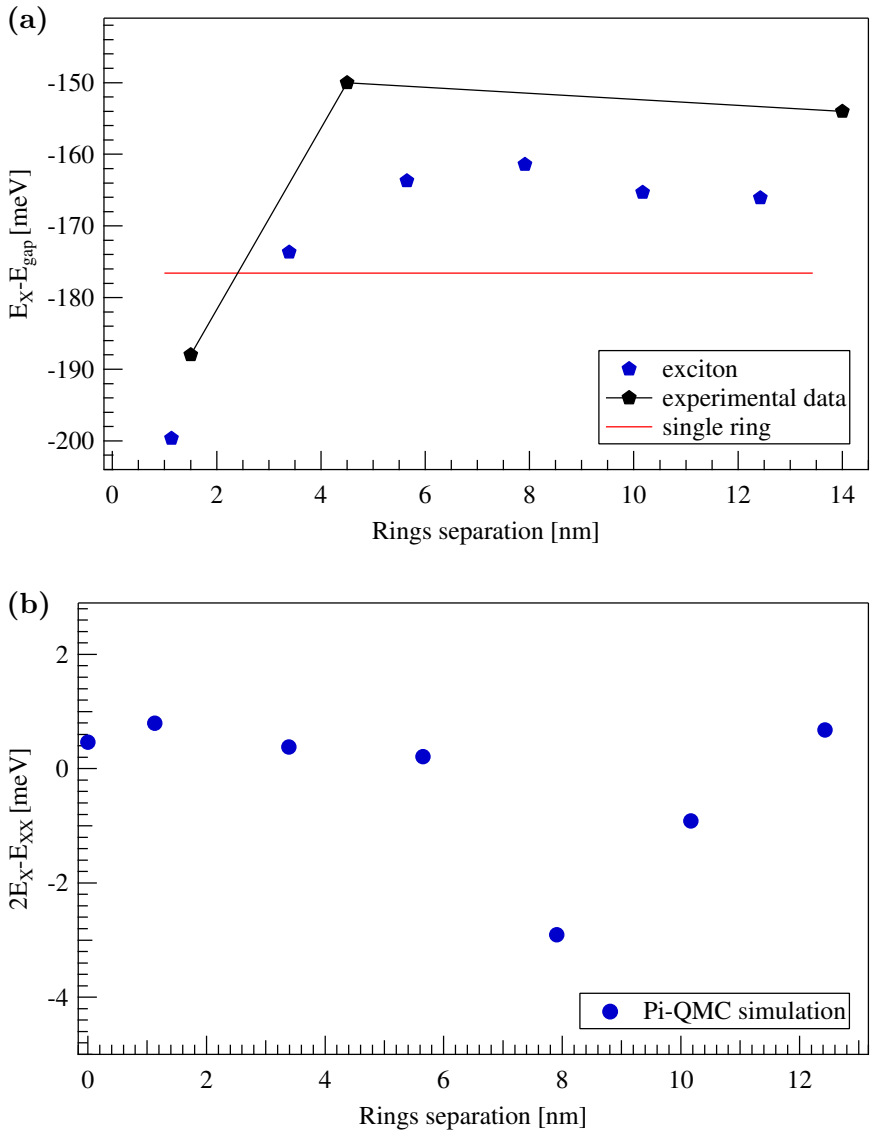

Figure 7.11: Path integral calculation of recombination rates for stacked quantum rings. In Fig. (a) exciton energy at which the exciton PL peak would be detected. (b) the energy shift of the bi-exciton PL peak.

Values of relative rates in stacked rings with 0 nm or larger separation are very similar while intermediate separations demonstrate a decrease in the strongly tunnelling coupling regime with minimal upward trend while closing to strong strain coupling interval. Also, for small ring separation the minimum in the exciton Γ_X corresponds to the maximum in Γ_{XX}/Γ_X.

System size dependence of recombination rates can be investigated by further studying the spatial extent of the exciton wave function in the stacked rings. The recombination rates depend on the coherent volume of the system which is filled by the excitonic wave function. The change of exciton radius, calculated from the

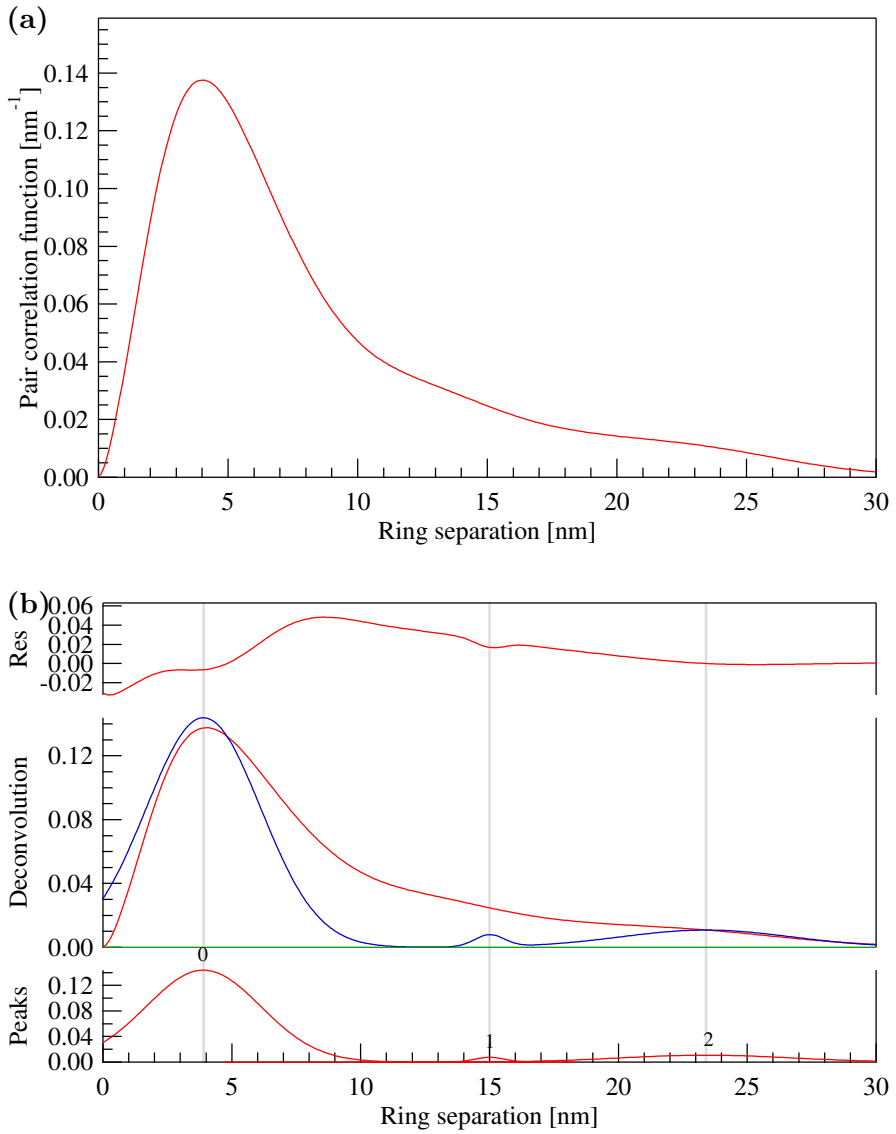

Figure 7.12: Example of deconvolution of pair correlation function. (a) pair correlation function for exciton in triple ring spaced ≈8 nm. (b) deconvolution of the pcf.

deconvolution of the pair correlation function (Fig. 7.12b) is plotted in Fig. 7.13. We can distinguish three possible separation in the tunnelling coupling regime. When the coherent volume is large, which corresponds to the situation in which three rings form one tall structure, the exciton radius can take two values. First value (a) in Fig. 7.13 corresponds to an electron orbiting a hole in the plane of the ring, whose width is ≈7 nm. The second distance (c) can be related to the electron orbiting the structure in a vertical direction or the electron and hole located on two opposite ends of the ring diameter and tunnelling through the rings core. Large coherent volume allows the electron and hole occupy the same one tall structure and their wave functions

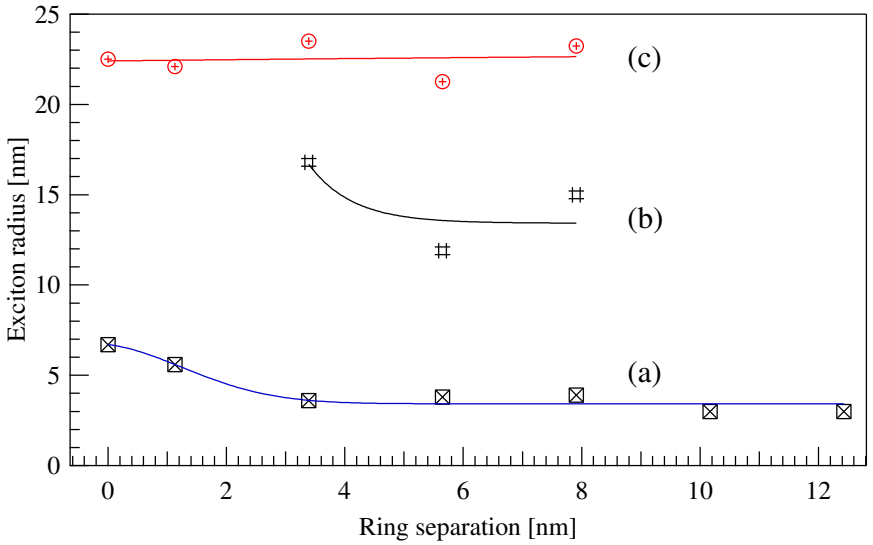

Figure 7.13: Average excitonic radius as a function of ring separation.

can freely spread and frequently overlap. When the barrier between the rings gets thicker, the hole becomes localised in one of the rings, however the electron is able to de-localise in all three rings. Third contribution (b) appears when the electron and hole in two neighbouring rings e.g. the hole in the top (bottom) structure and the electron in the middle one. When the ring separation further increases the length of the exciton radius becomes comparable to the structure height as strain coupling takes over and tunnelling is suppressed. This picture is in excellent agreement with absolute and relative decay rates Γ_X and also the tunnelling-strain coupling model discussed earlier. Recombination rates are smaller for tall structures as the probability of the electron and hole wave functions overlapping in a much broader well (three connected rings) is smaller than in a well corresponding to the single ring. When the coherence volume increases the decay ratio Γ_X also increases. On the other hand the relative decay ratio Γ_{XX}/Γ_X decreases. This is a really interesting and peculiar situation. The exciton in the vertically stacked quantum ring system appears to show all possible confinement limits with the average signature indicating weak confinement which corresponds to $\Gamma_{XX}/\Gamma_X \approx 0.7$. With increasing ring separation the excitonic radius demonstrates saturation towards its bulk value ≈ 12 nm Fig. 7.13(b). According to these properties of the wave function the system is in the strong confinement limit. However branch (c) in this same time indicates a very low confinement characteristic for the exciton bouncing around the rings. Apparently the relative bi-exciton ratio cannot be tuned only by ring separation as the range of relative change is rather small ($\Gamma_{XX}/\Gamma_X \approx$ from 0.6 to 0.7) however introduction of different ring parameters

together with an inter-ring separation may increase electronic correlation and improve the above ratio.

Our calculations for the exciton recombination rate in the stacked rings show good agreement with experimental data [255], however some values of excitonic energies obtained from PI-QMC are much smaller. We account for this through the simplicity of our atomistic model which is an ideal ring with constant height and thickness. Because of this the inter ring separation does not change around the structure. In the experiment [255] the ring structures are far from an ideal circle. Their physical appearance much more resembles a volcano crater with the height varying around the circumference and also non-uniform internal and external radii. These parameters significantly influence the exponential decay length of the wave function into potential barriers and therefore photo-luminescence energies. Nevertheless the proximity of our calculations with experimental data makes our simple model still valid.

Results obtained from PI-QMC simulations for the exciton recombination rates demonstrates more than good agreement with experimental data [255]. Unfortunately the experimental data for bi-exciton recombination rates are not available therefore we are not able to comment on the accuracy of relative decay rate in this case. We calculate the average probability of the recombination rate which can take place in one ring and simultaneously between neighbouring structures in the regime in which electron can easily tunnel between the rings. This corresponds to the weak confinement regime and makes obtaining Γ_{XX}/Γ_X ratio reasonable.

7.5 Lateral switching in vertical electric field

In previous chapter the growth of the vertically coupled quantum rings was discussed and how the inter-ring barrier thickness and strain related valence and conduction band asymmetry affects the structure properties, such as the total energy of the system, the probability distribution of the electron and hole and recombination rates. It was demonstrated that the piezoelectric potential distribution in the stacked structure, which strongly depends on the ring separation, has profound impact on the charge carrier ground state probability distribution and the electron and hole vertical separation. Additionally, piezoelectric field related broken symmetry of the system induces the electron and hole localisation in both the lateral plane and vertical direction.

The geometry and observable properties of the stacked structure are usually "hard coded" during the growth process by altering the growth parameters. This passive method leaves a little room for any further adjustment if such are needed in an experiment. Active control such a system, through application of an external electric field could offer additional degrees of freedom and result in the switching behaviour similar to the one discussed for the stacked dots.

In this section the impact of an external vertical electric field on the triple ring structure is reported. We continue to investigate the quantum ring system introduced in Section 6.2. The ring separation considered in this chapter is 3.4 nm, but this genuine phenomenon was observed for all the ring separations presented in this thesis.

7.5.1 The vertical electric field induced in plane switching

In Fig. 7.14 the lateral switching of probability distribution in the triple ring structure is presented. This behaviour result, similarly to the switching in the multiple dot, from the interplay between Coulomb interaction, piezoelectric and strain field distribution and orientation of the external electric field. As shown in Fig. 7.14 (a) and (b) this distribution not only rotate 90° in the lateral plane but also changes between (c) top and (d) bottom ring structure. As one can see in Fig. 7.15 four piezoelectric field regions which are rotated by with respect to each other 90° in the top and bottom ring. The piezoelectric regions in the middle ring are very weak compared to the top and bottom structure. Due to these sections which partition ring in quarters the ring has C_{2v} symmetry. Distribution of dominating regions of piezoelectric field is almost identical to the stacked quantum dot. The new feature is a set of smaller inner lobes in the ring core. The large external and smaller internal components are characterised by opposite signs of the field and, as it will be demonstrated, have the potential to creating in plane dipole.

When an external electric field is applied in the growth direction [001], due to an opposite charge, the electron-hole system is polarised and the vertical dipole is formed Fig 7.16. The external electric field forces the electron and hole to localise in the top and bottom ring, depending on the field orientation. One can observe that the value of the dipole moment can change only between $\pm 40\,\mathrm{kV/cm}$. After that it becomes constant. This is due to the vertical extent of the ring structure and the

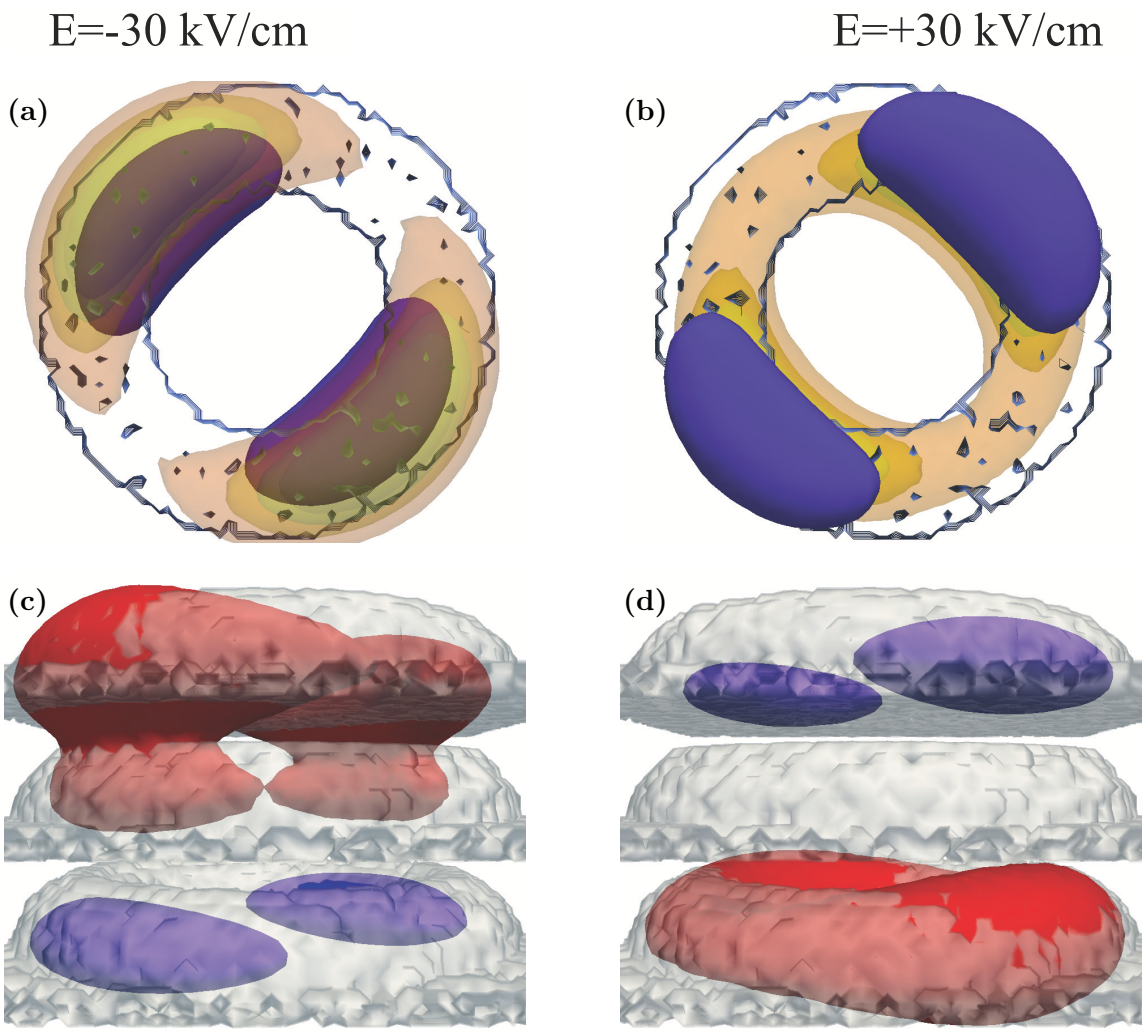

Figure 7.14: Lateral switching in a vertically coupled ring for two different orientations of the electric field. In Fig. (a) and (b) lateral switching in the [110] plane is illustrated. The external electric field creates indirect exciton which is vertically separated. Changing the orientation of electric field also switches the the charge carriers distribution between (c) the top and (d) bottom ring structure.

GaAs matrix, which forms a potential barrier so high, that even a strong electric field is not sufficient to help charge carriers overcome it.

Application of negative electric field in the vertical direction will induce localisation of the hole in the bottom ring and electron in the top structure. The exciton, which is polarised in the [001] direction, is attracted to the piezoelectric regions in the ring core that align with induced the electron-hole dipole. Indeed, the electron-hole system tends to align with the piezoelectric regions oriented as the dipole itself, in order to lower the energy of the exciton. If the external electric field is inverted then the sign of the dipole changes. Varying the orientation of the electric field will lower

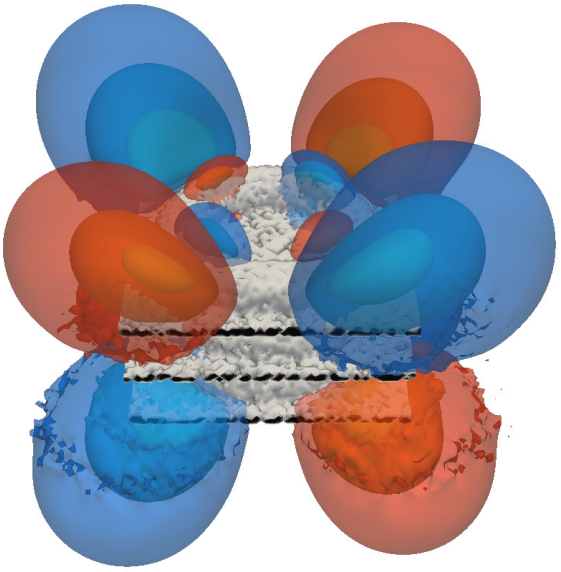

Figure 7.15: Piezoelectric field in triple ring.

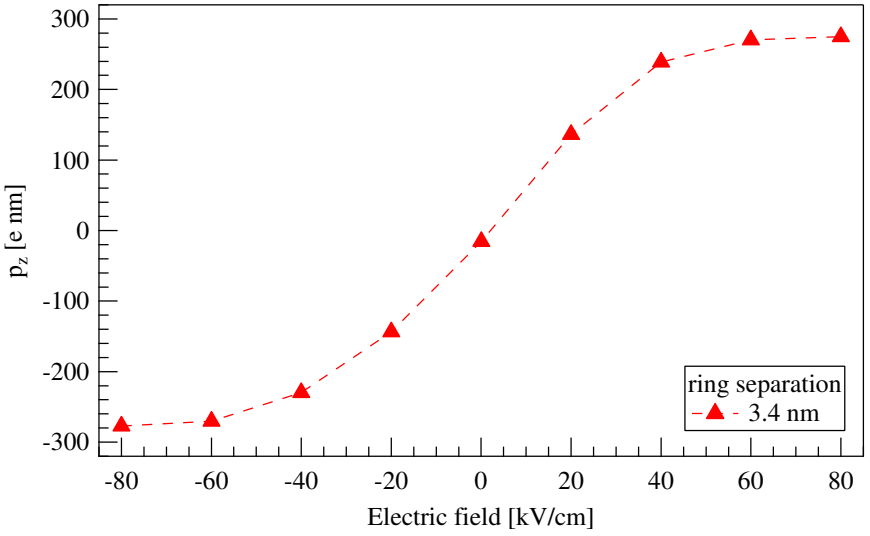

Figure 7.16: Dipole moment in the growth direction, p_z, for different values of electric field.

energetically the [110] or [1$\bar{1}$0] diagonal of the system this will drive the localisation of the excitonic complex in one of these planes. Mirror image of just outlined process takes simultaneously place in the opposite ring Fig. 7.14 (b) and (d). Due to the 90° rotation of the piezoelectric domain in the bottom ring compared to the top structure, lateral switching of the charge probability density distribution will be also rotated. This effect is mostly absent in the middle ring Fig. 7.14 except the electron distribution. The middle structure, depending on the ring separation, is the piezoelectric

potential free or almost free. Absence of this feature and also much smaller difference between the confining potential on the [110] and [1$\bar{1}$0] plane is unable to induce localisation of the exciton. Additionally, the middle structure in not energetically favourable for the hole, even without the electric field the hole avoids localisation in this region.

7.5.2 Lateral polarizability

Similarly to the vertically coupled quantum dot, the switching should be possible to detect in the experiment by measuring lateral polarizability of the exciton in the ring. Application of the electric field induces localisation of the exciton on the [110] diagonal in the top ring and on the [1$\bar{1}$0] plane in the bottom structure. When the orientation of the electric field is inverted the localisation of the exciton changes. As the result, significant change in the polarizability of the excitonic system can be observed.

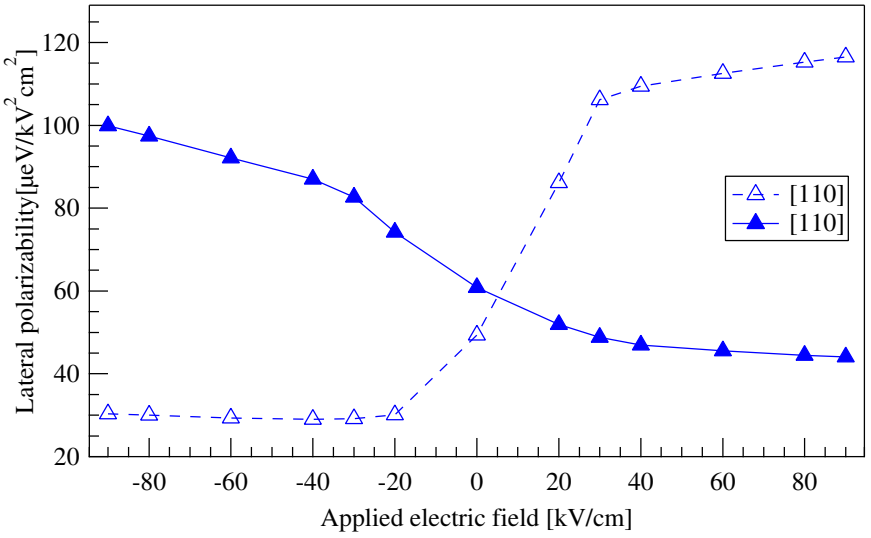

Figure 7.17: Lateral polarizability of exciton in the [110] and [1$\bar{1}$0] direction plotted against applied static, vertical electric field.

Application of an external electric field leads to indirect exciton. The electron and hole are bound together through the Coulomb interaction, however the charge carriers occupy different structures. This is apparent in the Fig. 7.18 in which the pair correlation function is plotted for zero and two opposite values of an external electric field. In the absence of an external electric field the pair correlation function reaches maximum value around 4 nm. This corresponds to the situation in which the electron and hole occupy the same ring structure forming direct exciton. In this situation a

vertical dipole is formed in the same ring structure. Increasing the value of an electric field forces the electron and hole in the opposite directions Fig. 7.16.

As one can see larger value of polarizability is associated with the [110] direction Fig. 7.17. Also the negative permanent dipole that exist even in the absence of an external electric field Fig. 7.16 demonstrates that the exciton prefers the alignment in the $1\bar{1}0$] direction, even if there is no an external field, with the hole shifted towards the bottom of the ring. This is a consequence that the heavy hole is trying to avoid the the regions of a strong compressive biaxial strain which in a quantum ring dominate the top part of the structure. The electron is free to move as the biaxial strain does not affect its mobility Fig. 7.14 (c) and (d). This behaviour also explains the permanent dipole in the quantum ring. Observed in the quantum ring alignment of the exciton probability distribution, and therefore polarizability in the one direction in the absence of an external electric field must be accounted for unique piezoelectric distribution and its interaction with a strain field as this feature was not observed in the stacked quantum dot systems discussed in Chapter 5.

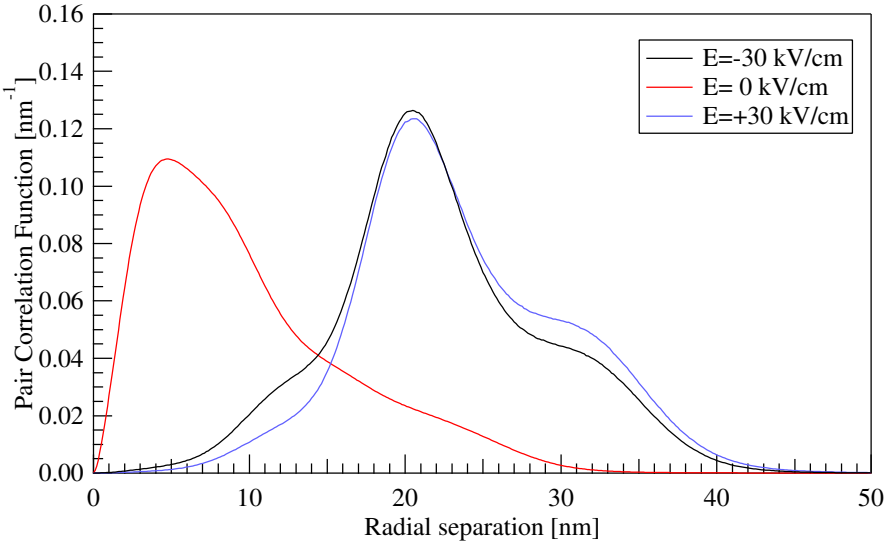

Figure 7.18: Average electron-hole separation pair correlation function plotted for zero and two opposite values of the electric field.

As one can see in Fig. 7.17 the crossing of polarizability between the [110] and $[1\bar{1}0]$ diagonal does not occur at zero electric field. This is consequence of initial localization of the exciton in the $[1\bar{1}0]$. At the point of crossing the both polarizabilities directions are equal and this is due to the electron delocalised around two rings. To provide the connection to the experiment the Stark PL shift is plotted in Fig. 7.19.

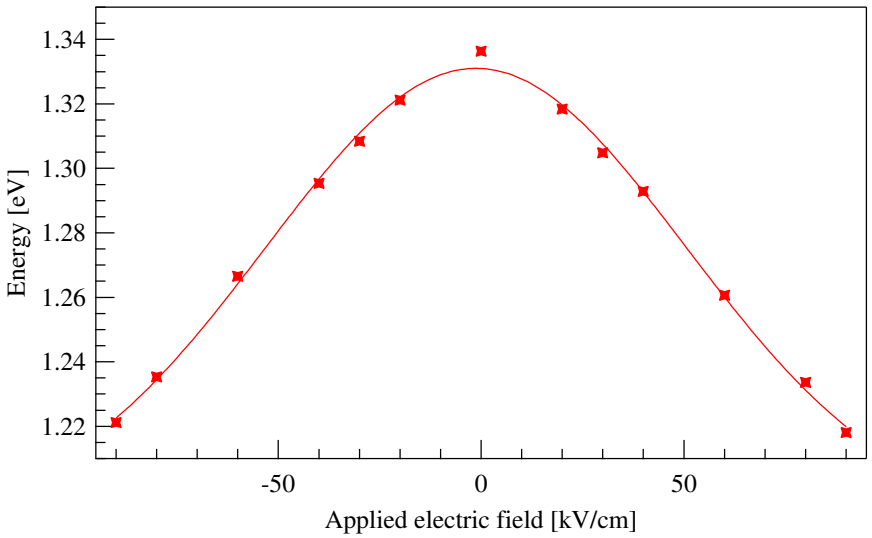

Figure 7.19: Photoluminescence shift for the exciton in the vertically stacked quantum ring as a function of electric field.

7.6 Conclusions

In the first part of this chapter it was found that non-uniform strain calculated from an atomistic model of vertically stacked quantum rings has a significant impact on inter-ring tunnel coupling, possibly leading to the change in the optical absorption. Calculated values of strain varying in all three structures and inter-ring barrier material with increasing ring separation resulted in a steady increase of the electron and hole energy. We observe significant impact of the piezoelectric potential on electron and hole localisation in a stacked structure and their ability to carry out inter-ring tunnelling. The electron, due to its light nature, is mostly delocalized in the all three rings as the impact of piezoelectric regions is partially compensated by electron's mobility. Also the presence of the hole in the top or bottom ring considered with the attracting nature of the Coulomb potential naturally encourages the electron to tunnel and form an exciton. The hole is mostly localised in the bottom or top ring, attracted to the negative piezoelectric regions. Potential in the inter-ring barrier prevents the hole from tunnelling, especially given that the middle structure in the tunnel coupling regime is almost piezoelectric potential free and piezoelectric fields in the top ring are not sufficient to induce localisation in a growth direction. We found that non-uniform strain yields two regions in which exciton and bi-exciton tunnelling properties are driven by different mechanisms.

We adopted a path-integral Monte Carlo approach developed in [188] for studying

exciton and bi-exciton recombination rates in stacked quantum rings. This method, initially designed for study of recombination rates in general 3D potentials for two-band effective mass models of self-assembled quantum dots, appears to produce reasonable results for vertically stacked quantum rings which demonstrates very good agreement with experiment. Our results show that stacked quantum structures may be at the same time in strong and weak confinement regimes, however in both cases Coulomb correlations seem to play an important role. Interesting is that with growing inter-ring separation the recombination rate increases monotonically while relative rates seems to fluctuate in a very narrow interval for all studied rings separations which is characteristics for weak confinement regimes.

It was found, that similarly like for the vertically staked quantum dot, the application of the vertical electric field results in the electron and hole probability distribution switching in the plane perpendicular to the field. The most important difference between the vertically stacked dot and ring system is a zero, otherwise, neutral switch position. In the stacked dot system in the absence of the static electric field the exciton tends to uniform, symmetrical distribution in the dot compare to the elongation in the [110] or $[1\bar{1}0]$ when the field is on. The probability distribution in the ring is somehow always on, therefore one pretty useful degree of freedom is lost. As previously, this effect can be quantified by measurement of the lateral polarizability. The mechanism of the lateral switching in stacked ring will compared to the one in the dot system and possible application discussed.

Chapter 8

Conclusions

In this thesis the results obtained from the simulations using path integral Quantum Monte Carlo for the the interacting electrons and holes were presented. It was demonstrated that the correct treatment of strain and piezoelectric field together with correlations in Coulomb interacting system is extremely important.

In Chapter 2 the theory of the path integral Quantum Monte Carlo (PI-QMC) was described and its relation to the thermal density matrix and statistical Monte Carlo sampling of the path integral using Metropolis algorithm discussed. The ways of improvement of the efficiency of the PI-QMC calculations throughout application of exact sampling of the free particle density matrix and multi-level sampling of the paths. The Pauli's exclusion principle states that two identical fermions can not occupy the same quantum state simultaneously. In the path integral approach this rule is known as the fermion sign problem. It was shown that exclusion principle in PI-QMC simulations can be successfully maintained by introduction of the fixed-node approximation. Finally the implementation of the excitonic recombination rate into path integral quantum Monte Carlo formalism was discussed and it was shown that recombination rate is a ratio of the thermal trace and radiative configurations of the electron-hole pairs.

In Chapter 3 the accuracy of the PI-QMC method was tested against analytical and other frequently used numerical methods. In particular the shifted 1/N expansion method was discussed. Written by myself test codes for two identical, Coulomb interacting fermions, based on this non-perturbative approach demonstrates exceptional agreement with used by us the PI-QMC program and also with other numerical

methods. All these test were coded using analytical expression, parabolic potential for quantum dot and Mexican hat for ring structure.

In Chapter 4, atomistic model of nanostructure computed using Qdot-tools was outlined. The strain resulting from the crystal lattice constant mismatch between InAs and GaAs was discussed and the valence force field method used to relax strain field in the atomistic model explained. The two-band effective mass model Hamiltonian calculated from atomistic model was introduced and effect of the strain on the valence band structure, especial the heavy hole light hole splitting discussed. It was shown that in the highly strained vertical structures the light hole and split-off energy band is significantly shifted with respect to the ground state heavy hole energy, therefore our two-band effective mass model is more than sufficient to correctly simulate the ground state the electron and heavy hole properties. Strain effects in the atomistic model allowed us to calculate piezoelectric domain by solving Poisson equation using a fast Fourier transform. The Poisson solver software initially designed for single structures by former member of Heriot-Watt semiconductor theory group Peter McDonald was then extended and improved by me to handle the vertically stacked structures.

Chapter 5 was dedicated to the lateral switching of the excitonic probability distribution in the vertically stacked quantum dot system. The single and vertically stacked system was introduced with more accurate confinement potential for the electron and hole modified by strain and piezoelectric field inclusion. It was demonstrated that effect of strain and piezoelectric contribution strongly affects the electron and hole probability distribution and exciton localization in the structure. It was found that the effect of piezoelectric field on the exciton localization in the stacked system can be accurately controlled using a vertical electric field. On the other hand this effect is completely absent in the single dot structures. It was pointed out that the lateral switching of the exciton probability distribution could be experimentally observed through polarizability measurements for exciton.

In Chapters 6 and 7 the vertically stacked quantum ring structures were discussed characterised by varying inter-ring separation. The fabrication method was introduced and basic properties outlined. The atomistic model of vertically stacked quantum ring was then introduced and properties of the model such as strain components and resulting from them piezoelectric domain distribution as a function of ring separation were discussed in details. It was shown that charge carriers dynamics in the vertically stacked ring should be analysed in two regimes. For small ring separations

the tunnelling coupling dominates as the inter-ring barrier is small, with larger ring separation the tunnelling coupling is suppressed due to the large ring separation and strong strain field which affects the electron and hole mobility. The recombination rate of the electron and hole in exciton and bi-exciton demonstrates good agreement with these coupling regimes and also shows that the vertically coupled structures are in the intermediate to weak confinement regime. It was also found that a vertical electric field applied to the vertically coupled ring induces exciton lateral switching similar to the one observed in the stacked dots.These results are in excellent agreement with experimental data and other theoretical studies.

The atomistic models studied in this thesis were limited to InGaAs alloys. An obvious extension to the work presented in this thesis would be use of other compounds such as GaSbAs. In this Type-II material the electron is localized in the bulk GaAs material outside the structure while the hole is confined to the nanostructure. This completely different, from InGaAs, distribution would make this system an interesting alternative with which to investigate discussed in Chapters 5 and 7 lateral switching phenomenon and coupling regimes.

One of the main motivations of this thesis is to demonstrate that even two-band effective mass model Hamiltonian PI-QMC can be useful simulation method to explore physical properties of semiconductors leading to interesting predictions and confirmation of experimental data. The path integral quantum Monte Carlo is constantly developing and evolving, this includes its application to low dimension nanostructures, which will open many new potential applications however there is still plenty to do.

Among the routes to improve is the limitation to only two band effective mass model Hamiltonian which allows us study only heavy hole exciton. The improvement can be done by, for instance, implementation of non-parabolic energy bands in PI-QMC.

The second very important problem is treatment of indistinguishable particles. Plenty of interesting problems involves investigation of excited states and full scale many body problems. Unfortunately, deficiency of accurate and efficient technique to treat interacting fermions significantly limits our capabilities of exploring such systems. As was described in Chapter 2 the fermion sign problem can be overcome using two ways. In the first one we can obtain accurate expression by explicit computation of many particle system determinant, albeit efficiency of this approach is low. On the

other hand, using fix-node approximation one can improves efficiency at the cost of accuracy. At the present there is not any other technique which provides both.

Finally, an inclusion of magnetic field is a real challenge, however it could open new possibilities of exploring the single and stacked quantum rings magnetic properties, such as Aharamov-Bohm effect. Implementation of magnetic field into PI-QMC results in the complex phase factor which enters the density matrix, which needs to be sampled and breaks the simulation, even if a simulation of single particle in magnetic field is attempted.

PI-QMC was designed to utilise to the maximum many core machines through efficient parallelization of computation process. Most of the simulations presented in this thesis was done on the Heriot-Watt cluster computers, however quality of the data obtained from simulations performed on Intel i7 cpu demonstrate equally good results with relatively small statistical error. This leads to the conclusion that the PI-QMC run even on the modern desktop computer can be an excellent tool to investigate problems in condensed matter physics and quantum field theory.

Appendix A

Corrections to the energy eigenvalues

A.1 Corrections to the energy eigenvalues

The zeroth-order of λ_n is given by,

$$\lambda_n^{(0)} = \epsilon_0 + \left(n + \frac{1}{2}\hbar\omega\right), \tag{A.1}$$

with ϵ_0 of the form,

$$\epsilon_0 = \frac{\hbar^2\bar{k}^2 - 2\bar{k}\hbar^2(2-a) + \hbar^2(1-a)(3-a)}{8m\bar{k}} + \frac{r_0^2\bar{k}V(r_0)}{Q}. \tag{A.2}$$

The higher order corrections to the energy eigenvaluse calculated using shifted 1/N expansion are presented below, following [196]. First-order correction results from the diagonal terms of matrix element $V_{ij} \equiv \langle i\,|V|\,j\rangle$,

$$\begin{aligned}\lambda_n^{(1)} = V_{nn} = \frac{1}{\bar{k}}[(1+2n)\tilde{\mu_2} + 3(1+2n+2n^2)\tilde{\mu_4} \\ +\frac{1}{\bar{k}^2}\left[(1+2n)\tilde{\zeta_2} + 3(1+2n+2n^2)\tilde{\zeta_4} + 5(3+8n+6n^2+4n^3)\tilde{\zeta_6}\right]\end{aligned} \tag{A.3}$$

Second correction results from the product of matrix elements,

$$\lambda_n^{(2)} = \sum_{i\neq n} \frac{V_{ni}V_{in}}{\lambda_{ni}} = -\frac{1}{\bar{k}\hbar\omega}[\tilde{\mu_1^2} + 6(1+2n)\tilde{\mu_1}\tilde{\mu_3} + (11+30n+30n^2)\tilde{\mu_3^2}]$$
$$-\frac{1}{\bar{k}^2\hbar\omega}[(1+2n)\tilde{\mu_2^2} + 12(1+2n+2n^2)\tilde{\mu_2}\tilde{\mu_4} + 2(21+59n+51n^2+34n^3)\tilde{\mu_4^2}$$
$$+2\tilde{\mu_1}\tilde{\zeta_1} + 6(1+2n)\tilde{\mu_1}\tilde{\zeta_3} + 30(1+2n+2n^2)\tilde{\mu_1}\tilde{\zeta_5} + 6(1+2n)\tilde{\mu_3}\tilde{\zeta_1}$$
$$+2(11+30n+30n^2)\tilde{\mu_3}\tilde{\zeta_3} + 10(13+40n+42n^2+28n^3)\tilde{\mu_3}\tilde{\zeta_5}] + \mathscr{O}\left(\frac{1}{\bar{k}^3}\right), \tag{A.4}$$

where $\lambda_{nj} = \lambda_n^{(0)} - \lambda_j^{(0)}$. Most quantum mechanical handbooks terminates expansions at this point, however another two higher order corrections are possible to derive in the framework of shifted expansion. Third-order correction is calculated using,

$$\lambda_n^{(3)} = \sum_{i,j\neq n} \frac{V_{ni}V_{ij}V_{jn}}{\lambda_{ni}\lambda_{nj}} - V_{nn}\sum_{i\neq n}\frac{V_{ni}V_{in}}{(\lambda_{ni})^2}$$
$$= \frac{1}{(\bar{k}\hbar\omega)^2}[4\tilde{\mu_1^2}\tilde{\mu_2} + 36(1+2n)\tilde{\mu_1}\tilde{\mu_2}\tilde{\mu_3} + 8(11+30n+30n^2)\tilde{\mu_2}\tilde{\mu_3^2} + 24(1+2n)\tilde{\mu_1^2}\tilde{\mu_4}$$
$$+8(31+78n+78n^2)\tilde{\mu_1}\tilde{\mu_3}\tilde{\mu_4} + 12(57+189n+225n^2+150n^3)\tilde{\mu_3^2}\tilde{\mu_4}] + \mathscr{O}\left(\frac{1}{\bar{k}^3}\right). \tag{A.5}$$

Finally the fourth-order correction is found using following relation,

$$\lambda_n^{(4)} = \sum_{i,j,k\neq n}\frac{V_{nl}V_{ij}V_{jk}V_{kn}}{\lambda_{ni}\lambda_{nj}\lambda_{nk}} - \sum_{i,j\neq n}\frac{V_{ni}(V_{in}V_{nj}+2V_{nn}V_{ij})V_{jn}}{(\lambda_{ni})^2\lambda_{nj}} + |V_{nn}|^2\sum_{i\neq n}\frac{V_{ni}V_{in}}{(\lambda_{ni})^3}$$
$$= -\frac{1}{\bar{k}^2}\frac{1}{(\hbar\omega)^3}[8\tilde{\mu_1}^3\tilde{\mu_3} + 108(1+2n)\tilde{\mu_1}^2\tilde{\mu_3}^2 + 48(11+30n+30n^2)\tilde{\mu_1}\tilde{\mu_3}^3$$
$$+30(31+109n+141n^2+94n^3)\tilde{\mu_3}^4] + \mathscr{O}\left(\frac{1}{\bar{k}^3}\right), \tag{A.6}$$

where,

$$\tilde{\mu_j} = \frac{\mu_j}{(2\alpha)^{j/2}}, \qquad \tilde{\zeta_j} = \frac{\zeta_j}{(2\alpha)^{j/2}}, \qquad \alpha = \frac{m\omega}{\hbar}, \qquad j = 1,2,3,.... \tag{A.7}$$

and where,

$$\omega = \sqrt{\frac{3\hbar^2}{4m^2} + \frac{r_0^4 V''(r_0)}{mQ}} = \frac{\hbar}{2m}\sqrt{3 + \frac{r_0 V''(r_0)}{V'(r_0)}}, \tag{A.8}$$

$$\mu_1 = \frac{(2-a)\hbar^2}{2m}, \tag{A.9}$$

$$\mu_2 = \frac{-3(2-a)\hbar^2}{4m}, \tag{A.10}$$

$$\mu_3 = -\frac{\hbar^2}{2m} + \frac{r_0^5 V^{(3)}(r_0)}{6Q}, \tag{A.11}$$

$$\mu_4 = \frac{5\hbar^2}{8m} + \frac{r_0^6 V^{(4)}(r_0)}{24Q}, \tag{A.12}$$

$$\zeta_1 = -\frac{\hbar^2(1-a)(3-a)}{4m}, \tag{A.13}$$

$$\zeta_2 = \frac{3\hbar^2(1-a)(3-a)}{8m}, \tag{A.14}$$

$$\zeta_3 = \frac{\hbar^2(2-a)}{m}, \tag{A.15}$$

$$\zeta_4 = -\frac{5\hbar^2(2-a)}{4m}, \tag{A.16}$$

$$\zeta_5 = -\frac{3\hbar^2}{4m} + \frac{r_0^7 V^{(5)}(r_0)}{120Q}, \tag{A.17}$$

$$\zeta_6 = \frac{7\hbar^2}{8m} + \frac{r_0^8 V^{(6)}(r_0)}{720Q}. \tag{A.18}$$

Appendix B

Particle in a three-dimensional harmonic oscillator

B.1 Particle in a three-dimensional harmonic oscillator

In this example a single particle is confined to a three-dimensional dimensional, harmonic trap of strength 30 meV at temperature 10 K. The Simple Harmonic Oscillator (SHO) is an important example because the exact analytical solution and density matrix are well known. Here, a one-dimensional harmonic oscillator in thermodynamic equilibrium will be consider for simplicity, as the mean thermal energy $\langle\hat{\mathscr{H}}\rangle$ of an oscillator in three-dimensions is three times that of a one-dimensional oscillator with the same frequency.

A system in thermal equilibrium with a heat reservoir at temperature T is an important example of a statistical mixture. The set of eigenstatets of $\hat{\mathscr{H}}$ contains a broad spectrum of various possible dynamic states. A given eigenstate which contributes with a different statistical weight depends on the eigenvalues of $\hat{\mathscr{H}}$ and is proportional to $\exp\{-\frac{E}{k_B T}\}$, where E is eigenenergy, T is temperature of the system and k_B is the Boltzmann factor. The density operator is used to a system in thermodynamic equilibrium,

$$\rho = \sum_n p_n \rho_n = \sum_n p_n \left|\rho_n\right\rangle\left\langle\rho_n\right| . \tag{B.1}$$

One can define the eigenstate of $\hat{\mathscr{H}}$ as follows $\{|\rho_n\rangle\}$ then, $\hat{\mathscr{H}}\,|\rho_n\rangle = E_n\,|\rho_n\rangle$. Then $p_n = N\exp\{-\frac{E_n}{k_BT}\}$, where the normalization constant N makes the total probability equal to 1.

$$\rho = \sum_n N\exp\{-\frac{E_n}{k_BT}\}\,|\rho_n\rangle\langle\rho_n| = N\exp\{-\frac{\hat{\mathscr{H}}}{k_BT}\}\underbrace{\sum_n |\rho_n\rangle\langle\rho_n|}_{1} = N\exp\{-\frac{\hat{\mathscr{H}}}{k_BT}\}. \tag{B.2}$$

Our intention is to calculate the partition function for the harmonic oscillator. We require $Tr\{\rho\} = Tr\{N\exp\{-\frac{\hat{\mathscr{H}}}{k_BT}\}\} = 1$ then,

$$\begin{aligned} Z = \sum_{n=0}^{\infty}\left\langle \rho_n \left| \exp\{-\frac{\hat{\mathscr{H}}}{k_BT}\}\right| \rho_n\right\rangle &= \sum_{n=0}^{\infty}\exp\left\{-\frac{(n+\frac{1}{2})\hbar\omega}{k_BT}\right\} \\ &= \exp\left\{-\frac{\hbar\omega}{2k_BT}\right\}\sum_{n=0}^{\infty}\exp\left\{-\frac{n\hbar\omega}{k_BT}\right\}. \end{aligned} \tag{B.3}$$

Using the expansion $\frac{1}{1-x} = 1 + x + x^2 + x^3 + \cdots = \sum_{n=0}^{\infty} x^n$, the sum in Eq.(B.3) yields,

$$\sum_{n=0}^{\infty}\exp\left\{-\frac{n\hbar\omega}{k_BT}\right\} = \sum_{n=0}^{\infty}\left(\exp\left\{-\frac{\hbar\omega}{k_BT}\right\}\right)^n = \frac{1}{1-\exp\left\{-\frac{\hbar\omega}{k_BT}\right\}}, \tag{B.4}$$

therefore partition function Z can be expressed as,

$$Z = \frac{\exp\left\{-\frac{\hbar\omega}{2k_BT}\right\}}{1-\exp\left\{-\frac{\hbar\omega}{k_BT}\right\}}. \tag{B.5}$$

The mean energy of the system yields,

$$\begin{aligned} \left\langle\hat{\mathscr{H}}\right\rangle = Tr\left\{\rho\hat{\mathscr{H}}\right\} &= \frac{Tr\left\{exp\left\{-\frac{\hat{\mathscr{H}}}{k_BT}\right\}\hat{\mathscr{H}}\right\}}{Z} \\ = \frac{\sum_{n=0}^{\infty}\left(n+\frac{1}{2}\right)\hbar\omega\exp\left\{-\frac{\left(n+\frac{1}{2}\right)\hbar\omega}{k_BT}\right\}}{Z} &= k_BT^2\frac{1}{Z}\frac{dZ}{dT}. \end{aligned} \tag{B.6}$$

In Eq.(B.6) the following property was used,

$$\frac{dZ}{dT} = \frac{d}{dT}\left(\frac{\sum_{n=0}^{\infty}\left(n+\frac{1}{2}\right)\hbar\omega}{k_BT}\right) = \frac{1}{k_BT^2}\sum_{n=0}^{\infty}\left(n+\frac{1}{2}\right)\hbar\omega\exp\left\{-\frac{\left(n+\frac{1}{2}\right)\hbar\omega}{k_BT}\right\} \tag{B.7}$$

Using Eq.(B.5) one can simplify Eq.(B.7) as follows,

$$\begin{aligned}\frac{dZ}{dT} &= \frac{\hbar\omega}{2k_BT^2}\frac{\exp\left\{-\frac{\hbar\omega}{2k_BT}\right\}}{1-\exp\left\{-\frac{\hbar\omega}{k_BT}\right\}} + \frac{\exp\left\{-\frac{\hbar\omega}{2k_BT}\right\}}{\left(1-\exp\left\{-\frac{\hbar\omega}{k_BT}\right\}\right)^2}\frac{\hbar\omega}{k_BT^2}\exp\left\{-\frac{\hbar\omega}{k_BT}\right\} \\ &= \frac{\hbar\omega}{2k_BT^2}Z + \frac{}{1-\exp\left\{-\frac{\hbar\omega}{k_BT}\right\}}Z\frac{\hbar\omega}{k_BT^2}.\end{aligned} \tag{B.8}$$

Eq.(B.8) leads to Planck's formula (to within a constant $\frac{1}{2}\hbar\omega$) for the mean energy of the quantized oscillator,

$$\langle\mathscr{H}\rangle = \frac{1}{2}\hbar\omega + \frac{\hbar\omega}{\exp\left\{\frac{\hbar\omega}{k_BT}-1\right\}}. \tag{B.9}$$

The energy of such a system is $E(x,p) = \frac{p^2}{2m} + 12m\omega^2x^2$. The mean energy in thermodynamic equilibrium at temperature T takes a form,

$$\langle E\rangle = \frac{\int_{-\infty}^{\infty}\int_{-\infty}^{\infty}E(x,p)\exp\left\{-\frac{E(x,p)}{k_BT}\right\}dxdp}{\int_{-\infty}^{\infty}\int_{-\infty}^{\infty}\exp\left\{-\frac{E(x,p)}{k_BT}\right\}dxdp} = k_BT. \tag{B.10}$$

If the temperature $k_BT \ll \hbar\omega$ then the three-dimensional quantum mechanical harmonic oscillator energy is $\langle\mathscr{H}\rangle = \frac{3}{2}\hbar\omega + 3\hbar\omega\exp\left\{-\frac{\hbar\omega}{k_BT}\right\}$ =45 meV for a 30 meV confining potential. The value of the energy calculated using a $1/N$ shifted expansion yields exactly 45 meV, which corresponds to the ground state of the system. In PI-QMC two different approaches are possible. In the first case the primitive action can be applied, whose convergence to the exact value depends on the number of time-slices used in the simulation; obtained in this manner the value of energy was 44.91±0.098 meV. On the other hand, use of the exact action results in the desired value of 45 meV.

Bibliography

[1] S. Tarucha, D.G. Austing, T. Honda, R. J. van der Hage, and L.P. Kouwenhoven. Shell filling and spin effects in a few electron quantum dot. *Phys. Rev. Lett.*, 77:3613–3616, 1996.

[2] S.M. Reimann and M. Manninen. Electronic structure of quantum dots. *Rev. Mod. Phys.*, 74:1283–1342, 2002.

[3] U. Banin, C.J. Lee, A.A. Guzelian, A.V. Kadavanich, A.P. Alivisatos, W. Jaskolski, G.W. Bryant, A.L. Efros, and M. Rosen. Size-dependent electronic level structure of InAs nanocrystal quantum dots: Test of multiband effective mass theory. *The Journal of Chemical Physics*, 109(6):2306–2309, 1998.

[4] S. Gangopadhyay and B.R. Nag. Energy levels in three-dimensional quantum-confinement structures. *Nanotechnology*, 8(1):14–17, 1997.

[5] C. Schneider, A. Rahimi-Iman, N.Y. Kim, J. Fischer, I.G. Savenko, M. Amthor, M. Lermer, A. Wolf, L. Worschech, V.D. Kulakovskii, I.A. Shelykh, M. Kamp, S. Reitzenstein, A. Forchel, Y. Yamamoto, and S. Hofling. An electrically pumped polariton laser. *Nature*, 497(7449):348–352, 2013.

[6] G. Bastard. *Wave Mechanics Applied to Semiconductor Heterostructures*. Wiley-Blackwell, 1990.

[7] Finite well diagram, . URL `http://ph.qmul.ac.uk/sites/default/files/finitewell.pdf`.

[8] STM picture of single well. URL `http://uk.mathworks.com/matlabcentral/fileexchange/23193-gaas-single-quantum-well/content/GaAs%20QW/GaAs_QW.m`.

[9] P. Harrison. *Quantum Wells, Wires and Dots*. John Wiley Sons, 3rd edition.

[10] Double well diagram, . URL `http://www.hep.manchester.ac.uk/u/forshaw/BoseFermi/`.

[11] Nextnano3 simulation result for double well potential. URL `http://www.nextnano.com/nextnano3/tutorial/1Dtutorial_DoubleQW.htm`.

[12] Bert Lorenz research group. Electron beam lithography. URL `http://www.nano.physik.uni-muenchen.de/research/rep99/Bert/bert.html`.

[13] E.S. Semenova, I.V. Kulkova, S. Kadkhodazadeh, M. Schubert, and K. Yvind. Metal organic vapor-phase epitaxy of InAs/InGaAsP quantum dots for laser applications at 1.5 μm. *Applied Physics Letters*, 99(10):1106, 2011.

[14] L.P. Kouwenhoven, D.G. Austing, and S. Tarucha. Few-electron quantum dots. *Rep. Prog. Phys.*, 64:701–736, 2001.

[15] A.V. Filinov, F.M. Peeters, C. Riva, Y.E. Lozovik, and M. Bonitz. Exciton molecules in quantum wells: Influence of the well width fluctuations. *Few-Body Systems*, 34(1-3):149–154, 2004.

[16] A. Kogan, G. Granger, M.A. Kastner, D. Goldhaber-Gordon, and H. Shtrikman. Singlet-triplet transition in a single-electron transistor at zero magnetic field. *Phys. Rev. B*, 67:113309, 2003.

[17] D.K. Ferry, M. Khoury, C. Gerousis, M.J. Rack, A. Gunther, and S.M. Goodnick. Single-electron charging effects in Si MOS devices. *Physica E: Low-dimensional Systems and Nanostructures*, 9(1):69–75, 2001. Proceedings of the Eleventh International Winterschool on New Developments in Solid State Physics, "New Frontiers in Low-Dimensional Physics".

[18] M. Grundmann. The present status of quantum dot lasers. *Physica E: Low-dimensional Systems and Nanostructures*, 5(3):167–184, 1999.

[19] H.J. Kimble. The quantum internet. *Nature*, 453:1023–1030, 2008.

[20] A. Baskaran and P. Smereka. Mechanisms of stranski-krastanov growth. *Journal of Applied Physics*, 111(4):044321–6, 2012.

[21] W.J. Schaffer, M.D. Lind, S.P. Kowalczyk, and R.W. Grant. Nucleation and strain relaxation at the InAs/GaAs (100) heterojunction. *Journal of Vacuum Science Technology B*, 1(3):688–695, 1983.

[22] D. Leonard, M. Krishnamurthy, C.M. Reaves, S.P. Denbaars, and P.M. Petroff. Direct formation of quantum sized dots from uniform coherent islands of InGaAs on GaAs surfaces. *Applied Physics Letters*, 63(23):3203–3205, 1993.

[23] G.S. Solomon, J.A. Trezza, A.F. Marshall, and J.S. Harris Jr. Vertically aligned and electronically coupled growth induced InAs islands in GaAs. *Phys. Rev. Lett.*, 76:952–955, 1996.

[24] L. Goldstein, F. Glas, J.Y. Marzin, M.N. Charasse, and G. Le Roux. Growth by molecular beam epitaxy and characterization of InAs/GaAs strained layer superlattices. *Applied Physics Letters*, 47(10):1099–1101, 1985.

[25] J. Stangl, V. Holý, and G. Bauer. Structural properties of self-organized semiconductor nanostructures. *Rev. Mod. Phys.*, 76:725–783, 2004.

[26] D.J. Eaglesham and M. Cerullo. Dislocation-free stranski-krastanow growth of Ge on Si(100). *Phys. Rev. Lett.*, 64:1943–1946, 1990.

[27] G.S. Solomon, J.A. Trezza, and J.S. Harris Jr. Effects of monolayer coverage, flux ratio, and growth rate on the island density of InAs islands on GaAs. *Applied Physics Letters*, 66(23):3161–3163, 1995.

[28] D. Leonard, K. Pond, and P.M. Petroff. Critical layer thickness for self-assembled InAs islands on GaAs. *Phys. Rev. B*, 50:11687–11692, 1994.

[29] G.S. Solomon, J.A. Trezza, and J.S. Harris Jr. Substrate temperature and monolayer coverage effects on epitaxial ordering of InAs and InGaAs islands on GaAs. *Applied Physics Letters*, 66(8):991–993, 1995.

[30] F. Klotz. *Spin effects in self-assembled semiconductor quantum dots*. PhD thesis, Technische Universität München, Lehrstuhl für experimentelle Halbleiterphysik E25, Walter Schottky Institut, July 2012.

[31] J. Oshinowo, M. Nishioka, S. Ishida, and Y. Arakawa. Highly uniform InGaAs/-GaAs quantum dots (15 nm) by metalorganic chemical vapor deposition. *Applied Physics Letters*, 65(11):1421–1423, 1994.

[32] A.Y. Cho. Morphology of epitaxial growth of GaAs by a molecular beam method: The observation of surface structures. *Journal of Applied Physics*, 41(7):2780–2786, 1970.

[33] L. Jacak, P. Hawrylak, and A. Wójs. *Quantum Dots (NanoScience and Technology)*. Springer-Verlag, 1998.

[34] L. Chu, M. Arzberger, G. Böhm, and G. Abstreiter. Influence of growth conditions on the photoluminescence of self-assembled InAs/GaAs quantum dots. *Journal of Applied Physics*, 85(4):2355–2362, 1999.

[35] J. Shumway, A.J. Williamson, A. Zunger, A. Passaseo, M. DeGiorgi, R. Cingolani, M. Catalano, and P. Crozier. Electronic structure consequences of In/Ga composition variations in self-assembled $In_xGa_{1-x}As$/GaAs alloy quantum dots. *Phys. Rev. B*, 64:125302, 2001.

[36] P. Hawrylak and M. Korkusinski. *Electronic Properties of Self-Assembled Quantum Dots in Single Quantum Dots: Fundamentals, Applications, and New Concepts, Topics in Applied Physics*. Springer-Verlag Berlin Heidelberg New York, 1 edition, 2003.

[37] W. Langbein, P. Borri, U. Woggon, V. Stavarache, D. Reuter, and A.D. Wieck. Control of fine-structure splitting and biexciton binding in $In_xGa_{1-x}As$ quantum dots by annealing. *Phys. Rev. B*, 69:161301, 2004.

[38] D.A.B. Miller, D.S. Chemla, T.C. Damen, A.C. Gossard, W. Wiegmann, T.H. Wood, and C.A. Burrus. Band-edge electroabsorption in quantum well structures: The quantum-confined stark effect. *Phys. Rev. Lett.*, 53:2173–2176, 1984.

[39] S.N. Walck and T.L. Reinecke. Exciton diamagnetic shift in semiconductor nanostructures. *Phys. Rev. B*, 57:9088–9096, 1998.

[40] M. Eto. Electronic structures of few electrons in a quantum dot under magnetic fields. *Japanese Journal of Applied Physics*, 36(6S):3924, 1997.

[41] R.J. Warburton, B.T. Miller, C.S. Dürr, C. Bödefeld, K. Karrai, J.P. Kotthaus, G. Medeiros-Ribeiro, P.M. Petroff, and S. Huant. Coulomb interactions in small charge-tunable quantum dots: A simple model. *Phys. Rev. B*, 58:16221–16231, 1998.

[42] M.E. Levinshtein, S. Rumyantsev, and M.Shur. *Handbook Serieson Semiconductor Parameters*, volume 2. World Scientific, 1996.

[43] K.H. Goetz, D. Bimberg, H. Jürgensen, J. Selders, A.V. Solomonov, G.F. Glinskii, and M. Razeghi. Optical and crystallographic properties and impurity incorporation of $Ga_xIn_{1-x}As$ ($0.44 < x < 0.49$) grown by liquid phase epitaxy, vapor phase epitaxy, and metal organic chemical vapor deposition. *Journal of Applied Physics*, 54(8):4543–4552, 1983.

[44] Y. Arakawa and H. Sakaki. Multidimensional quantum well laser and temperature dependence of its threshold current. *Applied Physics Letters*, 40(11): 939–941, 1982.

[45] D.M. Bruls, P.M. Koenraad, H.W.M. Salemink, J.H. Wolter, M. Hopkinson, and M.S. Skolnick. Stacked low-growth-rate InAs quantum dots studied at the atomic level by cross-sectional scanning tunnelling microscopy. *Applied Physics Letters*, 82(21):3758–3760, 2003.

[46] H.J. Krenner, S. Stufler, M. Sabathil, E.C. Clark, P. Ester, M. Bichler, G. Abstreiter, J.J. Finley, and A. Zrenner. Recent advances in exciton-based quantum information processing in quantum dot nanostructures. *New Journal of Physics*, 7(1):184, 2005.

[47] P.M. Petroff and S.P. DenBaars. Mbe and mocvd growth and properties of self-assembling quantum dot arrays in III-V semiconductor structures. *Superlattices and Microstructures*, 15(1):15–21, 1994.

[48] R. Dingle, W. Wiegmann, and C.H. Henry. Quantum states of confined carriers in very thin $Al_xGa_{1-x}As$ - GaAs - $Al_xGa_{1-x}As$ heterostructures. *Phys. Rev. Lett.*, 33:827–830, 1974.

[49] M.G. Burt. The justification for applying the effective-mass approximation to microstructures. *Journal of Physics: Condensed Matter*, 4(32):6651, 1992.

[50] A. Messiah. *QuantumMechanics*, volume 1 & 2. Dover Publications, 2014.

[51] Optical spectroscopy on a single InGaAs/GaAs quantum dot in the few-exciton limit. *Solid State Communications*, 114(4):227 – 230, 2000.

[52] F. Findeis, M. Baier, A. Zrenner, M. Bichler, G. Abstreiter, U. Hohenester, and E. Molinari. Optical excitations of a self-assembled artificial ion. *Phys. Rev. B*, 63:121309, 2001.

[53] J.J. Finley, P.W. Fry, A.D. Ashmore, A. Lemaître, A.I. Tartakovskii, R. Oulton, D.J. Mowbray, M.S. Skolnick, M. Hopkinson, P.D. Buckle, and P.A. Maksym. Observation of multicharged excitons and biexcitons in a single InGaAs quantum dot. *Phys. Rev. B*, 63:161305, 2001.

[54] D. Heiss. *Spin storage in Quantum Dot Ensembles and Single Quantum Dots.* PhD thesis, Walter Schottky Institut, Technische Universität München, July 2009.

[55] D. Gershoni, J.M. Vandenberg, S.N.G. Chu, H. Temkin, T. Tanbun-Ek, and R.A. Logan. Excitonic transitions in strained-layer $In_xGa_{1-x}As$/GaAs quantum wells. *Phys. Rev. B*, 40:10017–10020, 1989.

[56] S.W. da Silva, Yu.A. Pusep, J.C. Galzerani, D.I. Lubyshev, P.P. Gonzlez-Borrero, and P. Basmaji. Photoluminescence study of spin-orbit-split bound electron states in self-assembled InAs and $In_{0.5}Ga_{0.5}As$ quantum dots. *Journal of Physics: Condensed Matter*, 9(1):L13, 1997.

[57] Y.A. Goldberg and N.M. Schmidt. *Handbook Serieson Semiconductor Parameters*, volume 2. World Scientific, 1999.

[58] P.W. Fry, I.E. Itskevich, S.R. Parnell, J.J. Finley, L.R. Wilson, K.L. Schumacher, D.J. Mowbray, M.S. Skolnick, M. Al-Khafaji, A.G. Cullis, M. Hopkinson, J.C. Clark, and G. Hill. Photocurrent spectroscopy of InAs/GaAs self-assembled quantum dots. *Phys. Rev. B*, 62:16784–16791, 2000.

[59] P.W. Fry, I.E. Itskevich, D.J. Mowbray, M.S. Skolnick, J.J. Finley, J.A. Barker, E.P. O'Reilly, L.R. Wilson, I.A. Larkin, P.A. Maksym, M. Hopkinson, M. Al-Khafaji, J.P.R. David, A.G. Cullis, G. Hill, and J.C. Clark. Inverted electron-hole alignment in InAs-GaAs self-assembled quantum dots. *Phys. Rev. Lett.*, 84:733–736, 2000.

[60] L. Wang, J. Kim, and A. Zunger. Electronic structures of [110]-faceted self-assembled pyramidal InAs/GaAs quantum dots. *Phys. Rev. B*, 59:5678–5687, 1999.

[61] J.A. Barker and E.P. O'Reilly. Theoretical analysis of electron-hole alignment in InAs-GaAs quantum dots. *Phys. Rev. B*, 61:13840–13851, 2000.

[62] T. Köppen, D. Franz, A. Schramm, Ch. Heyn, D. Heitmann, and T. Kipp. Resonant raman transitions into singlet and triplet states in ingaas quantum dots containing two electrons. *Phys. Rev. Lett.*, 103:037402, 2009.

[63] J.J. Finley, A.D. Ashmore, A. Lemaître, D.J. Mowbray, M.S. Skolnick, I.E. Itskevich, P.A. Maksym, M. Hopkinson, and T.F. Krauss. Charged and neutral exciton complexes in individual self-assembled In(Ga)As quantum dots. *Phys. Rev. B*, 63:073307, 2001.

[64] F. Boxberg and J. Tulkki. Theory of the electronic structure and carrier dynamics of strain-induced (Ga, In)As quantum dots. *Reports on Progress in Physics*, 70(8):1425, 2007.

[65] M. Göppert-Mayer. *Ü*ber elementarakte mit zwei quantensprüngen. *Ann. d. Physik*, (9):273, 1931.

[66] D. Gammon, E.S. Snow, B.V. Shanabrook, D.S. Katzer, and D. Park. Fine structure splitting in the optical spectra of single GaAs quantum dots. *Phys. Rev. Lett.*, 76:3005–3008, 1996.

[67] M. Bayer, A. Kuther, A. Forchel, A. Gorbunov, V. B. Timofeev, F. Schäfer, J.P. Reithmaier, T.L. Reinecke, and S.N. Walck. Electron and hole g factors and exchange interaction from studies of the exciton fine structure in $In_{0.60}Ga_{0.40}As$ quantum dots. *Phys. Rev. Lett.*, 82:1748–1751, 1999.

[68] M. Bayer, G. Ortner, O. Stern, A. Kuther, A.A. Gorbunov, A. Forchel, P. Hawrylak, S. Fafard, K. Hinzer, T.L. Reinecke, S.N. Walck, J.P. Reithmaier, F. Klopf, and F. Schäfer. Fine structure of neutral and charged excitons in self-assembled In(Ga)As/(Al)GaAs quantum dots. *Phys. Rev. B*, 65:195315, 2002.

[69] M.E. Ware, E.A. Stinaff, D. Gammon, M.F. Doty, A.S. Bracker, D. Gershoni, V.L. Korenev, Ş. C. Bădescu, Y. Lyanda-Geller, and T.L. Reinecke. Polarized fine structure in the photoluminescence excitation spectrum of a negatively charged quantum dot. *Phys. Rev. Lett.*, 95:177403, 2005.

[70] A.S. Bracker, D. Gammon, and V.L. Korenev. Fine structure and optical pumping of spins in individual semiconductor quantum dots. *Semiconductor Science and Technology*, 23(11):114004.

[71] W.A. Coish and J. Baugh. Nuclear spins in nanostructures. *Physica status solidi (b)*, 246(10):2203–2215, 2009.

[72] M. Bayer, S.N. Walck, T.L. Reinecke, and A. Forchel. Exciton binding energies and diamagnetic shifts in semiconductor quantum wires and quantum dots. *Phys. Rev. B*, 57:6584–6591, 1998.

[73] W. Pauli. *Ü*ber den zusammenhang des abschlusses der elektronengruppen im atom mit der komplexstruktur der spektren. *Zeitschrift für Physik*, 31(1):765–783, 1925.

[74] H.W. van Kesteren, E.C. Cosman, W.A.J.A. van der Poel, and C.T. Foxon. Fine structure of excitons in type-ii GaAs/AlAs quantum wells. *Phys. Rev. B*, 41:5283–5292, 1990.

[75] F. Findeis, M. Baier, E. Beham, A. Zrenner, and G. Abstreiter. Photocurrent and photoluminescence of a single self-assembled quantum dot in electric fields. *Applied Physics Letters*, 78(19), 2001.

[76] S. Sanguinetti, M. Gurioli, E. Grilli, M. Guzzi, and M. Henini. Piezoelectric effects in InAs/GaAs (N11) self-assembled quantum dots. *Thin Solid Films*, 380 (1 & 2):198 – 200, 2000.

[77] A. Patanè, A. Levin, A. Polimeni, F. Schindler, P.C. Main, L. Eaves, and M. Henini. Piezoelectric effects in $In_{0.5}Ga_{0.5}As$ self-assembled quantum dots grown on (311)B GaAs substrates. *Applied Physics Letters*, 77(19):2979–2981, 2000.

[78] G. Wentzel. Eine verallgemeinerung der quantenbedingungen fur die zwecke der wellenmechanik. *Zeitschrift für Physik*, 38(6-7):518–529, 1926.

[79] H.A. Kramers. Wellenmechanik und halbzahlige quantisierung. *Zeitschrift für Physik A - Hadrons and Nuclei*, 39(10):828–840, 1926.

[80] L. Brillouin. La mćanique ondulatoire de schrodinger: une méthode générale de resolution par approximations successives. *Comptes Rendus de l'Academie des Sciences*, 138:24–26, 1926.

[81] P.W. Fry, J.J. Finley, L.R. Wilson, A. Lemaitre, D.J. Mowbray, M.S. Skolnick, M. Hopkinson, G. Hill, and J.C. Clark. Electric-field-dependent carrier capture

and escape in self-assembled InAs/GaAs quantum dots. *Applied Physics Letters*, 77(26):4344–4346, 2000.

[82] E. Beham, A. Zrenner, F. Findeis, M. Bichler, and G. Abstreiter. Level bleaching in a single quantum dot observed by photocurrent spectroscopy. *Physica E: Low-dimensional Systems and Nanostructures*, 13(2-4):139–142, 2002.

[83] D. Heiss, V. Jovanov, M. Bichler, G. Abstreiter, and J.J. Finley. Charge and spin readout scheme for single self-assembled quantum dots. *Phys. Rev. B*, 77: 235442, 2008.

[84] D. Heiss, V. Jovanov, M. Caesar, M. Bichler, G. Abstreiter, and J.J. Finley. Selective optical charge generation, storage, and readout in a single self-assembled quantum dot. *Applied Physics Letters*, 94(7):072108, 2009.

[85] A. Kress, F. Hofbauer, N. Reinelt, M. Kaniber, H.J. Krenner, R. Meyer, G. Böhm, and J.J. Finley. Manipulation of the spontaneous emission dynamics of quantum dots in two-dimensional photonic crystals. *Phys. Rev. B*, 71:241304, 2005.

[86] J.M. Elzerman, R. Hanson, J.S. Greidanus, L.H. Willems van Beveren, S. De Franceschi, L.M.K. Vandersypen, S. Tarucha, and L.P. Kouwenhoven. Tunable few-electron double quantum dots with integrated charge read-out. *Physica E: Low-dimensional Systems and Nanostructures*, 25(2-3):135–141, 2004. Proceedings of the 13th International Winterschool on New Developments in Solid State Physics - Low-Dimensional Systems.

[87] F.R. Waugh, M.J. Berry, D.J. Mar, K.L. Campman R.M. Westervelt, and A.C. Gossard. Single-electron charging in double and triple quantum dots with tunable coupling. *Phys. Rev. Lett.*, 75:705–708, 1995.

[88] M. Tabib-Azar. Microplasma chemical vapor deposition with atomic force microscope. *SPIE Newsroom*, 2013.

[89] M. Bayer, P. Hawrylak, K. Hinzer, S. Fafard, M. Korkusinski, Z. R. Wasilewski, O. Stern, and A. Forchel. Coupling and entangling of quantum states in quantum dot molecules. *Science*, 291(5503):451–453, 2001.

[90] G. Ortner, M. Bayer, A. Larionov, V.B. Timofeev, A. Forchel, Y.B. Lyanda-Geller, T.L. Reinecke, P. Hawrylak, S. Fafard, and Z. Wasilewski. Fine structure

of excitons in InAs/GaAs coupled quantum dots: A sensitive test of electronic coupling. *Phys. Rev. Lett.*, 90:086404, 2003.

[91] G. Ortner, M. Schwab, P. Borri, W. Langbein, U. Woggon, M. Bayer, S. Fafard, Z. Wasilewski, P. Hawrylak, Y.B. Lyanda-Geller, T.L. Reinecke, and A. Forchel. Exciton states in self-assembled InAs/GaAs quantum dot molecules. *Physica E: Low-dimensional Systems and Nanostructures*, 25(2-3):249 – 260, 2004. Proceedings of the 13th International Winterschool on New Developments in Solid State Physics - Low-Dimensional Systems.

[92] H.J. Krenner, M. Sabathil, E.C. Clark, A. Kress, D. Schuh, M. Bichler, G. Abstreiter, and J.J. Finley. Direct observation of controlled coupling in an individual quantum dot molecule. *Phys. Rev. Lett.*, 94:057402, 2005.

[93] A.S. Bracker, M. Scheibner, M.F. Doty, E.A. Stinaff, I.V. Ponomarev, J.C. Kim, L.J. Whitman, T.L. Reinecke, and D. Gammon. Engineering electron and hole tunnelling with asymmetric InAs quantum dot molecules. *Applied Physics Letters*, 89(23), 2006.

[94] E.A. Stinaff, M. Scheibner, A.S. Bracker, I.V. Ponomarev, V.L. Korenev, M.E. Ware, M.F. Doty, T.L. Reinecke, and D. Gammon. Optical signatures of coupled quantum dots. 311(5761):636–639, 2006.

[95] M. Scheibner, M. Yakes, A.S. Bracker, I.V. Ponomarev, M.F. Doty, C.S. Hellberg, L.J. Whitman, T.L. Reinecke, and D. Gammon. Optically mapping the electronic structure of coupled quantum dots. *Nat. Phys*, 4(4):291–295, 2008.

[96] L. Via, R.T. Collins, E.E. Mendez, Wang, and W.I. Excitonic coupling in GaAs/GaAlAs quantum wells in an electric field. *Phys. Rev. Lett.*, 58:832–835, 1987.

[97] L. Goldstein, F. Glas, J.Y. Marzin, M.N. Charasse, and G. Le Roux. Growth by molecular beam epitaxy and characterization of InAs/GaAs strained layer superlattices. *Applied Physics Letters*, 47(10):1099–1101, 1985.

[98] A. Zrenner, L.V. Butov, M. Hagn, G. Abstreiter, G. Böhm, and G. Weimann. Quantum dots formed by interface fluctuations in AlAs/GaAs coupled quantum well structures. *Phys. Rev. Lett.*, 72:3382–3385, 1994.

[99] J. Soubusta, R. Grill, P. Hlídek, M. Zvára, L. Smrčka, S. Malzer, W. Geißelbrecht, and G.H. Döhler. Excitonic photoluminescence in symmetric coupled double quantum wells subject to an external electric field. *Phys. Rev. B*, 60: 7740–7743, 1999.

[100] G. Schedelbeck, W. Wegscheider, M. Bichler, and G. Abstreiter. Coupled quantum dots fabricated by cleaved edge overgrowth: From artificial atoms to molecules. *Science*, 278(5344):1792–1795, 1997.

[101] L. Pfeiffer, K.W. West, H.L. Stormer, J.P. Eisenstein, K.W. Baldwin, D. Gershoni, and J. Spector. Formation of a high quality two-dimensional electron gas on cleaved GaAs. *Applied Physics Letters*, 56(17):1697–1699, 1990.

[102] Q. Xie, A. Madhukar, P. Chen, and N.P. Kobayashi. Vertically self-organized InAs quantum box islands on GaAs (100). *Phys. Rev. Lett.*, 75:2542–2545, 1995.

[103] H. Krenner. *Coherent Quantum Coupling of Excitons in Single Quantum Dots and Quantum Dot Molecules.* PhD thesis, Walter Schottky Institut, Technische Universitaẗ Muñchen, August 2005.

[104] G. Bester, J. Shumway, and A. Zunger. Theory of excitonic spectra and entanglement engineering in dot molecules. *Phys. Rev. Lett.*, 93:047401, 2004.

[105] G. Bester, A. Zunger, and J. Shumway. Broken symmetry and quantum entanglement of an exciton in $In_xGa_{1-x}As$-GaAs quantum dot molecules. *Phys. Rev. B*, 71:075325, 2005.

[106] Z. Yuan, B.E. Kardynal, R.M. Stevenson, A.J. Shields, C.J. Lobo, K. Cooper, N.S. Beattie, D.A. Ritchie, and M. Pepper. Electrically driven single-photon source. *Science*, 295(5552):102–105, 2002.

[107] K. Müller, G. Reithmaier, E.C. Clark, V. Jovanov, M. Bichler, H.J. Krenner, M. Betz, G. Abstreiter, and J.J. Finley. Excited state quantum couplings and optical switching of an artificial molecule. *Phys. Rev. B*, 84:081302, 2011.

[108] R. Krahne, V. Gudmundsson, C. Heyn, and D. Heitmann. Far-infrared excitations below the kohn mode: Internal motion in a quantum dot. *Phys. Rev. B*, 63:195303, 2001.

[109] K.D. Maranowski, A.C. Gossard, K. Unterrainer, and E. Gornik. Far infrared emission from parabolically graded quantum wells. *Applied Physics Letters*, 69 (23):3522–3524, 1996.

[110] P. Matagne, J.P. Leburton, D.G. Austing, and S. Tarucha. Hund's first rule and addition energy spectra of cylindrical quantum dots. *Physica E: Low-dimensional Systems and Nanostructures*, 13(2-4):679–682, 2002.

[111] M. Koskinen, M. Manninen, and S.M. Reimann. Hund's rules and spin density waves in quantum dots. *Phys. Rev. Lett.*, 79:1389–1392, 1997.

[112] S. Sasaki, D.G. Austing, and S. Tarucha. Spin states in circular and elliptical quantum dots. *Physica B: Condensed Matter*, 256-258(2):157–160, 1998.

[113] L.P. Kouwenhoven, T.H. Oosterkamp, S. Tarucha, D.G. Austing, and T. Honda. Coulomb oscillations in few-electron quantum dot. *Physica B: Condensed Matter*, 249-251:191–196, 1998.

[114] J. Motohisa, W.G. van der Wiel, J.M. Elzerman, S. De Franceschi, F. Nakajima, Y. Ogasawara, T. Fukui, and L.P. Kouwenhoven. Low temperature transport in dual-gated SETs fabricated by selective area metalorganic vapor phase epitaxy. *Physica E: Low-dimensional Systems and Nanostructures*, 13(2-4):687–690, 2002.

[115] J.M. Garcia, G. Medeiros-Ribeiro, K. Schmidt, T. Ngo, J.L. Feng, A. Lorke, J. Kotthaus, and P.M. Petroff. Intermixing and shape changes during the formation of InAs self-assembled quantum dots. *Applied Physics Letters*, 71(14): 2014–2016, 1997.

[116] T. Raz, D. Ritter, and G. Bahir. Formation of InAs self-assembled quantum rings on InP. *Applied Physics Letters*, 82(11):1706–1708, 2003.

[117] M.A. Kamarudin, M. Hayne, R.J. Young, Q.D. Zhuang, T. Ben, and S.I. Molina. Tuning the properties of exciton complexes in self-assembled GaSb/GaAs quantum rings. *Phys. Rev. B*, 83:115311, 2011.

[118] J. Cui, Q. He, X.M. Jiang, Y.L. Fan, X.J. Yang, F. Xue, and Z.M. Jiang. Self-assembled SiGe quantum rings grown on Si (001) by molecular beam epitaxy. *Applied Physics Letters*, 83(14):2907–2909, 2003.

[119] A. Lorke, R.J. Luyken, J.M. Garcia, and P.M. Petro. Growth and electronic properties of self-organized quantum rings. *Japanese Journal of Applied Physics*, 40(Part 1, No.3B):1857–1859, 2001.

[120] P. Offermans, P.M. Koenraad, J.H. Wolter, D. Granados, J.M. García, V.M. Fomin, V.N. Gladilin, and J.T. Devreese. Atomic-scale structure of self-assembled In(Ga)As quantum rings in GaAs. *Applied Physics Letters*, 87(13): 131902, 2005.

[121] D. Granados, J.M. García, T. Ben, and S.I. Molina. Vertical order in stacked layers of self-assembled In(Ga)As quantum rings on GaAs (001). *Applied Physics Letters*, 86(7):071918, 2005.

[122] V. Baranwal, G. Biasiol, S. Heun, A. Locatelli, T.O. Mentes, M.N. Orti, and L. Sorba. Kinetics of the evolution of InAs/GaAs quantum dots to quantum rings: A combined x-ray, atomic force microscopy, and photoluminescence study. *Phys. Rev. B*, 80:155328, 2009.

[123] T. Mlakar, G. Biasiol, S.N. Heun, L. Sorba, T. Vijaykumar, G.U. Kulkarni, V. Spreafico, and S. Prato. Conductive atomic force microscopy of InAs/GaAs quantum rings. *Applied Physics Letters*, 92(19):192105, 2008.

[124] D. Granados and J.M. Garcıa. In(Ga)As self-assembled quantum ring formation by molecular beam epitaxy. *Applied Physics Letters*, 82(15):2401–2403, 2003.

[125] H. Pettersson, R. Warburton, and A. Lorke. Excitons in self-assembled quantum ring-like structures. *Physica E: Low-Dimensional Systems and Nanostructures*, 6(1-4):510–513, 2000. ISSN 1386-9477.

[126] R.J. Warburton, C. Schulhauser, D. Haft, C. Schäflein, K. Karrai, J.M. Garcia, W. Schoenfeld, and P.M. Petroff. Giant permanent dipole moments of excitons in semiconductor nanostructures. *Phys. Rev. B*, 65(11):113303, 2002.

[127] D. Granados J. Martńez-Pastor J. Garcîa B. Alén, J. Bosch and L. González. Kinetics of the evolution of InAs/GaAs quantum dots to quantum rings: A combined x-ray, atomic force microscopy, and photoluminescence study. *Phys. Rev. B*, 75:45319, 2007.

[128] I. Galbraith, F.J. Braid, and R.J. Warburton. Magneto-excitons in semiconductor quantum rings. *physica status solidi (a)*, 190(3):781–785.

[129] J.A. Barker, R.J. Warburton, and E.P. O'Reilly. Electron and hole wave functions in self-assembled quantum rings. *Phys. Rev. B*, 69(3):035327, 2004.

[130] In segregation effects during quantum dot and quantum ring formation on GaAs (001). *Microelectronics Journal*, 35(1):7 – 11, 2004. 3rd Ibero American workshop on Nanostructures for applications to Micro and Optoelectronics.

[131] A. Lorke, Johannes L.R., A.O. Govorov, J.P. Kotthaus, J.M. Garcia, and P.M. Petroff. Spectroscopy of nanoscopic semiconductor rings. *Phys. Rev. Lett.*, 84: 2223–2226, 2000.

[132] P.G. McDonald. *Path Integral Quantum Monte Carlo simulations of coulomb correlations in semiconductor nanostructures*. PhD thesis, Heriot-Watt University, School of Engineering and Physical Sciences, August 2012.

[133] A. Lorke and R.J. Luyken. Many-particle ground states and excitations in nanometer-size quantum structures. *Physica B: Condensed Matter*, 256-258(0): 424–430, 1998.

[134] S. Viefers, P. Koskinen, P.D. Singha, and M. Manninen. Quantum rings for beginners: energy spectra and persistent currents. *Physica E: Low-dimensional Systems and Nanostructures*, 21(1):1–35, 2004.

[135] D. Granados, J.M. Garcia, T. Ben, and S.I. Molina. Vertical order in stacked layers of self-assembled In(Ga)As quantum rings on GaAs (001). *Applied Physics Letters*, 86(7), 2005.

[136] V. Ryzhii, I. Khmyrova, V. Mitin, M. Stroscio, and M. Willander. On the detectivity of quantum-dot infrared photodetectors. *Applied Physics Letters*, 78 (22):3523–3525, 2001.

[137] W. Lin, K. Wang, S. Chang, M. Shih, and S. Lin. Type-II GaSb/GaAs coupled quantum rings: Room-temperature luminescence enhancement and recombination lifetime elongation for device applications. *Applied Physics Letters*, 101(3), 2012.

[138] M. Baldo and V. Stojanovic. Optical switching: Excitonic interconnects. *Nat. Photon.*, 3(10):558–560, 2009.

[139] P. Kómár, E.M. Kessler, M. Bishof, L. Jiang, A.S. Sørensen, J. Ye, and M.D. Lukin. A quantum network of clocks. *Nature Physics*, advance online publication, 2014.

[140] G. Grosso, J. Graves, A.T. Hammack, A.A. High, L.V. Butov, M. Hanson, and A.C. Gossard. Excitonic switches operating at around 100 K. *Nature Photonics*, 3(10):577–580, 2009.

[141] A.A. High, E.E. Novitskaya, L.V. Butov, M. Hanson, and A.C. Gossard. Control of exciton fluxes in an excitonic integrated circuit. *Science*, 321(5886):229–231, 2008.

[142] D. Kim, S.G. Carter, A. Greilich, A.S. Bracker, and D. Gammon. Ultrafast optical control of entanglement between two quantum-dot spins. *Nat. Phys.*, 7 (3):223–229, 2011.

[143] J.A. Lott, N.N. Ledentsov, V.M. Ustinov, A.Yu. Egorov, A.E. Zhukov, P.S. Kopapos;ev, Zh.I. Alferov, and D. Bimberg. Vertical cavity lasers based on vertically coupled quantum dots. *Electronics Letters*, 33(13):1150–1151, 1997.

[144] H. Saito, K. Nishi, I. Ogura, S. Sugou, and Y. Sugimoto. Room temperature lasing operation of a quantum dot vertical cavity surface emitting laser. *Applied Physics Letters*, 69(21):3140–3142, 1996.

[145] P. Bhattacharya, S. Ghosh, and A.D. Stiff-Roberts. Quantum dot opto-electronic devices. *Annual Review of Materials Research*, 34(1):1–40, 2004.

[146] H.J. Krenner and P.M. Petroff. Quantum posts with tailored structural, electronic and optical properties for optoelectronic and quantum electronic device applications. *Solid State Communications*, 149(35-36):1386–1394, 2009.

[147] E.A. Stinaff, M. Scheibner, A.S. Bracker, I.V. Ponomarev, V.L. Korenev, M.E. Ware, M.F. Doty, T.L. Reinecke, and D. Gammon. Optical signatures of coupled quantum dots. *Science*, 311(5761):636–639, 2006.

[148] M.F. Doty, J.I. Climente, M. Korkusinski, M. Scheibner, A.S. Bracker, P. Hawrylak, and D. Gammon. Antibonding ground states in InAs quantum-dot molecules. *Phys. Rev. Lett.*, 102:047401, 2009.

[149] Y.H. Huo, B.J. Witek, S. Kumar, J.R. Cardenas, J.X. Zhang, N. Akopian, R. Singh, E. Zallo, R. Grifone, D. Kriegner, R. Trotta, F. Ding, J. Stangl, V. Zwiller, G. Bester, A. Rastelli, and O.G. Schmidt. A light-hole exciton in a quantum dot. *Nature Physics*, 10(1):46–51, 2014.

[150] A. Schliwa, M. Winkelnkemper, and D. Bimberg. Few-particle energies versus geometry and composition of $In_xGa_{1-x}As$/GaAs self-organized quantum dots. *Phys. Rev. B*, 79:075443, 2009.

[151] D.L. Huffaker, G. Park, Z. Zou, O.B. Shchekin, and D.G. Deppe. 1.3 μm room-temperature GaAs-based quantum-dot laser. *Applied Physics Letters*, 73(18): 2564–2566, 1998.

[152] H. Cao, H. Deng, H. Ling, C. Liu, V.A. Smagley, R.B. Caldwell, G.A. Smolyakov, A.L. Gray, L.F. Lester, P.G. Eliseev, and M. Osiński. Highly unidirectional InAs/InGaAs/GaAs quantum-dot ring lasers. *Applied Physics Letters*, 86(20):203117, 2005.

[153] A. Imamoglu, D.D. Awschalom, G. Burkard, D.P. DiVincenzo, D. Loss, M. Sherwin, and A. Small. Quantum information processing using quantum dot spins and cavity qed. *Phys. Rev. Lett.*, 83:4204–4207, 1999.

[154] P.G. McDonald, J. Shumway, and I. Galbraith. Lateral spatial switching of excitons using vertical electric fields in semiconductor quantum rings. *Applied Physics Letters*, 97(17):173101, 2010.

[155] J. Shumway. Shumway research group, . URL `http://shumway.physics.asu.edu/`.

[156] J. Shumway. Path integral quantum Monte Carlo, . URL `http://phys-tools.github.com/pi-qmc`.

[157] J. Shumway. Qdot-tools, . URL `http://code.google.com/p/qdot-tools/`.

[158] R.P. Feynman. Space-time approach to non-relativistic quantum mechanics. *Rev. Mod. Phys.*, 20:367–387, 1948.

[159] R.P. Feynman. Atomic theory of the λ-transition in helium. *Phys. Rev.*, 91: 1291–1301, 1953.

[160] R.P. Feynman. Atomic theory of liquid helium near absolute zero. *Phys. Rev.*, 91:1301–1308, 1953.

[161] R.P. Feynman. The λ-transition in liquid helium. *Phys. Rev.*, 90:1116–1117, 1953.

[162] H.F. Trotter. On the product of semi-groups of operators. *Proc. Amer. Math. Soc.*, 10:545–551, 1959.

[163] B. Simon. *Functional Integration and Quantum Physics*. Number 86 in Pure and Applied Mathematics, a Series of Monographs and Textbooks. Academic Press, 1979.

[164] E.L. Pollock. Properties and computation of the coulomb pair density matrix. *Computer Physics Communications*, 52(1):49–60, 1988.

[165] D.M. Ceperley. Path integrals in the theory of condensed helium. *Rev. Mod. Phys.*, 67:279–355, 1995.

[166] R.G. Storer. Path integral calculation of the quantum statistical density matrix for attractive coulomb forces. *Journal of Mathematical Physics*, 9(6):964–970, 1968.

[167] D.M. Ceperley. Lectures on path integral Monte Carlo. pdf, July 1998.

[168] D.M. Ceperley and E. Pollock. Path integral computation techniques for superfluid ^{4}He. In *In Proceedings of the Elba Conference on Monte Carlo Methods in Theoretical Physics*, pages 35–71, 1997.

[169] K.E. Schmidt and M.A. Lee. High accuracy trotter-formula method for path integral. *Physical Review E*, 51(6, A):5495–5498, 1995.

[170] L. Hostler and R.H. Pratt. Coulomb greens functions in closed form. *Physical Review Letters*, 10(11), 1963.

[171] B. Militzer. *Path Integral Monte Carlo Simulations of Hot Dense Hydrogen*. PhD thesis, Graduate Collage of the University of Illinois at Urbana-Champaign, 2000.

[172] J. Shumway and M. Gilbert. Path integral Monte Carlo simulations of nanowires and quantum point contacts. *Journal of Physics: Conference Series*, 35:190, 2006.

[173] K.R. Glaesemann and L.E. Fried. An improved thermodynamic energy estimator for path integral simulations. *The Journal of Chemical Physics*, 116(14): 5951–5955, 2002.

[174] M. Kastner. Monte Carlo methods in statistical physics: Mathematical foundations and strategies. *Communications in Non-linear Science and Numerical Simulation*, 15(6):1589–1602, 2010.

[175] W.H. Press, S.A. Teukolsky, W.T. Vetterling, and B.P. Flannery. *Numerical Recipes in Fortran 77: The Art of Scientific Computing*, volume 1. Press Syndicate of the University of Cambridge, 2 edition, 1992.

[176] J.A. Rice. *Mathematical Statistics and Data Analysis*. Duxbury Advanced. Thomson Higher Education, 2006.

[177] N. Metropolis, A.W. Rosenbluth, M.N. Rosenbluth, A.H. Teller, and E. Teller. Equation of state calculations by fast computing machines. *The Journal of Chemical Physics*, 21(6):1087–1092, 1953.

[178] R.A. Howard. Dynamic probabilistic system vol 1,. *International Journal for Numerical Methods in Engineering*, 4(2):303–304, 1972.

[179] D. Shin. *Path Integral simulations of semiconductor nanostructures and molecules*. PhD thesis, Department of Physics, Arizona State University, May 2007.

[180] A.W. Sandvik and J. Kurkijärvi. Quantum Monte Carlo simulation method for spin systems. *Phys. Rev. B*, 43:5950–5961, 1991.

[181] M. Troyer and U. Wiese. Computational complexity and fundamental limitations to fermionic quantum Monte Carlo simulations. *Phys. Rev. Lett.*, 94: 170201, 2005.

[182] D.M. Ceperley. Path-integral calculations of normal liquid ^{3}He. *Phys. Rev. Lett.*, 69:331–334, 1992.

[183] P.J. Reynolds, D.M. Ceperley, B.J. Alder, and W.A. Lester. Fixed-node quantum Monte Carlo for molecules. *The Journal of Chemical Physics*, 77(11):5593–5603, 1982.

[184] A.J. Williamson, R.Q. Hood, and J.C. Grossman. Linear-scaling quantum Monte Carlo calculations. *Phys. Rev. Lett.*, 87:246406, 2001.

[185] J.C. Grossman. Benchmark quantum Monte Carlo calculations. *The Journal of Chemical Physics*, 117(4):1434–1440, 2002.

[186] W.M.C. Foulkes, L. Mitas, R.J. Needs, and G. Rajagopal. Quantum Monte Carlo simulations of solids. *Rev. Mod. Phys.*, 73:33–83, 2001.

[187] D.M. Ceperley and L. Mitas. *Quantum Monte Carlo methods in Chemistry*, volume 93. John Wiley Sons, 1996.

[188] M. Wimmer, S.V. Nair, and J. Shumway. Biexciton recombination rates in self-assembled quantum dots. *Phys. Rev. B*, 73:165305, 2006.

[189] T. Takagahara. Biexciton states in semiconductor quantum dots and their non-linear optical properties. *Phys. Rev. B*, 39:10206–10231, 1989.

[190] E. Dekel, D. Gershoni, E. Ehrenfreund, J.M. Garcia, and P.M. Petroff. Carrier-carrier correlations in an optically excited single semiconductor quantum dot. *Phys. Rev. B*, 61:11009–11020, 2000.

[191] R.P. Feynman. *Statistical Mechanics: A Set of Lectures.* The Perseus Books Group, 2^{nd} edition, 1998.

[192] L.D. Mlodinow and M.P. Shatz. Solving the Schrödinger equation with use of 1/N perturbation theory. *Journal of Mathematical Physics*, 25(4):943–950, 1984.

[193] R.A. Ferrell and D.J. Scalapino. Statistical mechanics of one-dimensional Ginzburg-Landau fields. II. A test of the screening approximation 1/N expansion. *Phys. Rev. A*, 9:846–867, 1974.

[194] U. Sukhatme and T. Imbo. Shifted 1/N expansions for energy eigenvalues of the Schrödinger equation. *Phys. Rev. D*, 28:418–420, 1983.

[195] R. Barnana. Shifted 1/N expansion for energy eigenvalues of the exponential cosine screened Coulomb potential. *Phys. Rev. A*, 34:5108–5111, 1986.

[196] T. Imbo, A. Pagnamenta, and U. Sukhatme. Energy eigenstates of spherically symmetric potentials using the shifted 1/N expansion. *Phys. Rev. D*, 29:1669–1681, 1984.

[197] R.M.G. Garcia-Castelan, W.S. Choe, and Y.C. Lee. Correlation energies for two interacting electrons in a harmonic quantum dot. *Phys. Rev. B*, 57:9792–9806, 1998.

[198] Z. Yuan, B.E. Kardynal, R.M. Stevenson, A.J. Shields, C.J. Lobo, K. Cooper, N.S. Beattie, D.A. Ritchie, and M. Pepper. Electrically driven single-photon source. *Science*, 295(5552):102–105, 2002.

[199] V. Haxha and M.A. Migliorato. Calculating strain using atomistic simulations: A review. *Journal of Physics: Conference Series*, 242(1):012001, 2010.

[200] F.C. Frank and J. Van der Merwe. One-dimensional dislocations. *Proc. Roy. Sot. A*, 198(205), 1949.

[201] L. Wang, J. Kim, and A. Zunger. Electronic structures of [110]-faceted self-assembled pyramidal InAs/GaAs quantum dots. *Phys. Rev. B*, 59:5678–5687, 1999.

[202] P.N. Keating. Effect of invariance requirements on the elastic strain energy of crystals with application to the diamond structure. *Phys. Rev.*, 145:637–645, 1966.

[203] M. Harowitz, D. Shin, and J. Shumway. Path-integral quantum Monte Carlo techniques for self-assembled quantum dots. *Journal of Low Temperature Physics*, 140:211–226, 2005.

[204] M.C. Payne, M.P. Teter, D.C. Allan, T.A. Arias, and J.D. Joannopoulos. Iterative minimization techniques for ab-initio total-energy calculations: molecular dynamics and conjugate gradients. *Rev. Mod. Phys.*, 64:1045–1097, 1992.

[205] S. Wei and A. Zunger. Optical properties of zinc-blende semiconductor alloys: Effects of epitaxial strain and atomic ordering. *Phys. Rev. B*, 49:14337–14351, 1994.

[206] J. M. Luttinger. Quantum theory of cyclotron resonance in semiconductors: General theory. *Phys. Rev.*, 102(4):1030–1041, 1956.

[207] M.I. Dyakonov. Basics of semiconductor and spin physics. In MichelI. Dyakonov, editor, *Spin Physics in Semiconductors*, volume 157 of *Springer Series in Solid-State Sciences*, pages 1–28. Springer Berlin Heidelberg, 2008.

[208] C. Pryor. Eight-band calculations of strained InAs/GaAs quantum dots compared with one-, four-, and six-band approximations. *Phys. Rev. B*, 57:7190–7195, 1998.

[209] G. Bester, X. Wu, D. Vanderbilt, and A. Zunger. Importance of second-order piezoelectric effects in zinc-blende semiconductors. *Phys. Rev. Lett.*, 96:187602, 2006.

[210] A.J. Williamson, L.W. Wang, and A. Zunger. Theoretical interpretation of the experimental electronic structure of lens-shaped self-assembled InAs/GaAs quantum dots. *Phys. Rev. B*, 62:12963–12977, 2000.

[211] A. Schliwa, M. Winkelnkemper, and D. Bimberg. Impact of size, shape, and composition on piezoelectric effects and electronic properties of InGa)AsGaAs quantum dots. *Phys. Rev. B*, 76:205324, 2007.

[212] M. Grundmann, O. Stier, and D. Bimberg. InAs/GaAs pyramidal quantum dots: Strain distribution, optical phonons, and electronic structure. *Phys. Rev. B*, 52:11969–11981, 1995.

[213] G. Bester and A. Zunger. Cylindrically shaped zinc-blende semiconductor quantum dots do not have cylindrical symmetry: Atomistic symmetry, atomic relaxation, and piezoelectric effects. *Phys. Rev. B*, 71:045318, 2005.

[214] O. Madelung, editor. *Semiconductors - Basic Data*. Data in Science and Technology. Springer, 2nd revised edition edition, 1996.

[215] N.N Ledentsov, V.A. Shchukin, M. Grundmann, N. Kirstaedter, J. Böhrer, O. Schmidt, D. Bimberg, V.M. Ustinov, A.Yu. Egorov, A.E. Zhukov, P.S. Kop'ev, S.V. Zaitsev, N.Yu. Gordeev, Zh.I. Alferov, A.I. Borovkov, A.O. Kosogov, S.S. Ruvimov, P. Werner, U. Gösele, and J. Heydenreich. Direct formation of vertically coupled quantum dots in stranski-krastanow growth. *Phys. Rev. B*, 54:8743–8750, 1996.

[216] N. Perret, D. Morris, L. Franchomme-Fossé, R. Coîe; S. Fafard, V. Aimez, and J. Beauvais. Origin of the inhomogenous broadening and alloy intermixing in InAs/GaAs self-assembled quantum dots. *Phys. Rev. B*, 62:5092–5099, 2000.

[217] Q. Xie, A. Madhukar, P. Chen, and N.P. Kobayashi. Vertically self-organized InAs quantum box islands on GaAs (100). *Phys. Rev. Lett.*, 75:2542–2545, 1995.

[218] J. Tersoff, C. Teichert, and M.G. Lagally. Self-organization in growth of quantum dot superlattices. *Phys. Rev. Lett.*, 76:1675–1678, 1996.

[219] F. Liu, S.E. Davenport, H.M. Evans, and M.G. Lagally. Self-organised replication of 3d coherent island size and shape in multilayer heteroepitaxial films. *Phys. Rev. Lett.*, 82:2528–2531, 1999.

[220] D.G. Austing, T. Honda, K. Muraki, Y. Tokura, and S. Tarucha. Quantum dot molecules ". *Physica B: Condensed Matter*, 249-251:206–209, 1998.

[221] Z.R. Wasilewski, S. Fafard, and J.P. McCaffrey. Size and shape engineering of vertically stacked self-assembled quantum dots. *Journal of Crystal Growth*, 201-202:1131–1135, 1999.

[222] J. Shumway, A.J. Williamson, A. Zunger, A. Passaseo, M. DeGiorgi, R. Cingolani, M. Catalano, and P. Crozier. Electronic structure consequences of In/Ga composition variations in self-assembled $In_xGa_{1-x}As/GaAs$ alloy quantum dots. *Phys. Rev. B*, 64:125302, 2001.

[223] J.V. Barth, G. Costantini, and K. Klaus. Engineering atomic and molecular nanostructures at surfaces. *Nature*, 437(7059):671–679, 2005.

[224] S. Raymond, J.P. Reynolds, J.L. Merz, S. Fafard, Y. Feng, and S. Charbonneau. Asymmetric stark shift in $Al_xIn_{1-x}As/Al_yGa_{1-y}As$ self-assembled dots. *Phys. Rev. B*, 58:R13415–R13418, 1998.

[225] P.W. Fry, I.E. Itskevich, D.J. Mowbray, M.S. Skolnick, J.J Finley, J.A. Barker, E.P. O'Reilly, L.R. Wilson, I.A. Larkin, P.A. Maksym, M. Hopkinson, M. Al-Khafaji, J.P.R. David, A.G. Cullis, G. Hill, and J.C. Clark. Inverted electron-hole alignment in InAs/GaAs self-assembled quantum dots. *Phys. Rev. Lett.*, 84:733–736, 2000.

[226] P.W. Fry, I.E. Itskevich, S.R. Parnell, J.J. Finley, L.R. Wilson, K.L. Schumacher, D.J. Mowbray, M.S. Skolnick, M. Al-Khafaji, A.G. Cullis, M. Hopkinson, J.C. Clark, and G. Hill. Photocurrent spectroscopy of InAs/GaAs self-assembled quantum dots. *Phys. Rev. B*, 62:16784–16791, 2000.

[227] C. Santori, G.S. Solomon, M. Pelton, and Y. Yamamoto. Time-resolved spectroscopy of multiexcitonic decay in an InAs quantum dot. *Phys. Rev. B*, 65: 073310, 2002.

[228] W. Sheng and J. Leburton. Enhanced intraband stark effects in stacked InAs/-GaAs self-assembled quantum dots. *Applied Physics Letters*, 78(9):1258–1260, 2001.

[229] P.A. Dalgarno, J.M. Smith, J. McFarlane, B.D. Gerardot, K. Karrai, A. Badolato, P.M. Petroff, and R.J. Warburton. Coulomb interactions in single charged self-assembled quantum dots: Radiative lifetime and recombination energy. *Phys. Rev. B*, 77:245311, 2008.

[230] Y.P. Varshni. Temperature dependence of the energy gap in semiconductors. *Physica*, 34:149–154, 1967.

[231] V.M. Fomin, editor. *Physics of quantum rings*. Nanoscience and technology. Springer, 2014.

[232] L. Wendler and V.M. Fomin. Persistent currents in finite-width mesoscopic rings. the role of the interchannel coupling and of the electron-electron interaction. *physica status solidi (b)*, 191(2):409–447, 1995.

[233] I.O. Kulik and E. Recai, editors. volume 559 of *Mathematical and Physical Sciences*. NATO Science Series.

[234] V.M. Fomin. A special issue on modern advancements in experimental and theoretical physics of quantum rings. *Journal of Nanoelectronics and Optoelectronics*, 6(1):1–3, 2011.

[235] N. Sritirawisarn, F.W.M. van Otten, and R. Nötzel. Ordered 1-d and 2-d InAs/InP quantum dot arrays at telecom wavelength. *Journal of Physics: Conference Series*, 245(1):012004, 2010.

[236] W. Lei, Y.H. Chen, P. Jin, X.L. Ye, Y.L. Wang, B. Xu, and Z.G. Wang. Shape and spatial correlation control of InAs-InAlAs-InP (001) nanostructure superlattices. *Applied Physics Letters*, 88(6), 2006.

[237] H. Li, T. Daniels-Race, and M. Hasan. Effects of the matrix on self-organization of InAs quantum nanostructures grown on InP substrates. *Applied Physics Letters*, 80(8):1367–1369, 2002.

[238] N.A.J.M. Kleemans, I.M.A. Bominaar-Silkens, V. M. Fomin, V.N. Gladilin, D. Granados, A.G. Taboada, J.M. García, P. Offermans, U. Zeitler, P.C.M.

Christianen, J.C. Maan, J.T. Devreese, and P.M. Koenraad. Oscillatory persistent currents in self-assembled quantum rings. *Phys. Rev. Lett.*, 99:146808, 2007.

[239] Y. Liu, Z. Yu, B. Jia, Z. Xu, W. Yao, Z. Chen, P. Lu, and L. Han. Strain distributions and electronic structure of three-dimensional InAs/GaAs quantum rings. *Chinese Physics B*, 18(11):4667, 2009.

[240] B. Jia, Z. Yu, Y. Liu, W. Yao, H. Ye, and H. Feng. Strain distribution and electronic structures of the InAs/GaAs quantum ring molecule in an applied electric field. *Science China Physics, Mechanics and Astronomy*, 53(9):1594–1599, 2010.

[241] M. Tadic and F.M. Peeters. Excitonic properties of strained triple quantum-ring molecules. *Phys. Rev. B*, 79:153305, 2009.

[242] H. Norde. Ionized dopant concentrations in silicon-an analytical approach. *Solid-State Electronics*, 38(12):2059 – 2061, 1995.

[243] F. Guffarth, S. Rodt, A. Schliwa, K. Pötschke, and D. Bimberg. Many-particle effects in self-organized quantum dots. *Physica E: Low-dimensional Systems and Nanostructures*, 25(2-3):261–270, 2004. Proceedings of the 13th International Winterschool on New Developments in Solid State Physics - Low-Dimensional Systems.

[244] O.G. Schmidt, A. Rastelli, G.S. Kar, R. Songmuang, S. Kiravittaya, M. Stoffel, U. Denker, S. Stufler, A. Zrenner, D. Grützmacher, B.Y. Nguyen, and P. Wennekers. Novel nanostructure architectures. *Physica E: Low-dimensional Systems and Nanostructures*, 25(2-3):280–287, 2004. Proceedings of the 13th International Winterschool on New Developments in Solid State Physics - Low-Dimensional Systems.

[245] M.H. Szymanska, P.B. Littlewood, and R.J. Needs. Excitons in t-shaped quantum wires. *Phys. Rev. B*, 63:205317, 2001.

[246] R. Schuster, H. Hajak, M. Reinwald, W. Wegscheider, D. Schuh, M. Bichler, and G. Abstreiter. Strongly confined quantum wire states in strained t-shaped GaAs/InAlAs structures. *Physica E: Low-dimensional Systems and Nanostructures*, 21(2-4):236–240, 2004. Proceedings of the Eleventh International Conference on Modulated Semiconductor Structures.

[247] T. Noriaki, S. Chang-Sik, G.K. Tae, H. Kazunori, K. Kazuhiro, and O. Mutsuo. Time-resolved photoluminescence spectra of high-density InGaAs/AlGaAs quantum wire structures. *Physica E: Low-dimensional Systems and Nanostructures*, 21(2-4):300 – 303, 2004. Proceedings of the Eleventh International Conference on Modulated Semiconductor Structures.

[248] M.S. Skolnick and D.J. Mowbray. Recent developments in the physics and applications of self-assembled quantum dots. *Physica E: Low-dimensional Systems and Nanostructures*, 21(2-4):155–163, 2004. Proceedings of the Eleventh International Conference on Modulated Semiconductor Structures.

[249] N. Pauc, V. Calvo, J. Eymery, F. Fournel, and N. Magnea. Two-dimensional electron-hole liquid in single si quantum wells with large electronic and dielectric confinement. *Phys. Rev. Lett.*, 92:236802, 2004.

[250] P.W. Yu, D.C. Reynolds, G.D. Sanders, K.K. Bajaj, C.E. Stutz, and K.R. Evans. Electric-field effects of the excitons in asymmetric triangular $Al_xGa_{1-x}As$-GaAs quantum wells. *Phys. Rev. B*, 43:4344–4348, 1991.

[251] M. Orlita, R. Grill, M. Zvára, G.H. Döhler, S. Malzer, M. Byszewski, and J. Soubusta. Luminescence of coupled quantum wells: effects of indirect excitons in high in-plane magnetic fields. *Phys. Rev. B*, 70:075309, 2004.

[252] W. Heller, U. Bockelmann, and G. Abstreiter. Electric-field effects on excitons in quantum dots. *Phys. Rev. B*, 57:6270–6273, 1998.

[253] R. Heitz, O. Stier, I. Mukhametzhanov, A. Madhukar, and D. Bimberg. Quantum size effect in self-organized InAs/GaAs quantum dots. *Phys. Rev. B*, 62: 11017–11028, 2000.

[254] M. Sugawara. Theory of spontaneous-emission lifetime of wannier excitons in mesoscopic semiconductor quantum disks. *Phys. Rev. B*, 51:10743–10754, 1995.

[255] W. Ouerghui, J. Martinez-Pastor, J. Gomis, M.A. Maaref, D. Granados, and J.M. García. Lateral carrier tunnelling in stacked In(Ga)As/GaAs quantum rings. *The European Physical Journal B - Condensed Matter and Complex Systems*, 54(2):217–223, 2006.